Surface and Deep Hydrography across the Mid-Pleistocene Transition; Multi-proxy paleoceanographic reconstructions from the Southwest Indian Ocean

Aidan Starr

2021

Cardiff University

School of Earth and Environmental Science

Doctor of Philosophy in Earth Sciences

Summary

Studies of the Last Glacial Maximum have demonstrated a vital role for the carbon cycle in regulating climate on glacial-interglacial timescales, in particular emphasising the effects of storage or exhalation of CO_2 from the world's oceans. However the utility of proposed mechanisms over longer timescales, such as Early Pleistocene glacial cycles, remains unclear. The aim of this thesis is to investigate how changes in surface hydrography, deep ocean ventilation and flow, and marine biogeochemistry evolved across the Pleistocene, focusing on the Southwest Indian Ocean. New multi-proxy paleoceanographic records are generated from sediments cores in the Southwest Indian Ocean, at the boundary between the Subantarctic Southern Ocean and the subtropical Indian and Atlantic Oceans. These records, from International Ocean Discovery Program (IODP) Site U1475, span the Early to Late Pleistocene and include: Measurements of benthic *C. wuellerstorfi* and the deep-dwelling planktic *G. truncatulinoides* foraminifera stable isotopes; the accumulation of ice-rafted debris (IRD) deposited by Antarctic icebergs; and the 'Sortable Silt' mean grain-size proxy for near-bottom flow speed. The records are combined with published data from a nearby core (MD02-2588) and presented on the 'Agulhas Plateau composite'. The results show that during glacial intervals, IRD deposition and near-bottom flow speeds were high, deep chemical ventilation was reduced, and the mode-water to deep-water chemical gradient was stronger relative to interglacial times. The glacial Agulhas Plateau was characterised by a northerly expansion of Southern Ocean waters accompanied by a stronger or more proximal Antarctic Circumpolar Current, a stronger chemocline, and a reduction in northern-sourced deep water presence. In these records, the Mid-Pleistocene Transition begins around 1.25 Ma with a stepwise increase in IRD deposition and higher amplitude cycles in near-bottom flow speed.

The records also demonstrate that key interglacial periods are characterised by exceptionally sluggish deep-flow and a breakdown in vertical carbon stratification. Finally, the temporal phasing of the records describe a sequence of events whereby Southern Ocean surface conditions appear to lead deep circulation and global ice volume into ice ages; potential mechanisms to explain this phasing are outlined, involving shifts in the distribution of Antarctic iceberg melt.

Table of Contents

List of Figures

Abbreviations and Nomenclature

Nomenclature

- *myr* refers to 'millions of years' as a unit of time;
- *Ma* refers to 'millions of years ago' as a unit of age or time before present;
- *kyr* refers to 'thousands of years' as a unit of time;
- *ka* refers to 'thousands of years ago' as a unit of age or time before present;
- pCO_2 refers to the 'partial pressure of carbon dioxide in the atmosphere';
- *CDW, LCDW, and UCDW* refer to 'Circumpolar Deep Water'. *LCDW* and *UCDW* refer specifically to the denser and less dense forms, respectively, and *CDW* is used more generally;
- *STF and STFZ* refer to the Subtropical Front and Subtropical Frontal Zone, following the definitions of Graham and Boer (2013);
- *Insolation* refers to 'Incoming Solar Radiation';
- $\overline{\boldsymbol{SS}}$ refers to the mean grain size of the terrigenous sediment 'Sortable Silt' fraction, following McCave et al. (1995b);
- $\delta^{13}C_X$ and $\delta^{18}O_X$ refer to the carbon and oxygen isotope composition of X, respectively, where X is usually a foraminifera species or a water mass;
- $\Delta\delta^{13}C_{X-Y}$ and $\Delta\delta^{18}O_{X-Y}$ refer to the carbon and oxygen isotope gradient between X and Y, respectively, where X and Y are usually foraminifera species, ocean basins, or water masses;

Abbreviations

AABW = Antarctic Bottom Water;

AAIW = Antarctic Intermediate Water;

AASW = Antarctic Surface Water;

ACC = Antarctic Circumpolar Current;

AL = Agulhas Leakage;

AMOC = Atlantic Meridional Overturning Circulation;

AP_{comp} = Agulhas Plateau Composite;

ARC = Agulhas Return Current;

CAB = Congo Air Boundary;

CDW = Circumpolar Deep Water;

DBD = Dry Bulk Density;

DIC = Dissolved Inorganic Carbon;

DP = Drake Passage;

DSDP = Deep Sea Drilling Program;

EDS = Energy Dispersive X-ray Spectrometry;

ETP = Eccentricity Tilt Precession;

iNHG = intensification of Northern Hemisphere Glaciation;

IRD = Ice-Rafted Debris;

ITCZ = Intertropical Convergence Zone;

IODP = International Ocean Discovery Program;

IOW = Indian Ocean Waters;

IWT = Intermediate Water Temperature;

LCDW = Lower Circumpolar Deep Water;

LR04 = Lisiecki and Raymo's 2004 benthic oxygen isotope stack;

LSR = Linear Sedimentation Rate;

MAR = Mass Accumulation Rate;

MBT = Mid-Brunhes Transition;

MIS = Marine Isotope Stage;

MPT = Mid-Pleistocene Transition;

NADW = North Atlantic Deep Water;

NSW = Northern-Sourced Water;

ODP = Ocean Drilling Program;

PCHIP = Piecewise Cubic Hermite Interpolating Polynomial;

PDW = Pacific Deep Water;

PIC = Particulate Inorganic Carbon;

PF = Polar Front;

POC = Particulate Organic Carbon;

pMag = Paleomagnetic;

SAASW = Subantarctic Surface Water;

SAF = Subantarctic Front;

SALH = Silicic Acid Leakage Hypothesis;

SAMW = Subantarctic Mode Water;

SAZ = Subantarctic Zone;

SSW = Southern-Sourced Water;

STF = Subtropical Front;

STFZ = Subtropical Frontal Zone;

SWWB = Southern Hemisphere Westerly Wind Belt;

UCDW = Upper Circumpolar Deep Water;

VPDB = Vienna Pee Dee Belemnite;

Research Statement

Work in this thesis has been partially published in:

Starr, A., Hall, I. R., Barker, S., Rackow, T., Zhang, X., Hemming, S. R., ... & Ziegler, M. (2021). Antarctic icebergs reorganize ocean circulation during Pleistocene glacials. Nature, 589(7841), 236-241. DOI: https://doi.org/10.1038/s41586-020-03094-7

Tangunan, D., Berke, M. A., Cartagena-Sierra, A., Flores, J. A., Gruetzner, J., Jiménez-Espejo, F., **Starr, A.**, ... & Hall, I. R. (2021). Strong glacial-interglacial variability in upper ocean hydrodynamics, biogeochemistry, and productivity in the southern Indian Ocean. Communications Earth & Environment, 2(1), 1-13. DOI: https://doi.org/10.1038/s43247-021-00148-0

Furthermore, while working on this thesis I have contributed to the following peer-reviewed articles, results of which appear throughout (with references where necessary):

Cartagena-Sierra, A., Berke, M. A., Robinson, R. S., Marcks, B., Castañeda, I. S., **Starr, A.**, ... & Expedition 361 Scientific Party. (2021). Latitudinal Migrations of the Subtropical Front at the Agulhas Plateau Through the Mid-Pleistocene Transition. Paleoceanography and Paleoclimatology, 36(7). DOI: https://doi.org/10.1029/2020PA004084

Williams, T. J., Martin, E. E., Sikes, E., **Starr, A.**, Umling, N. E., & Glaubke, R. (2021). Neodymium isotope evidence for coupled Southern Ocean circulation

and Antarctic climate throughout the last 118,000 years. Quaternary Science Reviews, 260, 106915. DOI: https://doi.org/10.1016/j.quascirev.2021.106915

Barker, S., **Starr, A.**, van der Lubbe, H.J.L., Doughty, A., Knorr, G.,... & the IODP Exp 361 Shipboard Scientific Party. (submitted). Persistent influence of precession on northern ice sheet variability since the early Pleistocene. *Submitted to Science*.

van der Lubbe, H.J.L., Hall, I.R., Barker, S., Hemming, S.R., Baar, T.F., **Starr, A.**, Just, J., & Joordens, J.C.A. (2021). Indo-Pacific Walker circulation drove Pleistocene African aridification. Nature, *in press*.

Acknowledgements

A PhD could not be further from an individual undertaking, and this thesis would have been in no way possible without the mentorship, support, and friendship of others. First and foremost, I want to thank my primary supervisor, Ian Hall, for being an exceptional mentor and role model. He has endlessly supported my academic development, and has provided countless opportunities from which I have benefited immensely. I would also like to thanks my second supervisor, Steve Barker, for many stimulating discussions and insights into the world of paleoceanography. I also want to thank Sid Hemming, Jeroen van der Lubbe, Daniel Babin, Thomas Rackow, Xu Zhang and Gregor Knorr for endless stimulating discussions. I thank the 'Agulhas breakout group', including Margit Simon, Chris Charles, Melissa Berke and Alejandra Cartagena Sierra. I thank Becky Robinson and Basia Marcks for hosting me in Rhode Island, and Gisela Winckler for hosting me at LDEO. A special thanks goes to Liz Sikes, for being a brilliant mentor, and most importantly for providing me the most indulgent thanksgiving meal I could have hoped for! Thank you also to Vince Clementi, Ryan Glaubke, Nat Umling, and the rest of the 'CROCCA-2s' team. I also thank Claire Waelbroeck, Natalia Vazquez-Riveiros and the rest of the ACCLIMATE-2 team for an amazing time in the Southern Ocean. I would also like to thank the technical staff at Cardiff University for assisting with and teaching me the various techniques used throughout this thesis, notably: Lindsey Owen, Sandra Nederbragt and Duncan Muir.

Special thanks goes to my friends, in Cardiff and beyond, for keeping me suitably distracted at all the right times. In particular the 'Brodies Bunch', notably: Liam, Max, Jam, Harry, Chris, Phil, Sophie, and Jaz. Special thanks (I think) to Will for getting hooked on coffee and showing us all up at football. I also want to thank

Jimmy, Fergal, Mike and Dan, for providing all of the necessary adventures. Finally, I want to thank my family, for supporting me endlessly. Thank you Mum, Dad, Emma, Jonny, Grandad. A special thank you goes to my Grandma, for sharing with me her love of books. I also want to thank my love, Paige, for being the most supportive and caring partner I could ever hope for.

Dedication

To my Grandad,
for inspiring me endlessly,
and bestowing upon me a love for the sea.

1 | Introduction

> *... sea replaces what was once dry land, and where there is now sea, is at another time land. This process must however be supposed to take place in an orderly cycle.*
>
> - Aristotle, *Meterologica*

From global temperatures to precipitation patterns and wind fields, the climate system has changed throughout geological time and will continue to change into the future. Climate variations on a range of timescales have been identified: from millions of years, such as tectonically driven global warming and cooling (Zachos et al., 2001), to inter-annual variations associated for example with the El Niño-Southern Oscillation (Philander, 1983). Understanding the workings of the climate system is an increasingly prescient undertaking, with anthropogenic activities now known to be instrumental in forcing recent climate change. Over the past century, the rate of changes to the climate are seemingly unprecedented, with atmospheric CO_2 levels rising faster than has been seen for at least the past 20 kyr* (Joos and Spahni, 2008), accompanied by increases in global air temperature of ~1.0°C and global sea level of ~0.2 m since Pre-Industrial times (IPCC, 2021).

To understand climate change, it is essential to recognise feedbacks within the system, and to understand the relationship between internal dynamics and external forcing. One valuable way to achieve this is to study how the climate system has varied through Earth's history. By accessing records of past climate change and understanding the natural mechanisms behind long term change, glacial-interglacial cycles, and

*1 kyr = 1 thousand years

abrupt climate transitions, we may better foresee how the planet will respond to the ongoing effects of human activity.

1.1 Pleistocene Climates and Orbital Cycles

It has long been known that Earth's climate was not always like that of today. Since scientists in the 19th Century first theorised the occurrence of 'ice ages' (Agassiz et al., 1840; Adhèmar, 1842), geologists and paleoclimatologists have uncovered an extensive history of cycles whereby warm and cold conditions periodically prevailed and large continental ice sheets periodically waxed and waned. It was apparent from early on that these oscillations might be driven by changes in the geometry of Earth's orbit (e.g. Croll, 1867; Milankovìc, 1940), though the geological evidence necessary to test the nature of this connection remained scarce. In the 20th century, the popularisation of deep-sea sediment coring (e.g. Pettersson, 1948) and the development of geochemical tools for extracting the climate information stored in samples recovered (e.g. the $^{18}O/^{16}O$ ratio in calcite microfossils; Emiliani, 1955; Shackleton, 1977), made it possible to begin testing these theories.

For example, oxygen isotope records allowed the formalisation of glacial-interglacial cycles into Marine Isotope Stages (MIS; where the Holocene is MIS 1, the last glacial maximum is MIS 2, and so on; Figure 1.1). Relating this stratigraphy to calculations of past orbital geometry (e.g. Berger, 1977), and in addition to radioisotope measurements (e.g. radiocarbon and thorium series isotopes; Emiliani, 1955, 1971) and the identification of magnetic reversals (e.g. Shackleton and Opdyke, 1973) allowed the dating of sediment cores and provided a chronological framework for paleoclimate studies.

One of the products of this progress has been the development of long, continuous marine oxygen isotope records, providing perhaps the clearest overview of climate change over the Cenozoic era (e.g. Zachos et al., 2001; Lisiecki and Raymo, 2005; Westerhold et al., 2020). The ratio of $^{18}O/^{16}O$, or $\delta^{18}O$[†] recorded by calcium carbon-

[†]delta notation defined as $\delta^{18}O = ([(^{18}O/^{16}O)_{sample} / (^{18}O/^{16}O)_{standard}] - 1) \times 1000$

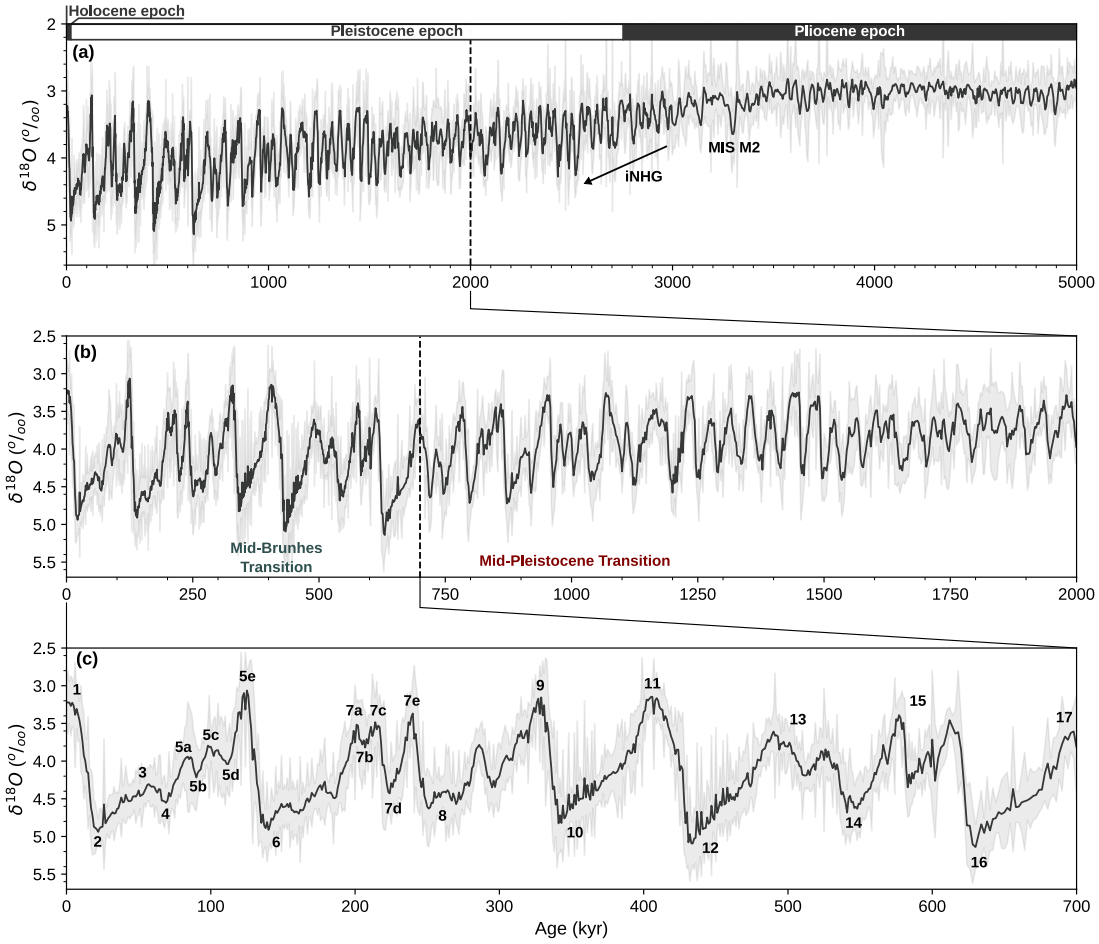

Figure 1.1: $\delta^{18}O_{benthic}$ Stack of Ahn et al. (2017). **(c)** 0 - 700 ka with Marine Isotope Stages (MIS) and selected sub-stages labelled following Railsback et al. (2015, and references therein). Even numbers represent glacial stages and odd numbers are interglacials (*sensu lato*). iNHG refers to the intensification of Northern Hemisphere Glaciation.

ate microfossils in deep-sea sediments provides a first-order approximation of continental ice volume (Shackleton, 1967), although additional factors are also at play. Stacks of $\delta^{18}O$ such as the 'Probabilistic Stack' (Figure 1.1; Ahn et al., 2017) average out local hydrographic changes recorded at individual locations and have become a cornerstone in Plio-Pleistocene sediment core studies (Imbrie et al., 1984; Shackleton et al., 1990; Pisias et al., 1990; Raymo et al., 1997; Lisiecki and Raymo, 2005; Ahn et al., 2017). Statistical analysis of records such as this have answered many questions regarding the nature of past climate variability, and have raised perhaps even more.

1.1.1 An overview of climate over 5.3 million years

Figure 1.1a shows that over the past 5 million years (myr), quasi-periodic glacial-interglacial cycles occurred amid a background of long-term trends, punctuated by state changes such as the intensification of Northern Hemisphere Glaciation (iNHG), the Mid-Pleistocene Transition (MPT) and the Mid-Brunhes Transition (MBT).

The long-term trend of increasingly heavy $\delta^{18}O$ reflects gradual global cooling and the development of ever larger continental ice sheets. This constitutes the tail-end of an even longer-term cooling trend across the Cenozoic which has been attributed to tectonic uplift (e.g. Raymo et al., 1990) and reconfigurations of ocean circulation patterns by the closure of oceanic seaways (e.g Keigwin, 1982; Haug and Tiedemann, 1998). This cooling was punctuated by periods of more rapid $\delta^{18}O$ increase related to the development of Antarctic and then Northern Hemisphere ice sheets (Lear et al., 2008; Shackleton et al., 1984), culminating in the intensification of glacial cycles with a distinct 41 kyr periodicity during the iNHG (Figure 1.1a).

An interval of quasi-periodic global glacial cycles known as the '41-kyr world' followed this transition, which also broadly marks the boundary between the Pliocene and Pleistocene epochs (Figure 1.1; ~2.6 Ma; Gibbard et al., 2010). A long-term cooling trend then persisted until around ~ 1 Ma (Snyder, 2016), at which point a transition occurred in the cyclic nature of the '41-kyr world'.

The Mid-Pleistocene Transition

This transition, known as the MPT, is characterised by the onset of longer, more asymmetrical glacial cycles, larger in amplitude (Clark et al., 2006). Several mechanisms have been proposed to explain the change in glacial dynamics which led to this transition from the '41-kyr world' into the so-called '100-kyr' world. Some of these relate to ice-sheet dynamics, such as a shift in the stability of the Laurentide Ice Sheet in response to erosion of sub-glacial regolith (Clark and Pollard, 1998; Tabor and Poulsen, 2016), or a transition from a land- to marine-terminating East Antarctic Ice Sheet (Raymo, 2006; Elderfield et al., 2012). A shift in ice-sheet behaviour may also have

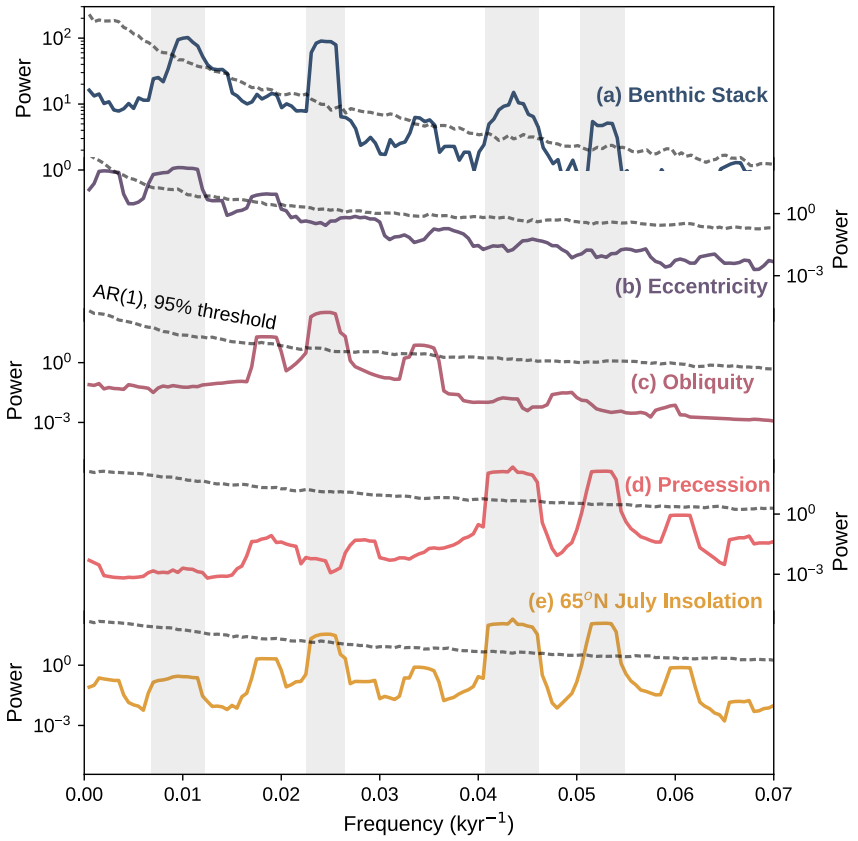

Figure 1.2: Spectral density estimates for **(a)** $\delta^{18}O_{benthic}$ Stack of Ahn et al. (2017); and orbital solutions from Berger and Loutre (1991) for **(b)** eccentricity, **(c)** obliquity, **(d)** longitude of perihelion (precession) and **(e)** mid-July insolation at 65^{o}N. Power spectra are estimated using the Multi-Taper Method.

been facilitated by a gradual decrease in atmospheric CO_2 levels (Willeit et al., 2019; Chalk et al., 2017). Alternative hypotheses emphasise sea-ice dynamics (Tziperman and Gildor, 2003), enhanced dust fluxes (for example as a result of glacial erosion or mid-latitude aridification; Willeit et al., 2019; Berends et al., 2021), and ocean circulation/mixing (Köhler and Bintanja, 2008; Hasenfratz et al., 2019).

The exact nature of the MPT is difficult to determine due to the different ways in which it manifests between different regions and proxy reconstructions. In sea surface temperature records the emergence of ~1/100-kyr spectral power occurs as early as ~1.5 Ma in some regions (Liu et al., 2008), and changes in the oceanic carbon cycle are evident from ~1.6 Ma (Wang et al., 2010; Lisiecki, 2014; Hodell and Channell, 2016). Detecting the MPT in benthic $\delta^{18}O$ records (Figure 1.1) is also complicated by the variable contributions from deep-sea temperature and global ice volume (Sosdian

and Rosenthal, 2009; Elderfield et al., 2012; Ford and Raymo, 2019); although inverse modelling techniques do support a substantial increase in ice volume across the MPT (de Boer et al., 2014; Berends et al., 2021).

Part of the difficulty in describing the MPT relates to ambiguities in defining the glacial cycles that follow. For example, the spectral power identified as representing the emergence of Late Pleistocene glacial cycles depends on whether one considers them to be paced by eccentricity cycles (e.g. Lisiecki, 2010), or by bundles of obliquity (Huybers and Wunsch, 2005), precession or a combination (Huybers, 2011).

Forcing and Timing of Glacial Cycles

A statistical analysis of marine sediment core records by Hays et al. (1976) confirmed the presence of periodicities matching those of changes in the precession and tilt (obliquity) of Earth's axis as well the eccentricity of Earth's orbit around the sun (Figure 1.2). However, the results of Hays et al. (1976) required a more complex explanation than offered by the canonical Milankovitch theory (Milankovič, 1940) to explain glacial cycles of the '100-kyr world'. This theory relates the waxing and waning of Northern Hemisphere ice sheets to the amount of summer insolation received at high northern latitudes; in other words, connecting orbital geometry to climate through the ability of solar radiation to melt snow and ice accumulated during the previous winter. The absence of clear 100-kyr eccentricity forcing in high latitude summer insolation (Figure 1.2; Berger and Loutre, 1991) makes it difficult to reconcile with the ~100-kyr periodicity of glacial cycles of the past 1 myr. The lack of an obvious mechanism linking glacial cycles to eccentricity became known as the '100-kyr problem', and continues to motivate the search to better understand the link between external orbital forcing and internal feedbacks in the climate system.

Recently, several advances have been made in understanding orbital forcing of Pleistocene climate cycles. For example, progress in techniques for dating paleoclimate archives such as improved radioisotope constraints from speleothems (Cheng et al., 2016; Bajo et al., 2020) and paleomagnetic constraints in marine sediments (e.g. Channell et al., 2009) as well as novel approaches to circumvent circular reasoning in ma-

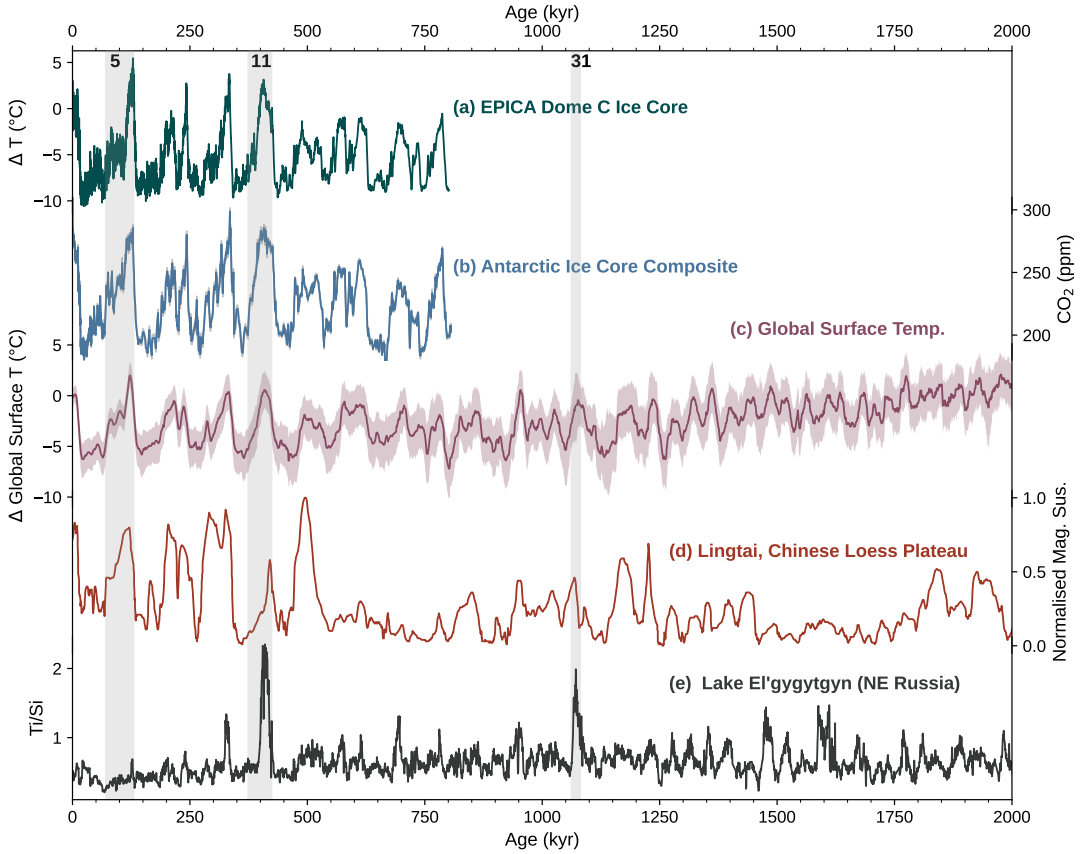

Figure 1.3: The last 2 myr of climate change viewed from selected ice core, marine, lacustrine, and terrestrial deposits. **(a)** Antarctic air temperature (anomaly from modern) recorded by δD from the EPICA Dome C ice core (Jouzel et al., 2007). **(b)** Composite record of atmospheric CO_2 concentration from Antarctic ice cores (Lüthi et al., 2008, and references therein). **(c)** Estimate of global surface temperature (anomaly from modern) from a compilation of sea surface temperature records (Snyder, 2016). **(d)** Normalised magnetic susceptibility from the Lingtai loess/paleosol sequence, located on the Chinese Loess Plateau (Sun et al., 2010). **(e)** Ti/Si ratio in a lake sediment core from Lake El'gygytgyn in Northeast Russia (Melles et al., 2012). Selected interglacials are highlighted in vertical shading, boundaries follow Lisiecki and Raymo (2005).

rine sediment records (e.g. Huybers, 2007, Barker et al., *submitted*) have constrained the timing of glaciations and deglaciations with respect to insolation cycles. These results suggest that glacial terminations aligned closely with bundles of obliquity and/or precession cycles, supporting the proposal that the ~100-kyr frequency in climate records is actually the result of two (80-kyr) or three (120-kyr) obliquity cycles (Huybers, 2011), with the the precise timing of glacial-interglacial transitions influenced additionally by precession (Cheng et al., 2009).

One finding which pervades paleoclimate reconstructions from the Late Pleistocene

is the importance of atmospheric CO_2 concentrations in triggering, amplifying, and modulating changes in glacial-interglacial climate (e.g. Shackleton, 2000). Even with satisfying hypotheses related to the external pacing of glacial cycles, the amplitude of climate fluctuations and the abruptness and asymmetry of transitions (e.g. Broecker and van Donk, 1970) demand additional forcing from internal mechanisms such as the carbon cycle. Ice core records demonstrate a tight link between the partial pressure of CO_2 in the atmosphere (pCO_2) and Antarctic air temperature on millennial (Ahn and Brook, 2008) and glacial-interglacial scales (Petit et al., 1999; Lüthi et al., 2008) during the Pleistocene. Moreover, pCO_2 increases rapidly across glacial terminations, with pulses in oceanic CO_2 outgassing aligning closely with changes in temperature and global climate (Rose et al., 2010; Marchitto et al., 2007).

A central role for ocean processes in the Pleistocene carbon cycle is expected, as it is the largest carbon reservoir which can readily interact with the atmosphere on kyr-timescales (Broecker, 1982). In the following section, I give a brief overview of circulation and biogeochemistry in the modern ocean, laying the groundwork to explore the past dynamics of these processes over the coming chapters.

1.2 Ocean Circulation

Covering over 70% of the Earth's surface, and owing to its large heat capacity, the ocean is dominant in absorbing and redistributing heat around the planet. The extent of this role is exemplified by the observation that over 90% of the heat gained by Earth between 1971 and 2010 was absorbed in the ocean (Zanna et al., 2019). Furthermore, the surface mixed layer of the ocean readily exchanges gasses such as CO_2 with the atmosphere, and the ventilation of the ocean interior by water-mass subduction thus provides a pathway for chemical tracers and heat out of the atmosphere (Khatiwala et al., 2009). Circulation patterns in the ocean act to redistribute heat and tracers around the world, resulting in distinct spatial patterns in thermohaline and biogeochemical properties.

The dynamic flow of water around the planet can be largely described by the con-

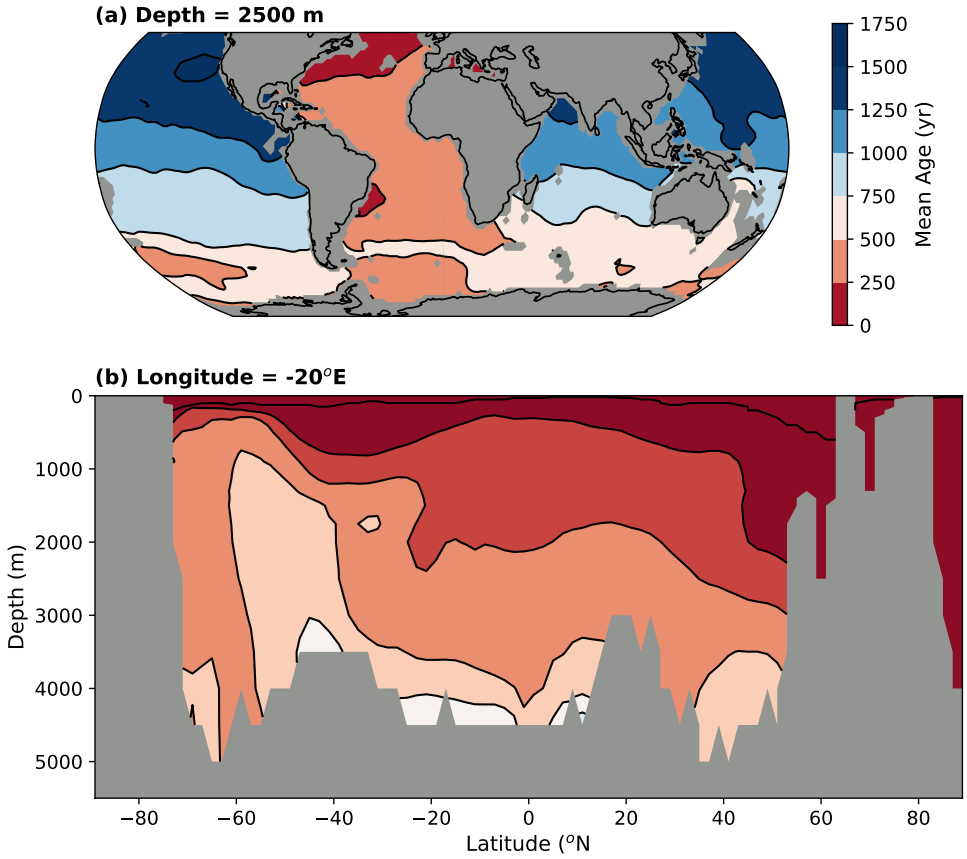

Figure 1.4: Mean age of water in the modern ocean inferred from radiocarbon measurements. **(a)** Isolines at 2500 m depth. **(b)** Meridional transect through the Atlantic Ocean at -20^{o}E. Blue colors represent older water; i.e. longer since exposure to the surface. *Dataset from Gebbie and Huybers (2012)*

cept of overturning circulation, whereby water sinks in some places and upwells in others, connecting generally light and warm surface waters with the denser, cooler deep ocean interior (e.g. Cessi, 2019). Two overturning circulations dominate much of global ocean, one with deep-water production occurring in the northern North Atlantic and the other with deep-water production today occurring in the high latitude Southern Ocean (Gordon, 1986; Gebbie and Huybers, 2012). This is seen in areas of relatively young waters (i.e. less time since exposure to the atmosphere) in the high latitude deep North Atlantic and Southern Oceans (Figure 1.4). These cells are closely intertwined (Talley, 2013; Marshall and Speer, 2012) with North Atlantic Deep Water (NADW) upwelling in the Southern Ocean, ultimately contributing to the Antarctic Bottom Water (AABW) overturning cell (see the 'figure-of-eight' schematic in Figure 1.5).

North Atlantic Deep Water

The NADW overturning cell is also referred to as Atlantic Meridional Overturning Circulation (AMOC), although the deep-water exported has an almost global reach. The dynamics of this cell have received much attention, particularly in the context of abrupt climate change, both in the geological past and immediate future (Broecker et al., 1985; Lynch-Stieglitz et al., 2007; Rahmstorf, 2002). The production of NADW is driven primarily by the density modification of near-surface waters in the high latitude North Atlantic, mostly through cooling, however the salinity of deep-water formation regions does exert some influence. This allows for the possibility of a positive feedback where increased salinity leads to more rigorous overturning, which supplies more salt through increased surface return flow (Rahmstorf, 2000), making the system non-linear and also sensitive to freshwater fluxes. Early work led to the idea that this allowed two stable states in the NADW cell: NADW production 'on', and NADW production 'off' (Manabe and Stouffer, 1988; Stommel, 1961). During the last glacial cycle, this concept has been expanded with three distinct modes describing 'stadial', 'interstadial' and 'Heinrich' NADW production states (Rahmstorf, 2002).

After production in the North Atlantic, NADW propagates southwards through the Atlantic basin (Dickson and Brown, 1994) before entering the Indian Ocean basin south of Africa, or becoming entrained in the eastward flowing Antarctic Circumpolar Current (ACC) and mixing with deep water from the Pacific, Indian and Southern Ocean basins to form the denser class of Circumpolar Deep Water (CDW) referred to as Lower Circumpolar Deep Water (LCDW).

The export of deep-water from the Atlantic basin is balanced by the return of surface and thermocline waters across the Indian-Atlantic ocean gateway and thermocline to intermediate waters through the Drake Passage gateway (Rintoul, 1991; de Ruijter et al., 1999). The 'warm-water return route' occurs through the so-called Agulhas Leakage. This is the term given to the exchange of warm and saline Indian Ocean waters into the South Atlantic through mesoscale eddies and filaments shed from the Agulhas Current as it retroflects in the south-west corner of the Indian Ocean

subtropical gyre (Lutjeharms and Ballegooyen, 1988). There is evidence to suggest that the magnitude of Agulhas Leakage has an impact on the strength of the AMOC and subsequently on global climate (Beal et al., 2011; Biastoch et al., 2008; Caley et al., 2012; Dyez et al., 2014; Peeters et al., 2004).

Antarctic Bottom Water Cell

The second overturning circulation cell is associated with Antarctic Bottom Water (AABW) production in the Ross Sea, Weddell Sea and Adelie Land sectors of the Southern Ocean (Foster and Carmack, 1976; Jacobs et al., 1970). The production of AABW is fed predominantly by deep upwelling south of the ACC. Following subduction, the cold and dense water follows one of two routes: if it is dense enough, it forms bottom water (AABW) that sinks and propagates northwards through the abyssal ocean, and if it is not dense enough it forms regional deep water masses (Sloyan and Rintoul, 2001). At lower latitudes, AABW upwells and mixes with deep water masses (NADW in the Atlantic Ocean, Indian Ocean Deep Water in the Indian Ocean and Pacific Deep Water in the Pacific Ocean) before flowing back towards the Southern Ocean predominantly in the form of the less dense CDW class known as Upper Circumpolar Deep Water (UCDW). A useful metric in this context is the 'age' of a water-mass, which refers to the time elapsed since a parcel of water was in contact with the atmosphere (Figure 1.4a). As water masses get 'older' they tend to accumulate respired carbon and nutrients sinking from the surface ocean (discussed below), and so spatial patterns of water-mass age can be informative tracers with implications for the carbon cycle. The return of CDW to the surface Southern Ocean can be seen in a meridional transect of the Atlantic Ocean, for example, as a tongue of relative old (>500 yr) water extending approaching the surface between 40^{o}S and 60^{o}S (Figure 1.4b).

Above this return flow, there is also a poleward flow of less dense northern-sourced deep water, for example NADW in the Atlantic basin. This signifies a divide between the two overturning cells, across which mixing can occur. The less dense UCDW upwells in the Sub-Antarctic Zone of the Southern Ocean, where it then spreads to-

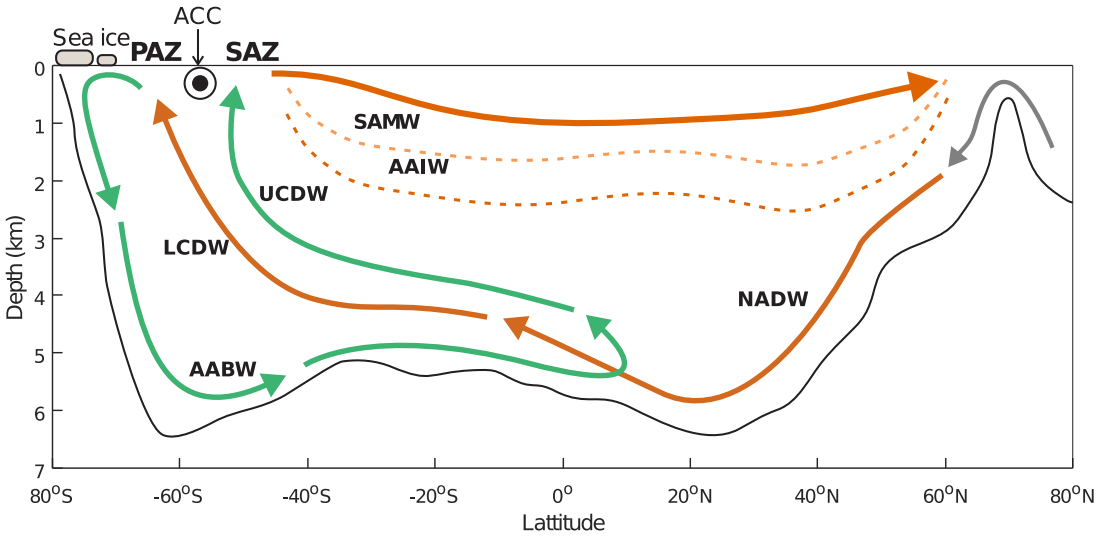

Figure 1.5: Meridional overturning schematic for the Atlantic Ocean following Talley (2013). The orange arrows represent the North Atlantic Deep Water (NADW) cell feeding into the Lower Circumpolar Deep Water (LCDW). The green arrows represent the Antarctic Bottom Water (AABW) cell, feeding into the Upper Circumpolar Deep Water (UCDW). Upwelling occurs in the Southern Ocean in response to the Ekman Divergence across the Antarctic Circumpolar Current (ACC). Subantarctic Mode Water (SAMW) and Antarctic Intermediate Water (AAIW) are subduction in the Subantarctic Zone (SAZ). The grey arrow represents deep water formation in the northern North Atlantic. The dashed lines represent selected water-mass boundaries. PAZ = Polar Antarctic Zone.

wards the (sub)tropics as Antarctic Intermediate Water (AAIW) and Sub-Antarctic Mode Water (SAMW), eventually returning to the North Atlantic to complete the intermediate depth overturning cell (Marinov et al., 2006; Toggweiler et al., 2006).

The mixing between southern-sourced AABW and northern-sourced NADW to form CDW represents a connection between the two overturning cells. The extent of the 'communication' between the two cells has been implicated in the Southern Ocean's capacity to store CO_2 (Hodell et al., 2003; Marinov et al., 2006; Toggweiler, 1999) as discussed below.

1.3 Reconstructing past ocean conditions

Above I have outlined some key aspects of modern ocean circulation, our understanding of which has been aided by an extensive history of *in situ* (e.g. Key et al., 2004), and remote (Goldstein et al., 1989) observations as well as data assimilation and nu-

merical modelling techniques (see historical perspective by Semtner, 1986). Clearly the applicability of direct or remote observation approaches in reconstructing past ocean conditions are limited, and paleoceanographers instead must reconstruct paleoenvironments through indirect methods, generally referred to as proxy reconstructions.

The field of paleoceanography is largely built on the principle that past environmental changes may be recorded in the stratigraphic accumulation of ocean sediments[‡]. Younger strata overlay older strata, and hence changes in the sediment properties with stratigraphic depth should represent changes in the sedimentary system, and hence environment, through time.

1.3.1 Environmental signals in terrigenous sediment

Deep-sea sediments can be divided into biogenic components originating mostly in the local water column, and allochthonous, non-biogenic material originating mostly from adjacent continents. The latter, known as the terrigenous fraction, is primarily clastic material supplied to the seafloor as aeolian dust, ice-rafted glaciogenic debris, and hemipelagic sediments from fluvial and shelf sources. Analysing the terrigenous fraction can provide information on climatic conditions in the sediment source region, as well as processes acting to transport the material, and dynamical processes affecting the deposited sediment, such as current sorting. Perhaps the simplest way in which environmental signals are archived is through the mineralogy and petrology of the sediment. For example, the composition of clay particles in sediments, the majority of which are detrital in origin, reflects the provenance of the water masses in which they are transported (Biscaye, 1965; Petschick et al., 1996), although changes through time may also reflect changes in hydroclimate and weathering on the adjacent continents (Moriarty, 1977). Because of this, clay mineralogy studies are often combined with additional proxies such as radiogenic isotope composition (see below). Moreover, the presence of coarse, detrital grains in (sub-) polar regions often reflects

[‡]Paleoceanography also makes use of stratigraphic media that are not sedimentary in nature, such as coral calcite bands and ice cores, however this thesis is primarily concerned with the sedimentary records of deep-sea sediment cores.

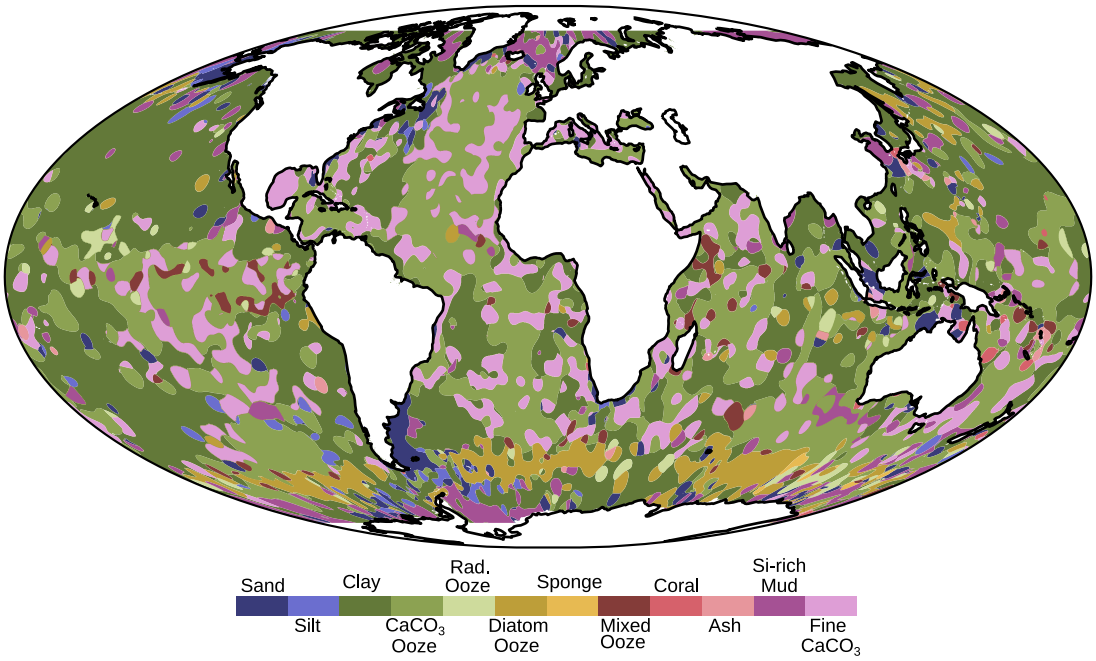

Figure 1.6: Map showing the seafloor sediment lithology census of Dutkiewicz et al. (2015). Colours correspond to surface sediment lithologies explained in the key, derived from ocean floor sediment samples.

the deposition of terrigenous sediments by icebergs or sea-ice (Lisitzin, 1960; Hough, 1950). The accumulation of ice-rafted debris (IRD) over time can therefore provide a proxy record of ice-rafting, or more specifically the melting of sediment-laden ice, at a given location (e.g. Conolly and Ewing, 1965; Watkins et al., 1974; Heinrich, 1988). Furthermore the petrology/mineralogy of ice-rafted material in addition to the elemental and isotopic composition can provide insights into the provenance of the icebergs or sea-ice from which the material was deposited (Farmer et al., 2003; Hemming et al., 1998; Nielsen et al., 2007a).

Grain-size analysis

Mechanisms of production, transport, and deposition of sediments inherently favour grains of certain characteristics, such as size ranges, and therefore provide different populations to the final buried strata (McCave and Hall, 2006). By isolating variations in the sediment grain size distribution attributed to different mechanisms, one can infer changes in said mechanisms through time; for example by isolating the pre-

dominantly current-sorted signal as in the 'Sortable Silt' paleo-flow speed method ($\overline{\mathbf{SS}}$; McCave et al., 1995b), or the aeolian dust signal through end-member decomposition (e.g. Stuut et al., 2002).

The sorting of deep-sea sediments occurs by the hydraulic action of near-bottom ocean flow. The resuspension and deposition of sediment by aggregate breakup and particle selection is dependent on the particle settling velocities and the fluid shear stress acting on them. McCave et al. (1995b) demonstrated that at a given stress, some grains and aggregates are deposited, whilst others with lower settling velocities remain in suspension. The sorting of fine[§], non-cohesive, sediment is therefore controlled mostly by selective deposition. By determining the mean grain size of the non-cohesive, fine sediment fraction (10-63μm; McCave et al. (1995b)), it is therefore possible to reconstruct the strength of near-bottom flow.

Records of the Sortable Silt mean grain size ($\overline{\mathbf{SS}}$) from marine sediment cores have provided insights into the history of current vigour in the North Atlantic (e.g. McCave et al., 1995a), South Atlantic (e.g. Spooner et al., 2018), Pacific (e.g. Hall et al., 2001), and Southern Oceans (e.g. McCave et al., 2013) across a range of geological timescales (Kleiven et al., 2011; Hall et al., 2003; Bianchi and McCave, 1999; Thornalley et al., 2018). However, as with all paleoceanographic proxies, this approach has limitations: firstly it provides an estimate only of local flow vigour and multiple locations are ideally needed to infer circulation changes on climatically-relevant scales. Secondly, $\overline{\mathbf{SS}}$ can be sensitive to the proximity of sediment sources (McCave and Hall, 2006) as well as local hydrodynamics influenced by sedimentary structures (McCave, 2008). Finally, whilst *in situ* field calibrations of $\overline{\mathbf{SS}}$ to geostrophic flow speed exist (McCave et al., 2017), the relationship varies between regions, though primarily in its intercept rather than the slope. This means that $\overline{\mathbf{SS}}$ might be better applied to reconstruct changes in flow speed rather than absolute flow speed.

[§]in this context, fine refers o <63μm; shear stress by near-bottom flow at sites of paleoceanographic interest, i.e. with high sedimentation rates, are rarely able to resuspend coarse sediments above this boundary (Miller et al., 1977)

Bulk sediment chemistry

Additional insights into past circulation can come from measuring the chemistry of sediments. For example, the preferential enrichment or depletion of certain chemicals into different grain sizes means the ratio of elements with affinities for coarse and fine phases, such as Zr/Rb (Wu et al., 2020), can be utilized to infer changes in sediment coarseness along a core, and can be measured relatively quickly by XRF scanning (Croudace and Rothwell, 2015). Furthermore, ratios between other elements can yield additional paleoenvironmental information, such as variations in terrestrial versus marine sediment sources (e.g. Fe/Ca, Ti/Ca, Fe/Si; Møller et al., 2006; Konfirst et al., 2011; Arz et al., 1998), the provenance of terrigenous sediments (e.g. Fe/K, Ti/Fe; Konfirst et al., 2011; Monien et al., 2012), the presence of particular sediment phases such as ice-rafted debris (e.g. Sr/Ca and Si/Sr, depending on mineralogy; Hodell et al., 2008), changes in the redox state of the sediment (e.g. Fe/Al, Fe/S; Sluijs et al., 2008) and biological productivity (e.g. Br/Ti, Ba/Al; Ziegler et al., 2008; Caley et al., 2011).

Furthermore, the isotopic composition of bulk sediments can provide proxies for the provenance of water masses over time. For example, water masses carry a radiogenic isotope signature reflecting the geology of the source regions, as well as inputs during its circulation through different regions (Chow and Patterson, 1962). Particles precipitated in equilibrium with seawater essentially trap the dissolved radioisotope signature of the water-mass present, and changes in the isotopic composition of certain sediment phases over time can therefore provide a history of water-mass changes (Frank, 2002). A widely used application of this principle is the reconstruction of deep water-mass provenance through time by determining the Nd (Palmer and Elderfield, 1986; Du et al., 2020; Rutberg et al., 2000), Pb (e.g. Burton et al., 1997; Reynolds et al., 1999) and/or Hf isotopes (e.g. Piotrowski et al., 2000; van de Flierdt et al., 2002). In addition to water-mass provenance, radiogenic isotopes can also provide insights into the vigour of overturning circulation, such as $^{231}Pa/^{230}Th$ ratio. Owing to differences in the solubility (and hence residence time) between the two isotopes (Anderson et al., 1983), the $^{231}Pa/^{230}Th$ ratio in the sediment can reflect the addition or removal of ^{231}Pa by lateral advection, in turn related to deep circulation

patterns (Henderson et al., 1999).

1.3.2 Environmental signals from biogenic sediments

Proxies utilizing the biogenic component of marine sediment cores are among the most widely-used in paleoceanography. As alluded to in the first few paragraphs of this chapter, the reconstruction of ocean temperature, ice volume, and carbon cycling from the geochemistry of microfossils, such as foraminifera (e.g. Emiliani, 1955; Shackleton, 1967), has been instrumental in building a more complete picture of the past ocean. Other microfossil groups are also widely studied, such as coccolithophores (e.g. Margolis et al., 1975; Beaufort et al., 1997), dinoflagellates (e.g. Edwards et al., 1991) as well as diatoms and radiolaria (e.g. Gersonde et al., 2005), which produce calcium carbonate, organic, and silica shells/walls/exoskeletons, respectively. Paleoeanographic uses for these microfossils range from measuring their elemental and isotopic compositions, to analysing the properties of organic molecules which they secrete into the ocean, and relating changes in community structure through time to environmental conditions under which different species prevail (i.e. assemblage counts or relative species abundance).

Foraminifera

The widespread distribution and (generally) good preservation of foraminifera shells, or 'tests', means that the fossil record of foraminifera provides an exceptional archive from which climate information can be extracted over a range of timescales. Indeed, stable isotope measurement on foraminifera (e.g. Emiliani, 1955; Shackleton and Opdyke, 1973; Shackleton, 1977), have enabled the development of a globally-coherent marine stratigraphy; graphical correlation of oxygen isotope records to reference curves (Prell et al., 1986) has become perhaps the most popular way to anchor sediment core records to an astronomical timescale (such as the orbitally-tuned 'stacks' of Lisiecki and Raymo, 2005; Ahn et al., 2017). In addition, the carbon isotope composition of foraminifera can yield important information about past ocean circulation and carbon cycling (e.g. Shackleton and Opdyke, 1973; Duplessy et al., 1984),

though the signal can reflect a complex combination of additional thermodynamic, ecological and post-depositional influences (Lynch-Stieglitz et al., 1995; Charles et al., 1993; Spero et al., 1997); this is discussed in more detail in Chapter 5. Stable isotope analysis can nonetheless provide a wealth of information regarding past climate and ocean conditions. In addition, a suite of additional geochemical proxies have been developed using the chemistry of foraminifera, including paleo-thermometers (such as Mg/Ca; Rosenthal et al., 1997), carbonate chemistry proxies (such as B/Ca and $\delta^{11}B$; Hemming and Hanson, 1992; Yu and Elderfield, 2007), and nutrient proxies (e.g. Cd/Ca; Boyle, 1981).

Moreover, paleoenvironmental information can also be gained by determining the community structure and abundance of certain species of foraminifera in marine sediments. For example, fossil species assemblages can be related to the distribution of modern assemblages in relation to hydrographic conditions (increasingly possible with the development of global 'core-top' datasets; e.g. Siccha and Kucera, 2017), and can therefore be used to infer the hydrographic conditions in which the fossil assemblage lived (Imbrie, 1971). This approach, known as transfer functions or the 'Modern Analogue Technique', has been widely used in paleoceanography both with foraminifera assemblages (e.g. Diz et al., 2007), diatom assemblages (e.g. Gersonde et al., 2005) and nannofossil assemblages (e.g. Marino et al., 2009). Notably, this approach allowed the 'CLIMAP'[¶] project to reconstruct paleoclimate conditions across the North Atlantic region during the Last Glacial Maximum interval (CLIMAP Project Members, 1976).

1.4 Glacial Paleoceanography

The precise contributions from different processes in driving the ~100ppm variation in pCO_2 during glacial cycles (Petit et al., 1999) remains unresolved, however a unifying finding from modelling and proxy studies alike is that ocean processes play a dominant role (e.g. Sarmiento and Toggweiler, 1984; Broecker and Peng, 1987; Sigman and Boyle, 2000). The Southern Ocean in particular is thought to exert a

[¶]CLIMAP = Climate Long Range Investigation, Mapping and Predictions

disproportionate influence on the global carbon cycle; Fischer et al. (2010) show that Southern Ocean ventilation and biological productivity changes can explain around 40ppm and around 15ppm, respectively, of the glacial pCO_2 decrease.

The first and most obvious mechanism by which the ocean might modulate atmospheric pCO_2 during glacial intervals is through the temperature dependence of CO_2 solubility in water: CO_2 is more soluble in colder water and colder glacial conditions would therefore allow more CO_2 to dissolve in the surface ocean. The actual impact of this mechanism however is counteracted by the decrease in ocean volume due to ice sheet growth, as well as salinity changes and the contraction of the terrestrial biosphere (Sigman and Boyle, 2000; Broecker, 1982). Instead, changes in ocean biogeochemistry and circulation must be considered.

1.4.1 The glacial biological pump

Roughly half of the world's primary productivity of biogenic carbon occurs through phytoplankton in the surface ocean (Buitenhuis et al., 2013). When these organisms die, much of this carbon is respired and recycled within the upper mixed layer (Weber et al., 2016), however a fraction also sinks into the deep ocean. This downward transfer of particulate organic carbon is referred to as the 'biological pump', and is an important process in regulating atmospheric pCO_2 through its ability to isolate carbon in the deep ocean for up to millennia. The export of particular organic carbon is counteracted in the surface ocean by the 'carbonate counter pump', whereby the formation of calcium carbonate shells by coccolithophores, foraminifera and pteropods removes carbonate ions from the water, increasing the level of dissolved CO_2 (Heinze et al., 1991; Frankignoulle et al., 1994). It is therefore important to discriminate between the production of particulate organic carbon (also known as the soft-tissue pump) and particulate inorganic carbon (the 'carbonate counter pump') in studies of the past carbon cycle (Duchamp-Alphonse et al., 2018).

Variations in the efficiency of the biological pump[‖] have long been considered to play

[‖]or, more specifically, the 'soft-tissue pump'. Hereafter 'biological pump' refers to this unless otherwise stated. See Ito and Follows (2005)

an important role in driving changes in atmospheric pCO_2 in the past, for example during Pleistocene glacial intervals (Broecker, 1982; Sigman and Boyle, 2000). Boyle (1988) demonstrated that a shift of carbon and nutrients into the deep ocean during glacial intervals might be an effective way of reducing atmospheric pCO_2, a mechanism known as 'vertical nutrient fractionation'. Furthermore, this redistribution of carbon would raise deep-sea carbonate dissolution, thus increasing ocean alkalinity and lowering atmospheric pCO_2 further (the 'carbonate compensation' mechanism; Broecker and Peng, 1987).

Perhaps the most comprehensively studied interval in terms of the past biological pump is the Last Glacial Maximum (LGM; 23 to 19 ka; Figure 1.7). Radiocarbon measurements (Broecker et al., 1990) and reconstructions of deep-water carbonate chemistry (Yu et al., 2013) and nutrient content (Oppo et al., 2018) from this interval generally point to an increased storage of respired carbon in the deep ocean, however it is less clear how much of this was due to a global increase in the biological pump (Galbraith and Skinner, 2020). In the Subantarctic Southern Ocean, records of surface nutrient utilization (Martínez-García et al., 2014; Robinson et al., 2005) and organic biomarker production (Ikehara et al., 2000; Martínez-Garcia et al., 2009) suggest that biological productivity was greater**, and reconstructed fluxes of biogenic material and associated minerals into the sediment (Anderson et al., 2014; Kohfeld et al., 2005) and reconstructed bottom water chemistry (e.g. dissolved oxygen concentration; Jaccard and Galbraith, 2011) imply a greater export of carbon to the deep ocean. The situation in the glacial North Atlantic is less clear: although some evidence exists for a more efficient carbon pump (Yu et al., 2019), it is unclear whether this is related to primary productivity or ocean circulation (Straub et al., 2013).

Conversely, in the Antarctic Zone of the Southern Ocean export fluxes were evidently lower (Jaccard, 2005; Jaccard et al., 2013; Kohfeld et al., 2005; François et al., 1997; Kumar et al., 1995). A similar scenario is seen in the Sub-polar North Pacific Ocean (Jaccard, 2005; Gebhardt et al., 2008). Lower productivity in high latitude polar oceans has been suggested to result from increased upper-ocean stratification and a reduced supply of deep ocean nutrients to the surface during glacials (François et al.,

**several caveats are associated with this statement surrounding nutrient supply and preservation/advection of biogenic particles (Sachs et al., 2000; Anderson et al., 2002)

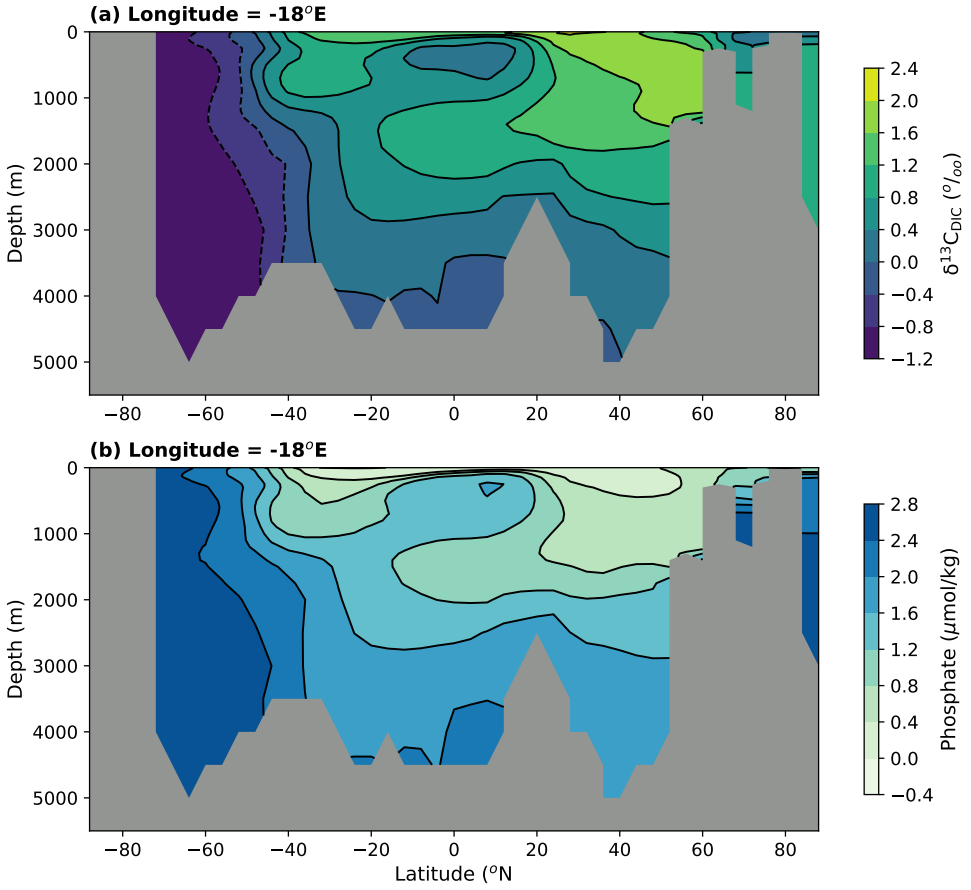

Figure 1.7: Meridional transects through a state estimate of the LGM ocean from a model inversion of compiled paleoceanographic observations (described in Oppo et al., 2018). **(a)** $\delta^{13}C$ and **(b)** Phosphate concentration from foraminifera-bound carbon isotopes and Cd/Ca ratios. *Dataset from Oppo et al. (2018)*

1997; Jaccard et al., 2013). This highlights an additional factor which much be taken into consideration when reconstructing the strength of the biological carbon pump: ocean circulation.

1.4.2 The Southern Ocean Leak

The significance of glacial productivity trends in the Southern Ocean comes down to the role that nutrient utilization in this region plays in regulating the preformed[††] nutrient content of much of the world's deep ocean (Marinov et al., 2006). This is

[††]The term 'preformed' when referring to deep ocean nutrients essentially means nutrients not utilized by biology, as opposed to 'regenerated' nutrients; the ratio between the two provides a metric for the global efficiency of the biological pump (Ito and Follows, 2005)

because a large proportion of water in the deep ocean is exposed to the atmosphere via upwelling in the Southern Ocean, bringing respired carbon and regenerated nutrients into the surface mixed layer. In the modern ocean these waters are returned to the ocean interior before the nutrients have been fully utilized, allowing for the escape of the upwelled carbon into the atmosphere (Sigman and Boyle, 2000; Marinov et al., 2008), and lowering the global efficiency of the biological pump. This process, known as the 'Southern Ocean Leak', has been identified as an important driver of atmospheric CO_2 fluctuations on glacial-interglacial timescales (Sarmiento and Toggweiler, 1984; Knox and McElroy, 1984; Siegenthaler and Wenk, 1984).

Stemming of the 'leak' during glacial intervals might have occurred through a variety of processes. For example, reduced mixing between the deep and surface Southern Ocean would limit the exposure of carbon and nutrient-rich deep water to the surface. Indirect evidence for this can be found in the decline of Antarctic Zone export productivity, considered to be driven by vertical stratification (François et al., 1997; Jaccard et al., 2013). Secondly, a physical barrier acting to trap CO_2 in surface waters, such as Antarctic sea-ice, would limit the out-gassing of upwelled carbon (Stephens and Keeling, 2000). Thirdly, increasing the biological utilization of nutrients in the Southern Ocean would reduce the preformed nutrient content of re-subducted water masses, therefore increasing the efficiency of the global biological pump (Sigman and Boyle, 2000).

Iron Fertilization

A key factor which today keeps Southern Ocean productivity low is biological limitation by micronutrients such as iron (Martin, 1990; Boyd et al., 2000). A relaxation of iron limitation in the past ocean, for example by increased dust (Martin, 1990) or glaciogenic (Raiswell et al., 2008) deposition in the Southern Ocean, or an increase in the upwelling of iron-rich deep waters (Tagliabue et al., 2014), would therefore facilitate more complete utilization of macronutrients. This in turn would lead to a more efficient biological pump, drawing down CO_2 (e.g. Watson et al., 2000). Increased dust fluxes are evident from ice core (Wolff et al., 2006) and marine sediment

core records (Martínez-Garcia et al., 2009; Lamy et al., 2014), and a tight link between these fluxes and patterns of biological productivity has been demonstrated (Martínez-García et al., 2014; Anderson et al., 2014; Ziegler et al., 2013). However, the extent to which dust fluxes can explain the remarkably high iron fluxes in some regions during glacial intervals has been questioned (Latimer and Filippelli, 2001) and it may be the case that conditions in the glacial Southern Ocean favoured multiple sources of bio-available iron. That being said, various carbon cycle models have demonstrated that estimated glacial-level dust fluxes can stimulate an lowering of atmospheric pCO_2 by up to 40 ppm (Brovkin et al., 2007; Köhler et al., 2005; Watson et al., 2000). Moreover, shifts in wind and hence dust deposition patterns would likely mirror shifts in ocean mixing and iron input from icebergs, sea ice or suspended sediment sources (Latimer and Filippelli, 2001; Meskhidze et al., 2007; de Baar et al., 1995; Noble et al., 2012).

1.4.3 Glacial Ocean Circulation

For the sequestration of carbon in the deep ocean to persist on long enough timescales to influence climate, physical mechanisms as well as biological processes must be called upon. Changes in upwelling or deep ocean mixing which act to isolate the deep ocean from the surface (and atmosphere) are therefore key in explaining the lowering of atmospheric pCO_2 during glacial intervals (Toggweiler, 1999; Sigman and Boyle, 2000).

In the modern ocean, deep water-masses (i.e. below around 2500m) are mostly brought to the surface by wind-driven upwelling around Antarctica (Toggweiler and Samuels, 1995), and so changes in the position and strength of the Southern Hemisphere westerly wind belt have been proposed as a driver of low glacial pCO_2 (Toggweiler et al., 2006). Furthermore, shifting westerly winds have been implicated in driving a surge of respired carbon out of the deep ocean by Southern Ocean upwelling during deglaciations (Anderson et al., 2009). More generally, these results highlight the importance of changes in the AABW overturning circulation cell (as described above), in the global carbon cycle. Interestingly, Karsten and Marshall (2002) and Watson and Garabato (2006) have shown that the strength of overturning in the Southern Ocean is in-

fluenced by surface buoyancy fluxes in addition to (and possibly even more so) wind forcing. This means that changes in glacial upwelling could also have occurred independently of changes in the westerly wind belt (Watson and Garabato, 2006). This highlights the importance of reconstructing both wind-driven and buoyancy-driven Southern Ocean changes in understanding past changes in deep ocean circulation and carbon storage.

An interesting caveat to descriptions of paleo-ocean circulation is the discrepancy between water-mass volumes or chemical properties and flow or mass transport (c.f. Wunsch, 2003). This means that any property that either does not change through time (during transport by ocean flow) or changes at a rate which is not constrained, cannot be utilized as paleoceanographic tracer of circulation strength, in the strictest sense (LeGrand and Wunsch, 1995). Reconstructions of circulation strength are therefore limited to radiometric approaches (radiocarbon, U-Th series isotopes, for example) and indirect measures of near-bottom shear stress using, for example the $\overline{\mathbf{SS}}$ proxy (McCave et al., 1995b). Continuing with the LGM case study, records of $^{231}Pa/^{230}Th$ from the North Atlantic suggest that substantial reductions in AMOC during the last glacial cycle occurred during discrete intervals (McManus et al., 2004; Böhm et al., 2014; Hall et al., 2006), although it is important to note the potential influence of changes in the composition of particles sinking from the surface (Chase et al., 2002). Records of the difference in radiocarbon age between surface and deep waters (for example measured on co-registered planktic and benthic foraminifera; Broecker et al., 1988) generally suggest a slowdown in the ventilation of the deep, implicating a more sluggish overturning circulation during the LGM (e.g. Robinson et al., 2005; Skinner et al., 2017). However, the fidelity of radiocarbon as a tool for reconstructing circulation rate has been questioned (Huybers, 2007; Campin et al., 1999) and model-data comparisons provide contradictory explanations for observed LGM radiocarbon patterns (Menviel et al., 2020; Kurahashi-Nakamura et al., 2017).

Reconstructions of circulation strength using the $\overline{\mathbf{SS}}$ flow-speed proxy are free from some of the biogeochemical complications which affect radioisotope studies, however pitfalls surrounding sediment source effects and local hydrodynamics interactions with bathymetry/bedforms can impede straightforward interpretations (McCave and

Hall, 2006). Using $\overline{\mathbf{SS}}$ measurements from a transect of cores in the North Atlantic, McCave et al. (1995b) showed that deep flow in the region was reduced during the LGM, with a potentially more vigorous mid-depth circulation. Spooner et al. (2018) found broadly the same pattern of strong mid-depth flow and sluggish deep flow from $\overline{\mathbf{SS}}$ measurements across a depth transect in the Southwest Atlantic Ocean, however other studies demonstrate either little change or a decrease in flow speed at intermediate depths in the North Atlantic (Hoffmann et al., 2019; Praetorius et al., 2008). Evidence from earlier glacial intervals support a reduction in the vigour of overflow from the Nordic Seas (Kleiven et al., 2011) as well as more sluggish deep circulation in the equatorial Atlantic (Gröger et al., 2003). Conversely, increased flow speeds were reconstructed during glacials in the Southwest Pacific Ocean (Hall et al., 2001), suggesting an invigoration in the deep western boundary current ventilating much of the deep Pacific. Similarly, higher glacial flow vigour has been observed in the western tropical Indian Ocean (van der Lubbe et al., *in press*), and the south-western Indian Ocean (Molyneux et al., 2007; Krueger et al., 2012; Martínez-Méndez et al., 2008), although more sluggish near-bottom flow speeds have been found in the deep Southeastern Indian Ocean (Williams et al., 2021). The wide range of results demonstrate that caution must be applied when extrapolating regional $\overline{\mathbf{SS}}$ data into hypotheses regarding large-scale or even global ocean circulation. That being said, when considering flow speed records across multiple depths and locations, especially from within different points in a common current system, it may be possible to infer changes in physical paleoceanography on a larger scale. This is explored in more detail in Chapter 6.

Deep mixing and stratification

The importance of constraining past circulation patterns and flow vigour largely rests on the importance of understanding the oceanic carbon cycle. Changes in deep stratification and convective mixing have been theorised to isolate the deep carbon store and lower atmospheric pCO_2 (Toggweiler, 1999). Toggweiler (1999) and Köhler et al. (2005) demonstrated with box models that reduced deep vertical mixing could reduce atmospheric pCO_2 by 21ppm and 35ppm, respectively, with at least the same

magnitude change again resulting from the carbonate compensation effect (Broecker and Peng, 1987). Inhibiting deep ocean ventilation through reduced mixing could result from changes in the density gradient between intermediate and deep water masses, in turn related to changes in deep-water formation and thermohaline properties (Schmittner and Galbraith, 2008).

Some paleoceanographic evidence supports this proposal, revealing a strong, mostly salinity-driven density gradient between intermediate and deep water-masses (Adkins, 2002; Roberts et al., 2016; Lund et al., 2011). Adkins (2002) suggest that this results from changes in buoyancy forcing between the deep-water formation regions of the AABW and NADW overturning cells, resulting a more saline AABW relative to NADW. Moreover, this stratification may be aided by the shoaling of the boundary between the cells, resulting in less vertical diapycnal mixing as the boundary moves further from rough topography on the seafloor, where internal waves generate enhanced mixing (Adkins, 2013). However, the impact of increased tidal mixing due to lower sea levels might counter this mechanism (Wilmes et al., 2021), and constraints on physical mixing versus chemical ventilation in the past ocean are required to better understand this scenario.

Glacial Deep Water-Mass Geometry

Large changes in the properties and geometry of deep water-masses in the past are evident from paleoceanographic proxies such as carbon isotopes (e.g. Curry and Oppo, 2005; Oppo et al., 2018, ; Figure 1.7a), Cd/Ca ratios (a tracer for past nutrient content; e.g. Marchitto and Broecker, 2006; Oppo et al., 2018, ; Figure 1.7a), and Nd isotopes (a conservative water-mass tracer; Du et al., 2020), although it is important to note that these reconstructions regularly disagree on the details (e.g. Gebbie, 2014).

Low carbon isotope ratios in the deep (roughly >2000m) Atlantic have been attributed to a northward invasion of corrosive southern-sourced bottom waters analogous to AABW (Oppo and Lehman, 1993; Curry and Oppo, 2005; Menviel et al., 2017; Muglia and Schmittner, 2021). This expansion of southern-sourced waters[‡‡] (SSW) is co-

[‡‡]deep and bottom waters originating in the Southern Ocean during glacial times are commonly

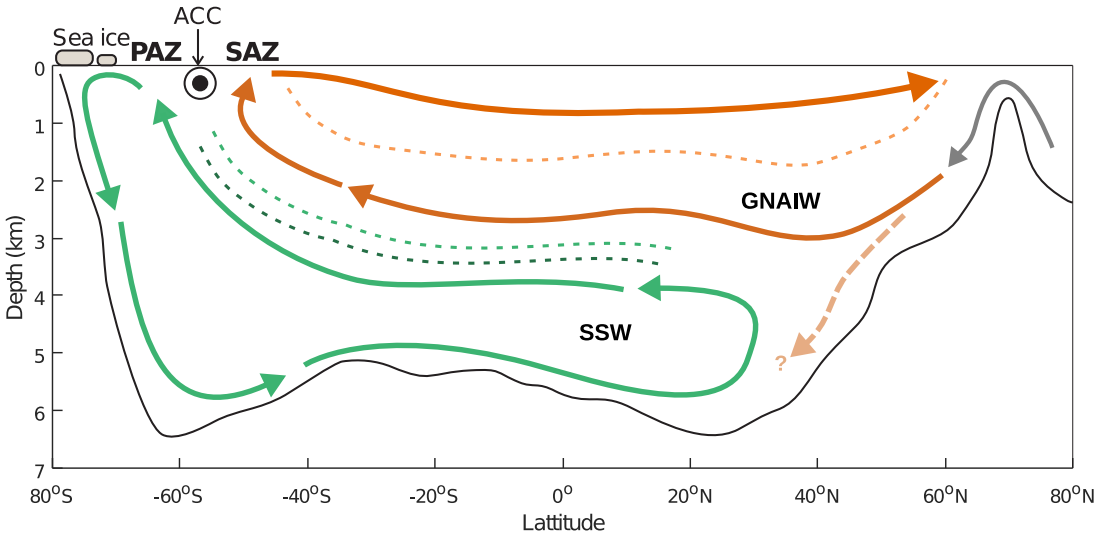

Figure 1.8: A proposed circulation scheme describing this LGM overturning circulation state following Sikes et al. (2017) and Ferrari et al. (2014). PAZ = Polar Antarctic Zone, SAZ = Subantarctic Zone, ACC = Antarctic Circumpolar Current, SSW = Southern-Sourced Water, GNAIW = Glacial North Atlantic Intermediate Water. The semi-transparent dashed arrow in the North Atlantic refers to equivocal results around the nature of NADW formation under glacial conditions (e.g. Böhm et al., 2014; Howe et al., 2016). Dashed lines represent simplified density gradients; the blue-green dashed lines showing the intermediate-deep density gradient between the two overturning cells (Adkins, 2013).

incident with NADW shoaling into a glacial intermediate water-mass, enriched in ^{13}C and depleted in nutrients, dubbed Glacial North Atlantic Intermediate Water (GNAIW) (Boyle and Keigwin, 1987). Glacial SSW was volumetrically superior to GNAIW, explained by its expansion northwards and the shoaling of the boundary between the two from ~4000m to <2000m (Figure 1.7). This has important implications for the global carbon cycle and atmospheric pCO_2 levels, because changing the relative volumes of water-masses with different preformed nutrient inventories, essentially equates to altering the efficiency of the global biological pump (Ito and Follows, 2005).

A proposed circulation scheme describing this LGM overturning circulation state is shown in Figure 1.8, although I note that alternative views of state of glacial ocean circulation are numerous (e.g. Howe et al., 2016; Kwon et al., 2012; Matsumoto and Lynch-Stieglitz, 1999). Interestingly, some modelling endeavours seeking to simulate the LGM ocean have yielded disparate results, difficult to reconcile with paleoceanographic observations. For example, suites of experiments performed under the

referred to as 'southern-sourced waters' or SSW

Paleoclimate Modelling Intercomparison Project (PMIP) have historically struggled to reproduce the shallow NADW seen in the data (e.g. Figure 1.7). Results from the third PMIP phase (PMIP3), and to a lesser extent PMIP4 (Kageyama et al., 2021), generally showed a stronger and deeper NADW for the LGM (see synthesis by Muglia and Schmittner, 2015). This suggests that either the interpretation of paleoceanographic data is wrong or, perhaps more likely, some vital forcing is missing or misrepresented in simulations of the LGM ocean. Muglia and Schmittner (2015) propose that deep NADW in PMIP3 models is driven by wind stress in the North Atlantic, and Zhang et al. (2013) show that stronger wind forcing over the Drake Passage region can also stimulate an anomalously strong/deep NADW cell in LGM simulations. Clearly, better constraints from paleoceanographic data can aide in more realistic simulations of past climates, particularly with respect to the LGM.

1.5 Paleoceanography on longer timescales: This Thesis

As demonstrated above, the field of paleoceanography has progressed a great deal over the past 50 years, furthering our understanding of how the ocean and climate interact and elucidating the relationship to external forcing on a range of scales. In this introduction, I have focused heavily on reconstructions spanning the LGM and Late Pleistocene glacial cycles, in part because a more extensive and diverse array of paleoceanographic reconstructions exist for recent glacial cycles compared to older intervals. This is partially due to to the relative ease and lower cost of recovering 'shorter' sediment cores which probe less-far back in time.

Explanations of changes in climate, and in particular changes in atmospheric pCO_2, over glacial-interglacial timescales theorise a central role for changes in ocean chemistry and circulation. For example, a more efficient biological pump, isolation of the deep ocean due to reduced vertical mixing and diminished upwelling, and modifications to the upper pathways associated with large-scale circulation have all been proposed as amplifying the deterioration of climate conditions during glacial intervals. However, the utility of these mechanisms to explain changes in climate on longer timescales, such as across the Mid-Pleistocene Transition and over Early Pleistocene

glacial cycles, remains unclear.

For the paleoceanography of these earlier times to be investigated, it requires longer, more complete sediment sections recovered for example by Deep Sea Drilling Program (DSDP), Ocean Drilling Program (ODP), Integrated Ocean Drilling Program and International Ocean Discovery Program (IODP) expeditions (see historical perspective by Becker et al., 2019).

The overarching aim of this thesis is to utilise new sediment cores from IODP Expedition 361 to generate multi-proxy reconstructions of surface and deep hydrography at the Agulhas Plateau over the Pleistocene. IODP Expedition 361 drilled six sites in the Southwest Indian Ocean, between 15^{o}S and 41^{o}S, targetting Plio-Pleistocene sequences with the aim of reconstructing the paleoceanography of the Agulhas Current system and wider Southwest Indian Ocean (Hall et al., 2017b). The new data generated in this thesis provide a history of oceanographic conditions from the southernmost location drilled, Site U1475, and are used to test and develop hypotheses regarding the role of the ocean regulating atmospheric CO_2 and climate. The specific aims are as follows:

1. Develop a long, continuous benthic stable isotope record from Site U1475 spanning the entirety of the Pleistocene epoch. The benthic oxygen isotope record will allow the construction of an astronomically-tuned age-depth model for the site, and the benthic carbon isotope record will provide insights into deep chemical ventilation and water-mass dynamics, in particular when compared to records from other regions and water depths.

2. Reconstruct a history of Antarctic iceberg drift south of Africa across Early Pleistocene glacial cycles, the Mid-Pleistocene Transition, and the Mid-Brunhes Transition, in order to identify links between far-travelling Antarctic icebergs and ocean circulation with respect to the development of glacial conditions.

3. Reconstruct a history of the chemical gradient between the intermediate and deep ocean at the northern edge of the Subantarctic Zone, in order to investigate how the export of carbon into the ocean interior evolved over multiple glacial

cycles and in the context of low-frequency variability shown elsewhere in the oceanic carbon cycle.

4. Use the 'Sortable Silt' mean grain size proxy to reconstruct changes in near-bottom flow speed on the Agulhas Plateau, where the deep flow regime is highly sensitive to changes in the strength and position of the ACC as well as deep water-mass dynamics (Molyneux et al., 2007). Extending the previous 150-kyr $\overline{\mathbf{SS}}$ record from this region over multiple glacial cycles will better constrain the evolution of circum-Antarctic flow under a range of climate boundary conditions.

1.5.1 Outline

In the following chapters I address each of the aims listed above, before synthesising the results presented and propose directions for future work. In addition, a description of the materials used and the methodologies applied throughout is given in Chapter 2.

Chapter 3: Determining Age-Depth Models for the Agulhas Plateau Composite

One of the most important considerations when constructing paleoclimate records are the available constraints on age. In Chapter 3, I present 3.2 myr long benthic stable isotope records from the Agulhas Plateau, and demonstrate the development of age-depth models used throughout this thesis. In addition I show an alternative age-depth model free from orbital tuning assumption.

Chapter 4: Antarctic icebergs lead ocean circulation into Pleistocene glacials; Evidence from 1.65 Million Years of Agulhas Plateau Ice-rafted Debris

As described above, palaeoceanographic evidence suggests that during glacial periods of at least the past 1.5 myr, large-scale ocean circulation and deep water-mass geometry had markedly different features from today. An absence of evidence to elu-

cidate the origin of these changes means that the sequence of events leading to global glacial conditions remains unclear. Some modelling studies have shown that altering the buoyancy forcing in the Southern Ocean can have a global reach, notably by modifying the formation of NADW (e.g. Seidov et al., 2005), however paleo-evidence for this has thus far been missing.

In Chapter 4, a new, high resolution record of ice-rafted debris accumulation is presented from the Agulhas Plateau. Located mostly out of the reach of coarse volcanic material present in the South Atlantic, this record represents a sensitive proxy for survivability of Antarctic icebergs across the Southern Ocean. Combined with a comprehensive analysis of phasing between this and other co-registered data, it is shown that a systematic lead is present for Antarctic iceberg drift over changes in deep ocean circulation during glacial cycles across the last 1.5 Ma. Finally, a new mechanism is proposed to explain this coupling, relating to the 'escape' of buoyancy anomalies from the Southern Ocean into the return limb of the Atlantic overturning cell.

Chapter 5: Extending the Agulhas Plateau Carbon Isotope Gradient Record: Modulation by Long Eccentricity

Secondly, whilst long records of stable carbon isotopes measured on benthic foraminifera from different core depths have shown that distinct gradients between the intermediate and deep ocean repeatedly developed over glacial cycles (e.g. Hodell et al., 2003), knowledge of shallower gradients expected to result from changes in Southern Ocean export productivity are limited to last last few glacial cycles (Ziegler et al., 2013; Charles et al., 2010). This is in part because of the difficulty in recovering long sediment core archives from relatively shallow locations, as well as the uncertainties inherent in aligning the stratigraphies of multiple core sites. Ziegler et al. (2013) instead used the gradient between benthic and deep-dwelling planktic foraminifera to reconstruct the chemical gradient between Southern Ocean mode waters and the deep ocean. This revealed a tight coupling between changes in atmospheric CO_2, Southern Ocean dust fluxes, and the mode water to deep ocean carbon isotope gradient.

Extending the Southern Ocean carbon isotope gradient back through the Pleistocene

provides an opportunity to investigate this coupling on longer timescales. For example, it would allow one to test hypotheses linking the Mid-Pleistocene Transition to Southern Ocean productivity (e.g. Chalk et al., 2017; Willeit et al., 2019). Where productivity proxies from single locations are limited by the question of local versus regional influences, and the advection and preservation of biogenic molecules in the sediment (e.g. Anderson and Winckler, 2005; Sachs et al., 2000), the mode to deep water carbon isotope gradient should instead integrate a larger area and be more robust to local influences.

In Chapter 5, a 1.55 myr-long record of mode to deep water carbon isotope gradient is presented from the Agulhas Plateau. This record reveals substantial long-term modulation of this gradient, matching low-frequency changes in Earth's orbital cycles. The potential origins of this signal are assessed, and a proposal is put forward relating the modulation of the carbon isotope gradient to the production of Subantarctic Mode Water.

Chapter 6: Changes in Physical and Chemical Ventilation of Deep-Water in the Southwest Indian Ocean across Climate Transitions of the past 1.9 Million Years

Finally, paleoceanographic reconstructions from the Southern Ocean across the last glacial cycle have proved invaluable in testing models which link deep ocean ventilation and wind-driven upwelling to atmospheric pCO_2 (e.g. Anderson et al., 2009; Ai et al., 2020). However, probing these processes with proxy records requires reconstructing elements of chemical and physical oceanography (i.e. the accumulation of respired carbon in the deep and changes in wind-driven ocean circulation).

In Chapter 6 of this thesis, a record of near-bottom flow speed is presented from the Agulhas Plateau, reconstructed using the 'Sortable Silt' mean grain size proxy (McCave et al., 1995b), reflecting variations in the strength and position of the Antarctic Circumpolar Current and, therefore, the Southern Hemisphere Westerly Wind Belt. By combining this record with records of deep chemical ventilation (benthic carbon isotopes), and changes in surface hydrography (previously published records of sea surface temperature and productivity) it is possible to explore the evolution of cou-

pling between wind-driven circulation and deep chemical ventilation across multiple glacial cycles, including remarkable interglacial intervals and climate transitions such as the MPT and MBT.

2 | Materials and Methods

2.1 Agulhas Plateau sediment cores

2.1.1 International Ocean Discovery Program Site U1475

The primary archive utilised in this thesis is International Ocean Discovery Program (IODP) Site U1475, comprising deep-sea sediment cores obtained during Expedition 361 in February 2016 (Hall et al., 2017b). The cores were recovered using an Advanced Piston Corer (APC), which retrieved a total of 1016 m of sediment from six holes. This thesis makes use of the triple APC continuous spliced sequence constructed by the stratigraphic correlation of RGB records for each hole (see Hall et al., 2017a, for a detailed description of the splice construction). The site is located on the southwestern Agulhas Plateau (41^{o}25.6'S; 25^{o}.6'E) at the interface between the Indian, Atlantic, and Southern Oceans; ~450 nmi south of the South African coast (Figure 2.1; Hall et al., 2017a).

2.1.2 Agulhas Plateau Oceanography

At a water depth of 2669 m, Site U1475 is presently bathed in a mixture of North Atlantic Deep Water (NADW) and Circumpolar Deep Water (CDW) (Arhan et al., 2003). Immediately south of the Agulhas Plateau, the sea-floor descends to depths of >4000m, situating the site in close proximity to the cold, dense Lower Circumpolar Deep Water (LCDW) and Antarctic Bottom Water (AABW) that fills much of the abyssal ocean in the Southern Hemisphere (Talley, 2013). In the deep basins sur-

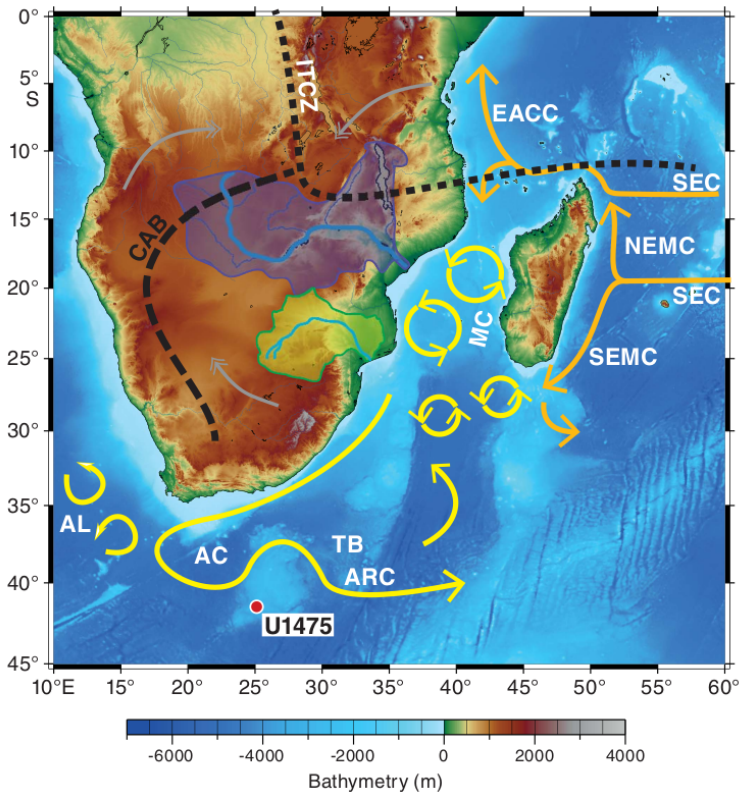

Figure 2.1: *Figure from Hall et al. (2017a).* Location of IODP Site U1475 with major surface ocean circulation patterns (arrows) and approximate summer position of the Intertropical Convergence Zone (ITCZ) and Congo Air Boundary (CAB) (dashed lines, from Reason and Rouault, 2006). AC = Agulhas Current, ARC = Agulhas Return Current, SEC = South Equatorial Current, SEMC = South East Madagascar Current, NEMC = North East Madagascar Current, EACC = East Africa Coastal Current, TB = Transkei Basin.

rounding the Agulhas Plateau, the gradual transition from NADW to LCDW occurs at ~3000m, however several lines of evidence indicate that this boundary shoaled during past glacial periods reaching ~2000m at times (e.g. Curry and Oppo, 2005). Site U1475 is therefore well-situated to document past changes in the geometry of northern and southern-sourced deep waters in relation to climate change since the Late Miocene.

Figure 2.2b shows a temperature-salinity diagram for the southwestern Agulhas Plateau (41°S, 25°E; WOA18[‡]). The surface hydrography is dominated by warm and relatively saline waters, mostly originating in the evaporative subtropical Indian Ocean. This Indian Ocean Water (IOW) is composed of a variety of water-masses including Subtropical Surface Water and Agulhas Waters. Site U1475 is directly influenced by the

[‡]World Ocean Atlas 2018 available at https://www.nodc.noaa.gov/OC5/woa18/

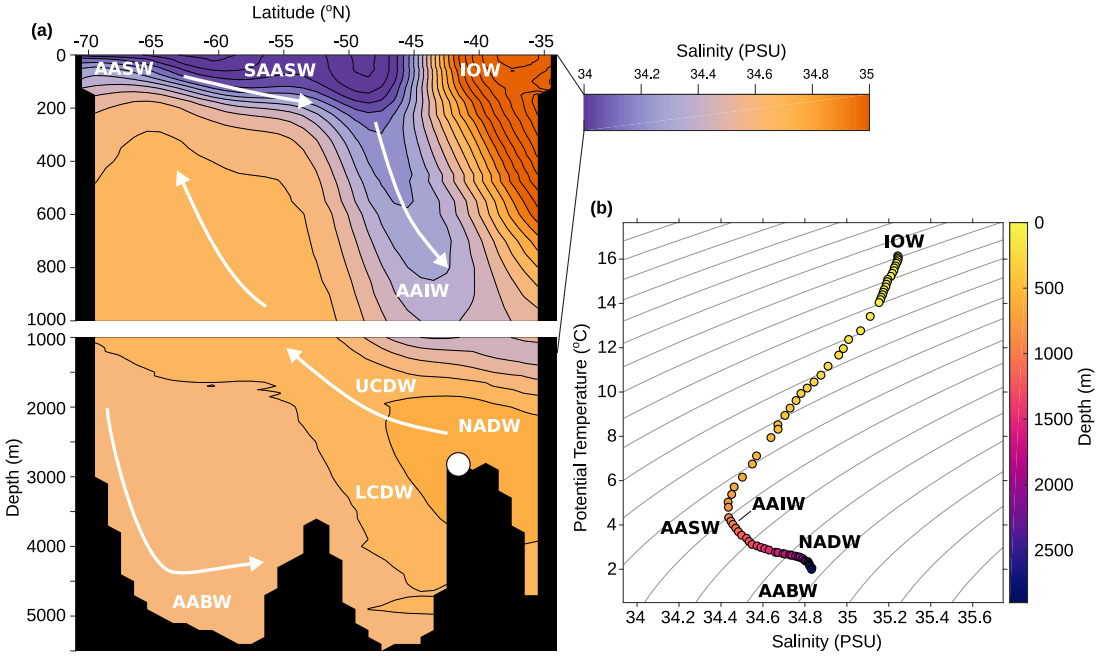

Figure 2.2: (a) Latitudinal salinity transect at 25°E (note the broken y-axis scale). The meridional component of water mass circulation (white arrows) follows Read and Pollard (1993). **(b)** Potential temperature - salinity diagram from 41°S, 25°E, 2669m (southwestern Agulhas Plateau) with water depth given as colour. The contours represent isopycnals at 0.25 kg^{-1} intervals. Key water mass end-members are labelled following Read and Pollard (1993). IOW = Indian Ocean Water, SAASW = Subantarctic Surface Water, AASW = Antarctic Surface Water, AAIW = Antarctic Intermediate Water, UCDW = Upper Circumpolar Deep Water, LCDW = Lower Circumpolar Deep Water, NADW = North Atlantic Deep Water, AABW = Antarctic Bottom Water. *data from the World Ocean Atlas 2018 (Zweng et al., 2019)*

southern extent of the eastward-flowing Agulhas Return Current (ARC), consisting of the relatively shallow Agulhas Waters not transported into the South Atlantic by the so-called 'Agulhas Leakage' south of Africa. As the ARC nears the Agulhas Plateau, the bathymetric rise steers them in an S-shape to the north (Boebel et al., 2003).

Figure 2.2b also indicates a range of less saline and slightly cooler surface waters, representing density modifications of IOW by South Atlantic water-masses from the west, transported as part of the Southern Hemisphere 'super-gyre' at the northern limit of the Antarctic Circumpolar Current (ACC) (Graham and Boer, 2013; Speich et al., 2007). Further density modification from colder water-masses from the south also occur. These water-masses, identifiable as Antarctic Surface Water (AASW) and Subantarctic Surface Water (SAASW), are partitioned from Agulhas waters in the ARC by a hydrographic front, characterized by a strong meridional gradient in SST at ~43°S. This SST gradient shows little to no seasonal variation and is associated

with the westward flowing ARC. Following Graham and Boer (2013), this front can be considered the 'dynamical subtropical front'* and is seemingly unrelated to the other seasonally variable hydrographic fronts in the the region.

Figure 2.2a shows the tongue of low salinity Antarctic Intermediate Water (AAIW) and Subantarctic Mode Water (SAMW) spreading downwards and northwards from the Southern Ocean surface. Intermediate-depth water around the Agulhas Plateau is characterised by a combination of 'old' mode and intermediate water-masses (SAMW and AAIW) which have been extensively modified to become warmer and more saline during circulation through the Indian Ocean, brought to the region by the Agulhas Current and ARC. Meanwhile, 'new' SAMW and freshly 'renewed' AAIW are contributed from the south, originating in the Subantarctic Zone (SAZ) through deep winter mixing and modification of AASW and SAASW. Mode water circulation in the region is therefore characterised by some combination of 'old', highly modified SAMW from the Indian Ocean, supplied by the ARC, and relatively fresher mode waters transported within and across the ACC and to a lesser extent the South Atlantic Current (Sloyan and Rintoul, 2001).

Figure 2.3, shows oxygen depth profiles for three locations in the region: one in the core of the ARC, one over the southern Agulhas Plateau (location of Site U1475/the AP_{comp}) and one further south in the SAZ. The northernmost site in the ARC flow path displays a clear subsurface oxygen minimum around 200m depth, likely representing IOW or the influence of low-oxygen subtropical thermocline waters (Lutjeharms and Ansorge, 2001). Over the southern Agulhas Plateau, the influence of these low-oxygen waters gives way partially to highly oxygenated AASW and SAASW, though a slight oxygen minimum still exists. This minimum is almost entirely absent at the southernmost site, where the water column above 100m is consistently more oxygenated than the other sites, reflecting enhanced air-sea exchange in the SAZ.

*The eastward extension of the western boundary current (Graham and Boer, 2013)

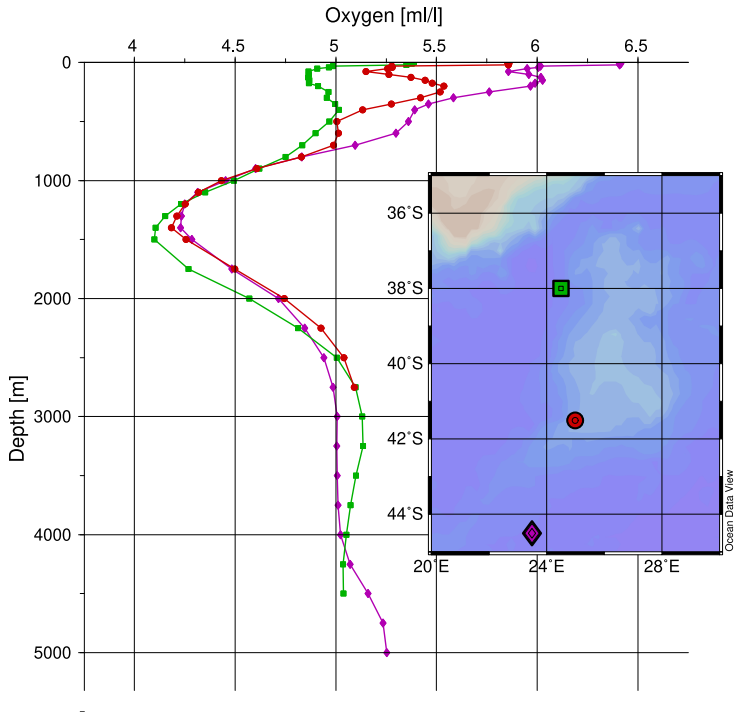

Figure 2.3: Dissolved oxygen concentration with depth for three sites in the Agulhas Plateau region, 35^{o}S to 45^{o}S and 20^{o}E to 30^{o}E. Site U1475/AP$_{comp}$ is represented in red. *Data from the WOCE Global Hydrographic Climatology (Gouretski, 2018)*

Sedimentology

The Agulhas Plateau is bathymetricaly isolated, ascending ~2500m above the surrounding deep basins: the Agulhas Passage to the north, the Agulhas Basin to the west, and the Transkei basin to the north-east (Figure 2.1). Subsequently, the delivery of terrigenous material from the African continent is small, as shown by the predominantly biogenic composition of Site U1475 (80% ± 6% on average) (Hall et al., 2017a). Two lithogenic units are identified in the Site U1475 sequence, though the records presented here consist only of Unit II, a light greenish to pale grey nannofossil ooze. The biogenic material in Unit II is dominated by nannofossils (55% ± 11%), microfossils (17% ± 6%) and diatoms (6% ± 4%). Quartz and clay minerals dominate the terrigenous fraction, with periodic occurrences of coarse-grained (>150μm) ice-rafted minerals (Hall et al., 2017a).

The relatively low siliceous fraction through the core reflects the distal position from

the circum-Antarctic opal belt where opal in sediments regularly exceeds 50% (Diekmann, 2007). Furthermore, the down-core $CaCO_3$% variability is relatively small (74-85%) based on shipboard $CaCO_3$ measurements (Hall et al., 2017a) and weight % potassium derived from natural gamma ray counts (Vleeschouwer et al., 2017; Gruetzner et al., 2019). The variability of sites further south typically exceeds this (e.g. Howard and Prell, 1994), implying lower glacial-interglacial variability in preservation and/or rain rate of carbonate at Site U1475 compared to more 'typical' Southern Ocean regimes. The preservation of $CaCO_3$ in deep marine sediments is controlled by the $CaCO_3$ saturation state of the overlying seawater, itself a function of seawater carbonate ion concentration and pressure (Archer, 1996). With depth, increasing pressure leads to increased $CaCO_3$ dissolution, resulting in a horizon below which dissolution exceeds preservation (known as the Carbonate Compensation Depth or CCD[§]). In the Agulhas Plateau region, the modern CCD is situated sufficiently deeper than Site U1475 (~4300m; Howard and Prell, 1994) preventing significant dissolution. Although the preservation may have varied in the past depending on the prevalence of supersaturated NADW and more corrosive southern-sourced deep waters (González-Dávila et al., 2011), it has been shown that, at least during the Late Pleistocene, carbonate dissolution was minimal (Molyneux et al., 2007; Diz et al., 2007).

Seismic data provide evidence for a strong current system present and highly interactive with respect to the sedimentary environment in the region, with Uenzelmann-Neben (2002) identifying several contourite sediment drifts on the southern Agulhas Plateau. Furthermore, abyssal circulation around the Agulhas Plateau is likely responsible for erosional activity and sedimentary hiatuses in the region, manifesting notably as an erosional moat encircling it, related to the intensification of bottom-currents during the Mid-Miocene (Uenzelmann-Neben, 2002). Located just below the crest of one of the aforementioned drift deposits, Site U1475 is above the the reach of the (modern-day) AABW circulation, evidently unaffected by erosional features, with no obvious hiatuses through the recovered section and a Holocene or Late Quaternary-aged core-top (Hall et al., 2017a; Gruetzner et al., 2019). This drift is instead deposited by south-eastward-flowing components of NADW, entering from

[§]The nomenclature surrounding the ocean carbonate system is at times convoluted and this definition of the CCD is in some ways an oversimplification

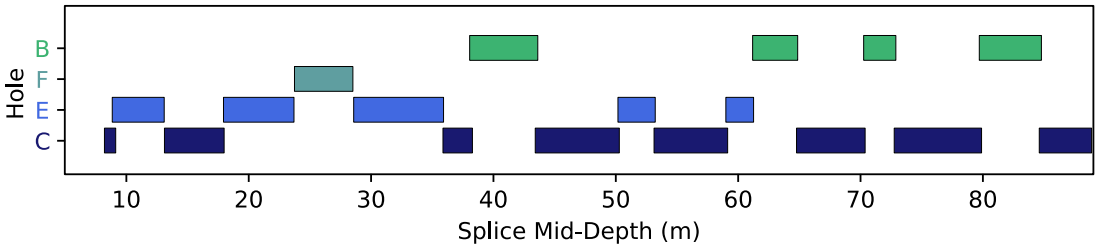

Figure 2.4: Figure showing the Site U1475 Holes from which samples for this study were obtained; all of which are part of the shipboard splice (Hall et al., 2017a)

the South Atlantic. In a region with such hydraulically-active bottom currents, Site U1475 offers a unique and valuable sedimentary archive, highly sensitive to changes in deep-sea circulation since the Late Miocene (Gruetzner et al., 2019).

2.2 Sampling Strategy and Processing

Samples for Site U1475 were requested from and sampled by the Kochi Core Centre and were obtained by the staff as either 'half-round' or 'wedge' samples. All samples were from the shipboard splice, consisting predominantly of Holes C, E, and B (Figure 2.4). In total, 1473 samples were processed for this thesis, spanning from 8.36m to 87.98m splice depth at a spacing of 4 cm. In preparation for proxy work, samples were submersed in deionized (DI) water and placed on an over-under spinner for 24 hours before being wet-sieved at 63μm, again with DI water. DI water was flushed through the sieve until calcite shells in the >63μm fraction were free from visible clay or silt particles. The fine (<63μm) and coarse (>63μm) fractions were then dried at 40^{o}C and weighed to give the respective fraction weight %. A sub-sample of the fine fraction was removed for grain-size analysis and the coarse fraction was sieved further to isolate the desired size fractions for IRD and stable isotope work (see below).

2.2.1 The Agulhas Plateau Composite record

The U1475 'pre-site survey' CASQ core MD02-2588 was recovered in 2002 by the R/V Marion Dufresne expedition MD128, situated near the location that would later be drilled as Site U1475 (MD02-2588: 41^{o}19.90'S, 25^{o}49.7'E; 2907 m depth). Since sev-

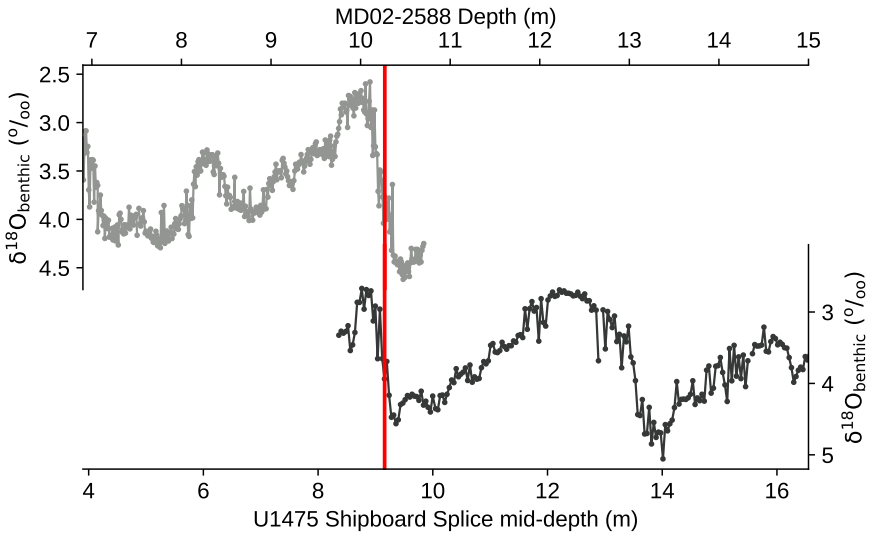

Figure 2.5: Construction of the Agulhas Plateau Composite by aligning the benthic $\delta^{18}O$ records from MD02-2588 (Ziegler et al., 2013) and Site U1475 (this thesis; see Chapter 3). The vertical red line shows the tie-point chosen between the two records, selected at the maximum rate of change to minimise uncertainty

eral high resolution multi-proxy records already existing for MD02-2588 (e.g. Marino et al., 2013; Ziegler et al., 2013), the upper 10.27m (roughly 300 kyr; see Chapter 3) of this core is used in place of the corresponding section of Site U1475. In order to present a continuous Agulhas Plateau sedimentary record, the lowest deglaciation of MD02-2588 was correlated to the respective deglaciation in Site U1475 using both the benthic $\delta^{18}O$ and benthic $\delta^{13}C$ records from both cores (Figures 2.5 and 3.2). This tie point occurs at 10.27 m in MD02-2588 and 9.16 m in U1475. The resulting stratigraphic framework is referred to hereafter as the Agulhas Plateau composite (AP_{comp}).

2.3 Analytical methods

2.3.1 Stable isotope analysis of foraminifera

For stable isotope analyses, foraminifera were picked from the washed >63µm sediment fraction further sieved into various size ranges (discussed for each species below) using a fine paint brush and deionized water under a binocular light microscope.

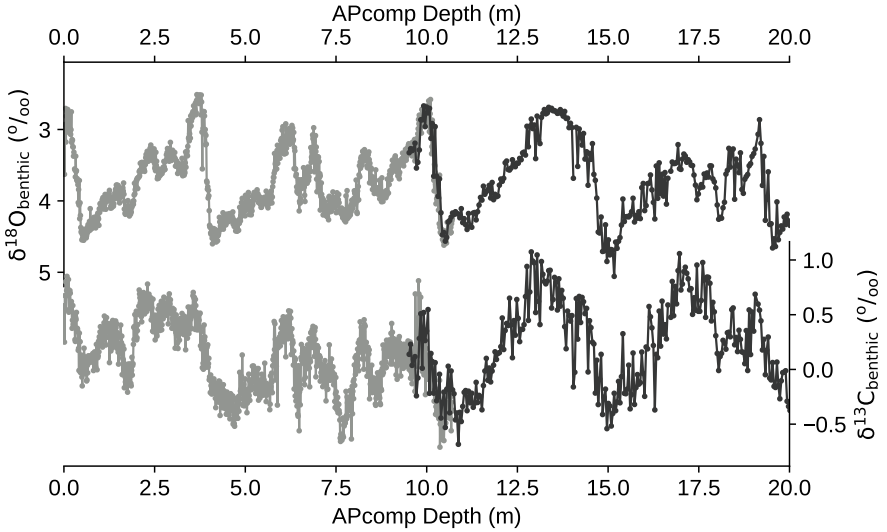

Figure 2.6: As for Figure 2.5, but presented on the AP_{comp} depth scale. Benthic $\delta^{18}O$ and $\delta^{13}C$ records from MD02-2588 (Ziegler et al., 2013) and Site U1475 (this thesis; see Chapter 3).

Cibicides wuellerstorfi

Cibicides wuellerstorfi (Schwager, 1886) is an epifaunal benthic foraminifera, considered to precipitate calcite with $\delta^{13}C$ in, or close to equilibrium with the ambient bottom water $\delta^{13}C_{DIC}$ (Woodruff et al., 1980; Belanger et al., 1981; McCorkle and Keigwin, 1994; Schmittner et al., 2017) and is thus a widely used paleoceanographic tool.

Where possible, 3 specimens were picked from the 250-315 μm fraction for stable isotope analysis. Individuals with broken or poorly preserved shells were rejected. Where fewer specimens were present, the >350 μm fraction was consulted as there is no evidence for a size-dependency in *Cibicides* species stable isotope composition (Corliss et al., 2002). Stable isotope measurements were performed at Cardiff University using a Thermo Finnigan MAT 253 mass spectrometer linked online to a Carbo Kiel carbonate preparation device with long term precision of ±0.05‰ for $\delta^{18}O$ and ±0.021‰ for $\delta^{13}C$ (±1σ). Results are calibrated to an internal laboratory standard (BCT 63μm) and presented relative to the Vienna Pee Dee Belemnite scale (‰ VPDB).

Globrotalia truncatulinoides (sinistral)

Globorotalia truncatulinoides (d'Orbigny, 1839) is an extant species of non-spinose *Globorotaliid* planktic foraminifera. *G. truncatulinoides* is characterised by a conical shape, a left- (sinistral) or right-coiling (dextral) final whorl consisting of 5 chambers (de Vargas et al., 2001). Here, only the sinistral form is measured, due to the wider temperature tolerance and shallower depth range of dextral specimens (Chiessi et al., 2007); justified further in Chapter 5.

To generate the down-core records, paired stable isotope ($\delta^{18}O$, $\delta^{13}C$) measurements were made on sinistral (left-coiling) *G. truncatulinoides* specimens from the 250-315μum size fraction. The number of specimens measured in each sample (hereafter n) was dependent on the availability of morphologically distinct and well-preserved *G. truncatulinoides* shells; the target number was 15 (see Chapter 5), however n ranged from 1 to 15.

For isotope analyses of large samples (n>7), 100 to 250μg of crushed sample was weighed using a Sartorius micro-balance (precision ±1μg) and measured a Finnigan Delta V Advantage coupled online with a Gasbench II. Long-term external precision is <0.06‰ for $\delta^{13}C$ and $\delta^{18}O$ and internal standard deviations are generally <0.1‰. Smaller samples (n≤7) were measured using a Thermo Finnigan MAT 253 mass spectrometer coupled online to a Carbo Kiel carbonate preparation device with a long term precision of ±0.05‰ for $\delta^{18}O$ and ±0.021‰ for $\delta^{13}C$ (±1σ). All results are calibrated to an internal laboratory standard (BCT63) and reported relative to the Vienna Pee Dee Belemnite scale.

Individual Foraminifer Analysis

The aim of measuring the isotope composition of multiple shells within a sample is to approximate the population average for a given stratigraphic interval. It has previously been proposed that a large number of specimens (30-50 individuals) are required to achieve a reproducible mean (Killingley et al., 1981; Löwemark et al., 2005; Schiffelbein and Hills, 1984), however this may be unrealistically large (Fraass

and Lowery, 2017) and the number will vary depending on the species in question, the sedimentation rate, and the local hydrographic variability. One way to constrain the relationship between precision and number of shells per sample is to measure the composition of multiple individual foraminifer from single samples. Some early studies attempting to quantify inter-specimen variability through Individual Foraminifera Analysis (IFA) found alarmingly high variance within a single sample (up to 2‰). However, the relatively large samples required by Mass Spectrometers at the time meant that IFA had to be performed on foraminifera from large size-fractions, introducing complications from the size-dependent fractionation of many species (Friedrich et al., 2012).

Here, 154 specimens from the 250 - 315μm size fraction, spanning 4 individual samples (2 from interglacial and 2 from glacial intervals) from Site U1475 were measured on a MAT 253 mass spectrometer following the 'small-sample' protocol outlined above. On average, the internal standard deviation for measurements of individual *G. truncatuloinoides* shells was 0.03‰ for $\delta^{13}C$ and 0.05‰ for $\delta^{18}O$. The intra-sample standard deviation (average across the 4 samples with sample means subtracted) is 0.40‰ for $\delta^{18}O$ and 0.31‰ for $\delta^{13}C$ (Figure 2.7a-b). From this, the standard error of the mean for each down-core sample can be estimated by dividing by the square-root of the number of shells measured (n). Following this approach, a sample with n = 15 specimens will have 95% confidence intervals of 0.20‰ for $\delta^{18}O$ and 0.16‰ for $\delta^{13}C$ (Figure 2.7c). Data-points consisting of n<3 specimens (n = 3 equates to a standard error of 0.46‰ and 0.35‰ for $\delta^{18}O$ and $\delta^{13}C$, respectively) are discarded, as this (admittedly somewhat arbitrary) boundary constitutes the number of samples below which the 95% confidence intervals exceed the inter-sample standard deviations. These estimates are used in Chapter 5 to calculate confidence intervals for the down-core *G. truncatulinoides* isotope records.

2.3.2 Ice-Rafted Debris

To determine the abundance of Ice-Rafted Debris (IRD) from Site U1475, the washed coarse samples (>63μm) were split between 3 and 5 times using a micropaleontology

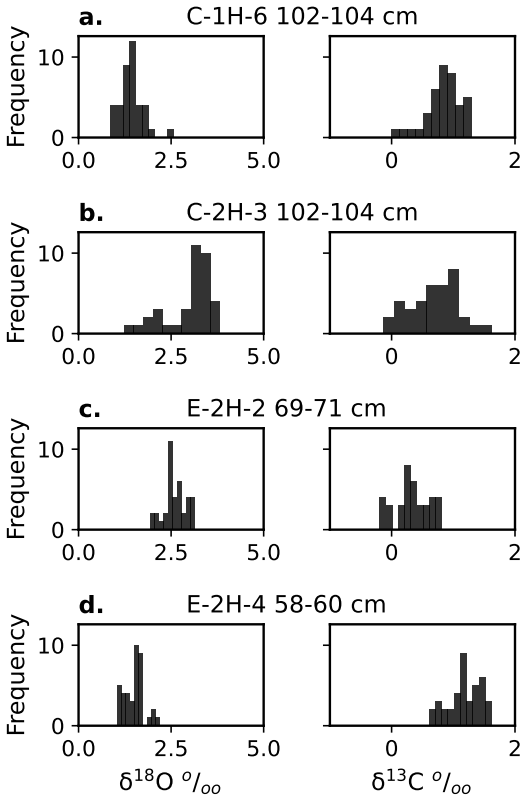

Figure 2.7: Histograms for $\delta^{18}O$ (left) and $\delta^{13}C$ (right) of *G. truncatuloinoides* obtained by Individual Foraminifera Analysis (IFA) on four stratigraphic samples on the U1475 Splice **(a-d)**. Samples **(a)** and **(d)** are from interglacial intervals and **(b)** and **(c)** are from glacial intervals

splitter to yield between 500 and 1000 entities (including foraminifera). The split sample was then sieved to isolate the >150μm fraction. This size fraction is routinely used in studies of IRD at ice-distal locations (Hemming, 2004, and references therein) and was chosen to exclude grains that may be transported by means other than ice-rafting (e.g. eolian or ocean current processes), whilst including enough material for robust counts. This methodology is comparable to that employed for MD02-2588. The IRD records presented in this thesis include measurements previously made on MD02-2588 (n=522; partially published in Marino et al., 2013; Simon et al., 2013)).

Detrital fragments were counted within the sub-samples under a stereo light microscope. No attempt was made to distinguish between mineralogies of clear phenocrysts, however grains that were obviously of volcanic (e.g. tephra) or authigenic (e.g. pyrite) were excluded from the IRD record as they may have originated by means other than iceberg-rafting (Nielsen et al., 2007a). Quartz and feldspar are often in-

distinguishable with confidence by eye, so 'volcanic' feldspar grains may unintentionally be included in the count. However, Energy Dispersive X-Ray Spectrometry (EDS) point analysis (see below) reveals that the dominant mineralogy is quartz and that volcanic mineralogies are relatively rare. Records were made for any notable minerals or grains identified, but no continuous quantitative record of mineralogy is provided due to the ambiguity of identifying minerals by stereo light microscopy (see Nielsen et al., 2007a).

Mass Accumulation Rates

Several methods for normalizing ice-rafted debris counts in marine sediments exist. For example, IRD counts can be converted to number of grains per gram of dry sediment (this thesis), concentration relative to the number of planktic foraminifera (the 'IRD Index'; Poore and Berggren, 1975), concentration relative to the total number of grains of any type in the given size fraction ('IRD Mass Ratio'; Allen and Warnke, 1991) or as a weight concentration (i.e. in mg of IRD per g of sediment; Teitler et al., 2010). Each method carries benefits and limitations reflecting the possibility of external factors effecting the index. For example, the ratio of IRD per planktic foraminifera or total grains present can change due to dissolution of carbonate material, or changes in biological productivity. One way to account for this, albeit imperfectly, is to calculate the accumulation rate of IRD using an estimate of sedimentation rate and the dry bulk density of the sediment.

To calculate mass accumulation rates, the raw IRD counts were converted into concentrations (equation 2.1) and then into apparent mass accumulation rates (MAR) by multiplication with Linear Sedimentation Rate (LSR)[†] and Dry Bulk Density (DBD; data from (Gruetzner et al., 2019)).

$$\text{Conc.}_{(\#\,\text{grains/g})} = \#\,\text{grains}_{(>150\mu\text{m})} \div \text{total sample dry weight}_{(\text{g})} \tag{2.1}$$

[†]this is not an ideal solution as it requires assuming linear sedimentation between age-depth tie points, an assumption which is unlikely to hold in reality

$$\mathrm{MAR}_{\mathrm{IRD}\ (\#\ \mathrm{cm^{-2}\,kyr^{-1}})} = \mathrm{Conc.}_{\ (\#\,\mathrm{grains/g})} \times \mathrm{LSR}_{\ (\mathrm{cm\,kyr^{-1}})} \times \mathrm{DBD}_{\ (\mathrm{g\,cm^{-3}})} \tag{2.2}$$

MD02-2588 IRD

The short overlapping sections of Site U1475 and the previously measured MD02-2588 show good agreement between IRD concentrations. No dry bulk density (DBD) data exists for MD02-2588 and so in order to convert the existing IRD data into MAR (equation 2.2), DBD was estimated by fitting a 2^{nd} order polynomial to the Site U1475 DBD data used in the splice and forecasting values for MD02-2588 samples (r^2 = 0.57).

IRD Mineralogy

Of the total samples, a subset were quasi-randomly chosen for mineralogical determination by Energy Dispersive X-ray Spectrometry (EDS) point analysis (n=8). The number of grains picked from each sample for EDS ranged from 1 to 8 and varied in appearance. Firstly, the grains were mounted to a sticky carbon mount using a fine brush and deionized water. The mounted sample was then carbon coated to ~15nm with 8 second bursts. The coated samples were then loaded onto a Zeiss Sigma HD field emission gun Scanning Electron Microscope (aperture 60 μm, amplitude 15kV). The grains were then imaged and elemental data was acquired at several points using 2 Oxford X-Max detectors with a combined area of 300 mm^2. The elemental oxide % data obtained is available in full in the appendix (Table A1).

2.3.3 Grain-size analysis

Grain size analysis can be employed to investigate changes in the delivery, deposition and sorting of marine sediments. In thesis, the 'sortable silt' flow speed proxy is reconstructed for the AP_{comp}.

Removal of Biogenic Components

Before measurements were made, the biogenic components (carbonate and opal) of the sediment were removed by 2-step digestion. First, 2-4g of the <63μm fraction were placed in excess 2M acetic acid for >12 hours. The excess acid was then removed by siphon and the step was repeated. Following the second removal of acid, the sample was rinsed with de-ionised water and left to settle overnight. After 24 hours, the sample was heated in an 85^oC water bath with excess 0.2% sodium carbonate (Na_2CO_3) for five hours. The sample was then left to cool and settle, before the excess Na_2CO_3 was removed and de-ionised water was added. The sediment was left to settle for >2 days before excess water was siphoned off and replaced. The sediment was left again to settle for 1-2 weeks before the excess water was removed and the sediment was washed into 60ml bottles with sodium hexametaphosphate (Calgon).

Coulter Counter

$\overline{SS}$ data for MD02-2588 and the upper 22.49 m of Site U1475 was obtained by Ian R. Hall, Cardiff University.

The $\overline{SS}$ flow speed proxy is derived by measuring the mean grain size of the 10-63 μm terrigenous size fraction. Before analysis, the samples were placed on a rotating wheel for >24 hours and then ultrasonicated for 3 minutes to ensure grains were entirely disaggregated. Measurements for Site U1475 samples were made using a Beckman Multisizer IV Coulter Counter (following the protocol of Bianchi et al. 1999) at Cardiff University (previously made measurements for Site MD02-2588 were made on a comparable Beckman Multisizer III). This instrument is an electrical resistance pulse counter, considered preferable to laser particle sizer alternatives for measuring the non-cohesive silt fraction (Bianchi et al., 1999). Samples were analysed at least 2 times until results converged to within 0.3 μm. The final $\overline{SS}$ value is reported as the average of these measurements. If the intra-sample standard deviation was high (>0.5μm), the data was dismissed and the sample re-measured. Furthermore, if the aperture of the Coulter Counter repeatedly 'blocked' the run was omitted and the

sample re-measured following inspection of a smear slide to ensure that the removal of biogenic components was sufficient. $\overline{\mathbf{SS}}$ data presented in Chapter 6 refer to the geometric mean of the 10-63μm fraction and are presented either in μm units or unitless with mean subtracted and standard deviation set to 1.

2.4 Overview of Statistical methods

In the following chapters, detailed descriptions are provided for any novel or unorthodox[‡] techniques used. Here I give a brief overview of statistical or numerical methods used. All analyses were performed in Python or MATLAB unless otherwise stated. Source code is available at www.github.com/AidanStarr/thesis and is provided in the appendix.

2.4.1 Spectral estimation

Spectral analysis in this context refers to investigating time series in the frequency-domain. In other words, it is an attempt to identify or isolate periodic components in a signal, such as the amplitude or wavelength of cycle(s) which might be present in the time series. In many ways, spectral analysis and paleoceanography go hand-in-hand, and the estimation of spectra in sediment core records has underpinned much of what we now know about past climate cycles (e.g. Hays et al., 1976).

In this thesis I make use of:

- the Blackman-Tukey Method to estimate autospectra, cross-spectra and coherency between records, as this is a well established approach in paleoclimate studies (e.g. Paillard et al., 1996) and allows the relatively fast, computationally efficient estimation of spectra for many segments and time series;
- Continuous Wavelet Transformation (CWT), which uses wavelets (in this case a Morlet wavelet) to estimate the evolutionary power of different frequencies

[‡]approaches seen less frequently in Paleoceanographic studies

(Torrence and Compo, 1998). CWT is a particularly useful approach for non-stationary time series (Weedon, 2003);

- Lomb-Scargle Periodogram, a spectral estimation approach which allows analysis of unevenly-spaced data (Lomb, 1976; Scargle, 1982) and is hence a popular choice for paleoclimate studies. In this thesis, I use the software package 'REDFIT-x' (Ólafsdóttir et al., 2016) which allows cross-spectrum analysis and provides red noise and chi^2 confidence intervals;

To avoid introducing spurious phasing of periodicities, in general I have attempted to keep time series on their original, uneven timescale. However, this is not always possible, depending on the availability of algorithms for unevenly spaced data or the required computational power. In these cases, the time series are interpolated to a linear timescale with a δt at least greater than the average original spacing, if not the maximum original spacing.

2.4.2 Phasing

In Chapter 4, the relationship between ice-rafted debris accumulation and benthic $\delta^{18}O$ and $\delta^{13}C$ is analysed using a combination of approaches. Firstly, for lagged cross-correlation analysis I use the 'Gaussian kernel' algorithm of Rehfeld et al. (2011) which allows cross-correlation estimation on unevenly spaced time series and has been shown to perform well with synthetic and real paleoclimate datasets (Rehfeld and Kurths, 2014).

Secondly, I use a 'Peak-Lag' algorithm modified from Barker et al. (2015) to include uncertainty estimation. This novel numerical approach is analogous to 'Event Synchronization' methods, and iteratively measures the offset between local maxima in the rate of change of two time series. this provides a uni-directional estimate of lead-lag relationships.

By testing the sensitivity of the algorithm to the smoothing filter selection, results presented in Chapter 4 were found to be robust (within 1σ of each other) for a range of filter designs (moving-average and Savitsky-Golay filters; orders between 1 and

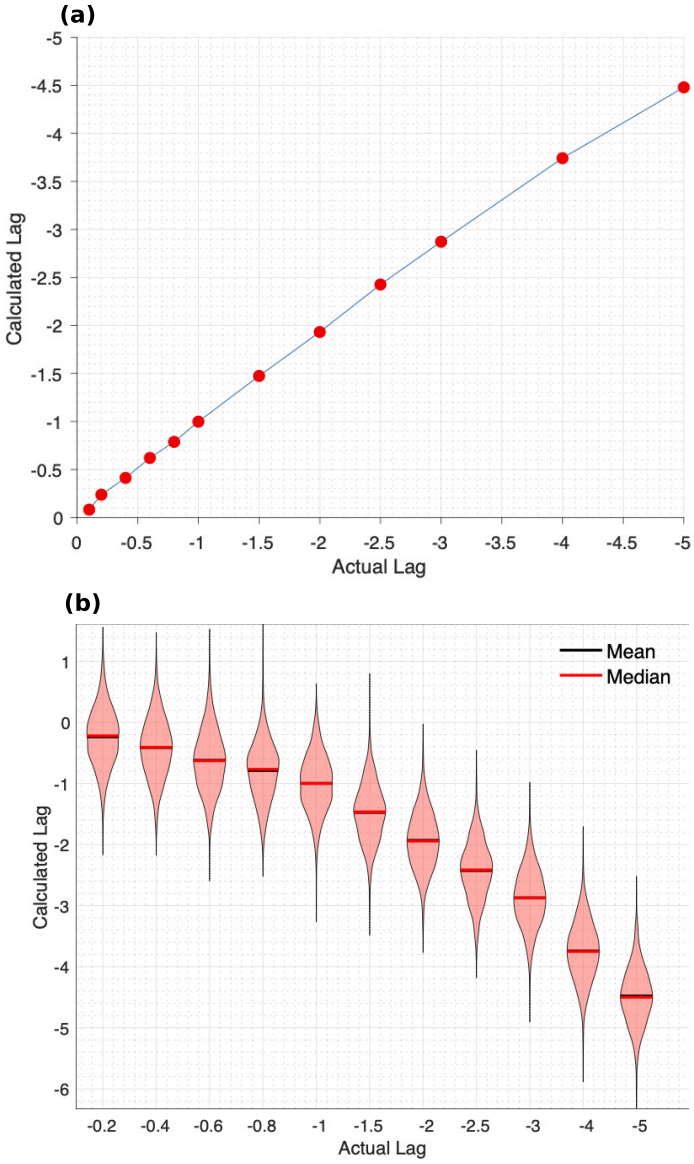

Figure 2.8: a. and b. Tests showing the peak-lag algorithm ability to detect relationships in a series of surrogate time-series with known lags applied. The 'actual lag' axes represent the known lag-time imposed between pairs of the surrogate series and the 'calculated lag' axes show the lag estimated by the algorithm. A perfect performance would manifest as a 1:1 straight line through the scatter points. The violin plots in **b.** show the mean, median and kernel probability density estimates of calculated lags from 10^4 iterations of the test.

21). Moreover, to test the confidence that the final result is significantly non-zero, I performed 1000 'Monte Carlo' simulations with zero-lag red noise surrogates (generated from an autoregressive model of the real data), finding that the lag identified in Chapter 4 is significantly different from the surrogate series ($p<10^{-10}$).

Finally, I test the utility of the algorithm to detect lead-lag relationships in a series of

surrogate time series with known lags applied by constructing synthetic time series from 3 sine waves (100, 41, 23-kyr periods), with higher-frequency oscillation (7-kyr period) and white-noise components added to emulate sub-orbital features and measurement/sedimentary noise. Known lags are imposed between pairs of the surrogate series. The results show that the algorithm performs well and is capable of detecting a lag of down to 0.4 kyr to a confidence of $p<10^{-10}$ (Figure 2.8a). The algorithm shows an inherent drift at higher lags (Figure 2.8b), meaning it underestimates lag times greater than 4 kyr.

2.5 Stable Isotope Compilation

Comparing $\delta^{13}C_{benthic}$ records from multiple sites can provide valuable insights into large-scale water mass distributions and circulation (e.g. Curry and Oppo, 2005; Barth et al., 2018; Lisiecki, 2010) and can aide in untangling the multiple factors which can influence $\delta^{13}C$ at a single location (e.g. Shackleton et al., 1992; Peterson and Lisiecki, 2018). Furthermore, calculating regional averages of compiled $\delta^{13}C_{benthic}$ is a useful way to improve the signal to noise ratio of single records and provide a regional view of changes in $\delta^{13}C$. Finally, the differences in $\delta^{13}C_{benthic}$ between regions and water depths can be related to the fractionation of carbon between ocean layers (e.g. Hodell and Venz-Curtis, 2006) or ocean basins (Raymo et al., 1990), with clear implications for the global carbon cycle.

To provide a stratigraphically-consistent framework of available benthic $\delta^{13}C$ records spanning the interval(s) of interest to this thesis, I compiled published records from 20 sediment core sites across the globe (Figure 2.9a; Table 2.1). Only records measured on *Cibicides* species were chosen (primarily *C. wuellerstorfi*). Each record not already presented on an LR04 age model was aligned to LR04, in the cases where the record was part of the LR04 stack, the age model from Lisiecki and Raymo (2005) was used (see appendix Figure A1 for alignment of records). Once on the LR04 age scale, each record was then transferred to a common, monotonically-increasing time axis by binning to 5 kyr bins[§].

[§]Appendix Code 3 gives the Python script to recreate the isotope compilation.

2.5.1 Regional Stacks

Figure 2.9b shows the compiled $\delta^{13}C_{benthic}$ records as well as the global average (note that this is not weighted by region so this average is biased towards the North Atlantic where the density of core sites is highest). Furthermore, averages are calculated for different regions (the shallow North Atlantic, deep South Atlantic, and deep Pacific). In Chapter 5, these regional stacks are used to provide estimates of end-member composition for North Atlantic Deep Water (NADW), Souther-Sourced Deep Waters, and Pacific Deep Water across the Pleistocene, which when compared to the AP_{comp} $\delta^{13}C_{benthic}$ record allow the calculation of % NADW through time.

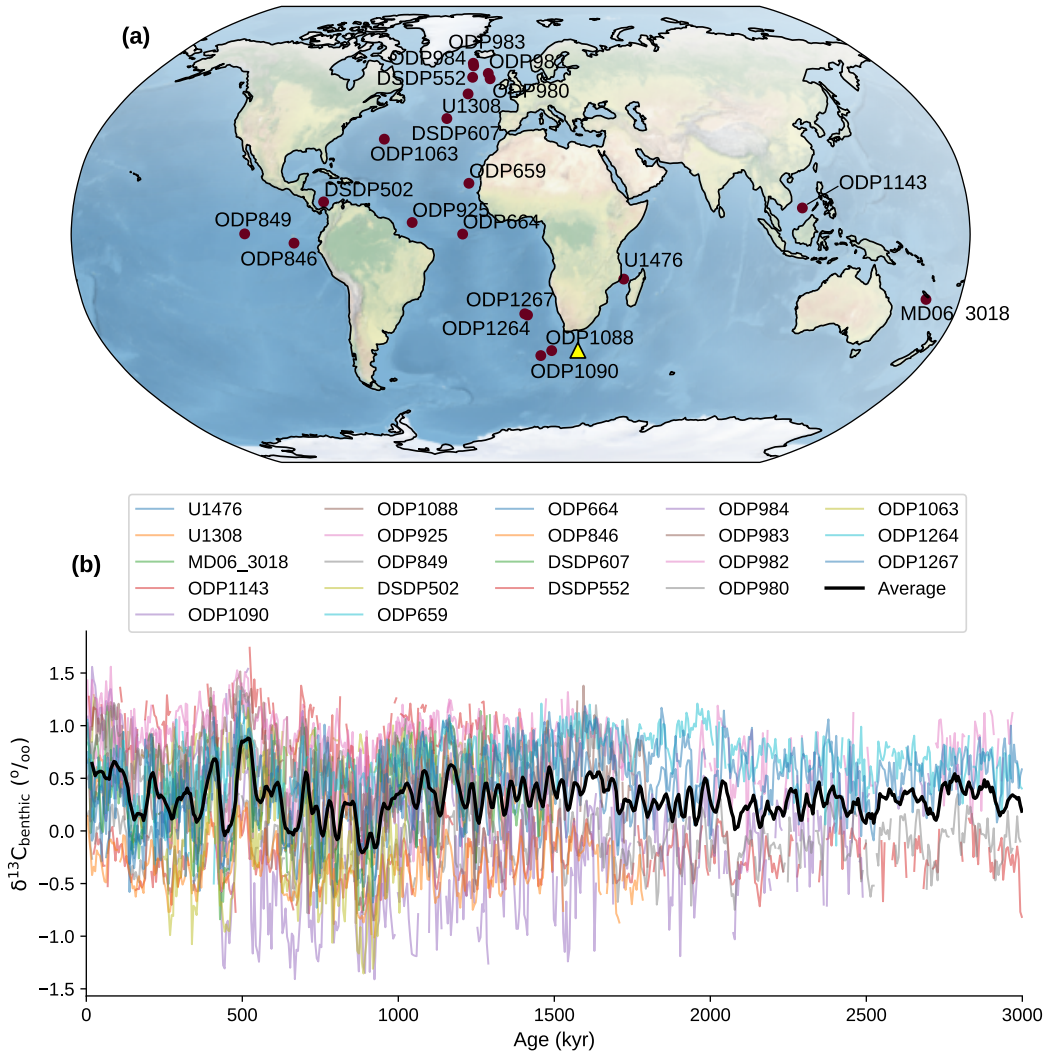

Figure 2.9: **(a)** Locations of cores used in the stable isotope compilation. **(b)** Time series of each record compiled (on the LR04 timescale), global average is given (thick black line).

The shallow North Atlantic stack is composed of sites from this region situated shallower than 2500m water depth (see table 2.1), the Deep South Atlantic stack uses sites deep than 3500m and poleward of 25^{o}S, and the Deep Pacific stack uses sites deeper than 3000 m in the open Pacific Ocean (i.e not including the South China Sea site ODP 1143).

Site	Lat. (^{o})	Lon. (^{o})	Depth (m)	Basin	Ref.
ODP1267	-28.10	1.71	4355	Atl	Bell2015
ODP1264	-28.53	2.85	2504	Atl	Bell2015
ODP1063	33.68	-57.62	4583	Atl	Poirier2014
ODP980	55.48	-14.70	2172	Atl	Oppo1998; Flower2000; McManus1999
ODP982	57.52	-15.87	1134	Atl	Venz1999; Venz2002
ODP983	60.40	-23.64	1983	Atl	Klieven2003; Raymo1998
ODP984	61.43	-24.08	1649	Atl	Raymo2004
DSDP552	56.04	-23.23	2301	Atl	Shackleton1984
DSDP607	41.00	-32.23	3427	Atl	Ruddiman1989; Raymo1989
ODP846	-3.09	-90.82	3296	Pac	Mix1995
ODP664	0.11	-23.23	3806	Atl	Raymo1997
ODP659	18.08	-21.03	3071	Atl	Sarnthein1989
DSDP502	11.49	-79.38	3051	Atl	deMenocal1992
ODP849	0.18	-110.52	3839	Pac	Mix1995
ODP925	4.20	-43.49	3041	Atl	Wilkens2017
ODP1088	-41.14	13.56	2082	Atl	Hodell2003
ODP1090	-42.91	8.90	3700	Atl	Hodell2003
ODP1143	9.35	113.28	2772	Pac	Wang2004
MD06_3018	-23.00	166.15	2470	Pac	Russon2009
U1308	49.88	-24.24	3883	Atl	Hodell2016
U1476	-15.81	41.77	2166	Ind	vanderLubbe2021; Barker2021

Table 2.1: Cores used in the stable isotope compilation; references are: Bell2015 = Bell et al. (2015); Poirier2014 = Poirier and Billups (2014); Oppo1998 = Oppo et al. (1998); Flower2000 = Flower et al. (2000); McManus1999 = McManus et al. (1999); Venz1999 = Venz et al. (1999); Venz2002 = Venz and Hodell (2002); Kleiven2003 = Kleiven et al. (2003); Raymo1998 = Raymo et al. (1998); Raymo2004 = Raymo et al. (2004); Shackleton1984 = Shackleton et al. (1984); Ruddiman1989 = Ruddiman et al. (1989); Raymo1989 = Raymo et al. (1989); Mix1995 = Mix et al. (1995); Raymo1997 = Raymo et al. (1997); Santhein1989 = Sarnthein and Tiedemann (1989); deMenocal1992 = deMenocal et al. (1992); Wilkens2017 = Wilkens et al. (2017, and references therein); Hodell2003 = Hodell et al. (2003); Wang2004 = Wang et al. (2004); Russon2009 = Russon et al. (2009); Hodell2016 = Hodell and Channell (2016); vanderLubbe2021 = van der Lubbe et al. (*in press*); Barker2021 = Barker et al. (*submitted*).

3 | Determining Age-Depth Models for the Agulhas Plateau Composite

3.1 Introduction

Records of the stable isotope composition of foraminifera from deep-sea sediment cores have been instrumental in shaping our understanding of past oceans and climate. Following the early work of Epstein and Lowenstam (1953) and Emiliani (1955) it has been shown that the temperature-dependent fractionation of oxygen isotopes into the shells of foraminifera can provide insights into past ocean temperatures. It is now known that the ratio of $^{18}O/^{16}O^{*}$ in fossil foraminifera reflects a combination of seawater temperature, local hydrography, and continental ice volume. Because the residence time of oxygen isotope in large ice sheets is longer than the mixing time of the ocean, and because deep ocean temperatures are thought to vary relatively little over thousand-year time-scales (e.g. Elderfield et al., 2012), $\delta^{18}O$ records from benthic foraminifera can act as a first order approximation for global ice volume (Shackleton, 1967). Furthermore, the global signal of the ocean $\delta^{18}O$ signal (on kyr timescales) means that these records provide a way of aligning the stratigraphies of sediment cores from different regions, and it has become commonplace in the field of paleoceanography to convert sediment core depth to age by aligning $\delta^{18}O$ to a regional or global $\delta^{18}O$ stack or composite (Imbrie et al., 1984; Prell et al., 1986; Bassinot et al., 1994; Lisiecki and Raymo, 2005; Ahn et al., 2017). To this end, a record of $\delta^{18}O_{benthic}$ is presented here for the Agulhas Plateau composite (APcomp), comprised of MD02-2588 and International Ocean Discovery Program Site U1475.

*referred to in delta notation as $\delta^{18}O$

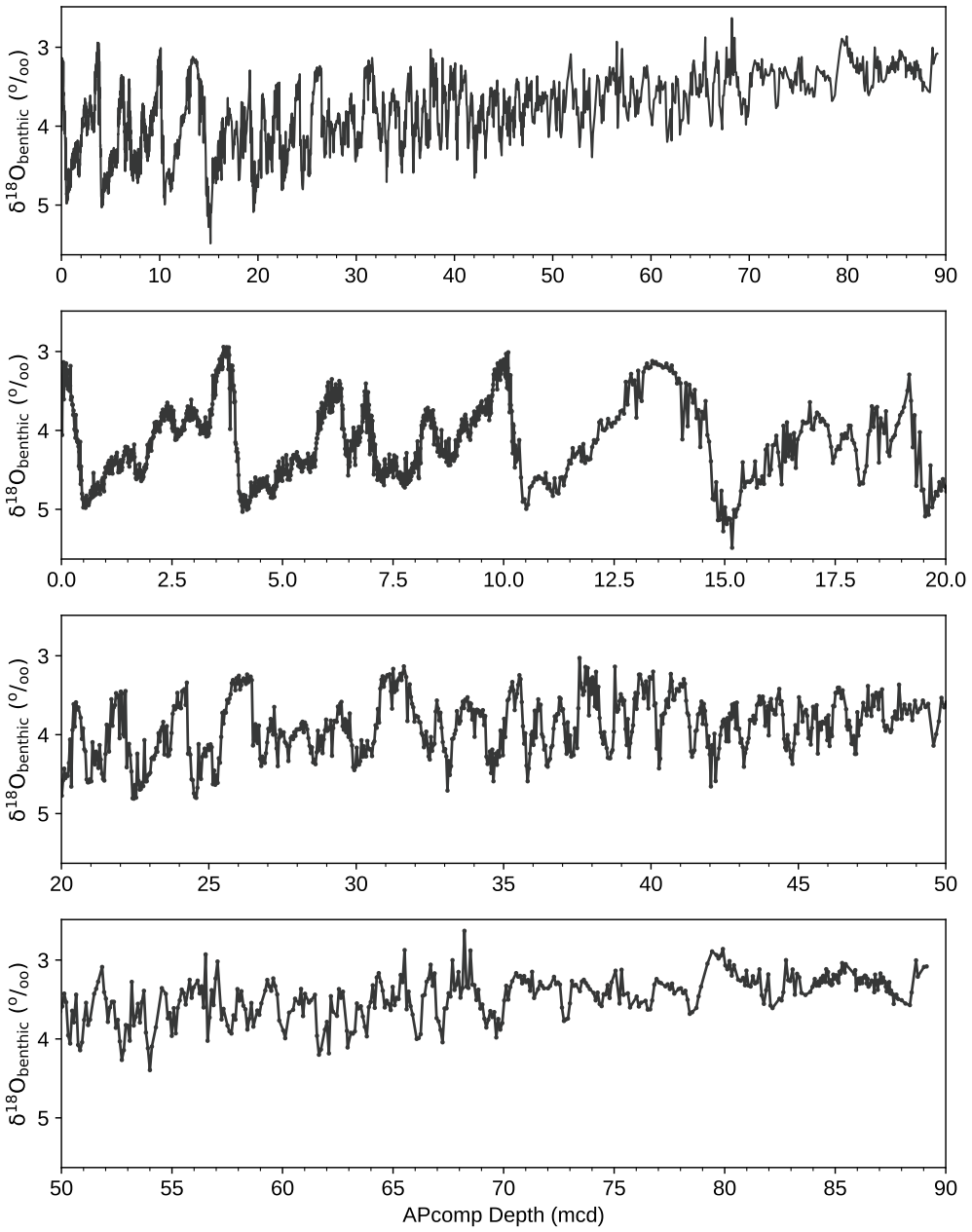

Figure 3.1: The AP_{comp} $\delta^{18}O_{benthic}$ record shown on depth. The upper ~11m are from MD02-2588, published previously by Ziegler et al. (2013)

3.2 Methods Summary

To avoid repetition I provide only a a brief summary of the stable isotope methodology here (a full description is available in Chapter 2). For stable isotope analysis, 2-3 specimens of *C. wuellerstorfi* were picked from the 250-315 μm fraction for stable

isotope analysis. Individuals with broken or poorly preserved shells were rejected. Where fewer specimens were present, the >350 μm fraction was consulted as there is no evidence for a size-dependency in *Cibicides* stable isotope composition (Corliss et al., 2002). Stable isotope measurements were performed at Cardiff University using a Thermo Finnigan MAT 253 mass spectrometer linked online to a Carbo Kiel carbonate preparation device with long term precision of ±0.05‰ for $\delta^{18}O$. Results are calibrated to an internal laboratory standard (BCT 63μm) and presented relative to the Vienna Pee Dee Belemnite scale (‰ VPDB).

3.3 Stable Oxygen Isotope Results

Figure 3.1 shows the AP_{comp} *C. wuellerstorfi* $\delta^{18}O$ record. The data span just under 90 m of core (n = 2832 samples, of which 1028 were previously presented for MD02-2588). $\delta^{18}O_{benthic}$ ranges from between 3 and 4 ‰ in the upper 40 m, and the variance (predominantly quasi-periodic cycles) increases towards the top of the core. Furthermore there is a clear trend towards heavier $\delta^{18}O_{benthic}$ values throughout the record.

3.3.1 MD02-2588 - Site U1475 Overlap

Figure 3.2 shows the overlap between MD02-2588 and Site U1475. This overlapping interval represents a single glacial-interglacial transition, showing little to no offset between adjacent measurements. Measurements on MD02-2588 were previously presented by Ziegler et al. (2013) and are higher resolution than Site U1475 (average δt for this interval is 0.3 kyr per sample for MD02-2588 and just under 1 kyr per sample for Site U1475 for this intervals based on the LR04 age scale; see below).

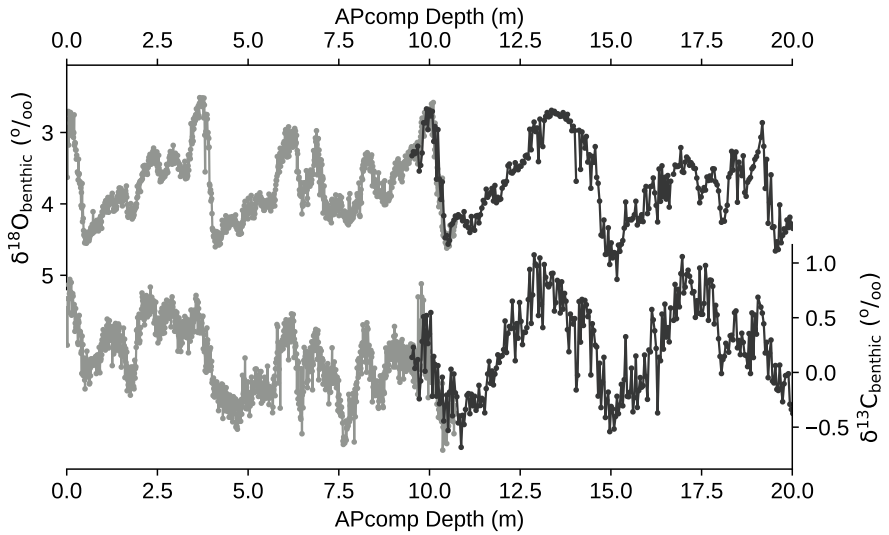

Figure 3.2: Overlap between MD02-2588 (light grey; Ziegler et al., 2013) and Site U1475 (dark grey) stable isotope records

3.4 Age-Depth Models

3.4.1 LR04 Age Model

An orbitally-tuned age-depth model was constructed for the AP_{comp} by correlating the *C. wuellerstorfi* $\delta^{18}O$ record to the updated global $\delta^{18}O_{benthic}$ stack (Prob-stack) of Ahn et al. (2017). The Prob-stack includes 180 globally distributed $\delta^{18}O_{benthic}$ records and provides an update of the LR04 stack. The Prob-stack and LR04 are similar over the intervals studied in this thesis and constitute the same timescale. I therefore refer to this age model as the 'LR04' timescale. From selected age-depth markers (n = 45; consisting 12 previously published radiocarbon dates and 33 $\delta^{18}O_{benthic}$ ties points), the final age-depth model was constructed using the deterministic age modelling routine Undatable (Lougheed and Obrochta, 2019) with 10^5 bootstrap simulations. I note that the 'Undatable' age model is very similar to a linearly interpolated alternative, however it provides an estimate of age uncertainty. On average, the 95% uncertainty for the AP_{comp} LR04 timescale is 6-kyr with a range of ± 5-kyr. The resultant sedimentation rates range from 1.2 cm/kyr to 7.6 cm/kyr, averaging 3.1 cm/kyr. The Brunhes/Matuyama magnetic reversal (0.781 Ma) and the Jaramillo Subchron (1.072 - 0.988 Ma) are identified in the U1475 down-core magnetic inclination, con-

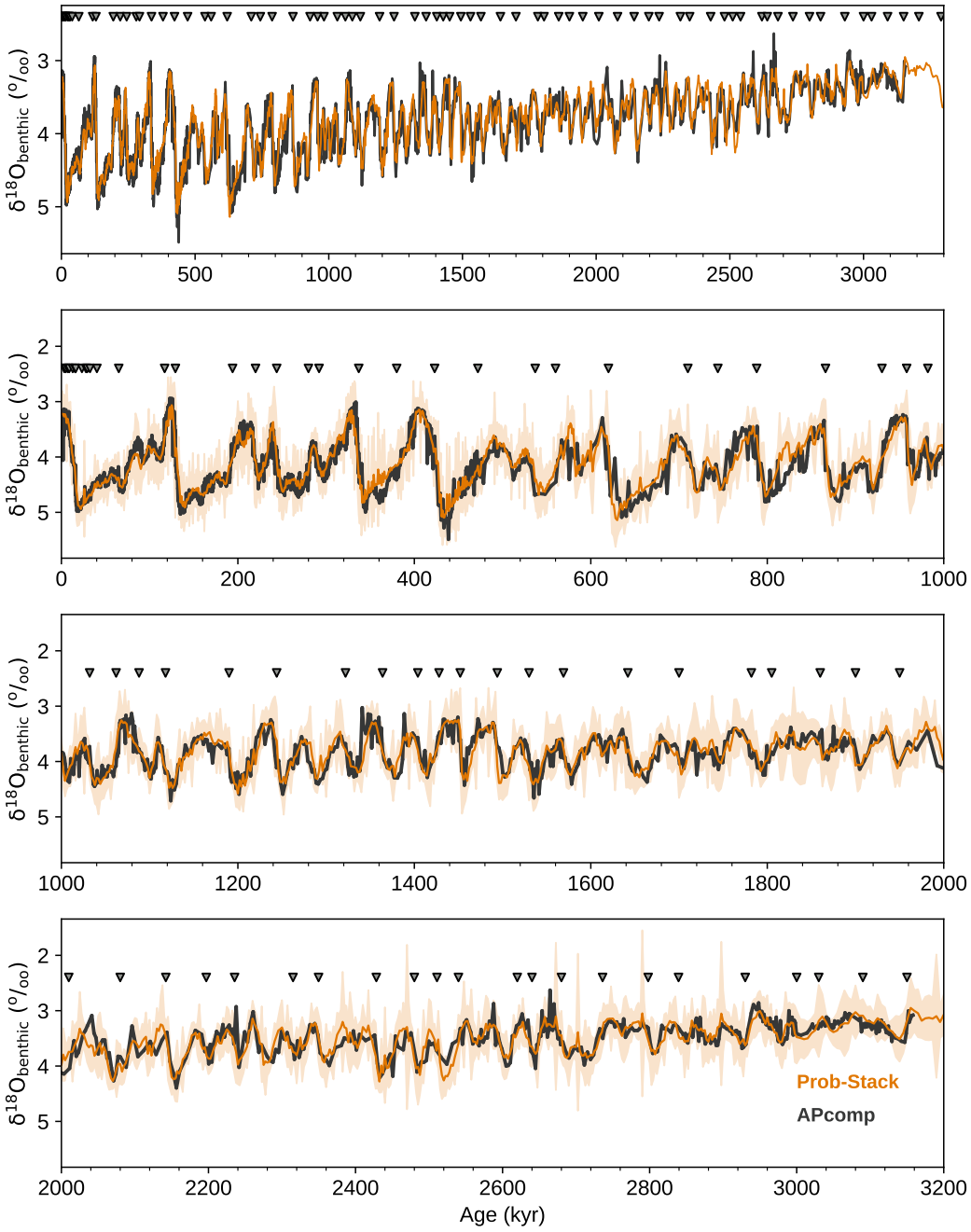

Figure 3.3: The 'LR04' timescale for the AP_{comp} (dark grey) tuned to the $\delta^{18}O_{benthic}$ stack of Ahn et al. (2017). Triangles show the position of tie-points identified. The orange shading shows the 95% uncertainty in the 'prob-stack' record (Ahn et al., 2017)

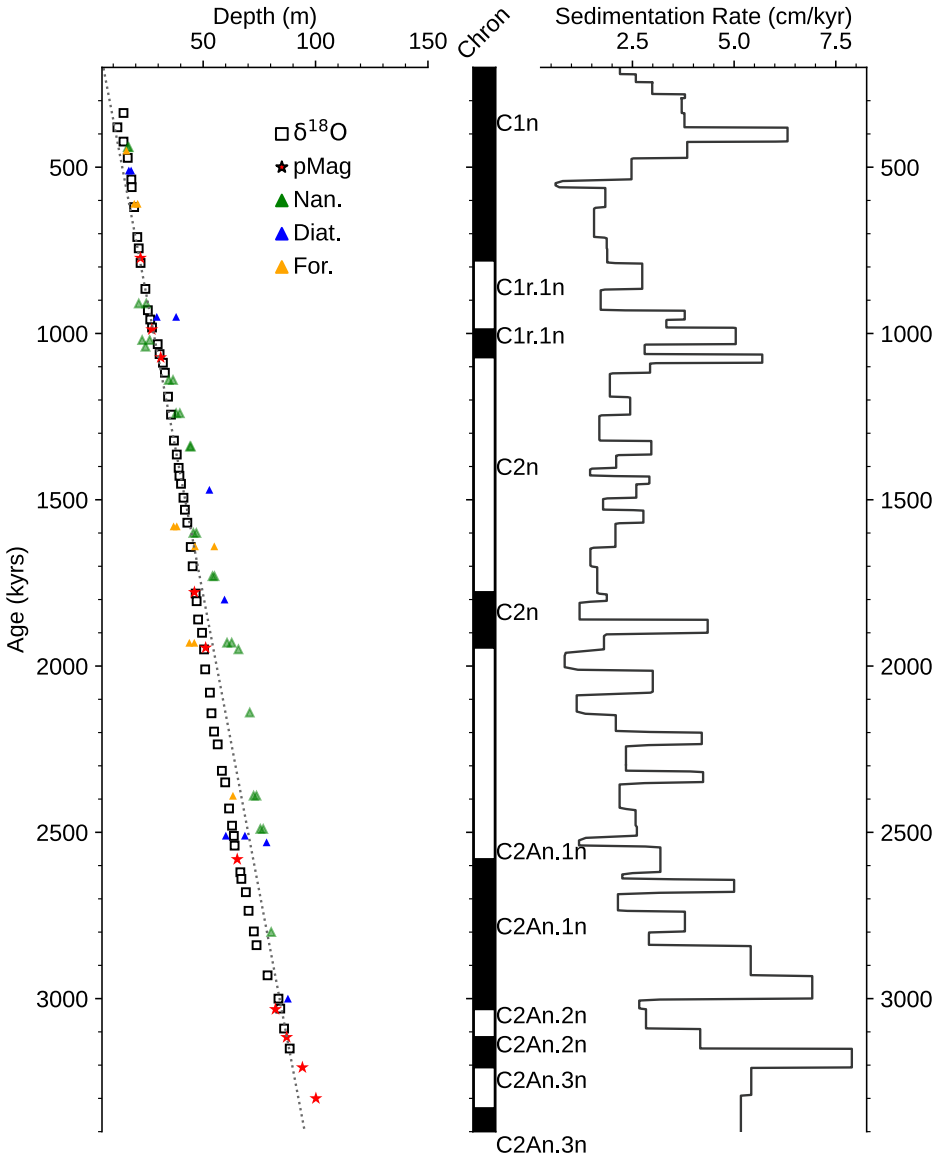

Figure 3.4: The age-depth relationship obtained by correlation to a global $\delta^{18}O_{benthic}$ stack: *left* shows a comparison to the age-depth model obtained by shipboard biostratigraphy and identification of paleomagentic reversals (Hall et al., 2017a). The dashed line shows the piecewise linear age model determined by Hall et al. (2017a) and the white squares show the $\delta^{18}O_{benthic}$ tie points identified in in this thesis. *Middle* shows the magnetic reversal chrons and subchrons identified on the Site U1475 splice (Hall et al., 2017a). *Right* shows the resulting linear sedimentation rate from the 'LR04' timescale described in the text.

firming the robustness of the final age-depth model.

The existing chronology for MD02-2588, established by Ziegler et al. (2013), consisted of 12 radiocarbon ages in the upper 40 kyr and then graphical correlation of $\delta^{18}O_{benthic}$ *C. wuellerstorfi* to the EPICA Dome C δD record. For the AP_{comp} 'LR04' age model, the Ziegler et al. (2013) age model is revised with a new tuning target of

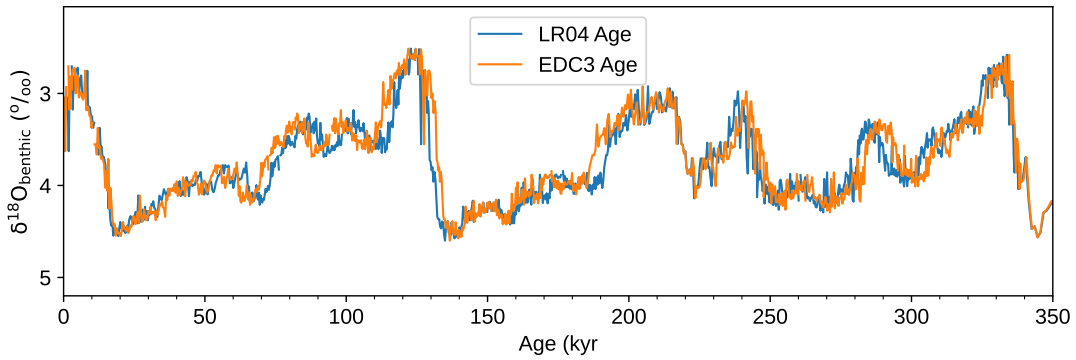

Figure 3.5: The MD02-2588 $\delta^{18}O_{benthic}$ record from Ziegler et al. (2013) presented on the original EDC3 age model (tuned to the δD record from the EPICA Dome C ice core (Jouzel et al., 2007)) as established by Ziegler et al. (2013). Also shown is the updated LR04 age model (see text).

the Prob-stack. The different tuning approaches result in only minor discrepancies between age models, reflecting the deviations between the LR04 and EPICA Dome C chronologies (Figure 3.5).

3.4.2 Correlation to the U1476 pMag Age Model

[This work relates to contributions to a publication Barker et al., in submission]
In addition to the LR04 age model described above, I also present an alternative age-depth model for the AP_{comp} by tuning the $\delta^{18}O_{benthic}$ record to the $\delta^{18}O_{benthic}$ record of IODP Site U1476, for which there is an 'absolute' age scale. The Site U1476 age model is presented by Barker et al. (in submission) and was produced by transferring $^{40}Ar/^{39}Ar$-dated paleomagnetic excursions and reversals from Ocean Drilling Program Site 983 (see Channell et al., 2020) to Site U1476 via their respective $\delta^{18}O_{benthic}$ records. Owing to the relatively constant sedimentation rates at Site U1476, due to its location away from major bottom currents, interpolation between these radiometrically-constrained age markers yields a robust age-depth model which is entirely independent of orbital assumptions. Furthermore, error propagation at each step means that the U1476 pMag age model is presented with associated age uncertainties.

The philosophy here is similar to that of the 'depth-derived' age scale of Huybers and Wunsch (2004), in that it presents a chronological framework useful for testing orbital forcing hypotheses without the circularity involved in doing so with orbitally-

tuned age models. The age model is utilised in this way in Chapter 5.

To align the AP_{comp} to the U1476 pMag age model, 44 tie-points are chosen by graphically aligning the two $\delta^{18}O_{benthic}$ records (Figure 3.6c). The U1476 $\delta^{18}O_{benthic}$ record spans 0 - 2000 ka, and so no tie points older than this are possible. Furthermore, paleomagnetic reversals which have been identified on the Site U1475 splice are included as additional constraints (Hall et al., 2017a). The resulting implied sedimentation rates range from 0.6 cm/kyr to 6.6 cm/kyr, averaging 3.1 cm/kyr. The pMag age model as well as the LR04 age model are provided in the appendix (Tables A2 and A3). The upper 1600 kyr of the pMag age model (the interval used in Chapter 5) is shown in Figure 3.6. This chronology is not used elsewhere in this thesis.

3.4.3 Late Pleistocene Site U1475 Age Model

[This work was produced in contribution to publication Tangunan et al. (2021)]
While in this thesis the upper 300 kyr of MD02-2588 are presented in place of the upper 300 kyr Site U1475 (i.e. the AP_{comp}), proxy records have been produced for this interval of Site U1475 (Tangunan et al., 2021). In order to refine the shipboard biostratigraphic age model for this upper section of Site U1475, it was stratigraphically aligned to the corresponding section of MD02-2588 by graphically aligning records of sediment reflectance (a*, L*), and XRF Ca/Fe ratio from both sites. The resulting age model (n = 18 tie points) was then confirmed by comparing the Site U1475 sediment colour (blue) to the MD02-2588 $\delta^{18}O_{benthic}$ record (Figure 3.7). MD02-2588 age model from Ziegler et al. (2013) was then applied to the equivalent interval of Site U1475.

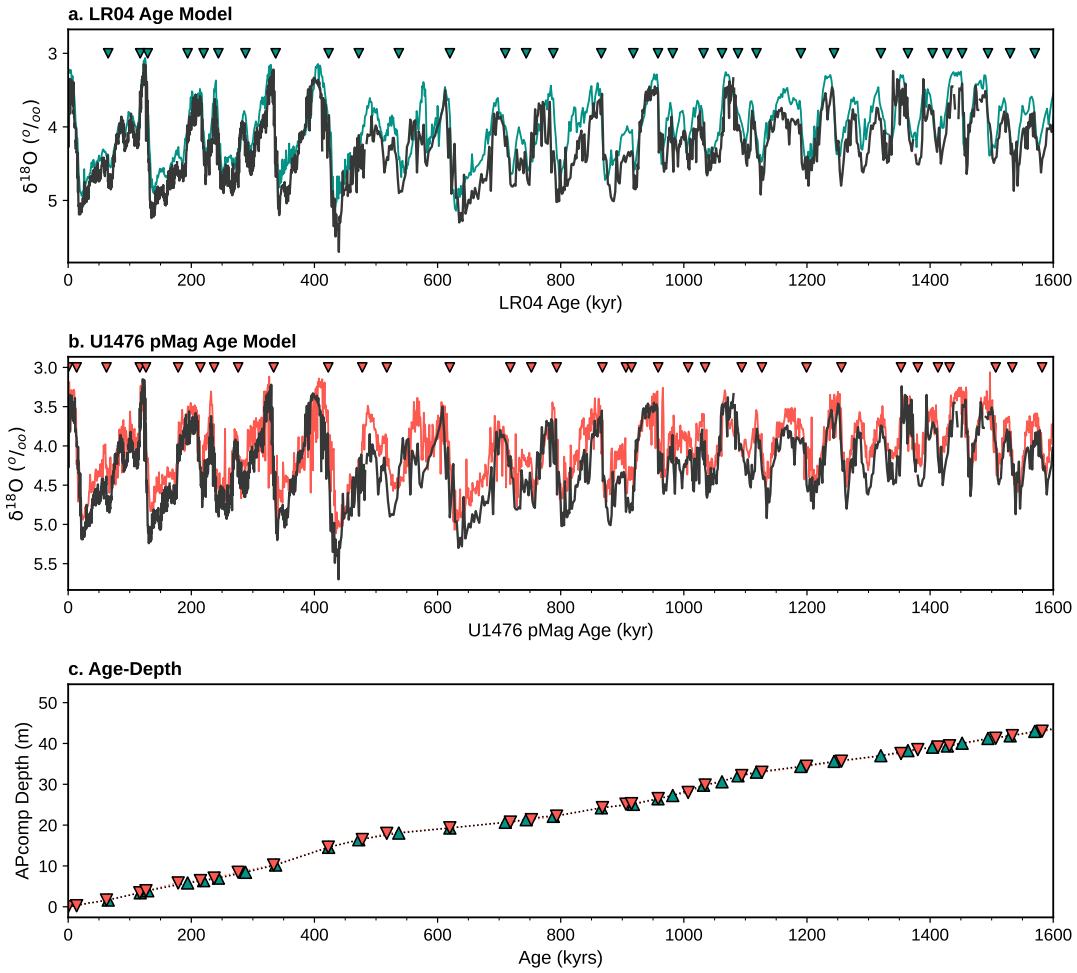

Figure 3.6: Comparison between the 'LR04' and 'pMag' age models described in the text for the AP_{comp}. **(a)** AP_{comp} $\delta^{18}O_{benthic}$ (grey) and the $\delta^{18}O_{benthic}$ 'prob-stack' (teal; Ahn et al., 2017). **(b)** AP_{comp} $\delta^{18}O_{benthic}$ (grey) and IODP Site U1476 on the U1476 'pMag' timescale (Barker et al., in submission). **(c)** Age-depth relationship for both age models (LR04 in teal and pMag in orange).

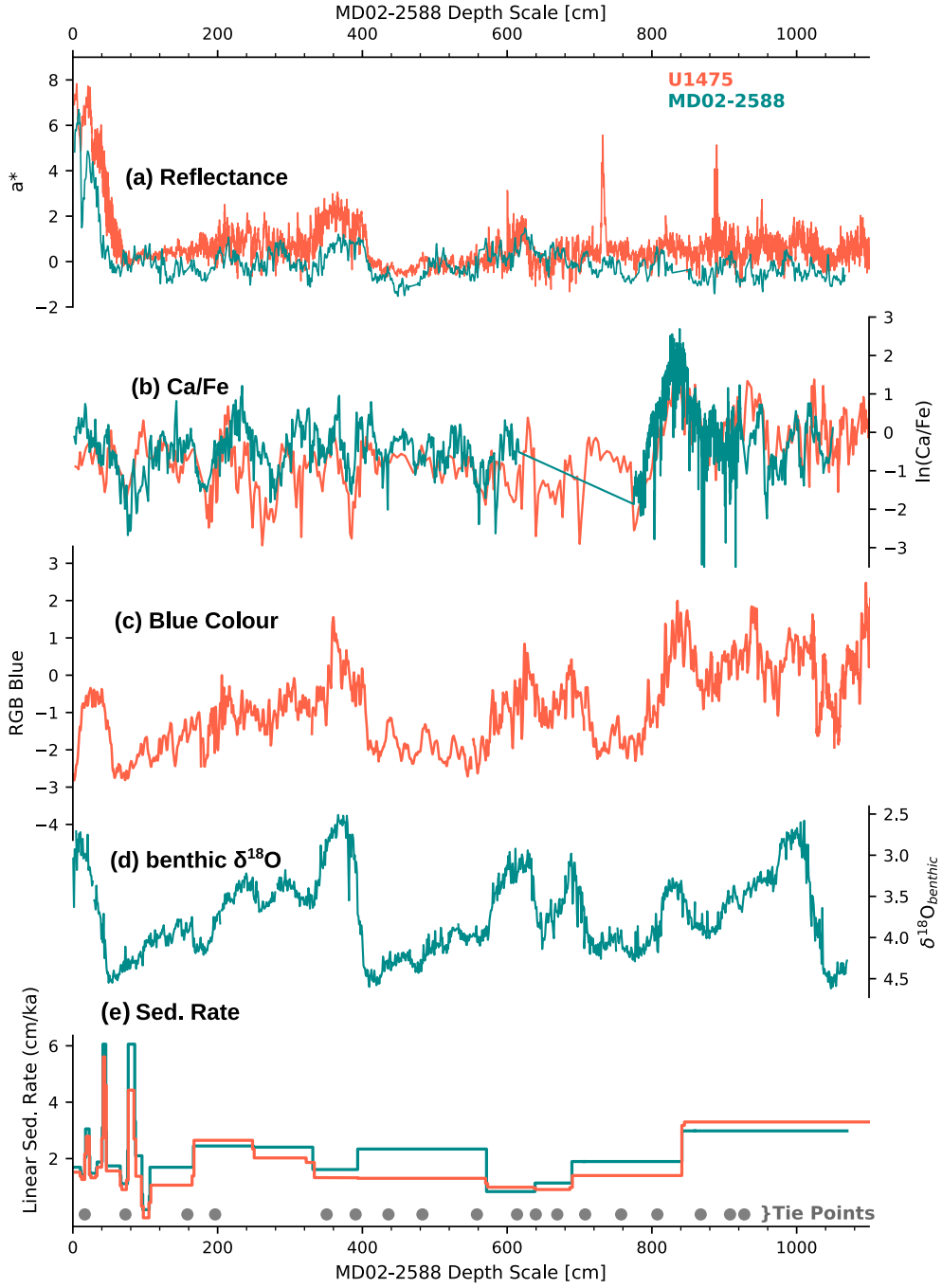

Figure 3.7: Age-depth model for Site U1475 (orange) tied to sediment core MD02-2588 (green). Site U1475 records are plotted against the published records of MD02-2588 (Ziegler et al., 2013, I.R. Hall, unpublished MD02-2588 XRF data). **(a)** Sediment reflectance, **(b)** XRF Ca/Fe ratio, **(c)** Site U1475 sediment color (blue band), **(d)** $\delta^{18}O_{benthic}$ from MD02-2588 (Ziegler et al., 2013), **(e)** Linear sedimentation rate for both core sites. *Figure from Tangunan et al. (2021)*

4 | Antarctic icebergs lead ocean circulation into Pleistocene glacials; Evidence from 1.65 Million Years of Agulhas Plateau Ice-rafted Debris

4.1 Introduction

In the modern ocean, the dominant feature of large-scale mass and heat transport is the Atlantic Meridional Overturning Circulation (AMOC), characterised by the deep, southward spread of North Atlantic Deep Water (NADW) towards the Southern Ocean (SO), balanced by the northward return of surface, mode, intermediate, and bottom waters (Bower et al., 2019; Talley, 2013). The geometry and vigour of this circulation influences global climate on various timescales. For example, paleoceanographic evidence suggests that during glacial periods of the past 1.5 million years the AMOC was markedly different from modern (Lisiecki, 2014): in the Atlantic basin, deep waters of Southern Ocean origin increased in volume whilst above them the core of the NADW shoaled (Hesse et al., 2011). Whilst this reorganization has previously been explained through changes in North Atlantic processes (e.g. Crowley and Häkkinen, 1988; Mix and Fairbanks, 1985), this paradigm has been challenged by studies invoking 'upstream' disruptions (e.g. variable Agulhas Leakage; Caley et al., 2012; Knorr and Lohmann, 2003), modifying the shallow return of waters to the North Atlantic required to complete this 'Upper Cell' of the overturning circulation. Furthermore, the southward and northward components of the Upper Cell are connected via wind- and buoyancy-related processes in the SO, with much of

the outcropping NADW first taking an indirect route, via the so-called 'Lower Cell' of overturning circulation, before joining the AMOC return limb via the upper cell (Talley, 2013).

Southern Ocean conditions have been increasingly invoked by modelling studies (Watson et al., 2015; Knorr and Lohmann, 2003; Ferrari et al., 2014) seeking to explain glacial NADW dynamics, however paleoceanographic evidence supporting such a causal link remains scarce (Govin et al., 2009), particularly over multiple glacial-interglacial cycles. One reason for this is the relative difficulty in obtaining continuous, well-dated sediment sequences from the mid to high latitude SO, where dating the carbonate-poor sediment can be difficult* (e.g. Zheng et al., 2002). This means that relatively less is known about Southern Ocean ice-sheet-ocean interactions compared to in the Northern Hemisphere (see review by Hemming, 2004). That being said, there is a long history of paleoceanographic studies in the Southern Ocean (e.g. Donahue, 1965; Keany et al., 1976), accelerated greatly by the advent of coordinated ocean drilling programmes. Notably, a north-south transect of sediment cores recovered during Ocean Drilling Program Leg 177 (Hodell, 1999) has yielded reconstructions of surface (Becquey and Gersonde, 2002; Kunz-Pirrung et al., 2002; Martínez-Garcia et al., 2011) and deep (Hodell and Venz-Curtis, 2006; Venz and Hodell, 2002; Diekmann and Kuhn, 2002) hydrography across much of the Plio-Pleistocene, some of which have been linked directly to Antarctic ice-sheet dynamics (Kanfoush, 2000; Teitler et al., 2010). Furthermore, the recent suite of International Ocean Discovery Program (IODP) expeditions targeting high quality sediment sequences in the Southern Ocean has provided, and will likely continue to provide, opportunities to constrain ocean-cryosphere links in the region. These include the southerly sites recovered by Expedition 361 (Hall et al., 2017a) as well as Expedition 382 (Weber et al., 2021) and 383 (Lamy et al., 2021).

In this chapter, a tight surface-deep coupling between the presence of far-travelled Antarctic icebergs and deep-water mass structure is revealed by combining new and previously published (Marino et al., 2013; Simon et al., 2013) records of ice-rafted debris mass accumulation rate (IRD_{MAR}), and carbon and oxygen isotope records from

*Though not impossible (Weber et al., 2012; Hillenbrand et al., 2009; Pugh et al., 2009)

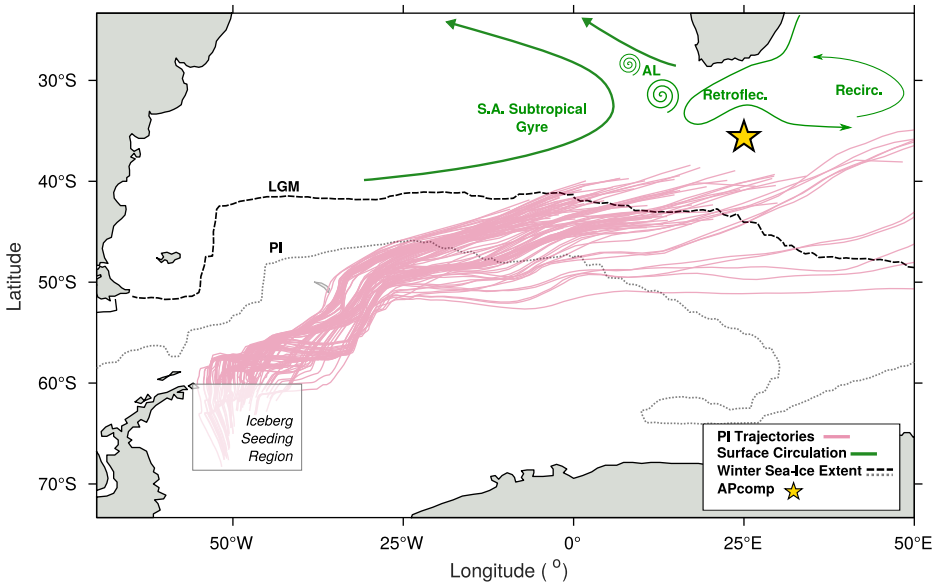

Figure 4.1: Iceberg trajectories simulated by Pyberg under Pre-Industrial (PI) conditions (see text). Winter sea ice extent from Gersonde et al. (2005) (15% concentration contour for September) for PI and last glacial maximum. Surface ocean circulation is modified from Bower et al. (2019); AR = Agulhas Retroflection, AL = Agulhas Leakage, ARC = Agulhas Return Current. The shaded grey band represents the Subtropical Frontal Zone (STFZ; Graham and Boer, 2013)

benthic foraminifera ($\delta^{13}C_{benthic}$, $\delta^{18}O_{benthic}$) from sediment cores recovered from the Agulhas Plateau, presented on the 'Agulhas Plateau Composite' (hereafter the AP_{comp}; see Chapter 2). Analysis of this multi-proxy evidence shows that northward shifts in Antarctic iceberg melt in the Indian-Atlantic Southern Ocean systematically preceded deep-water mass reorganisations by 1-2 thousand-years (kyr) during Pleistocene glaciations. With the aid of iceberg trajectory model experiments, a proposed mechanism for this link is put forward.

4.1.1 Southern Ocean Ice-Rafted Debris

The Agulhas Plateau is situated at the southern boundary of the Indian-Atlantic Ocean Gateway (Figure 1a); the upper water column is dominated by eastward flowing Indian Ocean surface waters retroflected as the Agulhas Return Current (i.e. not 'leaked' into the South Atlantic; Lutjeharms and Ansorge, 2001). To the south, the relatively cold and fresh waters of the SAZ meet their northern limit, forming steep hydrographic gradients at the subtropical frontal zone (STFZ; Figure 1). Iceberg pres-

ence (and subsequently IRD deposition) at this location can therefore be influenced by regional hydrography as well as the export, survivability, and transport of icebergs into and across the SO. One way in which to untangle these influences is to compare IRD records from multiple locations or to compare IRD deposition with other paleoceanographic proxies for sea surface temperature, sea ice extent or surface circulation.

The coverage of available Southern Ocean IRD records may be less than in the North Atlantic, but several existing records do provide some insight into past Antarctic iceberg dynamics. For example, Kanfoush (2000) identified multiple discrete IRD peaks across three cores along a latitudinal transect of the Atlantic SO, attributing these events to millennial-scale calving of the Antarctic ice-sheet. However, the origin of ice-rafted minerals in the Atlantic Subantarctic Zone (SAZ) has been the topic of some discussion, due to the multiple potential sources of coarse-grained sediment in the region. Coarse-grained volcanic material in Pleistocene sediments from the Atlantic SAZ has been interpreted as originating from the South Sandwich Isles (Kanfoush, 2000; Nielsen et al., 2007b) and to a lesser extent Bouvet Island and the Antarctic Peninsula (Smith et al., 1983). Conversely, the presence of quartz in these sediments is typically attributed to long-distance transport by Antarctic icebergs (Kanfoush et al., 2002; Keany et al., 1976). However, Nielsen et al. (2007b) show that clear mineral grain assemblages originally identified at quartz IRD (Kanfoush, 2000; Kanfoush et al., 2002) were in fact composed predominantly of plagioclase and olivine originating from the South Sandwich Islands, likely transported by sea-ice rather than icebergs.

Clearly the interpretation of Southern Ocean IRD records is not always straightforward, and comparisons made between different studies can be hindered by different methodologies and the variable definition of 'IRD'. For example, close to Antarctica a definition such as the '>150μm fraction' is problematic due to the potential for grains of this size to originate from other processes, whilst coarser grain-size definitions will likely miss the majority of IRD at more distal locations. Furthermore, local sedimentation rates and winnowing can introduce features in records of IRD concentration not directly related to ice-rafted sediment deposition (Diekmann et al.,

2003b; Cofaigh et al., 2001). Figure 4.2 shows a compilation of some available IRD records from the Indian and Atlantic Southern Ocean sectors spanning the last glacial cycle. Only records with an available $\delta^{18}O$ record were selected to allow age-depth alignment to a common target (the 'Prob-Stack' of Ahn et al., 2017), however considerable age model uncertainties on the order of 10-kyr are still present (estimated by the deterministic age-modelling software 'Undatable'; Lougheed and Obrochta, 2019). With these uncertainties in mind, it is clear that heterogeneities in the timing and extent of IRD deposition exist in the glacial SO, which, in addition to methodological discrepancies, likely result from changes in surface hydrography (i.e. iceberg survivability) rather than iceberg calving (Keany et al., 1976; Labeyrie et al., 1986;

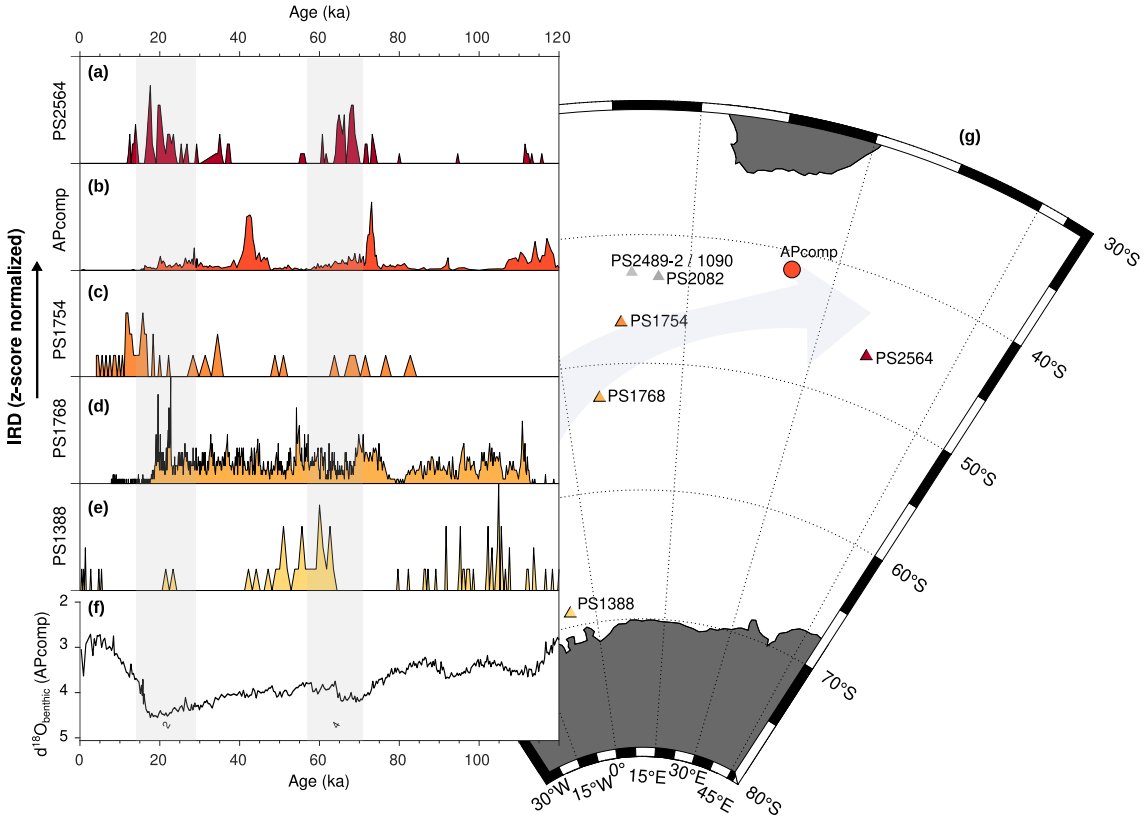

Figure 4.2: Selected records of Southern Ocean IRD across the last glacial cycle with age models modified to the 'LR04' age scale (see text). **(a)** PS2564 IRD data from Diekmann et al. (2003a); aligned to LR04 using $\delta^{18}O_{benthic}$ (*unpublished data-set shared by A. Mackensen 2019*). **(b)** AP_{comp} IRD record (Simon et al., 2013). **(c)** PS1754 IRD data from Diekmann et al. (2003a), aligned to LR04 using $\delta^{18}O_{planktic}$ (Niebler, 1995) and radiocarbon dates (Frank, 1996). **(d)** PS1768 IRD data from Diekmann et al. (2003a), aligned to LR04 using $\delta^{18}O_{planktic}$ (Niebler, 1995) and radiocarbon dates (Frank, 1996). **(e)** PS1388 IRD data from Diekmann et al. (2003a), aligned to LR04 using $\delta^{18}O_{benthic}$ from Mackensen et al. (1989) **(f)** AP_{comp} $\delta^{18}O_{benthic}$ (Ziegler et al., 2013). **(g)** Map showing core locations

Howard and Prell, 1992). In this chapter, I investigate the potential implications of a diachronous pattern of iceberg melt in the SO, through a new continuous IRD record and the results of iceberg trajectory model experiments.

4.2 Methods Summary

The Agulhas Plateau composite (AP_{comp}) is a stratigraphic framework consisting of proximal sediment core sites MD02-2588 (41^{o}19.90'S, 25^{o}49.7'E, 2907m) and IODP Site U1475 (41^{o}25.6'S, 25^{o}15.6'E, 2669m). Here, existing records of $\delta^{18}O_{benthic}$ and $\delta^{13}C_{benthic}$ (Ziegler et al., 2013) and IRD counts (Marino et al., 2013; Simon et al., 2013) from the upper 10.27m of MD02-2588 are combined with new IRD and stable isotope data from Site U1475. Data here are presented on the 'LR04' timescale. Full details of splice construction and chronology development can be seen in Chapter 3. Sedimentation rates range from 1.2 cm/kyr to 7.6 cm/kyr, averaging 3.1 cm/kyr and the records presented have a temporal resolution ranging from ~0.3 kyrs in the Late Pleistocene to ~1.5 kyrs in the early-mid Pleistocene. Stable isotope measurements were made on the benthic foraminifera *Cibicidoides wuellerstorfi*. Results are calibrated to an internal laboratory standard (BCT63) and presented relative to the Vienna Pee Dee Belemnite scale (see Chapter 2 for full methods).

4.2.1 Ice-Rafted Debris methodology

Ice-rafted debris concentration was determined by counting detrital mineral grains in the >150μm sediment fraction (subsampled using a micropaleontology splitter to yield 500 to 1000 entities) before normalization to sample weight (IRD concentration in #g) and then multiplication by apparent bulk mass accumulation rate, derived from estimates of dry bulk density (DBD) from Gruetzner et al. (2019) and linear sedimentation rate. The temporal evolution, spectral characteristics, and timing of peaks in the IRD record are largely unaffected by conversion from concentration to Mass Accumulation Rate (MAR) (Figure 5.6). This methodology is equivalent to that employed for MD02-2588, the measurements for which were previously published

by (Simon et al., 2013; Marino et al., 2013, ; n = 522), however DBD was estimated by fitting a 2^{nd} order polynomial to the overlapping interval of Site U1475 ($r^2 = 0.57$) as no DBD data is available for MD02-2588. The resulting IRD mass accumulation rate is referred to as IRD_{MAR}

No quantitative distinction was made between mineralogies of phenocrysts present, however grains that were clearly of volcanic (e.g. tephra) or authigenic (e.g. pyrite) origin were excluded from the IRD counts. Energy Dispersive X-Ray Spectrometry (EDS) point analysis (see Chapter 2 for full methodology) was used to identify the mineralogies of several grains from a selection of samples (total grains = 31). Of the 31 measured, 23 were quartz (mostly 'clean' quartz with some Fe-K and Fe members), 7 were orthoclase (K-feldspar), and 1 was garnet (Almandine member). Identification of minerals from EDS spectra followed Reed (2005) and raw data is provided in the appendix (Appendix Table 1).

4.2.2 Iceberg Trajectory Modelling

[Performed by Thomas Rackow, Alfred Wegener Intitute[†]]

As described in Starr et al. (2021), iceberg trajectory experiments were performed with the numerical model Pyberg (https://github.com/trackow/pyberg), an offline Python implementation of the FESOM-IB iceberg drift and decay module (Rackow et al., 2017). The model simulates iceberg trajectories and alongtrack rates of melting using established iceberg physics (Bigg et al., 1997; Gladstone et al., 2001; Lichey and Hellmer, 2001). In this study, PyBerg was forced by the outputs from a comprehensive fully coupled atmosphere–ocean general circulation model, COSMOS (ECHAM5-JSBACH-MPI-OM). COSMOS is composed of the atmospheric model ECHAM5, a land surface component JSBACH, and the ocean model MPI-OM (including sea-ice dynamics that is formulated using viscous-plastic rheology) with a resolution of $3^o \times 1.8^o$

[†]experiments were designed by AS, Ian R. Hall and Stephen Barker (Cardiff University, UK), Gregor Knorr and Thomas Rackow (Alfred Wegener Institute for Polar and Marine Research, Germany), and Xu Zhang (Institute of Tibetan Plateau Research, Chinese Academy of Sciences, China); PyBerg development and model experiments were performed by Thomas Rackow (Alfred Wegener Institute for Polar and Marine Research); COSMOS climate model outputs were provided by Xu Zhang (Institute of Tibetan Plateau Research, Chinese Academy of Sciences, China); all results have been previously published in Starr et al. (2021))

in the horizontal and 40 uneven vertical layers. The climate model experiments are described in detail in Zhang et al. (2013) and a summary is given in Table 4.1.

For each experiment, icebergs were initialized between 63^oW and 50^oW in the iceberg alley of the Weddell Sea following observations of near-coastal iceberg positions and horizontal sizes (Wesche and Dierking, 2015). The total initial iceberg mass in the iceberg alley is 49.59 Gt. Along-track melt-rates were gridded and summed on a 1^ox1^o regular grid to produce the meltwater distribution. The modelled pre-industrial trajectories are consistent with modern observational datasets (Tournadre et al., 2016; Schodlok et al., 2006) and the last glacial maximum results are mostly consistent with previously published model results (Bigg, 2020).

4.2.3 Statistical Analysis

Several approaches are used to analyse the phasing and statistical properties of the IRD and stable isotope records. Firstly, lagged cross-correlation between IRD_{MAR} against $\delta^{18}O_{benthic}$ and $\delta^{13}C_{benthic}$ is determined with a kernel-based cross-correlation algorithm (from Rehfeld et al., 2011), performed on the original, irregularly-spaced data, in order to avoid the possibility of spurious phasing introduced by linear interpolation.

Secondly, a 'peak-lag' algorithm was designed to iteratively measure the offset between peaks in the rate of change of IRD_{MAR} and $\delta^{13}C_{benthic}$. This algorithm was modified from the approach of Barker et al. (2015) and analogous to 'Event Synchronisation' techniques. It works by smoothing the time series, finding the first difference, and then measuring the offset in local maxima of both signals. The sensitivity of this approach to the smoothing parameters chosen was tested by 'Monte Carlo'

Experiment	Boundary Conditions	Angular Preccesion	Obliquity	Eccentricity
PI	PI (CO_2 280ppm)	102.04^o	23.45	0.0168
LGM	LGM (CO_2 185ppm)	114.42^o	22.95	0.0190
LGM27ka	LGM (CO_2 185ppm)	196.532^o	22.25	0.0175

Table 4.1: Experimental design for the three climate model simulations used to force the iceberg trajectory model in this study (COSMOS model simulations from Zhang et al., 2013)

simulations of synthetic time series (described in Chapter 2), yielding similar results for different smoothing approaches (i.e. moving average versus Savitsky-Golay). Furthermore, this provides 99% red noise 'Monte Carlo' confidence limits.

Thirdly, to produce the phase wheels in Figure 4.5, the Blackman-Tukey method is employed with a Bartlett window (using the Analyseries software (Paillard et al., 1996), bandwidth < 0.0035) after linearly interpolating (δt=1.5 kyr) and standardizing (mean = 0, standard deviation = 1) the data.

In addition, time series are divided into glacial cycles (as in figure 4.11) by identifying the intervals between peak interglacial conditions (identified as local minima in $\delta^{18}O_{benthic}$ separated by a minimum distance of 25 kyr) and the next time $\delta^{18}O_{benthic}$ crosses an 'interglacial threshold' of 3.32‰ (C. wuellerstorfi scale, equivalent to 3.75‰ when scaled to the *Uvigerina* scale used in the LR04 stack (Lisiecki and Raymo, 2005)), which is lower than adopted by (Past Interglacials Working Group of PAGES, 2016), but prevents defining the interstadial MIS 5c as an interglacial (Tzedakis et al., 2009). Within each interval, the cumulative integral of IRD_{MAR} and $\delta^{18}O_{benthic}$ is found before normalizing the values to percentages of total 'accumulation' for that interval.

Finally, the time-evolutive spectral power in the AP_{comp} IRD_{MAR} time series is estimated by applying a continuous wavelet transform (using zero-padding and a Mortlet mother wave with the algorithm of Grinsted et al., 2004). To visualize the results, the power in the frequency bands between 1/39 kyr to 1/43 kyr are extracted to represent frequencies associated with obliquity, and 1/92 kyr to 1/108 kyr to represent frequencies associated with eccentricity. This gives an estimate of relative not absolute spectral power in these bands.

4.3 Results

The glacial AP_{comp} is characterised by generally higher IRD_{MAR} and lower $\delta^{13}C_{benthic}$ (Figure 5.6) compared to interglacials, reflecting the increased presence of Antarctic icebergs and the reduced deep ventilation, respectively (see below). A long-term

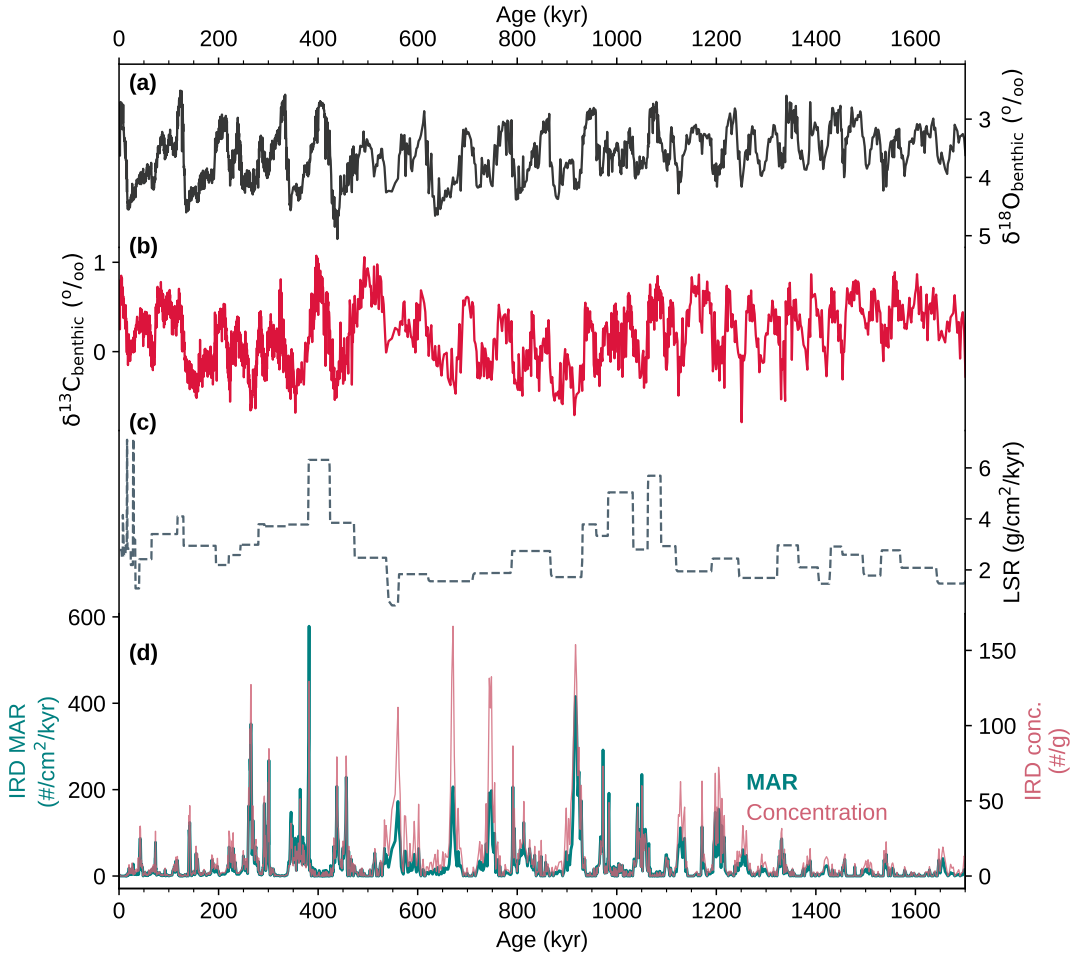

Figure 4.3: AP_{comp} IRD record. **(a)** $\delta^{18}O_{benthic}$ for the AP_{comp} (see text). **(b)** $\delta^{13}C_{benthic}$ (see text). **(c)** Linear sedimentation rate (LSR) from interpolation between age-depth tie points. **(d)** IRD concentration (right axis; pink) and mass accumulation rate (MAR; left axis; teal).

trend in glacial IRD maxima is also clear, with step-wise increases in glacial abundance at MIS 36 (~1.2 Ma) and MIS 24 (~900 kyr ago) and a decrease after MIS 6 (~190 kyr ago).

4.3.1 Surface-Deep Phasing

A significant negative correlation is present between IRD_{MAR} and $\delta^{13}C_{benthic}$ (r^2 = -0.39), becoming stronger when IRD_{MAR} is log-transformed (r^2 = -0.54). The reason for log-transforming the IRD_{MAR} data is twofold: firstly, it has a strongly skewed distribution with a small number of very high values. Secondly, log-IRD_{MAR} may be a more sensitive indicator of paleo-iceberg drift, for example the probability of ice-

berg presence in the Southern Ocean decreases by orders of magnitude with distance north of the main iceberg belt in the Weddell Sea sector (Merino et al., 2016). To explore the phasing of the close relationship between the co-registered surface and deep AP_{comp} conditions, three independent statistical approaches are employed. The strongest correlation between the two records (r^2 = -0.59) occurs when IRD_{MAR} leads $\delta^{13}C_{benthic}$ by 2±1 kyr, and spectral coherency analysis reveals a lead for IRD_{MAR} in all three major Milankovitch frequency bands. Additionally, the 'peak-lag' algorithm

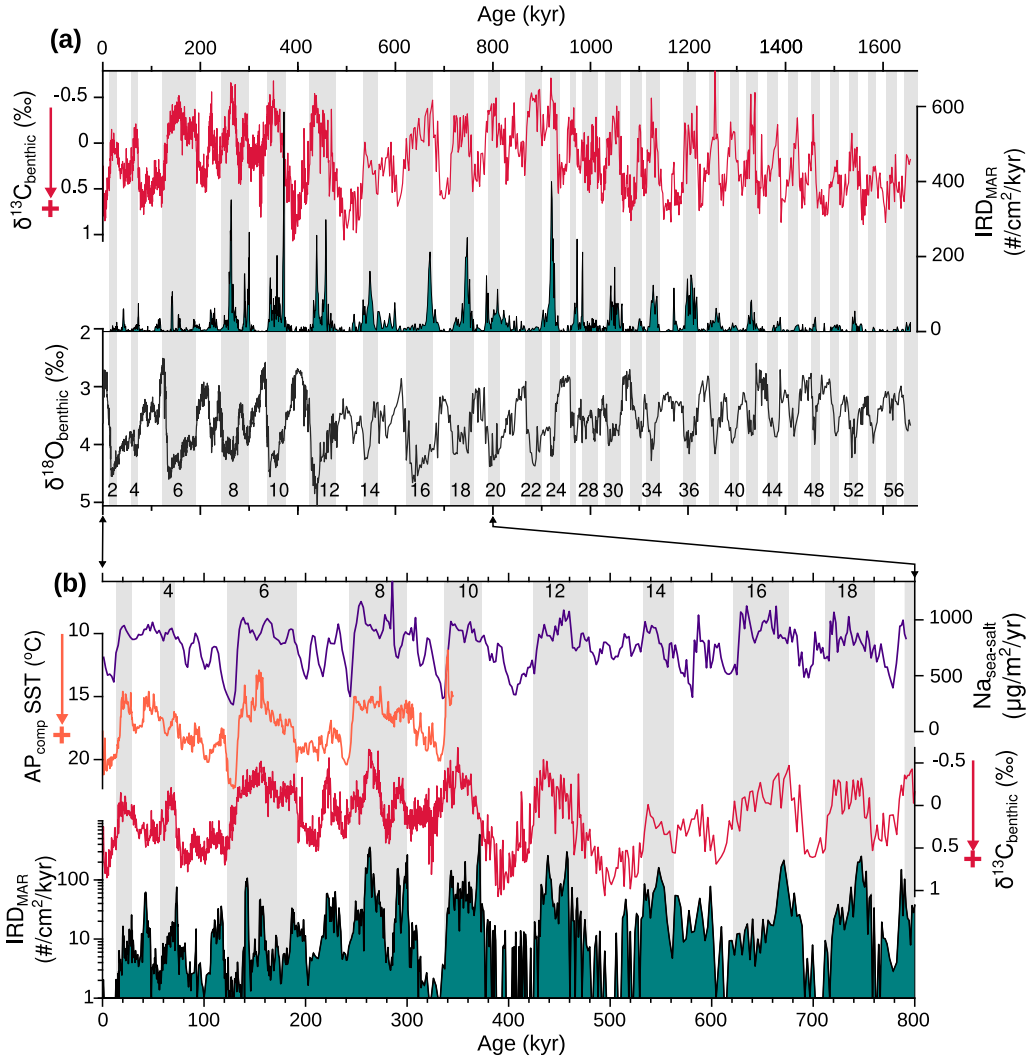

Figure 4.4: **(a)** Time-series of $\delta^{13}C_{benthic}$ (top; pink, note reversed scale), IRD_{MAR} (middle; teal), and $\delta^{18}O_{benthic}$ (lower; grey, note reversed scale) from the AP_{comp} for the past 1.65 Ma, with glacial Marine Isotope Stages shaded grey. The interval 0-800 kyr ago is expanded in panel **(b)** which additionally includes the $Na_{sea\text{-}salt}$ accumulation from the EPICA Dome C Antarctic ice core (Wolff et al., 2006), a proxy for Southern Ocean sea-ice extent (top, purple). The AP_{comp} $U^{k'}_{37}$ SST record (Romero et al., 2015) is also shown (second from top, orange). Note the log-scale for IRD_{MAR} in **(b)**

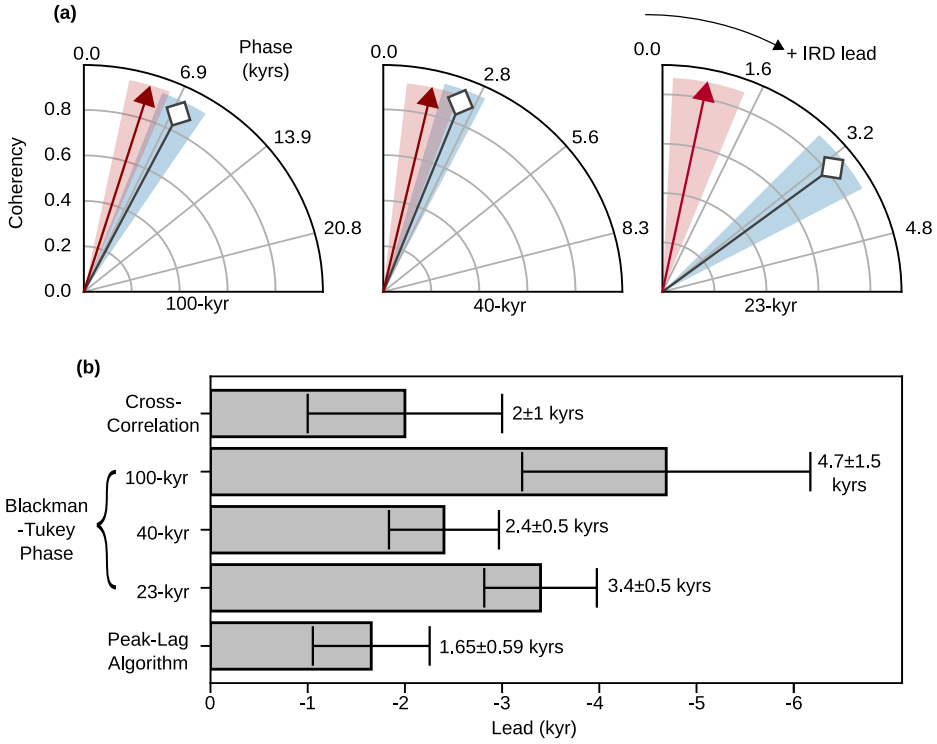

Figure 4.5: Summary of results from statistical analysis of IRD_{MAR} versus $\delta^{18}O_{benthic}$ phasing. **(a)** Blackman-Tukey coherency phase of IRD_{MAR} against $\delta^{13}C_{benthic}$ (red; triangular-head arrows) and $\delta^{18}O_{benthic}$ (blue; diamond-head arrows) in the 1/100 kyr, 1/41 kyr, and 1/23 kyr frequency bands. These phase wheels are cropped at 0-90^{o}, with clockwise rotation indicating a larger lead for IRD_{MAR} (given in kyr on the curved axes). The arrow length represents coherency and the shaded areas give the 95% uncertainty in phase. IRD_{MAR} leads $\delta^{13}C_{benthic}$ and $\delta^{18}O_{benthic}$ in phase for all 3 frequencies. **(b)** Summary of lead times for IRD_{MAR} over $\delta^{13}C_{benthic}$ determined by three independent approaches, with estimates of 95% uncertainty given by the back bars.

reveals that maxima in the IRD_{MAR} occur on average 1.65±0.59 kyr before maxima in the rate of $\delta^{13}C_{benthic}$ decrease (Figure 4.5). Together, these approaches independently demonstrate that IRD_{MAR} systematically leads $\delta^{13}C_{benthic}$ at the AP_{comp}; the unidirectional result from the 'peak-lag' algorithm quantifies this lead best as 1-2 kyr.

4.4 Discussion

4.4.1 Interpreting IRD

Understanding the relationship between IRD_{MAR} and $\delta^{13}C_{benthic}$ requires a framework for interpreting each proxy with consideration for the potentially confounding

influences. For example, high IRD_{MAR} during glacial intervals might be interpreted as representing a shift in iceberg trajectories. This interpretation is coherent with published IRD records which show that deposition close to Antarctica is generally highest during interglacial periods (Keany et al., 1976; Diekmann et al., 2003a) and periods of ice-sheet retreat (Diekmann et al., 2003a; Weber et al., 2014) (e.g. glacial terminations), whilst at SAZ locations IRD maxima typically occur during glacial periods (this chapter; Keany et al., 1976; Teitler et al., 2010). This suggests that glacial conditions in the Southern Ocean favour the increased transport of icebergs away from Antarctica, as the early decay of icebergs is reduced and the overall survivability and transport enhanced. This might be due to cooler surface temperatures (Gersonde et al., 2005), increased sea-ice (Gersonde et al., 2005; Wolff et al., 2006), and changes in surface circulation, possibly relating to the intensity and/or position of the Southern Hemisphere Westerly Wind Belt (Kohfeld et al., 2013). Moreover, iceberg drift in the ocean is associated with, and can facilitate sea-ice formation (Merino et al., 2016), and sea-ice presence in turn can inhibit the wave-driven erosion of icebergs (Wagner et al., 2018) and even govern iceberg movement under severe ice conditions (Schodlok et al., 2006). Enhanced sea-ice concentration and extent is a well-documented feature of the glacial Southern Ocean (e.g. Gersonde et al., 2005; Allen et al., 2011), and the close correspondence between the AP_{comp} IRD_{MAR} record and an Antarctic ice core proxy for sea ice extent (Wolff et al., 2006) (Figure 4.4) over the past 8 glacial cycles suggests that such a feedback may be important.

Furthermore, iceberg trajectory modelling results indicate that glacial conditions are associated with an equatorward shift and lengthening of trajectories relative to preindustrial simulations (Figure 4.8) and modern observations (Tournadre et al., 2016). Whilst long-term IRD_{MAR} variability in the SAZ is likely influenced by varied calving rates and the evolution of the Antarctic ice-sheet (Pollard and DeConto, 2009), the PyBerg modelling results demonstrate that a dramatically altered distribution of icebergs does not require a substantial change to ice-sheet mass balance. Of course, iceberg presence and therefore IRD deposition at the AP_{comp} does require at least some calving of icebergs to occur, and therefore necessitates a sufficiently large (marine-terminating) ice-sheet. Considering evidence that East Antarctica maintained a marine-terminating ice-sheet across the warm interglacials MIS 11 (Raymo and Mitrovica,

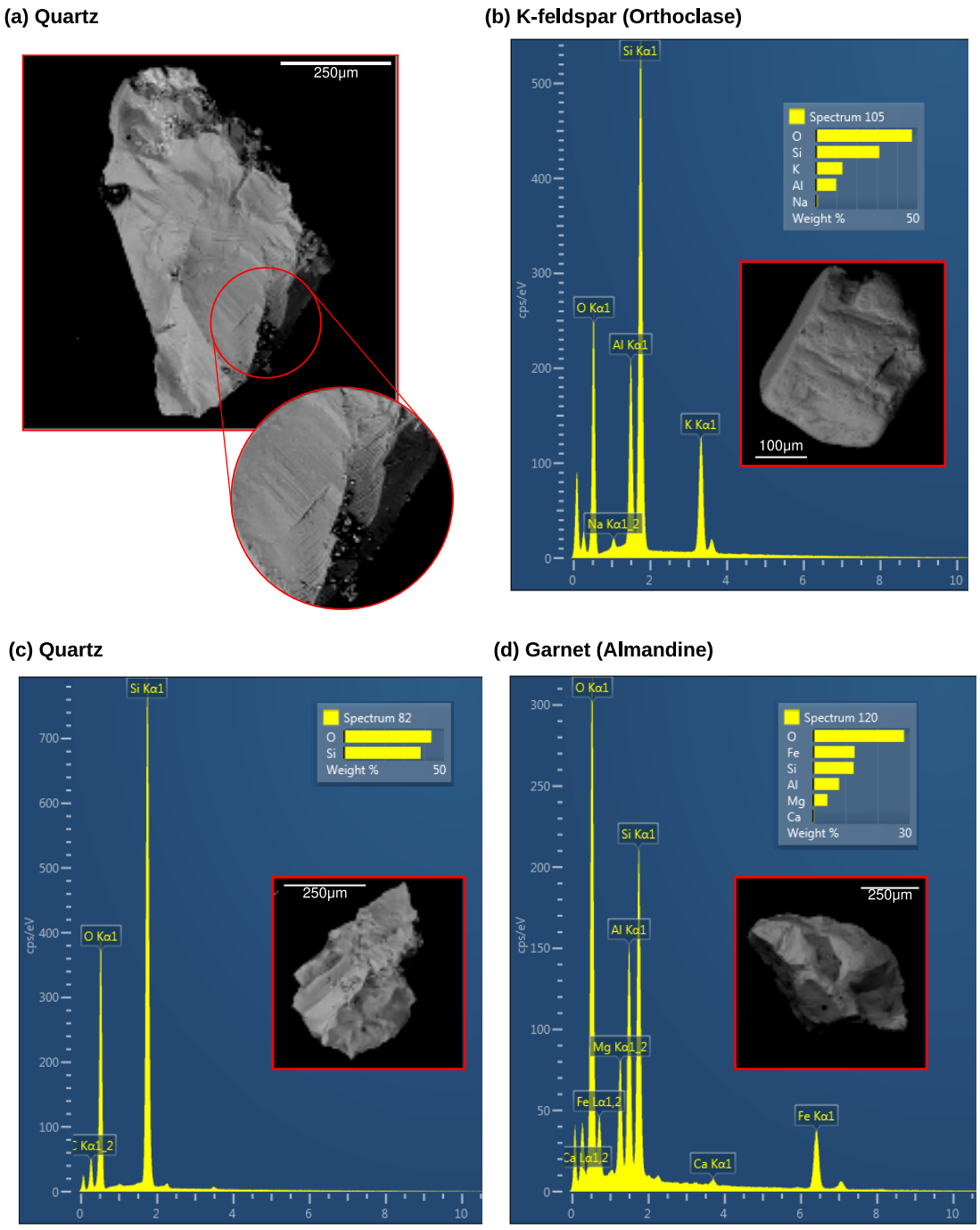

Figure 4.6: **(a)** An SEM image of a quartz grain from Site U1475 with an enlarged view of surface micro-textures in the inset panel. **(b-d)** SEM images of IRD grains with examples of relative peak intensities for elements derived from EDS point analyses. **(b)** shows a spectrum typical of K-feldspar (orthoclase), **(c)** of quartz, and **(d)** of garnet (almandine member). Scale bars are given in white on all SEM images.

2012; Teitler et al., 2010) and MIS 31 (Teitler et al., 2015), it is likely that the calving-ice-sheet-condition would have been consistently met during the glacial intervals across the Mid to Late Pleistocene.

As outlined above, the interpretation of IRD in the Southern Ocean is dependent on at least some knowledge of petrological origin. The observed AP_{comp} IRD assemblage of predominantly quartz with some K-feldspar and garnet is distinct from the plagioclase-dominated clear mineral assemblages found close to Bouvet Island (Nielsen et al., 2007a; Teitler et al., 2010). This mineralogy implies a continental Antarctic origin (Diekmann and Kuhn, 1999): the high quartz proportion may suggest a Ronne Ice Shelf, Filchner Ice Shelf, or Antarctic Peninsula origin (Diekmann and Kuhn, 1999) whilst the presence of garnet implies a metamorphic origin (Manoj et al., 2013), possibly indicating a contribution from the East Antarctic ice-sheet (Diekmann and Kuhn, 1999; Teitler et al., 2010). Micro-textures such as striations and step-like fractures identified on selected quartz grains further support a glacial origin (Mahaney, 2002; John et al., 2015).

4.4.2 Interpreting $\delta^{13}C_{benthic}$

The deep circulation at the AP is characterised by competing water masses of Northern and Southern Hemisphere origin (Arhan et al., 2003). Northern-sources waters (NSW; referring to NADW and glacial analogues) today extends to 3000m water depth as they exit the Atlantic Ocean into the Southern Ocean (Bower et al., 2019). A weakening and/or shoaling of NSW, as in some glacial reconstructions (Hesse et al., 2011), would result in increased presence of Southern-Sourced Waters (SSW) at the Agulhas Plateau, consisting of some combination of Lower Circumpolar Deep Water and Antarctic Bottom Water, flowing clockwise around the SO, and spreading northwards into the neighbouring subtropical basins (Talley, 2013). The relative contribution of NSW versus SSW at the AP is reconstructed here through the $\delta^{13}C$ of *Cibicidoides wuellerstorfi*, an epifaunal benthic foraminifer shown previously to be closely related to the $\delta^{13}C_{DIC}$ of ambient seawater (Schmittner et al., 2017). $\delta^{13}C_{benthic}$ is a widely applied proxy to trace past changes in deep ocean ventilation by ocean circu-

lation (e.g. Lisiecki, 2014; Hesse et al., 2011). However, as with the IRD proxy, the $\delta^{13}C_{benthic}$ record may be influenced by numerous environmental processes. In other words, it is not a simple water mass tracer, and may be affected additionally by productivity signals (Mackensen and Licari, 2003) and thermodynamic effects on air-sea exchange resulting in non-stationary water mass end-members (e.g. Lear et al., 2016).

A potential way to clarify the controls on $\delta^{13}C_{benthic}$ is to compare the reconstructed time series with records representing potential water mass end-members. This allows essentially correcting for changes in water mass end-member composition over time (i.e. related to air-sea exchange). Here, a simple binary mixing model (following Oppo and Fairbanks, 1987) is used to estimate the % of NSW from $\delta^{13}C_{benthic}$. The correlation between calculated NSW% and the raw $\delta^{13}C_{benthic}$ record then provides some insight into the extent to which $\delta^{13}C_{benthic}$ can be attributed to changes in water mass composition. Using stacked $\delta^{13}C_{benthic}$ records representing NSW and SSW over the past 1.5 Ma the following mixing equation is used:

$$\%NSW = 100x\frac{(\delta^{13}C_{AP_{\text{comp}}} - \delta^{13}C_{SSW}}{\delta^{13}C_{NSW} - \delta^{13}C_{SSW}}) \tag{4.1}$$

Where $\delta^{13}C_{NSW}$ is a shallow North Atlantic stack and $\delta^{13}C_{SSW}$ is a deep South Atlantic stack (see Chapter 2 for full details of the carbon isotope compilation used throughout this thesis). For comparison, %NSW is also calculated using a Pacific Deep Water (PDW) stack as the second end-member, as in reality the 'Southern' deep water-mass present in the glacial Atlantic is likely some combination of the two. For example, whilst several studies employ a PDW end-member (Oppo and Fairbanks, 1987; Raymo et al., 1997; Lang et al., 2016), this was originally in part due to the absence of suitable Southern Ocean end-member records (Raymo et al., 1997). Indeed, Venz and Hodell (2002) later applied the same approach with newly available deep Southern Ocean $\delta^{13}C_{benthic}$ records. However, recent evidence indicates that PDW was present in the glacial South Atlantic Ocean in larger proportions than previously thought (Yu et al., 2020) and so a PDW end-member may be preferable after all.

The results show that %NSW is well correlated to AP_{comp} $\delta^{13}C_{benthic}$ (SSW end-member, r^2=0.39; PDW end-member, r^2=0.75), supporting our interpretation that

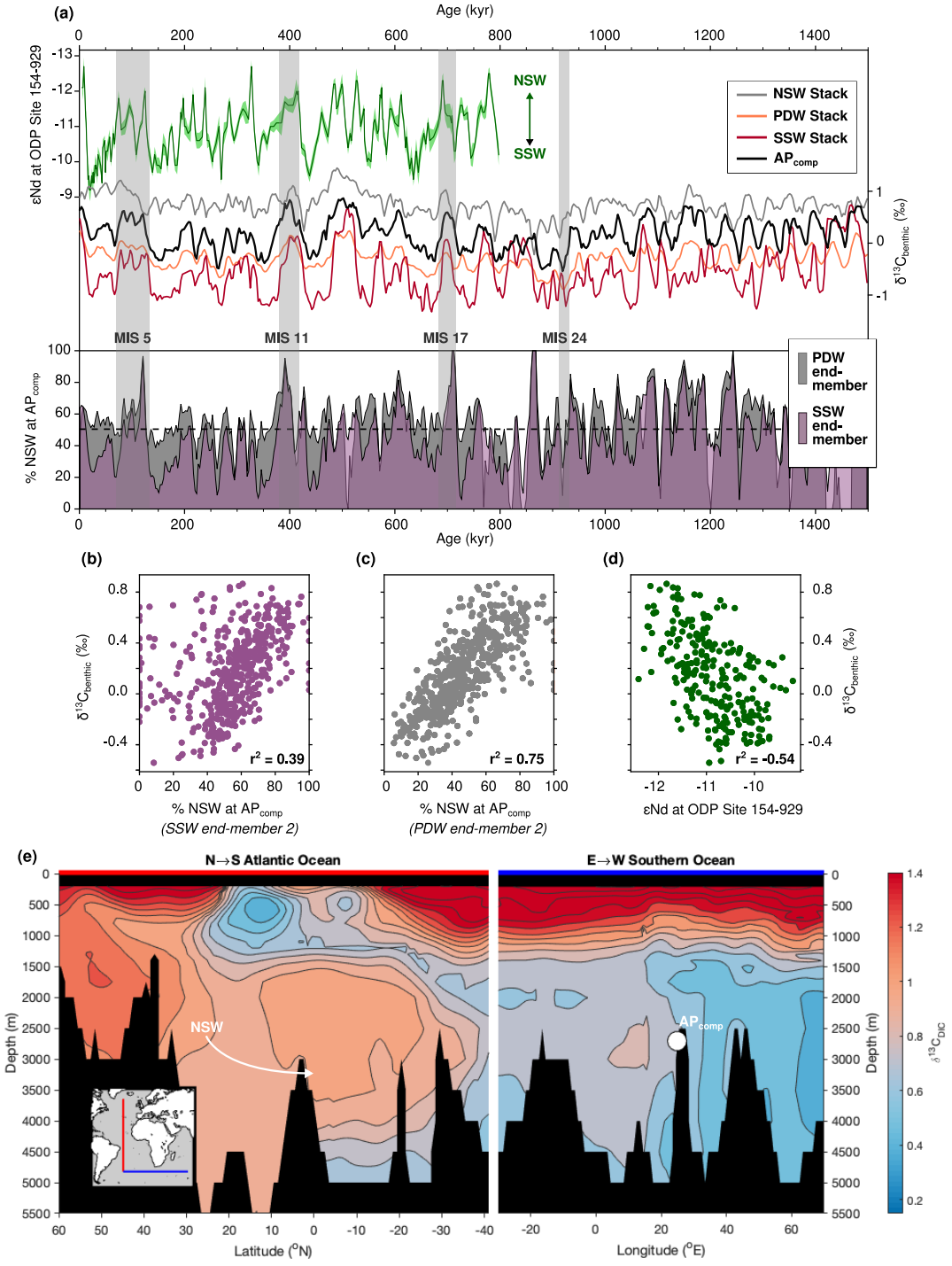

Figure 4.7: (a) Authigenic εNd deep equatorial Atlantic ODP Site 154-929 (from Howe and Piotrowski, 2017). Smoothed $\delta^{13}C_{benthic}$ stacks for Northern-Sourced Water (NSW), Pacific Deep Water (PDW) and Southern-Sourced Water (SSW) end-members (see Chapter 2 for stack construction and constituent core sites) and the AP_{comp} $\delta^{13}C_{benthic}$ record. Selected Marine Isotope Stages (MIS) are shown as grey vertical shading. The bottom time series in **a.** shows % NSW at the AP_{comp} calculated using a binary mixing model with NSW and a PDW (grey) or SSW (purple) end-members. **(b)** Scatter plots of AP_{comp} $\delta^{13}C_{benthic}$ vs. %NSW calculated with an SSW (left) and PDW (middle) end-member, and vs. the εNd isotope record of Howe and Piotrowski (2017) (right). Pearson's correlation coefficient r^2 is given. **(c)** Shows Pre-Industrial $\delta^{13}C$ of Dissolved Inorganic Carbon (from Eide et al. (2017) along a North-South (blue) and then East-West (red) transect, with the AP_{comp} position shown as a white circle.

relative NSW presence at the site is the dominant control on $\delta^{13}C_{benthic}$. Furthermore, $\delta^{13}C_{benthic}$ shows a strong negative correlation to authigenic ϵNd from ODP Site 929 in the deep North Atlantic (r^2=-0.54; Howe and Piotrowski, 2017). Finally, the use of $\delta^{13}C_{benthic}$ as a water mass tracer in this context find support from basin-wide data compilations and modelling studies (e.g. Hesse et al., 2011). The timing of $\delta^{13}C_{benthic}$ changes recorded in the AP_{comp} can therefore be instructive in identifying the origin of deep circulation changes with respect to surface Southern Ocean conditions recorded in the co-registered IRD_{MAR} data.

4.5 Discussion: The 'Southern Escape' of freshwater

With a framework for interpreting the proxy records in place, the next question that arises relates to the significance of the close coupling observed between IRD and $\delta^{13}C_{benthic}$. *What are the implications for a consistent lead of iceberg melt over deep ocean circulation change at the AP_{comp}?*

In the modern ocean the conveyor of icebergs traversing the Southern Ocean constitutes a major transport of meteoric freshwater away from the Antarctic ice-sheet, particularly in the Weddell Sea sector (Silva et al., 2006): a sizeable fraction of modern iceberg mass (up to 35% for giant icebergs; Rackow et al., 2017; Silva et al., 2006) can be exported north of 63^o S. By estimating iceberg meltwater inputs from PyBerg iceberg trajectory experiments, it is evident that a substantial redistribution of freshwater in the Southern Ocean can occur under glacial conditions, as the latitude at which iceberg meltwater is greatest shifts several degrees to the north, with meltwater input south of 50^oS diminishing (Figure 4.10). Interestingly, this pattern of diachronous IRD deposition between glacial and interglacial conditions has been observed since the earliest studies of Southern Ocean IRD accumulation (Watkins et al., 1974; Keany et al., 1976). In fact, there is a striking similarity between the pattern of iceberg melt between the Antarctic and Subantarctic zones proposed by Watkins et al. (1974) and the meltwater distribution estimated by the glacial PyBerg simulations (Figure 4.12b). Furthermore, meltwater in the region between 0-50^oE nearly doubles in the glacial compared to the pre-industrial experiment (22.7% and

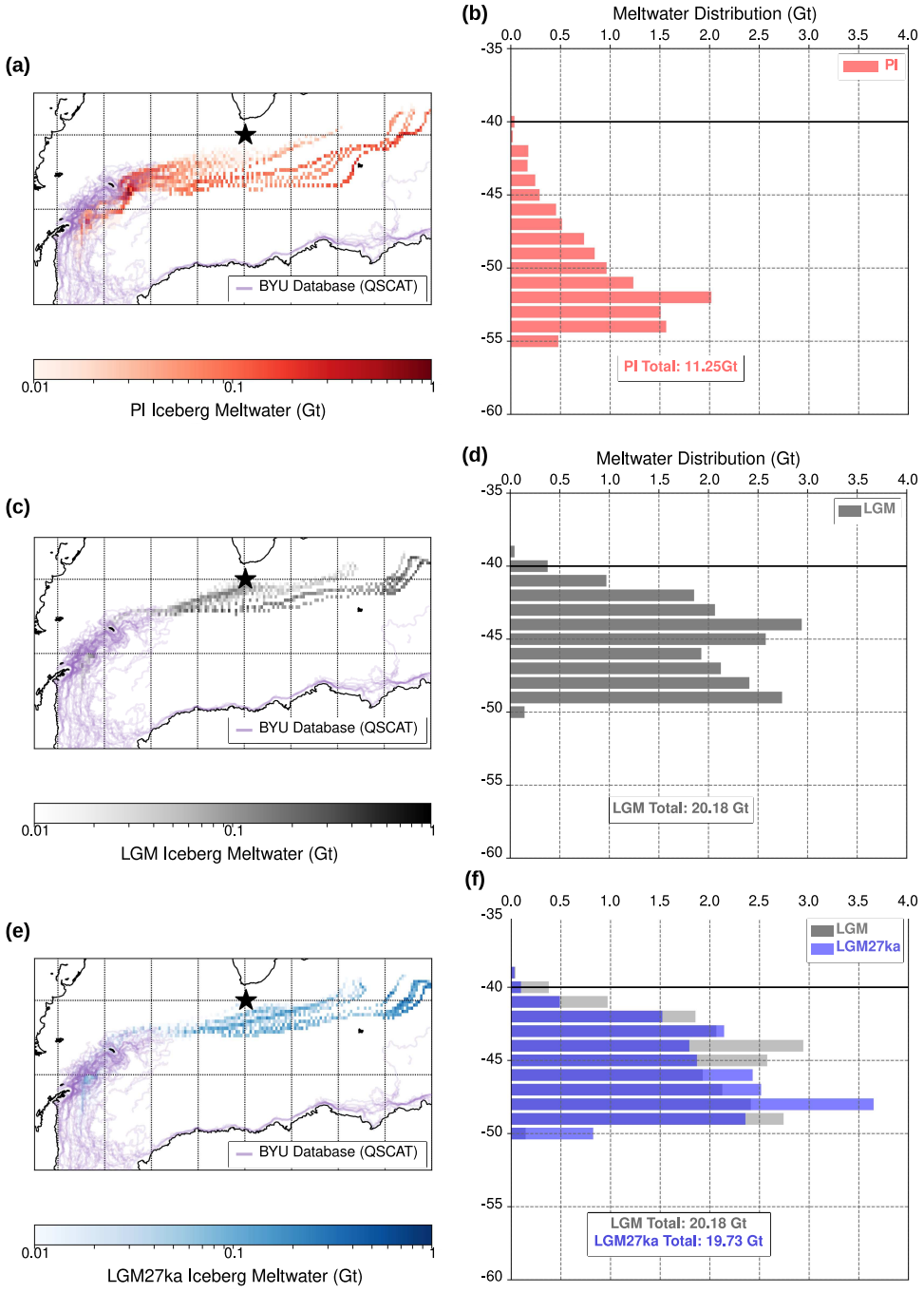

Figure 4.8: Pyberg results modified from Starr et al. (2021). **(a), (c), and (e)** Meltwater distribution estimated for 1^o x 1^o cells by PyBerg experiments **(a)** Pre-Industrial (PI), **(c)** Last Glacial Maximum (LGM), **(c)** Last Glacial Maximum 27ka (LGM27ka). Purple lines are observed modern iceberg trajectories (from QSCAT; Budge and Long, 2018); modelled PI trajectories appear substantially longer than the observed because PyBerg tracks icebergs after then become too small to be identified and hence tracked by modern observational techniques. **(b), (d), and (f)** Zonal-average meltwater estimates for each latitude between 0 and 50^oE for PI **(b)**, LGM **(d)**, and LGM27ka **(e)**

40.7%, respectively, of the total initial iceberg mass). Whilst this is clearly an idealized representation, with no change in calving-rate imposed between experiments, it demonstrates that changes in Southern Ocean conditions can dramatically alter the buoyancy budget of the SO. For example in the modern SO, the meltwater associated with iceberg maxima can readily exceed the local precipitation-evaporation balance (Rackow et al., 2017).

A connection between Southern Ocean surface forcing and the deep ocean has been explored through a variety of theoretical lenses. A common theme occurs wherein enhanced sea-ice (formation and extent) results in an expansion of the region of net surface buoyancy loss (Watson et al., 2015; Ferrari et al., 2014), due to increased brine rejection close to, and subsequent melt occurring away from, the continent. However, the ability of sea-ice buoyancy forcing alone to explain the full NSW shoaling implied by paleoceanographic evidence has been questioned (Sun et al., 2018) and such a direct link is challenged by the failure of climate models without artificial levels of additional cooling in the Southern Ocean (Zhang et al., 2013) to simulate a shoaled glacial NSW. The equatorward shift in Antarctic iceberg melt, a feature absent from the aforementioned models, may be a key, previously unconsidered component in connecting the surface Southern Ocean to overturning circulation. This would allow positive buoyancy anomalies to effectively 'escape' the Southern Ocean into the return AMOC limb; ultimately influencing deep-water formation in the Upper (NSW) instead of the Lower (SSW) overturning cell.

The return limb of AMOC consists of surface to intermediate waters entering the South Atlantic gyre (Talley, 2013) through northward Ekman transport across the Southern Ocean and entrainment in South Atlantic Subtropical Gyre, or via the shedding of warm and saline mesoscale eddies by the so-called Agulhas Leakage (Gordon, 1986). The importance of this return limb is illustrated by the role of Agulhas Leakage in the resumption of NADW formation at glacial terminations, when an increase in the inter-ocean exchange of salt transfers positive density anomalies into the Atlantic basin, triggering the resumption of a strong, deep AMOC mode (Knorr and Lohmann, 2003; Scussolini et al., 2015). It follows that the inverse scenario, reducing the density export into the South Atlantic for example through the 'southern escape'

of iceberg meltwater, would have the opposite effect: suppressing NADW formation.

Such a mechanism finds support from Southern Ocean 'hosing' experiments which find that freshwater addition in the Southern Ocean (in these experiments, south of 60^oS) can affect NADW formation (Seidov et al., 2005; Stouffer et al., 2007) due to Ekman spread of surface waters away from the SO. However, these experiments also generate a weaker Lower Cell: the paleoceanographic evidence for which remains equivocal. Whilst sea-ice formation may have stimulated the Lower Cell (Schmittner, 2003), grounded ice cover in coastal regions of AABW formation may have had an opposing effect (Pollard and DeConto, 2009; Menviel et al., 2017). Some paleoceanographic records do appear to hint at an increase in AABW convection (Govin et al., 2009), however the 1-2 kyr lag time observed here is difficult to reconcile with a direct Southern Ocean mechanism; the temporal offset between IRD_{MAR} and $\delta^{13}C_{benthic}$ may instead favour a teleconnection operating with a threshold behaviour. For example, while the northward export of icebergs to the SAZ would directly decrease the buoyancy flux in AABW formation regions, NADW formation may initially remain strong enough to prevent the northward/upward expansion of SSW. This would continue until the associated 'escape' of buoyancy anomalies into the Upper Cell gradually weakened NADW formation across some threshold whereby the expansion of SSW into the deep Atlantic is possible.

4.5.1 Orbital Pacing and Sequence of Events

With this mechanism in mind, the timing of events at the AP_{comp} in the context of global climate is examined next. In agreement with evidence for an early climate signal in the Southern Ocean during interglacial-glacial transitions (Govin et al., 2009; Imbrie et al., 1992; Brathauer and Abelmann, 1999), IRD_{MAR} is shown to lead $\delta^{18}O_{benthic}$ at all three significant orbital frequency bands (Figure 4.5). Under the assumption that $\delta^{18}O_{benthic}$ changes synchronously with global climate[‡], this would imply that IRD_{MAR} peaks lead relative to global climate (or at least Northern Hemisphere ice volume). Moreover, a distinct inter-hemispheric asynchrony is suggested

[‡]In reality $\delta^{18}O_{benthic}$ has been shown to evolve asynchronously between ocean basins (Skinner and Shackleton, 2005), and so this assumption is a tentative one

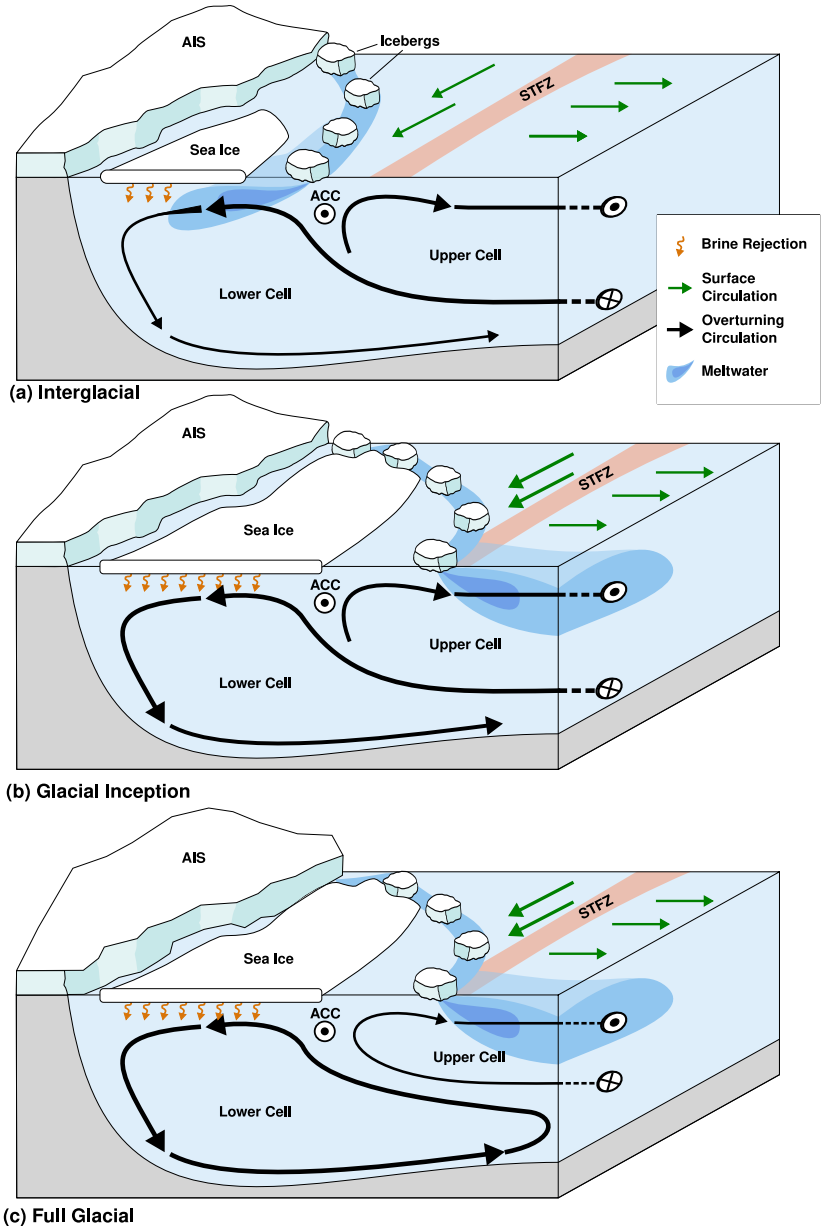

Figure 4.9: 'Southern Escape' schematic from Starr et al. (2021). **(a)** Shows an idealized representation of the Southern Ocean during Interglacial conditions. The front panel gives meridional-averaged overturning circulation following Marshall and Speer (2012). Arrow width represents the relative strength of each circulation cell (wider being stronger). Dark blue shading represents iceberg meltwater being entrained into the Lower Cell as icebergs melt south of the main Antarctic Circumpolar Current (ACC) belt. Orange wavy arrows represent brine rejection from sea-ice formation. The peach-coloured band represents the Subtropical Frontal Zone (STFZ) delineating the Subtropical regime to the north and the (sub)Antarctic regime to the South. **(b)** Same as (a), but for conditions during Glacial Inception; i.e. the transition from interglacial to glacial conditions. **(c)** Same as (a) and (b), but for full glacial conditions (occurring after (b)).

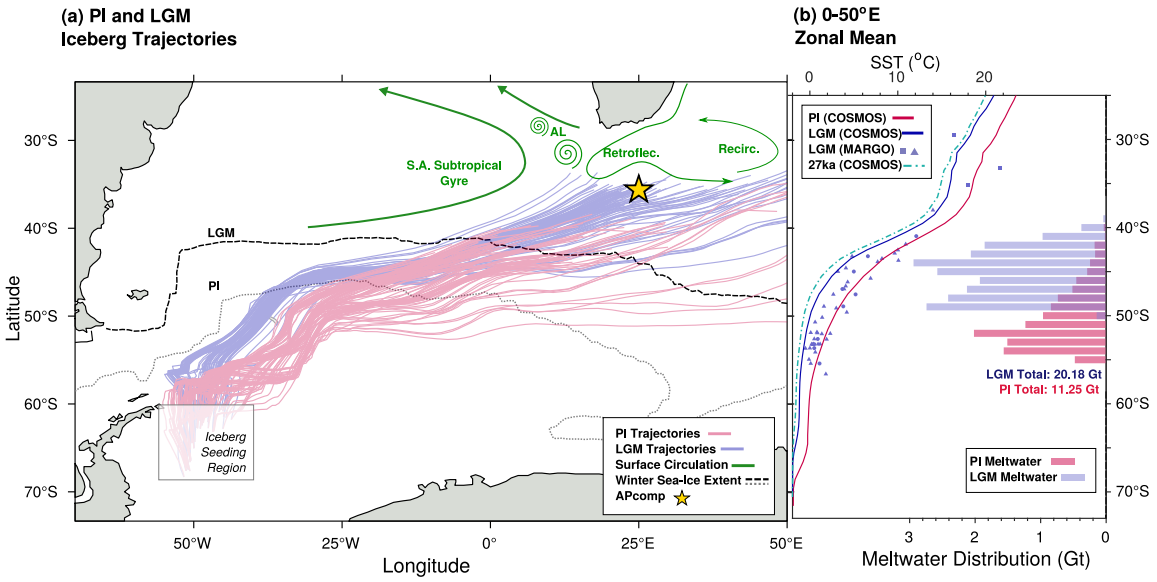

Figure 4.10: **(a)** Same as Figure 4.12 but including LGM iceberg trajectories from PyBerg. **(b)** 0-50^{o}E zonal mean SST under PI (pink) and LGM (blue) conditions. SST proxy data are from Gersonde et al. (2005) (blue symbols; triangle = diatom, circle = radiolarian, square = alkenone). Model SST data are from COSMOS experiments (Zhang et al., 2013). The estimated meltwater distribution is given as total meltwater input in the 0-50^{o}E zone as simulated by PyBerg (see text), with values for the PI (pink) and LGM (blue) being the percentage of the total initial iceberg mass (added as icebergs in the yellow 'seeding region') which melts in the region.

by the phasing of IRD between the Southern Ocean and the North Atlantic: IRD peaks at the AP_{comp} typically precede IRD peaks at ODP Site 982 (Venz et al., 1999) (Figure 4d). A sequence of events emerges in which at the onset of glacial periods a northward expansion of Antarctic iceberg melt occurs, facilitated by increased sea ice extent and surface cooling in the Southern Ocean (Govin et al., 2009), preceding the descent into full global glacial conditions as indicated by maxima in the global $\delta^{18}O_{benthic}$ record. The external forcing of this sequence of events may therefore be identified by the external forcing of SST and sea-ice in the SO; a role for which obliquity has been invoked (e.g. Timmermann et al., 2014). Indeed, cooler surface conditions in the low obliquity PyBerg model experiment (LGM27ka), compared to last glacial maximum experiment (Figure 4.8) cause icebergs to travel further and decay more slowly between 'iceberg alley' and the Atlantic-Indian SAZ. This is consistent with existing SST reconstructions from the Agulhas Plateau (Romero et al., 2015) revealing colder SST during lower obliquity (Figure 2b).

The pacing of IRD_{MAR} peaks by obliquity is apparent during cycles before ~1.2 Ma

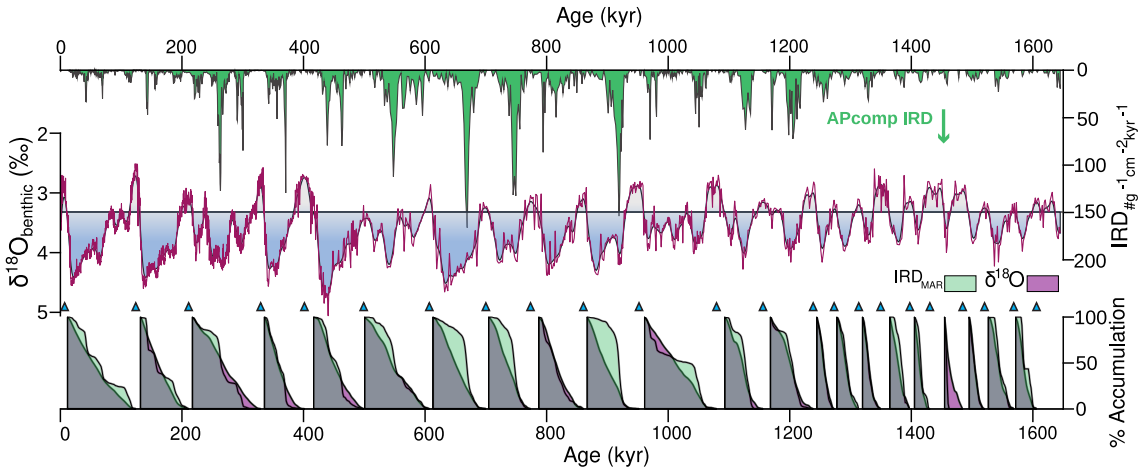

Figure 4.11: Results of the 'glacial accumulation' algorithm with each shaded curve representing IRD_{MAR} (green) and $\delta^{18}O_{benthic}$ (purple) integrated and normalized to 100% within each glacial cycle. Above, the $\delta^{18}O_{benthic}$ record is shown (purple, solid) with green triangles denoting the peak interglacials defined and the dashed black line showing the $\delta^{18}O_{benthic}$ threshold above which the transitions from glacial to interglacial conditions are defined.

(MIS 36) and after ~0.4 Ma (MIS 11; Figure 4b), however is somewhat obscured in-between during the Mid-Pleistocene Transition (MPT). During the MPT, the dominant cyclicity in IRD_{MAR} shifts from ~1/40 kyr to ~1/100 kyr, possibly reflecting a transition to a non-linear response to orbital forcing associated with larger ice-sheets (Willeit et al., 2019). The surface-deep lead (IRD_{MAR} versus $\delta^{13}C_{benthic}$) however is relatively constant (at 1-2 kyr) for the entire 1.65 Ma record, however the lead of Southern Ocean processes over maxima in $\delta^{18}O_{benthic}$ (and hence glacial conditions) is variable, increasing between ~1.2 Ma and ~0.4 Ma. For example, during MIS 24-26, >80% of the total IRD_{MAR} accumulated within the first 50% of the glacial cycle (Figure 4a). This is compared to ~60% accumulation by halfway through the pre- and post-MPT cycles. An increase in this lead of Southern Ocean processes over global ice volume may have resulted from growing larger ice-sheets across the MPT (which would take longer to develop), with the return to a shorter lead time in the Late Pleistocene implying that the rate of ice-sheet growth had increased to accommodate this larger size. Interestingly, recent evidence from the North Atlantic suggests that the rate of northern ice-sheet growth may have accelerated across the MPT, reaching a maximum after ~0.6 Ma, as a consequence of increasing Atlantic Inflow into the Nordic Seas since ~1.2 Ma (Barker et al., view). Furthermore, glacial IRD_{MAR} maxima at the AP_{comp} increase across the MPT (Figure 4d), beginning at MIS 36 (~1.2

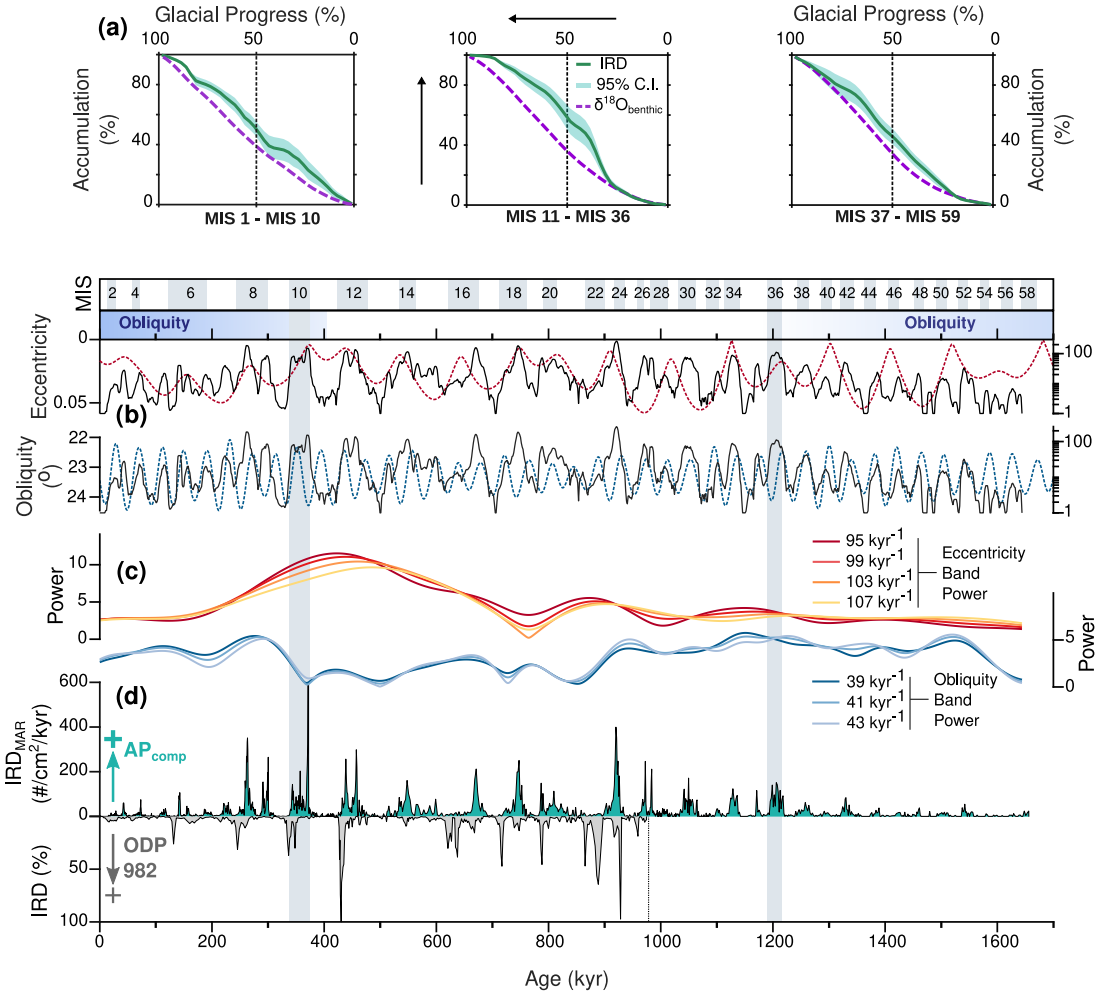

Figure 4.12: **(a)** Results from the 'glacial accumulation' analysis: The cumulative integral is taken for IRD_{MAR} and $\delta^{18}O_{benthic}$ within each glacial interval and normalized to 100% in time and value. Glacial Progress % is relative time between the onset and termination of each glacial interval. Accumulation is the normalized cumulative integral, for example 50% indicates that half of the total IRD_{MAR} deposited in that cycle has been deposited. The three panels show the average and 95% bootstrap confidence intervals for Marine Isotope Stage 1 (MIS 1) to MIS 10 (left), MIS 11 to MIS 36 (middle), and MIS 37 to MIS 59 (right). **(b)** IRD_{MAR} on a log-scale (black) with eccentricity (red, dashed line) and obliquity (blue, dashed line) from Laskar et al. (2004). Shaded grey bars (top) highlight glacial MIS and the blue gradient bar indicates periods with dominant obliquity pacing. **(c)** Wavelet analysis (Mortlet wave with zero-padding) of IRD_{MAR}, showing temporal evolution of relative power in the eccentricity (red-orange lines) and obliquity (blue lines) frequency bands. **(d)** AP_{comp} IRD_{MAR} record (green; top) and a 1 Ma record of IRD (% IRD relative to planktic foraminifera) from the North Atlantic ODP Site 982 (Venz et al., 1999) (bottom; grey; note reversed y-axis).

Ma) and likely reflecting enhanced export of icebergs across the SAZ, coincident with surface cooling and freshening in the Atlantic Southern Ocean (Rodríguez-Sanz et al., 2012).

While this long-term trend may be driven by increasingly iceberg-favourable (cooler) conditions in the region (Rodríguez-Sanz et al., 2012), a role for some change in the discharge of Antarctic icebergs can not be ruled out, especially amid a background of global cooling and possible transitions in the character of Antarctic ice-sheets (Raymo, 2006). Nonetheless, the southern escape of freshwater (IRD_{MAR}) into the SAZ appears to scale with the magnitude of glacial AMOC perturbations as indicated by $\delta^{13}C_{benthic}$ minima; notably, the IRD_{MAR} maximum (and $\delta^{13}C_{benthic}$ minimum) at ~0.9 Ma coincides with the implied collapse in AMOC as recorded in the nearby deep Cape Basin (Pena and Goldstein, 2014). This apparent scaling, as well as the consistent temporal coupling between the southern escape of freshwater and deep water-mass perturbations across this interval, implicate this feedback as a central ingredient in setting overturning circulation state across the MPT and in doing so, perhaps promoting the sequestration of atmospheric CO_2 during the longer glacial intervals of the 100-kyr world (Lear et al., 2016; Farmer et al., 2019; Chalk et al., 2017).

5 | Extending the Agulhas Plateau Carbon Isotope Gradient Record: Modulation by Long Eccentricity?

5.1 Introduction

5.1.1 Background

Long-term fluctuations in paleoclimate records provide an insight into the response of Earth's climate to a range of internal and external forcing (e.g. Westerhold et al., 2020). For example, changes in ice sheet, ocean circulation, and biogeochemical dynamics across Pleistocene glacial-interglacial cycles represent the role and response of these systems with respect to periodic changes in Earth's orbital geometry. Moreover, not all glacial and interglacial intervals are created equally; the exact combination of orbital eccentricity, axial tilt (obliquity), and the position of perihelion (precession), varies among Marine Isotope Stages (MIS), leading to diversity in paleoclimate conditions among glacial and interglacial intervals (Tzedakis et al., 2009; Lang and Wolff, 2011). In addition, long-term climate transitions can modify the nature of these cycles, for example the Mid-Pleistocene Transition (MPT) and Mid-Brunhes Transiton (MBT; also known as the Mid-Brunhes Event) which predominantly modified the character of glacial and interglacial conditions, respectively (e.g. Clark et al., 2006; Barth et al., 2018). Ocean processes appear to be important features of these transitions (Yin, 2013; Pena and Goldstein, 2014), suggesting that ocean circulation and coupled marine biogeochemistry are tightly linked to changes in global climate

across a range of timescales.

The importance of ocean processes in the global climate system can be attributed in large part to their potential to inject or sequester CO_2 to or from the atmosphere (see reviews by Sigman and Boyle, 2000; Sigman et al., 2010). Firstly, the potential storage relies on pathways of ventilation in which surface waters, which are in contact with the atmosphere, are transported into the isolation of the deep ocean interior. The most important of these ventilation pathways can be categorised as (1) deep-water formation in the North Atlantic, (2) deep- and bottom-water formation in the high latitude Southern Ocean and (3) mode and intermediate water formation in the mid-latitude Southern Ocean (Khatiwala et al., 2012). While pathways (1) and (2) transport the largest volume of water into the interior, it is pathway (3) which is most significant in heat and carbon uptake (Khatiwala et al., 2009; Zanna et al., 2019). Furthermore, the subduction of intermediate-depth water masses such as Subantarctic Mode Water (SAMW) and Antarctic Intermediate Water (AAIW) via this pathway is also responsible for supplying nutrients to the low-latitude thermocline (Sarmiento et al., 2004). Intermediate waters mass formation also occurs in the North Atlantic (e.g. Talley and McCartney, 1982) and Mediterranean (e.g. van Aken, 2000) regions, and a substantial formation of 'Glacial North Atlantic Intermediate Water' has been proposed to occur during glacial times (Duplessy et al., 1988; Oppo and Lehman, 1993).

The potential release of deeply-stored carbon into the atmosphere conversely relies on the transport of abyssal and deep waters to the surface, occurring predominantly in the mid-latitude Southern Ocean (Marshall and Speer, 2012). This upwelling predominantly consists of Circumpolar Deep Water (CDW), composed of a mixture of deep and bottom water masses from the Atlantic, Indian, and Pacific basins, returning to the surface along sloping isopycnals which outcrop in the Southern Ocean (adiabatic) with a small contribution from diabatic vertical mixing (Marshall and Speer, 2012). The fate of this water between reaching the surface and being subducted back into the ocean interior is vital in mediating the 'leak' of deeply sequestered CO_2 to the atmosphere. For example, the incomplete biological utilization of nitrate and phosphate from this upwelled nutrient-rich water in the modern Southern Ocean limits

the efficiency of the so-called biological carbon pump and facilitates CO_2 out-gassing (Marinov et al., 2006). During past glacial intervals, the stimulation of primary productivity in the Subantarctic Zone (SAZ) of the Southern Ocean, for example via iron fertilization associated with dust deposition, is thought to have stemmed the efflux of CO_2 to the atmosphere (Sigman and Boyle, 2000).

5.1.2 Carbon isotope gradients

The relationship between ocean ventilation, out-gassing, and the concentration of atmospheric CO_2 (pCO_2) relies on a complex interaction between physical and biogeochemical processes. A useful metric for assessing the efficiency of the ocean carbon sink is the vertical stratification of carbon between ocean layers (Boyle, 1988). Moreover, the multitude of biological and thermodynamic processes which drive this partitioning can also drive isotopic fractionation of the carbon species involved; observable in the spatial distribution of $^{13}C/^{12}C$ in Dissolved Inorganic Carbon (DIC) in the ocean (Figure 5.1b), reflecting a combination of the biological, physical, and thermodynamic history of each water mass (Kroopnick, 1985). For example, the preferential uptake of ^{12}C during primary production leaves the surrounding ocean enriched in ^{13}C (high $\delta^{13}C$*), whilst remineralization of this organic matter at depth lowers the deep $\delta^{13}C_{DIC}$. The vertical gradient between shallow and deep ocean $\delta^{13}C_{DIC}$ will therefore increase with a more efficient biological carbon pump. Indeed, during past intervals of lower pCO_2, the $\delta^{13}C_{DIC}$ gradient between the surface/intermediate and deep Southern Ocean increased, both on millennial (Charles et al., 2010; Ziegler et al., 2013) and glacial-interglacial timescales (Broecker, 1982; Ninnemann and Charles, 1997).

One approach to reconstruct this gradient in the past is to compare the $\delta^{13}C$ of benthic foraminifera ($\delta^{13}C_{benthic}$) from sediment core locations in different water depths (i.e. depth transects; Mulitza et al., 1998; Hodell et al., 2003), however this approach is hindered by the availability of cores from the desired water depths and the need to align the age scales of each core. Alternatively, the $\delta^{13}C$ gradient between 'co-

*defined in delta notation as $\delta^{13}C_{DIC} = ([(^{13}C/^{12}C)_{DIC} / (^{13}C/^{12}C)_{standard}] - 1) \times 1000$

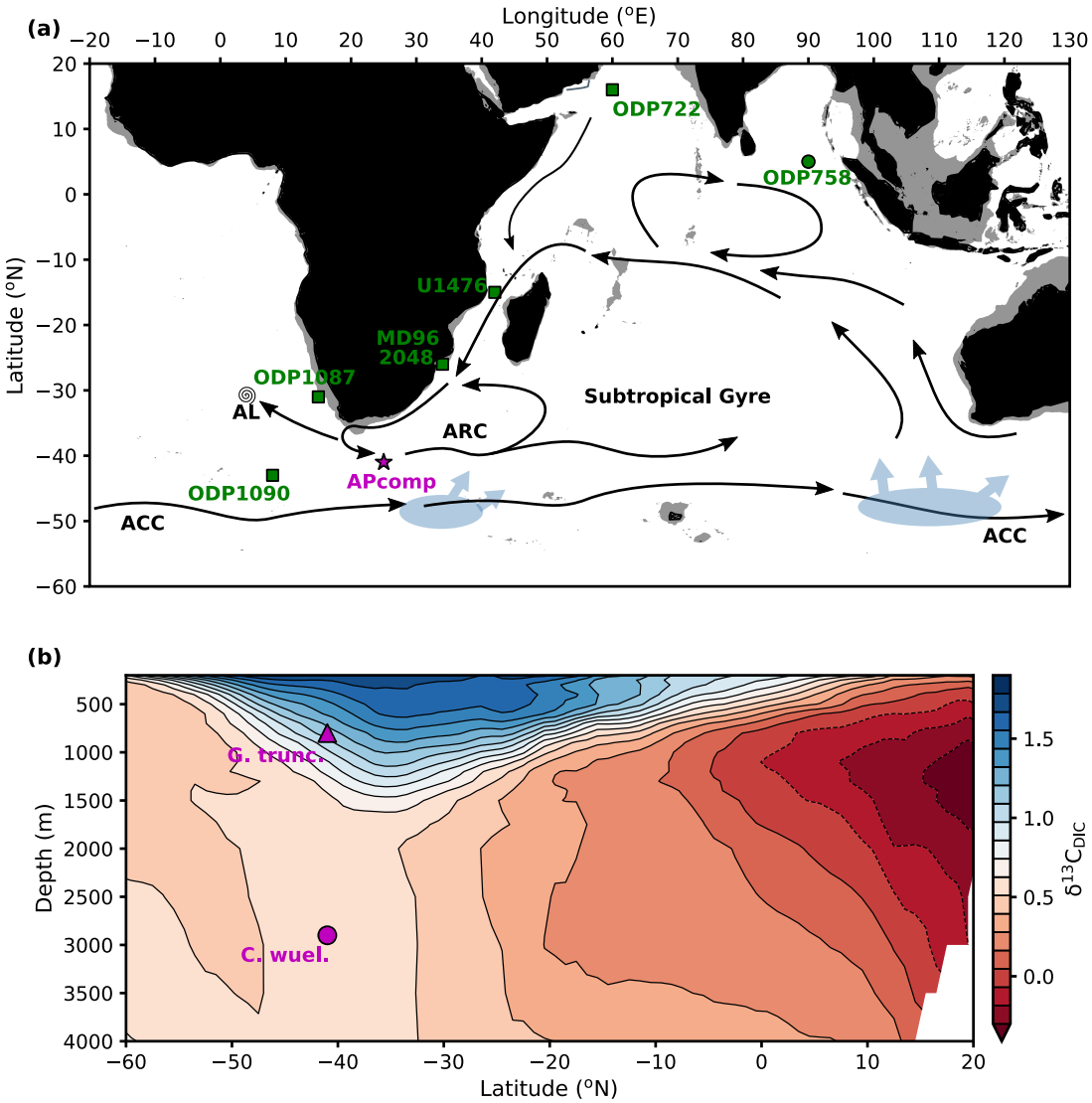

Figure 5.1: **(a)** Map showing the location of sediment cores discussed in this chapter with schematic mode/intermediate water circulation from You (1998); Reid (2003). ARC = Agulhas Return Current, AL = Agulhas Leakage, ACC = Antarctic Circumpolar Current. The sea-floor shallower than 400m is shaded (data from ETOPO1 1 Arc-Minute Global Relief Model, Geophysical Data Center, 2009). **(b)** Meridional transect of $\delta^{13}C_{DIC}$ zonally-average between 20 and 60°E (Eide et al., 2017)

registered' planktic and benthic foraminifera species from identical samples can be reconstructed from a single sediment core site (e.g. Ziegler et al., 2013; Duplessy et al., 1988; Shackleton et al., 1983), provided the depth habitat and species-specific calcification effects are known and/or can be accounted for. For example, $\delta^{13}C$ of the deep-dwelling planktic foraminifera species *Globorotalia truncatulinoides* (D'Orbigny, 1839), is thought to be a faithful recorder of $\delta^{13}C_{DIC}$ in the permanent thermocline (Chiessi et al., 2007; Ziegler et al., 2013; Hu et al., 2020), provided a consistent identification strategy is employed (Charidemou, 2018), and so its gradient with $\delta^{13}C$ of a benthic species such as *C. wuellerstorfi* (thought to calcify in near-equilibrium with the $\delta^{13}C_{DIC}$ of bottom water; Schmittner et al., 2017), provides an estimate of the $\delta^{13}C_{DIC}$ gradient between the subsurface and deep ocean. Because *G. truncatulinoides* preferentially occupies SAMW depths in the Southern Ocean (Martínez, 1997), the gradient between $\delta^{13}C_{trunc}$ and $\delta^{13}C_{benthic}$ at the Agulhas Plateau can be considered a proxy for $\delta^{13}C_{SAMW}$ - $\delta^{13}C_{CDW}$; hereafter referred to as $\Delta\delta^{13}C_{(SAMW-CDW)}$ (Ziegler et al., 2013).

5.1.3 This Study

The evolution of ocean ventilation and the carbon cycle is increasingly well-studied across the Late Pleistocene (e.g. Gottschalk et al., 2016), however, our understanding of this system across longer timescales, such as those associated with cycles in orbital eccentricity (~100 kyr and ~400 kyr periodicities) remains unresolved. Here, I present a 1.55 Million Year (myr) long record of $\Delta\delta^{13}C_{(SAMW-CDW)}$ from the Agulhas Plateau in the Subantarctic Southern Ocean. New and previously published stable isotope records of *G. truncatulinoides* (s)[†] (0-350 ka published in Ziegler et al., 2013) and *C. wuellerstorfi* (0-350 ka published in Ziegler et al., 2013) are combined to extend the record of $\Delta\delta^{13}C_{(SAMW-CDW)}$ back to the Early Pleistocene.

[†]'sinistral' or left-coiling form

5.2 Methods Summary

The Agulhas Plateau Composite (AP_{comp}) is a stratigraphic framework consisting of proximal sediment core sites MD02-2588 (41^o19.90' S, 25^o49.7' E, 2907 m) and International Ocean Discovery Program Site U1475 (41^o25.6' S, 25^o15.6' E, 2669 m) from the Subantarctic Southern Ocean (see Chapter 2 for full site description and details of splice construction). Data are primarily presented on the 'LR04' timescale determined by graphical correlation of $\delta^{18}O_{benthic}$ to the probabilistic benthic stack (Ahn et al., 2017), however spectral analysis is also included of the AP_{comp} records on the International Ocean Discovery Program (IODP) Site U1476 'absolute age scale' (Barker et al., *Manuscript Submitted*), created by graphical correlation of $\delta^{18}O_{benthic}$ curves between AP_{comp} and Site U1476 (15^o49.25' S, 41^o46.12' E, 2166 m). This provides an alternative age scale independent of orbital assumptions; in other words one in which spurious spectral peaks are unlikely to be introduced by tuning sediment depth to orbital forcing models. Further details of both age models can be found in Chapter 3. The sampling strategy here is the same as outlined in Chapter 4 (and published in Starr et al., 2021), however the abundance of *G. truncatulinoides* specimens limits the resolution of the final isotope record in some intervals.

5.2.1 *G. truncatulinoides* isotope analysis and confidence intervals

Down-core stable isotope records ($\delta^{18}O$, $\delta^{13}C$) were obtained for sinistral (left-coiling) *G. truncatulinoides* (hereafter *G. truncatulinoides* refers to the sinistral form unless otherwise stated) specimens from the 250-315μm size fraction. The number of specimens measured in each sample (hereafter n) was dependent on the availability of morphologically distinct and well-preserved *G. truncatulinoides* shells; the target number was 15 (see below), however n ranged from 3 to 15. Isotope analyses of large samples (n>7) were measured a Finnigan Delta V Advantage coupled online with a Gasbench II and smaller samples (n≤7) were measured using a Thermo Finnigan MAT 253 mass spectrometer coupled online to a Carbo Kiel carbonate preparation device. All results are calibrated to an internal laboratory standard (BCT63) and re-

ported relative to the Vienna Pee Dee Belemnite scale. For Individual Foraminifera Analysis (IFA), single *G. truncatulinoides* specimens were picked from 4 samples and measured on a MAT 253 mass spectrometer, following the protocol outlined above. All analyses were made at Cardiff University.

Planktic foraminifera species generally display higher inter-test variability than benthic species within a given stratigraphic sample, as seasonal, inter-annual, and decadal climate variations are more prevalent in the upper ocean than in the deep. This means that more shells are required per sample to average out high-frequency variability and provide a representative estimate of the time-averaged population mean. In order to constrain the relationship between precision and number of shells required in this study, 154 individual *G. truncatulinoides* shells from 4 individual samples from Site U1475 were analysed (Figure 5.2). From the resulting standard deviations (averaged across the 4 samples with sample means subtracted), the standard error of the mean for each down-core sample can be estimated by dividing by the square-root of the number of shells measured (n)[‡]. From the standard error, it possible to estimate the 95% uncertainty intervals. For n = 1, the 95% confidence intervals are ∼0.8‰ and ∼0.6‰ for $\delta^{18}O$ and $\delta^{13}C$, respectively. Following this approach, a sample with n = 15 specimens will have 95% confidence intervals of 0.20‰ for $\delta^{18}O$ and 0.16‰ for $\delta^{13}C$ (Figure 5.2c). Data-points consisting of n<3 specimens (n = 3 equates to a standard error of 0.46‰and 0.35‰for $\delta^{18}O$ and $\delta^{13}C$, respectively) are discarded, as this (admittedly somewhat arbitrary) boundary constitutes the number of samples below which the 95% confidence intervals exceed the inter-sample standard deviations. The associated uncertainty is reported for the remaining samples to ensure transparency, particularly important in intervals of low *G. truncatulinoides* abundance. A record of the number of specimens measured per sample for the MD02-2588 *G. truncatulinoides* isotope datasets is not available, however Ziegler et al. (2013) state that '∼10' individuals were picked for analysis; this is the number used for the estimation of confidence levels for the upper 300 ka of the AP_{comp}.

The *G. truncatulinoides* carbon isotope and oxygen isotope records are hereafter referred to as $\delta^{13}C_{trunc}$ and $\delta^{18}O_{trunc}$, respectively. The carbon isotope gradient between

[‡]See appendix Code 2.

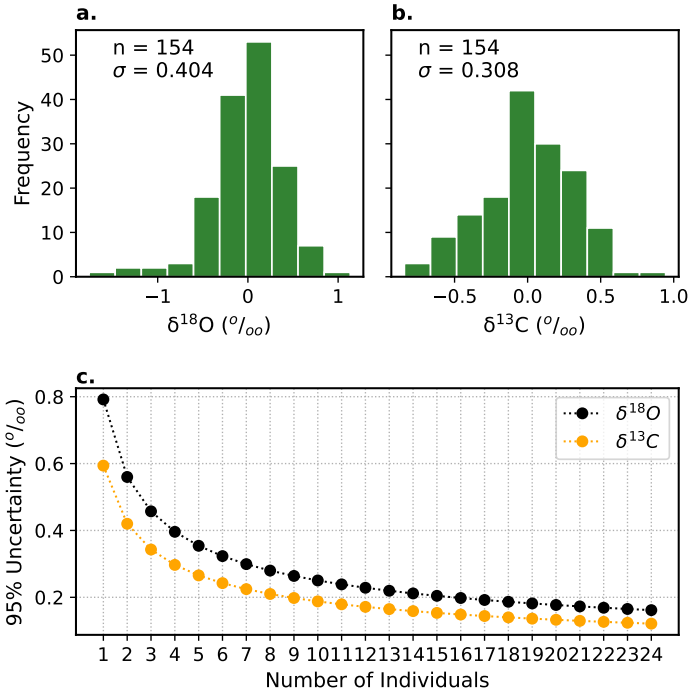

Figure 5.2: (a-b) Histograms showing IFA results for $\delta^{18}O$ (a) and $\delta^{13}C$ (b). Means are subtracted from every measurement on each of the four U1475 samples. n is the total number of shells measured, σ gives the average standard deviation for the four samples. **c** Standard Error of the Mean estimated for measurements of n = 1 to 24 specimens, using the σ from (a) and (b).

$\delta^{13}C_{trunc}$ and $\delta^{13}C_{benthic}$ is referred to as $\Delta\delta^{13}C_{(SAMW-CDW)}$[§].

5.2.2 Binning and Interpolation

As demonstrated in Figure 5.2, standard error increases as the number of constituent specimens (n) decreases. This means that as the availability of *G. truncatulinoides* specimens (and hence n) varies as a function of time, the signal to noise ratio of the data is also non-stationary. This has implications for the interpretation of long-term trends and for the statistical analysis of the data. In order to address this, two techniques are employed to increase and standardize the signal to noise ratio of the data: binning and interpolation. For the former, the data are binned by averaging every data point that falls within 6 kyr discrete intervals. For each bin, uncertainty is estimated from the total number of shells across all samples within the bin and the

[§]although I note that the bottom water mass at the AP_{comp} may not always be strictly be CDW

standard deviations found by analysis of individual shells, outlined above. This is then propagated with the statistical error of the binning itself to estimate 95% confidence limits.

The second approach employed is down-sampling to a linear age scale (dt = 6 kyr) using the Piecewise Cubic Hermite Interpolating Polynomial (PCHIP) approach, whereby monotonic cubic splines are fitted to segments of the original data in order to find the value at the new points (using the 'SciPy' implementation based on Fritsch and Butland, 1984). This has the advantage that the shape is preserved, and the first derivative is continuous. PCHIP confidence intervals are then estimated by a combination of 'Monte-Carlo' and bootstrap re-sampling. The procedure can be summarized as follows:

1. Each data point is re-sampled from a normal distribution with a standard deviation matching that of the sample to simulate the error associated with each original data-point;
2. The new re-sampled time series then has 5% of its values randomly removed;
3. A PCHIP interpolator is then fitted and the resulting curve is stored;
4. Steps 1-3 are repeated 10,000 times, creating an ensemble of 10,000 interpolated time series on the new downsampled, linear age scale;
5. The median is taken to be the new series, and the 95% and 5% percentiles are taken as the confidence interval;

The resulting binned and PCHIP down-sampled time series are broadly indistinguishable, with equivalent minimum and maximum values. Due to the utility of the PCHIP approach in preserving the underlying shape of the data and the more comprehensive uncertainty estimation approach, the time series are discussed in this form unless otherwise stated. All statistical analysis (described below), however, were performed on the original raw time series, and I emphasize that the conclusions made are independent of the binning or interpolation technique chosen.

5.2.3 Spectral Analysis

Due to the uneven spacing of the time series, all analyses are performed on the original data to avoid introducing spurious peaks or phase shifts which may occur when interpolating to a monotonic age scale (Yiou et al., 1996). Before spectral analysis, all data were standardized and a 2^{nd} order polynomial trend was removed. The REDFIT-X software (Ólafsdóttir et al., 2016) was used to calculate the Lomb-Scargle periodgram (Lomb, 1976; Scargle, 1982) as well as cross-spectrum density and spectral coherency against a synthetic curve combining orbital eccentricity, obliquity, and precession (known as ETP). To test the sensitivity of the results to the de-trending method and Lomb-Scargle parameters chosen, the analysis was also performed using a variety of settings. Figure 5.3 shows that the low-frequency peaks (the focus of this chapter) are robust to changes in the number of overlapping 50% segments (n50), the window shape used (Hanning, Rectangular, or Welch), and the method used to detrend the time series (linear, 2nd order and 3rd order polynomials removed). Furthermore, the low-frequency peaks are robust to the choice of age model,giving similar results when using the Site U1476 absolute age scale, which is independent of orbital tuning (unlike the LR04 timescale which is derived from an orbital ice volume model; Lisiecki and Raymo, 2005).

Next, band-pass filters were designed with a central frequency determined by the spectra with a resolution bandwidth of ± the 6dB resolution bandwidth output by REDFIT-X. In order to compare the data presented here to previously published paleoclimate records, Lomb-Scargle periodograms and cross-spectra against ETP were computed for several other time series. All data was treated as described above. Records which revealed a significant ~400 kyr periodicity (either in auto-spectrum or cross-spectrum versus ETP) were then included in the band-pass filtering shown in Figure 5.12.

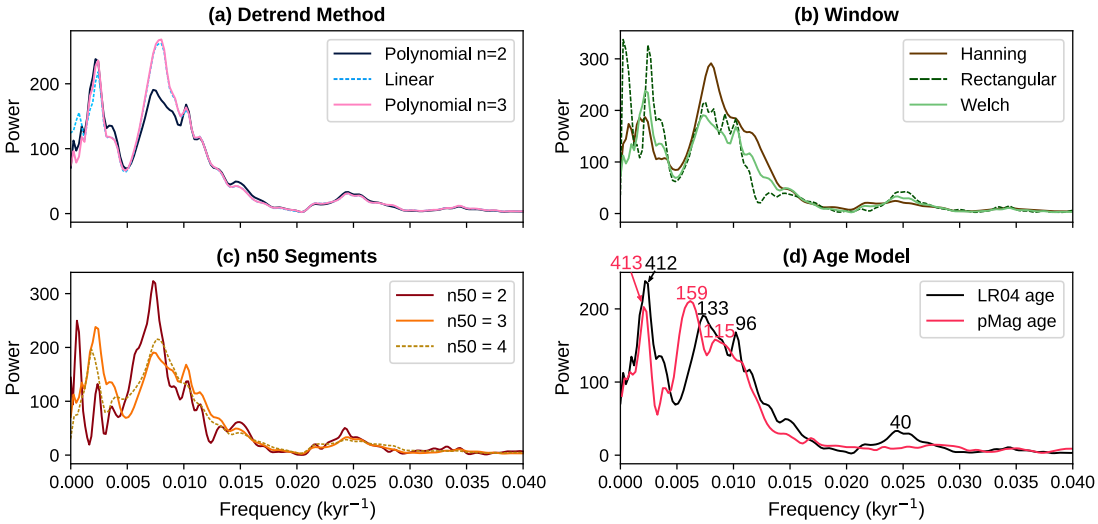

Figure 5.3: Lomb-Scargle periodograms for $\Delta\delta^{13}C_{(SAMW-CDW)}$, varying **(a)** de-trending method, **(b)** window type, **(c)** number of overlapping 50% segments, **(d)** the LR04 versus the U1476 'pMag age model' (Barker et al., *Submitted*)

5.3 Understanding *G. truncatulinoides* abundance

5.3.1 Life History and Evolution

The first notable observation from this study is the low abundance of *G. truncatulinoides* during several intervals across the Early to Mid-Pleistocene (Figure 5.6). Although a quantitative record of *G. truncatulinoides* abundance is not provided (i.e. the record of number of tests is truncated at 15 as this was the maximum number of shells measured per sample), an absence of shells available for analysis (n) implies periodic collapses in the population of *G. truncatulinoides* at the AP_{comp} location.

G. truncatulinoides is a deep-dwelling, non-symbiotic species of planktic foraminifera which forms the majority of its calcite test at the depth of the permanent thermocline (LeGrande et al., 2004; Cléroux et al., 2007). By comparing the core-top $\delta^{18}O_{trunc}$ with water column $\delta^{18}O_{seawater}$ and temperature, Ziegler et al. (2013) propose a calcification depth for of 300-400m at the AP, in agreement with plankton tow studies in the south-east Atlantic (Lončarić et al., 2006). It is worth noting that the population present at the modern AP may be genetically different from those further back in time, and evolutionary trends and divergences can occur over the timescales covered

in this study (>1 Ma). The evolutionary history of *G. truncatulinoides* is relatively well understood, originating in the south-west Pacific Ocean around 2.8 Ma (Lazarus et al., 1995) before appearing briefly in the Atlantic Ocean ~2.5 Ma and then more widely outside of the Pacific after 2 Ma (Sexton and Norris, 2008). Within the morphologically defined *G. truncatulinoides* species there have been 5 (Quillévéré et al., 2013) cryptic genotypes identified in modern populations, exhibiting distinct hydrographic tolerances and thus geographic distributions. The appearance and adaptation of different genotypes may result in temporal changes in the oceanographic range of *G. truncatulinoides* in the fossil record; for example, the Subantarctic, cold-tolerant types III and IV evolved ~300 ka (de Vargas et al., 2001) suggesting that the oceanographic conditions which may have limited *G. truncatulinoides* abundance at the AP_{comp} at times in the Early to Mid-Pleistocene, may not have influenced the abundance of the later, more cosmopolitan genotypes (appearing around ~300 ka) in the same way. However, no divergence events appear to be coincident with the intervals of low abundance intervals observed at the AP_{comp}, and the dispersal of *G. truncatulinoides* to its current geographic distribution was complete by ~2 Ma (Sexton and Norris, 2008), suggesting that low abundance cannot be attributed to evolutionary processes.

Secondly, *G. truncatulinoides* exhibits substantial vertical habitat migrations throughout its life cycle, meaning water column stratification can disrupt its reproduction (Lohmann and Schweitzer, 1990), as deep winter mixing is required to bring juvenile or reproductive-stage adult *G. truncatulinoides* to the surface mixed layer (Hemleben et al., 1985). It follows that increased stratification, possibly resulting from reduced wintertime mixing, might provide an explanation for the intervals of low *G. truncatulinoides* abundance. However, comparing the modern[¶] distribution of *G. truncatulinoides* (ForCenS dataset; Siccha and Kucera, 2017) with a mixed-layer depth climatology (Sallée et al., 2021) does not reveal a clear relationship between the two (Figure 5.4c). Further investigation of modern *G. truncatulinoides* abundance against other hydrographic variables (from GLODAPv2; Olsen et al., 2016) reveals a stronger response to oxygen concentration at 400m; abundance declines sharply below ~180µmol/kg (Figure 5.4d). Indeed, *G. truncatulinoides* appears to track oxygen isolines in the North and South Atlantic and Indian Ocean subtropical gyres (Figure

[¶]More specifically, sediment core-top

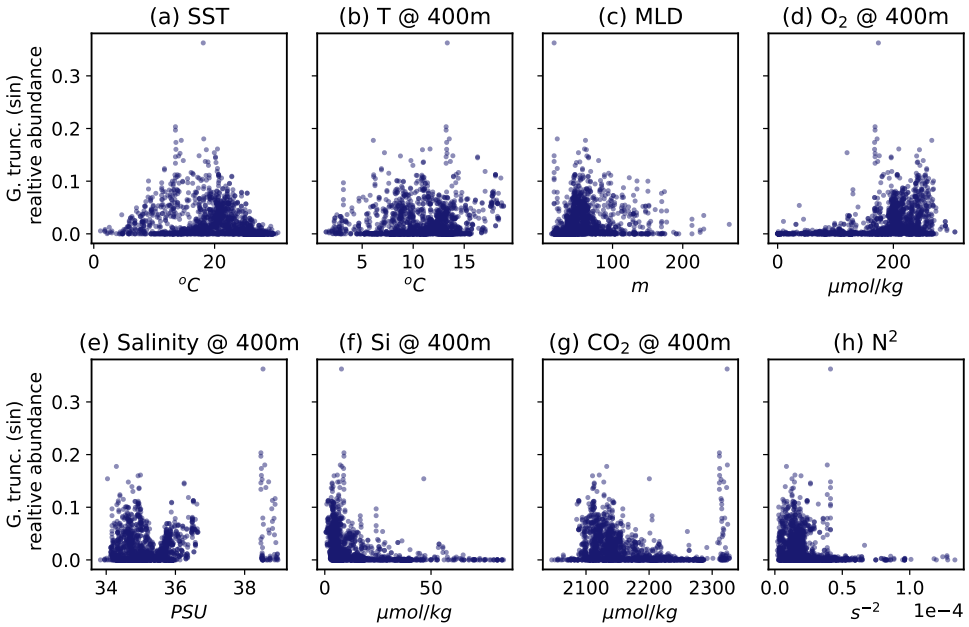

Figure 5.4: Core-top distribution of *G. truncatulinoides (s)* relative abundance from ForCenS (Siccha and Kucera, 2017) against sea surface temperature **(a)**, temperature at 400m **(b)**, Mixed-Layer Depth **(c)**, dissolved oxygen at 400m **(d)**, salinity at 400m **(e)**, silica concentration at 400m **(f)**, CO_2 at 400m **(g)**, and buoyancy frequency N^2 **(h)**. Hydrographic data from Sallée et al. (2021) and Olsen et al. (2016).

5.5). This may be linked to the role of deep mixing discussed above; a cessation of wintertime mixing would result in lower subsurface oxygen concentration. Interestingly, Reichart et al. (1998) show that peaks in *G. truncatulinoides* abundance in the Arabian Sea over the past 225 kyr coincided with reduced oxygen minimum zone intensity, which they link to periods of deep convective winter mixing.

5.3.2 Drivers of *G. truncatulinoides* abundance across the MPT

The Mid-Pleistocene disappearance of *G. truncatulinoides* is not restricted to the AP and has been observed also in the equatorial and North Atlantic (Kaiser et al., 2019), south-east Atlantic (Ufkes and Kroon, 2012) and south-west Pacific Ocean (Crundwell et al., 2008). This widespread disappearance is generally observed between MIS 21 and MIS 15, although the exact timing varies between locations. It is plausible that some change in the thermohaline properties, nutrient and/or oxygen content of the intermediate and mode waters ventilating much of the low-latitude thermocline (i.e. SAMW and Antarctic Intermediate Water) could have driven this phe-

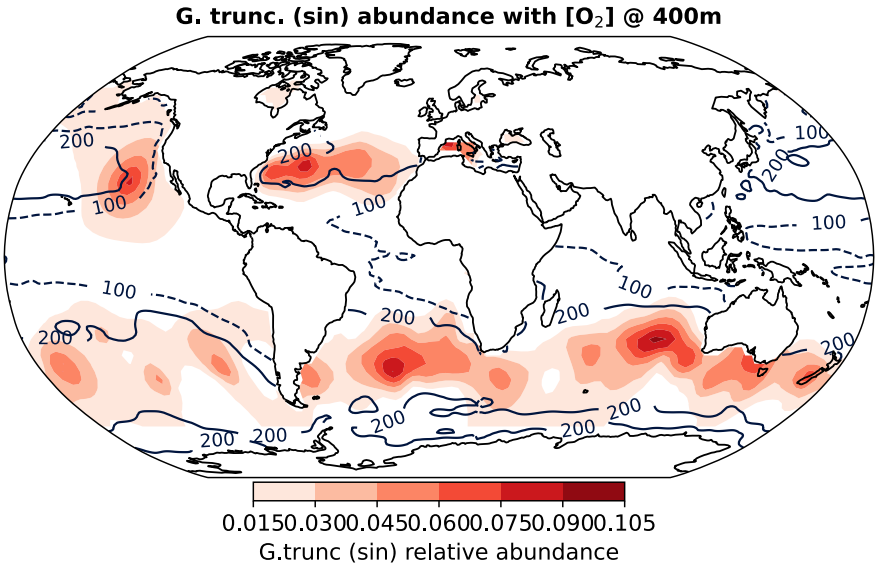

Figure 5.5: Core-top distribution of *G. truncatulinoides (s)* relative abundance from the ForCenS dataset (Siccha and Kucera, 2017). Navy contours show dissolved oxygen concentration at 400m water depth in 100 µmol/kg increments. Oxygen data is from GLODAPv2 (Olsen et al., 2016).

nomenon (Kaiser et al., 2019), particularly as foraminifera calcifying in shallower water depths, such as *G. truncatulinoides* (dextral), appear to persist across this interval. Furthermore, this interval coincides with pulses in the extinction of multiple benthic foraminifera species at intermediate depths (Mancin et al., 2013; Kender et al., 2016), the last in a longer-term benthic foraminifera extinction event since the Late Pliocene (Hayward et al., 2007). A detailed explanation of this phenomenon is beyond the scope of this chapter, however the evidence outlined above appear to suggest of a major shift in the formation or properties of intermediate water circulation across the MPT, although an ecological or evolutionary process cannot be discounted.

5.4 Results

5.4.1 Stable isotope time series

$\delta^{13}C_{trunc}$ is characterized by glacial-interglacial variations with maxima (minima) occurring during interglacial (glacial) intervals (Figure 5.6). However, the distinct glacial-interglacial variations dominant in the $\delta^{13}C_{benthic}$ record are obscured some-

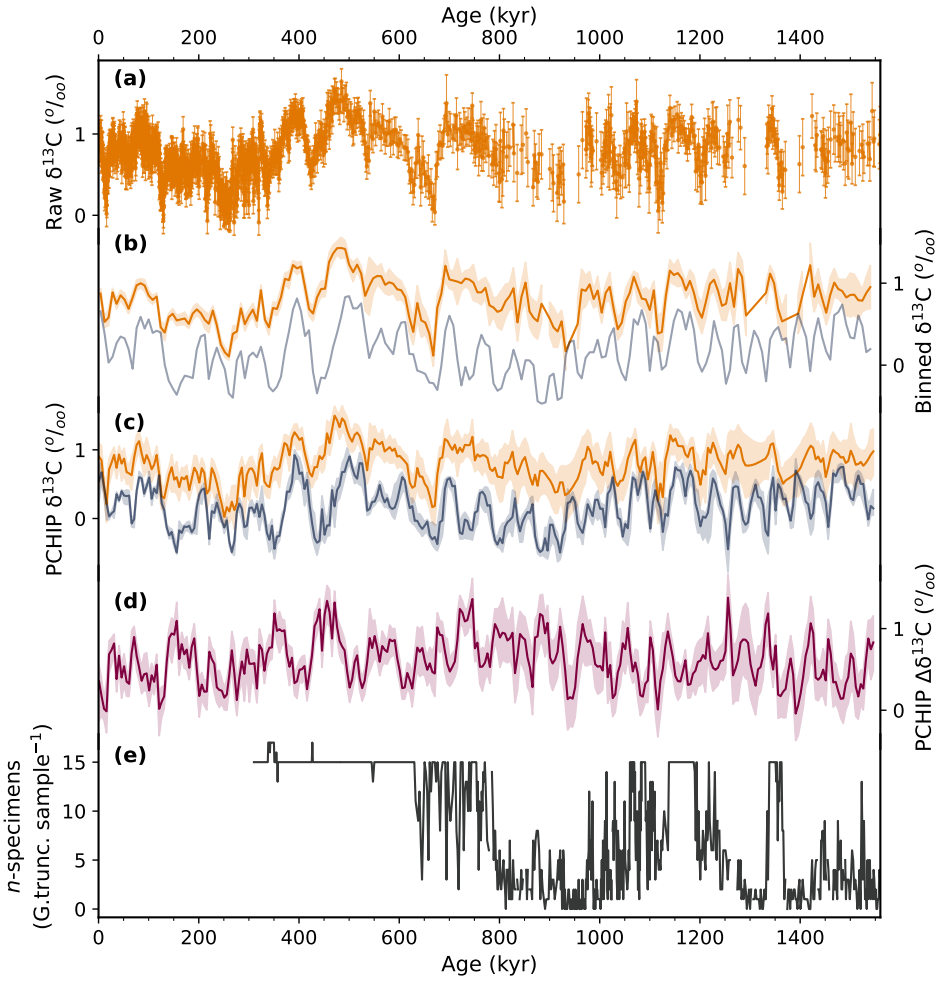

Figure 5.6: *G. truncatulinoides* stable isotope results. **(a)** Raw $\delta^{13}C_{trunc}$ time series with 95% confidence intervals shown as vertical bars. **(b)** G. trunc (orange) and C. wuellerstorfi (navy) binned time series (bin size 6 kyr). **(c)** G. trunc (orange) and C. wuellerstorfi (navy) interpolated by PCHIP (see text). **(d)** PCHIP interpolated $\Delta\delta^{13}C_{(SAMW-CDW)}$ **(e)** The number of G. truncatulinoides shells included in each sample (*n*). The 95% confidence level in (b) and (c) is shaded.

what by low-frequency variations in $\delta^{13}C_{trunc}$. With these distinct long-term fluctuations, $\delta^{13}C_{trunc}$ displays similarities to low-latitude planktic $\delta^{13}C$ records. For example, comparison to the Mediterranean *Globigerinoides ruber* 'Stack' (Figure 5.7a; Wang et al., 2010) and western equatorial Pacific *Globigerinoides sacculifer* $\delta^{13}C$ (Schmidt et al., 1993) reveals intervals of prolonged high $\delta^{13}C$ relative to $\delta^{13}C_{benthic}$, such as from MIS 8 and MIS 12 and between MIS 16 and MIS 24. These long cycles are punctuated by periodic $\delta^{13}C_{trunc}$ minima of ~0 ‰ during MIS 8, 16, 14, 34, and 44, where the mid-depth $\delta^{13}C_{trunc}$ values converge with $\delta^{13}C_{benthic}$ values (Figure 5.7). These excursions are recognisable as the carbon isotope minima which appear in

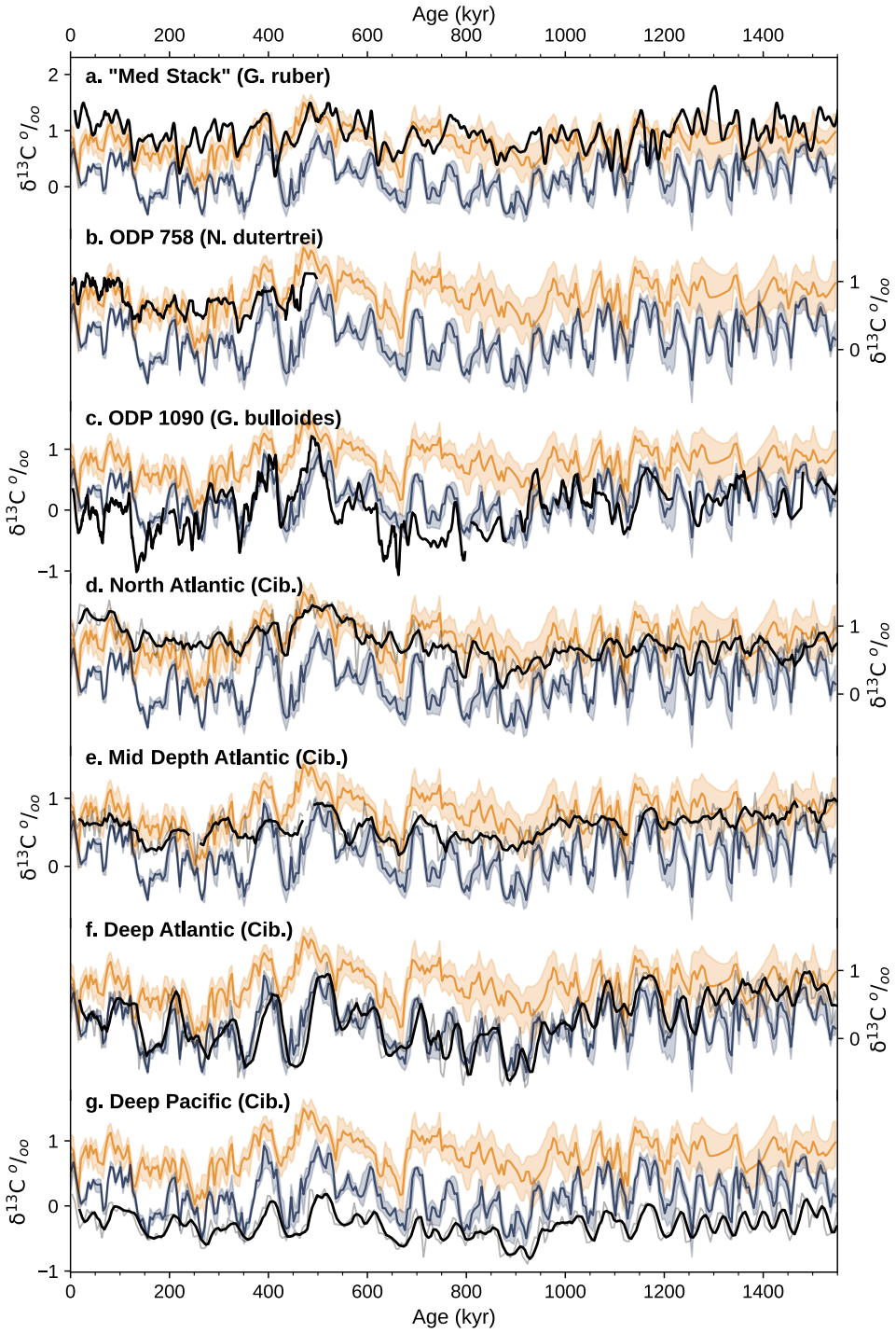

Figure 5.7: Comparison of *G. truncatulinoides* (orange) and benthic δ^{13}C (navy) with selected δ^{13}C records and regional stacks. **(a)** Mediterranean *Globigerinoides ruber* 'Stack' (Wang et al., 2010). **(b)** Equatorial Indian Ocean ODP Site 758 *Neogloboquadrina dutertrei* (Bolton et al., 2013). **(c)** South Atlantic ODP Site 1090 *Globigerina bulloides* (Hodell et al., 2003). **(d-g)** Regional stacks of benthic δ^{13}C (*Cibicides* species); see Chapter 2 for full description of data compilation and stacking. All records are presented on the LR04 timescale

records of surface and (well ventilated) intermediate water masses in the Atlantic, Indian and Pacific Oceans (Spero and Lea, 2002; Romahn et al., 2014; Shackleton et al., 1983; Oppo and Fairbanks, 1989), thought to be linked to a release of low $\delta^{13}C$ CO_2 into the atmosphere from the deep ocean, and the subsequent spread of that signal through either mode/intermediate water ventilation (Spero and Lea, 2002) or air-sea exchange (Lynch-Stieglitz et al., 2019). Further $\delta^{13}C_{trunc}$ minima are associated with the terminations of each glacial stage back to at least MIS 16, however the resolution and data sparsity of the AP_{comp} record during earlier glacial intervals precludes any conclusion on the presence or absence of these carbon isotope minima during earlier terminations. Interestingly, $\delta^{13}C_{trunc}$ is consistently high relative to $\delta^{13}C$ of mixed-layer species in the Atlantic SAZ (*Globigerina bulloides and Neogloboquadrina pachyderma* at ODP Site 1090; Hodell et al., 2003), which co-varies much more closely with $\delta^{13}C_{benthic}$ (Figure 5.7). This might reflect the connection between upwelled deep-water in the Southern Ocean and surface waters to the south of the Agulhas Plateau, however it may also reflect the effect on $\delta^{13}C_{foraminifera}$ of carbonate ion or temperature differences between the sites, post-depositional alterations (ODP 1090 is situated at 3700m water depth, possibly within reach of the carbonate saturation in the past; Hodell et al., 2001) or species-specific offsets (Spero et al., 1991). Finally, similarities between $\delta^{13}C_{trunc}$ and the $\delta^{13}C$ of *Neogloboquadrina dutertrei* from the equatorial Indian Ocean (Bolton et al., 2013, Figure 5.7b) might reflect the signature of 'ocean tunnelling' of SAMW into the Indian Ocean thermocline (Liu and Alexander, 2007; Ninnemann and Charles, 1997), or a common forcing between the two location.

Both $\delta^{13}C_{trunc}$ and $\delta^{13}C_{benthic}$ show the imprint of large-scale secular changes in the oceanic ^{13}C pool (Hoogakker et al., 2006), however this whole ocean signal should theoretically be removed in $\Delta\delta^{13}C_{(SAMW-CDW)}$. Glacial-interglacial variations in $\Delta\delta^{13}C_{(SAMW-CDW)}$ are clearer than in $\delta^{13}C_{trunc}$, with increased gradients coinciding with glacial intervals and vice versa. Glacial $\Delta\delta^{13}C_{(SAMW-CDW)}$ maxima range from ~1 ‰ to ~1.5‰ and interglacial minima range from ~0.5‰ to ~0.0‰; the amplitudes of both are modulated by long-term fluctuations. The highest $\Delta\delta^{13}C_{(SAMW-CDW)}$ values occur during glacial MIS 12, 18, 22, 38 and 42, whilst the lowest interglacial values occur during MIS 1, 5, 25, 31, 33, 45. $\Delta\delta^{13}C_{(SAMW-CDW)}$ variations on sub-orbital timescales have been described in detail elsewhere for the upper 350 ka of the AP_{comp}

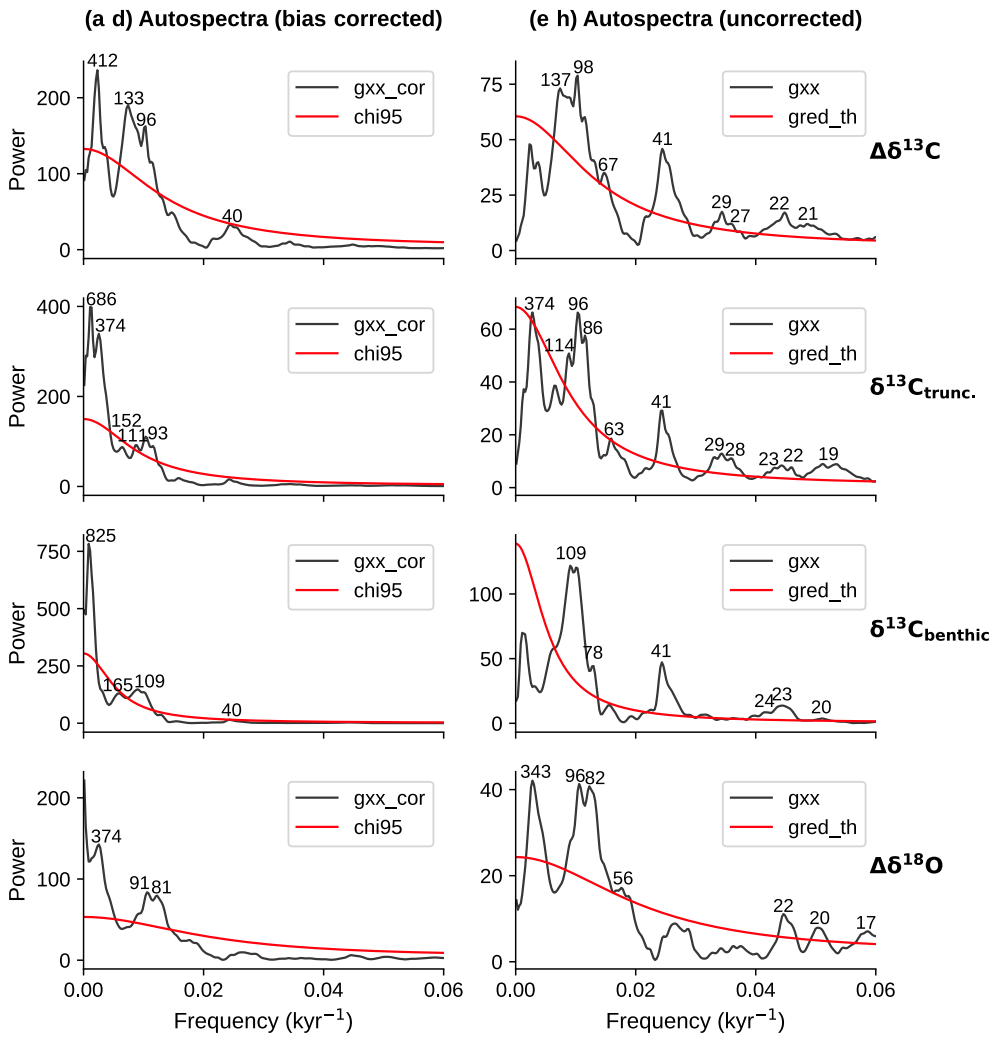

Figure 5.8: Results of spectral analysis of $\delta^{13}C_{trunc}$, δ^{13}Cbenthic, $\Delta\delta^{13}C_{(SAMW-CDW)}$ and $D\delta^{18}O$. **(a-d)** Bias-corrected Lomb-Scargle periodograms computed with REDFIT-X (Ólafsdóttir et al., 2016) with the 95% *chi*^{2} confidence level and significant peaks labelled (in kyr periods). **(e-h)** As for (a-d) but without bias-correction and with the theoretical red noise floor. **(i-l)** Cross-spectra against ETP (see text). **(n-o)** Coherency against ETP with 95% (red) and 99% (yellow) confidence levels given.

record (Ziegler et al., 2013; Charidemou, 2018) and so the focus here is therefore on longer timescales.

5.4.2 Frequency-domain results

Spectral analysis of the raw time series (Figure 5.8) reveals peaks at periodicities matching various orbital parameters (Laskar et al., 2004). Firstly, $\delta^{13}C_{trunc}$ displays peaks centred on 1/93, 1/111, 1/152, 1/374, and 1/686 kyr, each of which exceed the

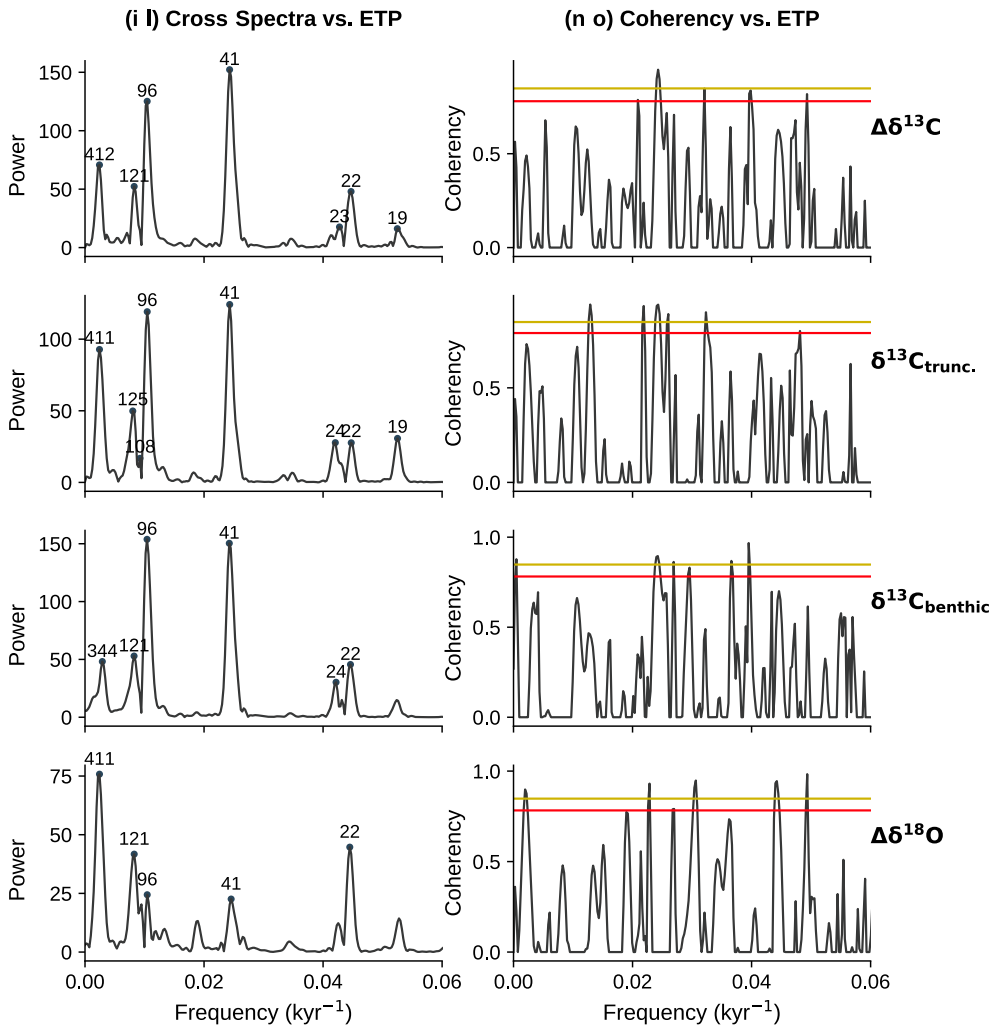

Figure 5.8 (Cont.)

95% chi^2 and 95% Monte-Carlo significance level. A further peak is visible above the noise floor at 1/41 kyr[‖], however this fails to exceed the chi^2 or Monte-Carlo confidence levels. Next, δ^{13}Cbenthic displays significant peaks at 1/40, 1/109, 1/165, and 1/825 kyr and $\Delta\delta^{13}C_{(SAMW-CDW)}$ displays significant peaks at 1/40, 1/96, 1/133, and 1/412 kyr. Due to the variable and, in places, low resolution of the time series, it is possible that high-frequency signals are lost or suppressed (aliasing), however cross-spectral and coherency analysis suggest that whilst not statistically significant in the auto-spectra of the full series, there is significant coherence between all three records and precession (Figure 5.8i-o). Discussions exist around the utility and performance

[‖]For each record, some higher-frequency peaks aligning with obliquity and precession bands are significant in the 'uncorrected' auto-spectra, however do not exceed chi^2 or Monte-Carlo significance levels when bias-corrected (Figure 5.8)

of various spectral density significance tests (e.g. Meyers, 2012) and I acknowledge the possibility of rejecting real peaks and accepting noise as significant; focus is instead given to the evolution of these cyclic components through time, using band-pass filtering.

5.5 Discussion: Interpreting $\delta^{13}C$

5.5.1 Drivers of $\delta^{13}C_{SAMW}$ and $\Delta\delta^{13}C_{(SAMW-CDW)}$

$\Delta\delta^{13}C_{(SAMW-CDW)}$ reflects the degree of similarity between foraminiferal calcite precipitated by *G. truncatulinoides* in SAMW and *C. wuellerstorfi* in CDW. The $\delta^{13}C_{DIC}$ of deep waters at the Agulhas Plateau has been shown to strongly reflect variations in deep water-mass provenance on glacial-interglacial timescales (Starr et al., 2021), in turn 'faithfully' recorded by *C. wuellerstorfi* (Schmittner et al., 2017). However the controls on $\delta^{13}C_{trunc}$ are less clear. Firstly, the carbon isotope composition of DIC in SAMW ($\delta^{13}C_{SAMW}$) can be affected by multiple processes which may be difficult to untangle. Secondly, fractionation during the calcification of *G. truncatulinoides* shells can augment the signal of SAMW that is archived in $\delta^{13}C_{trunc}$.

The isotopic composition of DIC in the ocean is a function of (1) biological export of ^{12}C from surface to deep; (2) air-sea exchange between ocean and atmospheric carbon; and (3) the mixing of water masses with different $\delta^{13}C$ signatures. Taking $\delta^{13}C_{SAMW}$ as an example, these processes can be decomposed (and simplified) as follows:

$$\delta^{13}C_{SAMW} = \delta^{13}C_{preformed} + \delta^{13}C_{biology} \tag{5.1}$$

$$\delta^{13}C_{preformed} = \delta^{13}C_{air-sea} + \delta^{13}C_{source} \tag{5.2}$$

$$\delta^{13}C_{air-sea} = f(air-sea fractionation, temperature) + \delta^{13}C_{atm} \tag{5.3}$$

In this framework, $\delta^{13}C_{SAMW}$ subducted in the Southern Ocean is controlled by biological fractionation ($\delta^{13}C_{biology}$), fractionation during air-sea exchange ($\delta^{13}C_{air-sea}$;

itself a function of temperature and atmospheric $\delta^{13}C_{atm}$) and the $\delta^{13}C$ of the source water mass (i.e. strength and signature of upwelling CDW; $\delta^{13}C_{source}$). In order to interpret records of past $\delta^{13}C$, it is important to first consider these potentially confounding drivers.

5.5.2 Driver 1: Biological fractionation

Equation (1.1) shows that $\delta^{13}C_{SAMW}$ is driven by a combination of preformed $\delta^{13}C$ and biological activity. Early studies attributed the vertical fractionation of carbon isotopes in the ocean to biological productivity (export of ^{13}C-depleted carbon from the shallow to deep ocean; Kroopnick, 1985), in particular during glacial times (e.g. Broecker, 1982). But is biology the primary driver of $\delta^{13}C_{SAMW}$ and $\Delta\delta^{13}C_{(SAMW-CDW)}$ observed in this study? Multiple lines of evidence exist for an increase in SAZ productivity under glacial conditions: nitrogen isotopes (Martínez-García et al., 2014) suggest a more complete utilization of nutrients, and regional increases in the flux of biogenic detritus and associated minerals imply an increase in the export of carbon to the deep (Kohfeld et al., 2005). Whilst results from the wider Southern Ocean show that productivity decreased in the glacial Antarctic Zone (Jaccard et al., 2013), increased biological export in the SAZ is coherent with a stronger chemocline between SAMW and the deep ocean (Ziegler et al., 2013). Furthermore, a more isolated lower overturning cell (Toggweiler, 1999) would act to amplify the impact of biological export on $\Delta\delta^{13}C_{(SAMW-CDW)}$ by effectively trapping respired carbon in the deep ocean.

The role of biological export in at least partially driving $\Delta\delta^{13}C_{(SAMW-CDW)}$ during Late Pleistocene glacial conditions is therefore well constrained, however further back in time, as fewer records are available, the picture becomes more ambiguous. For example, whilst there is evidence for elevated productivity in the SAZ during glacials of at least the last 1.5 Ma (Martínez-Garcia et al., 2011; Diekmann and Kuhn, 2002), no single productivity record can explain the $\Delta\delta^{13}C_{(SAMW-CDW)}$ record presented here completely. It may be that $\Delta\delta^{13}C_{(SAMW-CDW)}$ integrates a larger area of the Southern Ocean than is captured by biomarker and organic carbon accumulation from a single location. For example, organic biomarker records from the Agulhas

Plateau (Tangunan et al., 2021; Cartagena-Sierra et al., 2021) show some similarity to $\Delta\delta^{13}C_{(SAMW-CDW)}$, but also diverge across given intervals (such as the MPT), possibly due to regional differences in SAZ productivity. The utility of biological explanations for the long-term modulation of $\Delta\delta^{13}C_{(SAMW-CDW)}$ is discussed in more detail below.

5.5.3 Driver 2: Source water composition

In addition to biological fractionation, $\delta^{13}C_{SAMW}$ is also controlled by the 'preformed' $\delta^{13}C_{DIC}$ in the SAZ. This is a function of air-sea fractionation effects (see below) and the $\delta^{13}C$ of waters entering the SAZ from the south. For example, as CDW upwells around Antarctica it brings to the surface old, ^{13}C-depleted carbon from the deep. Northward Ekman transport advects this water into the SAZ where it undergoes water mass transformation (forming SAMW or Antarctic Intermediate Water). Therefore, if CDW upwelling intensifies, $\delta^{13}C_{SAMW}$ should become more similar to $\delta^{13}C_{CDW}$. This signal would then be propagated through much of the global thermocline (Ninnemann and Charles, 1997). This scenario has been proposed to explain the widespread deglacial minima in planktic $\delta^{13}C$ records (Spero and Lea, 2002) and the varying intensity of deglacial carbon isotope minima between basins has even been used to infer the major loci of upwelling around Antarctica (Hu et al., 2020). Moreover, this upwelling pulse has been linked to a negative excursion in $\delta^{13}C_{atm}$ during at least the two most recent deglaciations (Schmitt et al., 2012), due to the injection of ^{13}C-depleted carbon into the atmosphere. Conversely, Lynch-Stieglitz et al. (2019) show that a Southern Ocean origin for the deglacial planktic $\delta^{13}C$ minima may not be so clear, proposing that these excursions are instead related to the imprint of ^{13}C-depleted atmospheric CO_2 on the surface ocean through air-sea exchange. Whilst this may be the case for the North Atlantic, the intensity and $\delta^{13}C$ composition of Southern Ocean upwelling will nevertheless influence the $\delta^{13}C_{SAMW}$ due to the close oceanographic connection between the two. Moreover, even without a change in upwelling strength, the proportion of NADW in upwelled CDW will alter the source water $\delta^{13}C$ composition, although this would also be reflected in $\delta^{13}C_{benthic}$ at the AP_{comp} and should be inconsequential for $\Delta\delta^{13}C_{(SAMW-CDW)}$.

5.5.4 Driver 3: Air-sea fractionation

As shown in equation (1.2), the effect of air-sea exchange on the $\delta^{13}C_{SAMW}$ (and hence $\Delta\delta^{13}C_{(SAMW-CDW)}$) must also be considered. In the modern ocean, the temperature dependent fractionation during air-sea exchange causes SAMW to be relatively enriched in $\delta^{13}C$ compared to global nutrient stoichiometry (Lynch-Stieglitz et al., 1995). For changes in $\delta^{13}C_{SAMW}$ and $\Delta\delta^{13}C_{(SAMW-CDW)}$ to be attributed to non-thermodynamic processes, the ambient temperature of SAMW would therefore need to remain relatively constant over the past 1.5 Ma. Following Ziegler et al. (2013), the temperature of calcification can be approximated from the gradient between $\delta^{18}O_{trunc}$ and $\delta^{18}O_{benthic}$ ($\Delta\delta^{18}O$). This relies on the assumption that the temperature component of $\delta^{18}O_{benthic}$ was relatively constant in the past, supported by records of bottom water temperatures from the Pacific Ocean (Elderfield et al., 2012; Ford and Raymo, 2019) which remained near-freezing for most of the interval in question. Using the approximate 0.25‰/1^oC relationship between $\delta^{18}O$ and temperature (Kim and O'Neil, 1997), the calcification temperature anomaly (from the Holocene mean) can be approximated. The resulting ΔT estimate shows a long-term trend, decreasing by $\sim 1.2^oC$ per Ma (Figure 5.9b), in agreement with the intermediate water temperature record of McClymont et al. (2016) showing a 1.8^oC per Ma decrease over this interval (Figure 5.9c). Finally, to convert this into $\delta^{13}C_{air-sea}$, the 0.1‰ per 1^oC change in temperature relationship is used (Mook et al., 1974).

The resulting estimate (Figure 5.9b) implies that the air-sea fractionation effect on $\delta^{13}C_{trunc}$ was most extreme at MIS 4 (+0.5‰) and MIS 20 (+0.4‰), both characterized by low $\delta^{18}O$, possibly driven by colder SAMW. Aside from these excursions, glacial-interglacial $\delta^{13}C_{air-sea}$ variations are small (on the order of ~0.2‰) and when the estimated $\delta^{13}C_{air-sea}$ is subtracted from $\delta^{13}C_{trunc}$, changes to $\Delta\delta^{13}C_{(SAMW-CDW)}$ are also small (<0.25‰ excluding MIS 4 and MIS 20). Little influence of air-sea exchange on $\delta^{13}C_{trunc}$ is consistent with previous findings for the past 350 kyr (Ziegler et al., 2013) and with the relatively small changes in temperature reconstructed for the surface Southern Ocean during past glacial intervals (e.g. Waelbroeck et al., 2009). The influence of air-sea exchange on glacial-interglacial AP_{comp} $\Delta\delta^{13}C_{(SAMW-CDW)}$ variations is considered to be small, with exceptions during MIS 4 and MIS 20. That

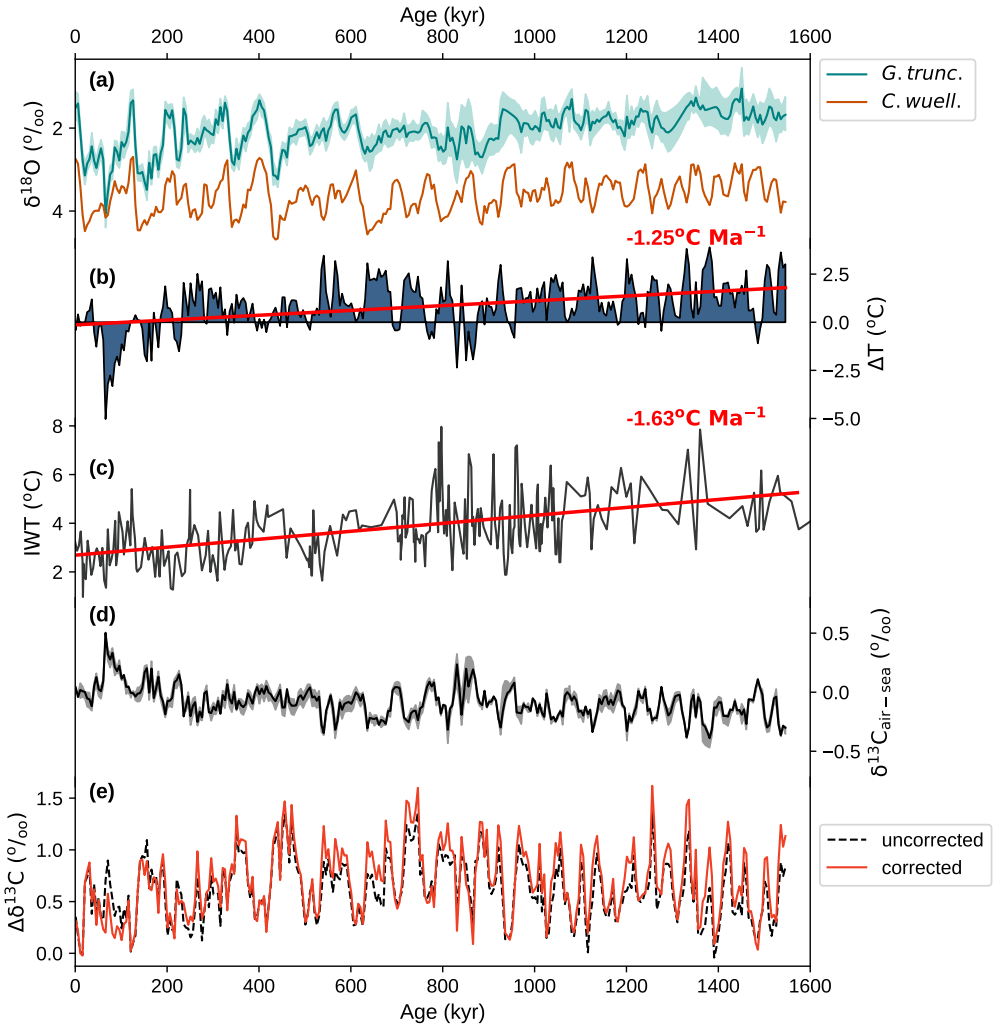

Figure 5.9: Estimating the thermodynamic influence on $\delta^{13}C_{trunc}$ and $\Delta\delta^{13}C_{(SAMW-CDW)}$. **(a)** $\delta^{18}O_{trunc}$ and $\delta^{18}O_{benthic}$ (PCHIP interpolated). **(b)** Estimated temperature anomaly from Holocene, derived from $\Delta\delta^{18}O$ (see text). **(c)** Intermediate Water Temperature (IWT) record from Deep Sea Drilling Project Site 593 (McClymont et al., 2016). Linear regressions through **(b)** and **(c)** are shown in red. **(d)** Estimated $\delta^{13}C_{air-sea}$ (derived from δT in panel (b) with 95% confidence intervals shaded. **(e)** $\Delta\delta^{13}C_{(SAMW-CDW)}$ uncorrected and corrected for $\delta^{13}C_{air-sea}$.

being said, there does appear to be a periodic component to the $\Delta\delta^{18}O$ (and hence ΔT) record, with a period of ~400 kyr. The possibility that the 1/400 kyr cycle in $\Delta\delta^{13}C_{(SAMW-CDW)}$ is of thermodynamic origin is discussed below.

5.5.5 Departures from equilibrium in $\delta^{13}C_{G.trunc.}$

In addition to multiple factors influencing $\delta^{13}C_{SAMW}$, foraminifera do not always calcify in equilibrium with seawater DIC. For example, calcification at lower temper-

ature decreases the metabolic uptake of ^{12}C, increasing $\delta^{13}C$ (Bemis et al., 2000), and higher carbonate ion concentrations have been shown to decrease $\delta^{13}C$ (Spero et al., 1997). Further departures from equilibrium can be introduced by physiological processes such as respiration (Spero et al., 1991). However, core-top studies from the south-west Pacific (Hu et al., 2020; Charidemou, 2018) and Indian Ocean (Williams et al., 1977) show that *G. truncatulinoides* largely reflect the $\delta^{13}C_{DIC}$ in the surrounding seawater, with departures from equilibrium of no more than 0.6‰. *G. truncatulinoides* in the modern ocean is therefore a fairly good recorder of $\delta^{13}C_{DIC}$ across a relatively large temperature range. That being said, changes in foraminifera diet and carbonate chemistry (Kohfeld et al., 2000) cannot be ruled out as influencing past $\delta^{13}C_{trunc}$

5.6 Discussion: Trends and Cycles in $\Delta\delta^{13}C_{(SAMW-CDW)}$

5.6.1 Glacial-Interglacial variations

$\Delta\delta^{13}C_{(SAMW-CDW)}$ at the Agulhas Plateau likely integrates multiple processes which effect the vertical partitioning of carbon and nutrients in the ocean (Morée et al., 2018). During glacial intervals, the isolation of the lower cell of overturning circulation coupled with the production, export and remineralization of organic matter resulted in the accumulation of DIC in the deep (Muglia et al., 2018). For this isolation of respired carbon to be effective at reducing pCO_2 the efficiency of biological productivity in the SAZ, where respired nutrients and carbon are upwelled to the surface, must also be called upon. Increased (decreased) utilization of nutrients in this region can therefore promote decreased (increased) efflux of carbon into the atmosphere.

Since the pioneering work of Martin (1990), much attention has been paid to role of iron in stimulating increased Southern Ocean productivity during glacial intervals. In the modern Southern Ocean (as with other 'High-Nutrient Low-Chlorophyll' regions), iron is acts as a limiting nutrient in phytoplankton growth, meaning that an increased supply of iron (such as from wind-blown dust) during glacial intervals

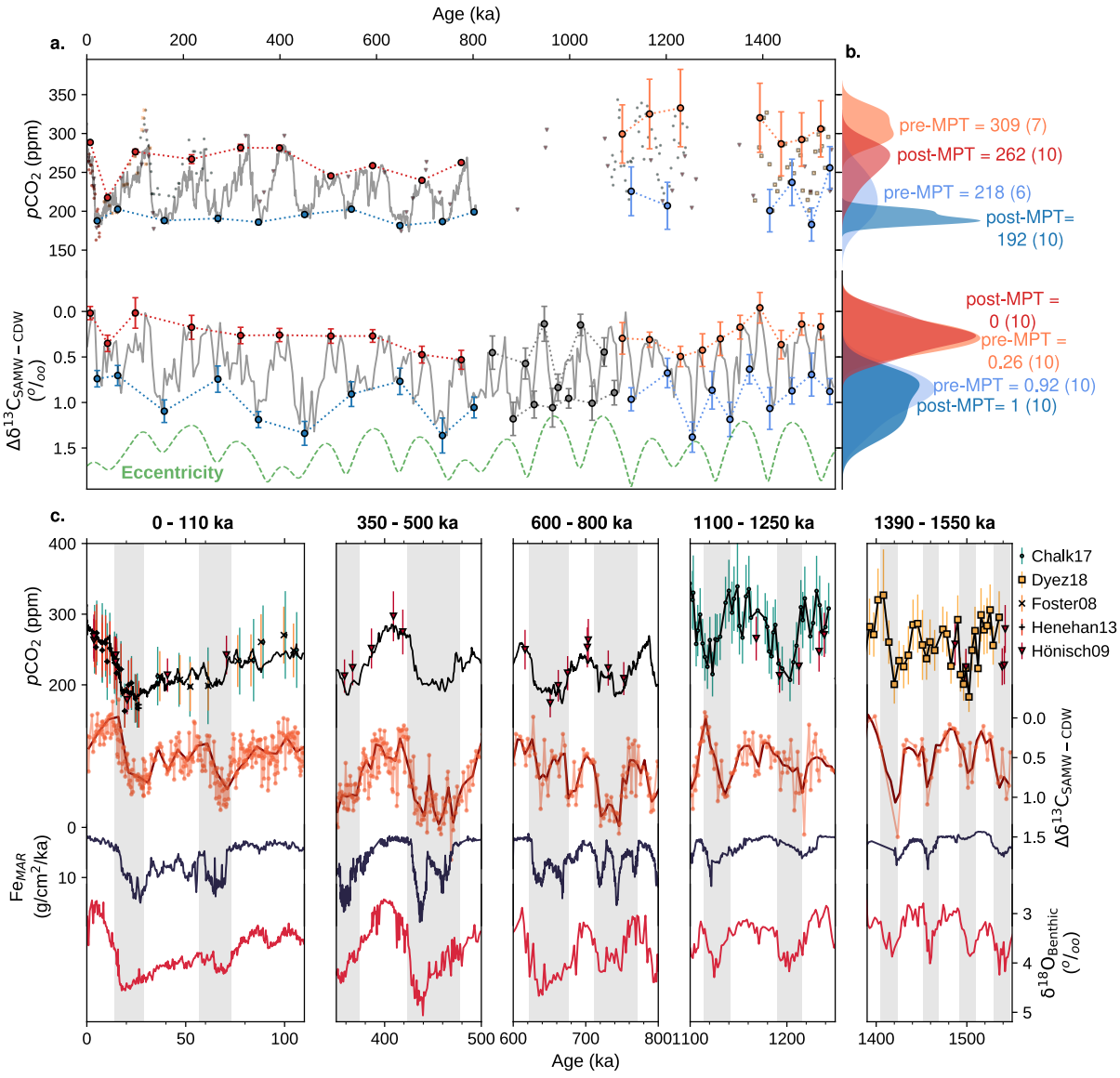

Figure 5.10: **(a)** Records of pCO_2 from the EPICA Dome C ice core (Masson-Delmotte et al., 2010) and sediment core boron isotope reconstructions, with $\Delta\delta^{13}C_{(SAMW-CDW)}$ (this study) and orbital eccentricity (green, dashed; Laskar et al., 2004). Original data are given in grey and maximum (minimum) values for $\Delta\delta^{13}C_{(SAMW-CDW)}$ (pCO_2) each glacial MIS are shown as blue circles with 95% confidence error bars. Orange/red circles show the same but for minimum (maximum) interglacial $\Delta\delta^{13}C_{(SAMW-CDW)}$ (pCO_2) values. **(b)** Kernel density estimates for glacial (blues) and interglacial (reds) pCO_2 (upper) and $\Delta\delta^{13}C_{(SAMW-CDW)}$ (lower) before and after the MPT. **(c)** Time slice panels showing ice core (black line; Masson-Delmotte et al., 2010, and references therein) and boron-isotope based sediment core (markers; Chalk et al., 2017; Dyez et al., 2018; Foster, 2008; Henehan et al., 2013; Honisch et al., 2009) reconstructions of pCO_2. $\Delta\delta^{13}C_{(SAMW-CDW)}$ is shown in orange (PCHIP smoothed overlay in dark orange), iron accumulation from ODP Site 1090 is shown in navy (Martínez-Garcia et al., 2011) and $\delta^{18}O_{(benthic)}$ from the AP_{comp} is shown in pink.

might increase productivity (Watson et al., 2000). Ziegler et al. (2013) show that $\Delta\delta^{13}C_{(SAMW-CDW)}$ maxima over the past 350 ka coincide with peaks in dust accumulation in the South Atlantic and Antarctic ice cores. However, bioavilable iron can also be supplied to the surface Southern Ocean through deep mixing (Tagliabue et al., 2014), sedimentary and hydrothermal fluxes (Sieber et al., 2021), and even iceberg melt (Raiswell et al., 2008). Untangling these sources in paleoclimate records is challenging because environmental changes can favour different mechanisms simultaneously (e.g. a shift in the westerly wind belt might increase dust deposition in the northern SAZ whilst also enhancing iceberg drift to the region). That being said, there is a large body of evidence attributing iron-fertilization to dust fluxes, especially in the Atlantic Southern Ocean (e.g. Shoenfelt et al., 2018; Anderson et al., 2014). Figure 5.10 shows that across glacial-interglacial cycles, $\Delta\delta^{13}C_{(SAMW-CDW)}$ covaries with the accumulation of iron at ODP Site 1090 (Martínez-Garcia et al., 2011), with high iron during glacial intervals matching high $\Delta\delta^{13}C_{(SAMW-CDW)}$. However, the magnitude of glacial-interglacial fluctuations in $\Delta\delta^{13}C_{(SAMW-CDW)}$ is relativity large relative to iron accumulation during early cycles (before the MPT).

Furthermore, the inference of a stronger glacial chemocline linked to Southern Ocean iron fertilization would also carry implications for pCO_2 levels. Whilst such a link is visible on shorter timescales (Figure 5.10c), it again breaks down when viewed across the MPT (Figure 5.10a-b). For example, average glacial pCO_2 decreased by between 20-40 ppm across the MPT (Figure 5.10b; Chalk et al., 2017; Honisch et al., 2009) whilst no statistically significant change in $\Delta\delta^{13}C_{(SAMW-CDW)}$ is evident. As discussed above, multiple factors can influence $\Delta\delta^{13}C_{(SAMW-CDW)}$, such as air-sea fractionation and circulation changes. However, both the long-term cooling trend (as estimated from $\Delta\delta^{18}O$; Figure 5.9) and observed changes in deep water-mass geometry (e.g. Pena and Goldstein, 2014) across this interval would theoretically increase the gradient between SAMW and CDW, rather than cancel out the increase that one might expect to accompany lower pCO_2. It may be the case that changes in stratification/-circulation not revealed by $\Delta\delta^{13}C_{(SAMW-CDW)}$ are responsible for the sequestration of carbon across the MPT, however it appears that transitions in the intermediate-deep (Hodell and Venz-Curtis, 2006) or Atlantic - Pacific (Raymo et al., 1997) carbon isotope gradient preceded the proposed MPT pCO_2 decline (Chalk et al., 2017; Honisch

et al., 2009) by >200 kyr. Moreover, a decoupling between $\Delta\delta^{13}C_{(SAMW-CDW)}$ and pCO_2 between different glacial intervals appears to be related to the presence of long cycles modulating $\Delta\delta^{13}C_{(SAMW-CDW)}$ (Figure 5.10a).

5.6.2 (Quasi-) 1/400 kyr cycles

The dominant low-frequency signal in the $\Delta\delta^{13}C_{(SAMW-CDW)}$ and $\delta^{13}C_{trunc}$ records presented here is centred ~1/400 kyr (Figure 5.8), coinciding with cycles in Earth's long eccentricity in the same frequency band. Orbital eccentricity exerts a relatively small influence on annual mean insolation, and its effect on climate is instead predominantly through its modulation of precession (Laepple and Lohmann, 2009). It follows that eccentricity forcing is classically associated with low-latitude climate systems (Berger et al., 2006). *How does a seemingly low-latitude forcing influence the long-term evolution of Agulhas Plateau $\Delta\delta^{13}C_{(SAMW-CDW)}$?*

A pervasive link between long eccentricity forcing and changes in the oceanic carbon reservoir has been identified at multiple times throughout the Cenozoic (Holbourn et al., 2007; Wang et al., 2010). However, the 1/400 kyr cycles present in many Early Pleistocene oceanic carbon cycle records become obscured during the Mid- to Late Pleistocene (Wang et al., 2010), lengthening towards a ~500 kyr periodicity and distorting the phase relationship with eccentricity (Figure 5.11). Whilst this transition (and loss of 1/400 kyr cyclicity) is evident in the AP_{comp} $\delta^{13}C_{benthic}$ record, both the $\delta^{13}C_{trunc}$ and $\Delta\delta^{13}C_{(SAMW-CDW)}$ records maintain a ~1/400 kyr component throughout (Figure 5.12). Furthermore, records of secular changes in coccolithophore production (Rickaby et al., 2007) and carbonate accumulation/dissolution (Bassinot et al., 1994; Barker et al., 2006) appear to align more closely with these quasi-500 kyr period carbon cycle fluctuations than with the 400 kyr eccentricity cycle *sensu stricto* (Figure 5.11). This is best shown in the timing of carbon isotope maximum events (Cmax II and Cmax III; Figure 5.11) identified by Wang et al. (2004), thought to embody whole-ocean carbon cycle shifts. These maxima are spaced by ~500 kyr following 1.2 Ma and are out of phase with 1/400 kyr-band eccentricity minima and $\Delta\delta^{13}C_{(SAMW-CDW)}$ maxima. This suggests that the long term fluctuations in the global

carbon cycle outlined above are either unrelated or obscured relative to the long eccentricity modulation of AP_{comp} $\Delta\delta^{13}C_{(SAMW-CDW)}$.

One explanation for this link might be through SAZ primary productivity. For example, during the high eccentricity interval from 500 - 700 ka, biomarker accumulation in the AP_{comp} (Cartagena-Sierra et al., 2021) was reduced relative to the low eccentricity interval which followed. However, this relationship breaks down during the eccentricity high at ~1 Ma, where primary production appears to be enhanced. It is important to note that whilst the AP_{comp} biomarker accumulation record shows a cross-spectral density peak at ~1/400kyr when compared to ETP, it does not have statistically significant auto-spectral peak at this frequency. Furthermore, records of Southern Ocean productivity and iron supply (Martínez-Garcia et al., 2011) show a glacial increase across the MPT, whereas pre-MPT glacial $\Delta\delta^{13}C_{(SAMW-CDW)}$ is equally as high as during post-MPT glacials (Figure 5.10). The long-term trends in Southern Ocean productivity are difficult to reconcile with long-term modulation of $\Delta\delta^{13}C_{(SAMW-CDW)}$, suggesting that a straightforward productivity explanation is unlikely.

Could there instead be a low-latitude productivity signal? SAMW at the Agulhas Plateau is likely a mixture between 'new' SAMW from the SAZ to the south, and subtropical mode waters transported in the Agulhas Current (re-circulated SAMW or Subtropical Mode Water; Koch-Larrouy et al., 2010). Changing the $\delta^{13}C$ of the subtropical mode water component could therefore alter $\Delta\delta^{13}C_{(SAMW-CDW)}$ at the Agulhas Plateau. Biological productivity in the low-latitude Indian Ocean might respond to eccentricity either directly by insolation cycles or by nutrient run-off related to the African or South Asian Monsoon systems (Wang et al., 2004). One might expect increased export productivity in the Indian Ocean to cumulatively enrich ^{13}C in the recirculated/subtropical mode water, resulting in ^{13}C-enriched mode water at the Agulhas Plateau and thus a stronger gradient. However, primary productivity in the equatorial Indian Ocean responds to eccentricity with an opposite phase compared to $\Delta\delta^{13}C_{(SAMW-CDW)}$ because high local insolation (modulated by intervals of high eccentricity) is shown to drive higher productivity (Beaufort et al., 1997; Tangunan et al., 2017). Moreover, much of the subtropical Indian Ocean through which SAMW spreads is highly oligotrophic, with exceptionally low organic matter export (Harms

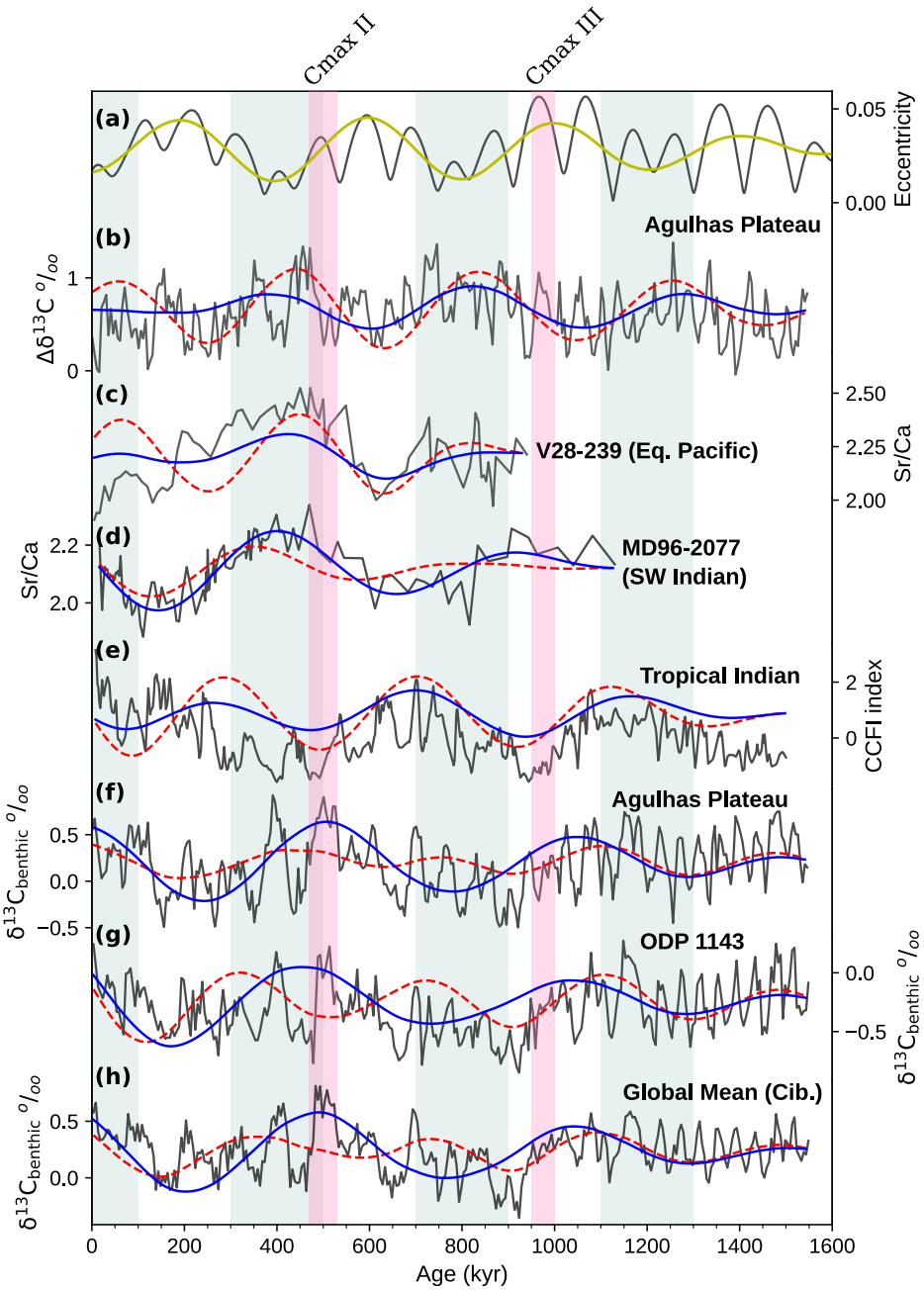

Figure 5.11: Quasi-1/400 kyr cycles in Pleistocene carbon cycle records. **(a)** Full eccentricity (grey) and 1/400 kyr component (yellow) from Laskar et al. (2004). **(b)** AP_{comp} $\Delta\delta^{13}C_{(SAMW-CDW)}$ (this study), **(c-d)** Sr/Ca from the equatorial Pacific (c) and south-west Indian Ocean ((d); Rickaby et al., 2007). **(e)** Composite Coarse Fraction Index (CCFI) from the tropical Indian Ocean (Bassinot et al., 1994). **(f-g)** $\delta^{13}C_{benthic}$ from the AP_{comp} (f), South China Sea ((g); Wang et al., 2004), and global mean of all sites spanning this interval (h; see Chapter 2). Solid blue lines show a 1/500 kyr bandpass filter and dashed red lines show 1/400 kyr bandpass filter. Vertical blue shading highlights intervals of low eccentricity (in the 1/400 kyr band) and vertical pink shading shows the carbon isotope maxima events identified by Wang et al. (2004)

et al., 2021). Based on this reasoning, it is unlikely that the 1/400 kyr modulation of $\Delta\delta^{13}C_{(SAMW-CDW)}$ can be attributed to primary productivity at low-latitudes.

5.6.3 The Hadley Cell connection

Perhaps the most informative comparison to make in exploring eccentricity modulation of $\Delta\delta^{13}C_{(SAMW-CDW)}$ is the co-registered $\Delta\delta^{18}O$ record. As described above, spectral analysis of this time series reveals a statistically significant 1/374 kyr peak (indistinguishable from 1/400 kyr at the frequency bandwidth of the analysis). At times of high $\Delta\delta^{13}C_{(SAMW-CDW)}$ (in the 1/400 kyr band), $\Delta\delta^{18}O$ is closer to zero, suggesting that *G. truncatulinoides* (SAMW) and *C. wuellerstorfi* (CDW) were calcifying in water more similar in temperature, $\delta^{18}O_{seawater}$, or both. Lower SAMW temperatures might influence $\delta^{13}C_{trunc}$ in a number of ways. Firstly, air-sea exchange at lower temperatures would leave the surface water more enriched in ^{13}C (see above), although one would expect to see these periodicities in direct temperature proxy records from the SAZ (c.f. Martínez-Garcia et al., 2011; Cartagena-Sierra et al., 2021). Secondly, the colder calcification temperature of *G. truncatulinoides* might result in a higher $\delta^{13}C_{trunc}$ relative to $\delta^{13}C_{DIC}$ due to temperature-sensitive metabolic effects (Bemis et al., 2000).

In addition, changes in $\delta^{13}C_{DIC}$ of the mode waters present at the Agulhas Plateau might provide an explanation. For example, modifying the export of SAMW from the Southern Ocean might alter the mixture of 'new' SAMW (high $\delta^{13}C$; cold; low $\delta^{18}O$) and 'old' subtropical mode water (low $\delta^{13}C$; warmer; high $\delta^{18}O$) present at the Agulhas Plateau. SAMW formation occurs through deep winter-time convection, which is intricately linked to air-sea fluxes in the Southern Ocean (e.g. Sallée et al., 2006). Processes which introduce instabilities into the surface ocean in regions of SAMW formation, such as cross-frontal mixing (Rintoul and England, 2002; Dong et al., 2008; Koch-Larrouy et al., 2010), have also been shown to promote the convection of SAMW. Interestingly, an imprint of long eccentricity on frontal dynamics in the Southern Ocean has been previously proposed (Bard and Rickaby, 2009; Caley et al., 2012; Starr et al., 2021); in the next section I review the evidence for such a

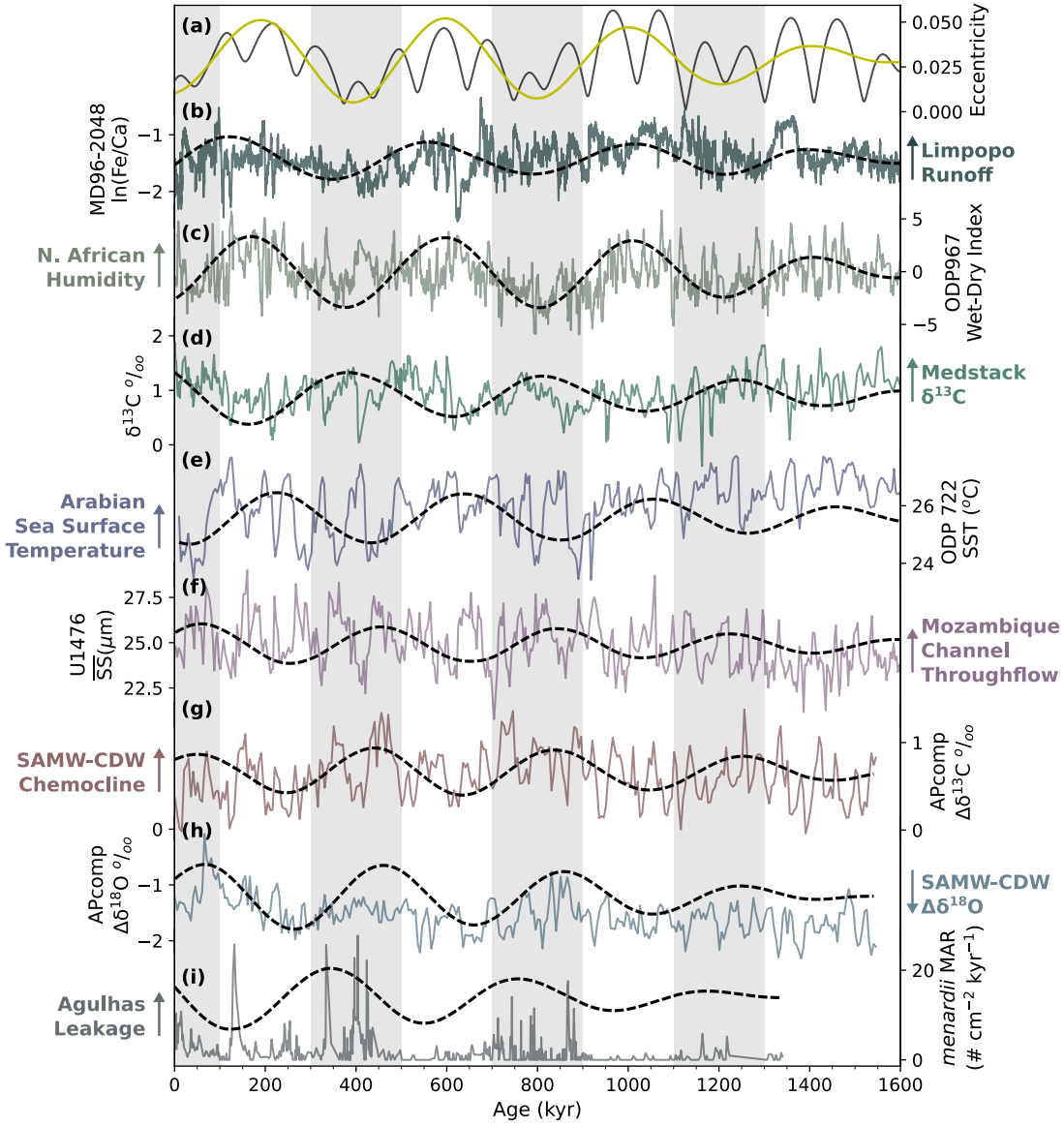

Figure 5.12: **(a)** Full eccentricity (grey) and 1/400 kyr component (yellow) from Laskar et al. (2004). **(b)** Limpopo run-off record from MD96-2048 (Caley et al., 2018), **(c)** Wet-Dry index from ODP Site 967 in the Mediterranean (Grant et al., 2017), **(d)** 'Med-stack' $\delta^{13}C_{planktic}$ composite record (Wang et al., 2010), **(e)** Alkenone-derived sea surface temperature record from ODP Site 722 (Herbert et al., 2010), **(f)** IODP Site U1476 $\overline{SS}$ record (van der Lubbe et al., *manuscript accepted*), **(g)** $\Delta\delta^{13}C_{(SAMW-CDW)}$ Ziegler et al. (this study; 2013), $\Delta\delta^{18}O_{(SAMW-CDW)}$ Ziegler et al. (this study; 2013), *Globorotalia menardii* accumulation at ODP Site 1087 (Caley et al., 2012)

link.

Bard and Rickaby (2009) describe a scenario whereby low eccentricity truncates low latitude insolation maxima, reducing the intensity of the Hadley Cell and 'drawing the STF northward'. Moreover, Yin (2013) shows that the latitudinal pressure gradient (i.e. the difference in intensity between the subpolar high and subtropical low) is dominated by the insolation gradient during Austral winter, which in turn is modulated by eccentricity. This could plausibly introduce a 400 kyr periodicity into records of Southern Ocean frontal dynamics (Caley et al., 2012; Bard and Rickaby, 2009). Equatorward expansion of the SAZ has been shown to result in the advection of cold, (sub)Antarctic surface waters into the south-west Indian Ocean subtropical gyre, leading to cooling of the upstream Agulhas Current (Simon et al., 2013). This might explain the close covariation between $\Delta\delta^{13}C_{(SAMW-CDW)}$ and sea surface temperature off the coast of south-eastern Africa over the past 800 kyr (Bard and Rickaby, 2009). Moreover, there is evidence for a ~1/400 kyr cyclicity, albeit weak, in the AP_{comp} IRD record (Starr et al., 2021), however the additional influence of high-latitude processes (i.e. Antarctic Ice Sheet dynamics) likely obscures this relationship substantially. A mechanism which influences Southern Ocean front dynamics might also be expected to influence records of circum-Antarctic flow-speed (associated with the Antarctic Circumpolar Current), however no such 1/400 kyr cyclicity is present in the co-registered AP_{comp} $\overline{\mathbf{SS}}$ record (Chapter 6). As elaborated on in the next chapter, this may relate to a decoupling between the Polar Front, the Subantarctic Front, and the Subtropical Front; records of surface hydrography reflecting the STF (Cartagena-Sierra et al., 2021) vary differently to $\overline{\mathbf{SS}}$ during certain intervals in the Pleistocene.

With these caveats in mind, a tentative mechanism might operate as follows:

1. Low eccentricity results in lower maximum equatorial insolation;
2. This reduces the latitudinal pressure gradient, weakening the Hadley Cell;
3. The resulting equator-ward migration of Southern Ocean fronts increases cross-frontal mixing, introducing; instabilities in the upper water column of the south-west Indian Ocean;

4. This favours deep winter convection, increasing the subduction of SAMW;

5. More SAMW fills the Indian Ocean thermocline, resulting a more enriched ($\delta^{13}C$) mode water mass at the Agulhas Plateau;

Is there evidence supporting a 400 kyr periodicity in records reflecting atmospheric circulation patterns? A persistent long eccentricity imprint on African hydro-climate is revealed in proxy records of Limpopo River run-off (Figure 5.12b; Caley et al., 2018), wet-dry cycles in the Saraho-Arabian dust belt (Figure 5.12c; Grant et al., 2017; Larrasoaña et al., 2003), and Mediterranean $\delta^{13}C_{planktic}$ (Figure 5.12d Wang et al., 2010) through the Pleistocene. In northern Africa, this imprint has been linked to low eccentricity suppressing the maximum low latitude insolation and the aridification of the Saharo-Arabian dust belt (Trauth et al., 2009). In eastern (sub)tropical Africa, low (high) eccentricity is related to lower (higher) rainfall due to migrations in the rain belt associated with the ITCZ (and hence the Hadley Cell Caley et al., 2018; Chase, 2021). Finally, 1/400 kyr cyclicity in a record of Mozambique Channel Throughflow (Figure 5.12f; van der Lubbe et al., *in press*) supports a sensitivity of atmospheric (and ocean) circulation in the Indian Ocean to long eccentricity. As shown by Li et al. (2017), there is a persistent 1/400 kyr periodicity in the zonal Pacific temperature gradient, tightly linked to the circulation modes in the Indian Ocean which drive Mozambique Channel Throughflow (van der Lubbe et al., *in press*). To summarise, there are multiple lines of proxy evidence for an imprint of long eccentricity cycles on atmosphere and ocean circulation around Africa.

5.7 Concluding remarks: Eccentricity and the carbon cycle?

Considering the central role ascribed to SAMW ventilation in ocean nutrient and carbon cycling (e.g. Khatiwala et al., 2009; Sarmiento et al., 2004), it is perhaps surprising to not see an equivalent 400 kyr periodicity in records of atmospheric CO_2 . The paradoxical decoupling between the oceanic carbon cycle and atmospheric CO_2 on ~400 kyr timescales has been previously discussed, for example by Barker et al. (2006) who suggest that high coccolithophore production during the low eccentricity

MBT interval might be essentially cancelled out by an increase in carbonate dissolution. An interesting proposition might arise from this to explain the decoupling of $\Delta\delta^{13}C$ and pCO_2, by relating the production of SAMW with an increase in (low latitude) biological productivity, counteracted by the resulting increase in mean ocean carbonate saturation state. This is because SAMW constitutes a primary vessel supplying nutrients from the surface Southern Ocean to much of the global low-latitude thermocline (Sarmiento et al., 2004). Perhaps during intervals of low eccentricity, an intensification of SAMW formation (due to the Hadley Cell contracting) transports more nutrients to the (sub)tropics, promoting an increase in carbonate production and also increasing carbonate dissolution (assuming no change in Ca^{2+} ion flux into the ocean), balancing out any potential change in pCO_2 from the organic carbon flux associated with coccolithophore production (Buitenhuis et al., 2001).

The ~1/400 kyr cycles in $\Delta\delta^{13}C$ presented here appear to provide support for a Southern Ocean driver of secular fluctuations in coccolithophore production (Rickaby et al., 2007). Furthermore, the obscured periodicity of long cycles in carbonate production (and dissolution; Figure 5.11) compared to the un-obscured cycles in $\Delta\delta^{13}C$ suggests there may be a non-linear sensitivity of coccolithophore production to mode water nutrient supply, rather directly to eccentricity itself (Rickaby et al., 2007).

5.7.1 Silicic Acid Leakage

To test the hypothesis that long-term fluctuations in SAMW formation driven by expansions and contractions of the Hadley Cell circulation might 'transfer' the 1/400 kyr eccentricity cycle into the oceanic carbon cycle, one would also need to consider the nutrient make-up of the SAMW being exported. For example, changes in the silicic acid content of SAMW has been proposed to exert an important control on the low-latitude productivity which mode water ventilation fuels: a high ratio of Si to macronutrients such as nitrate exported to the low latitude ocean will result in a dominance of diatom over coccolithophore productivity (a model known as the 'Silicic Acid Leakage Hypothesis (SALH); Matsumoto et al., 2002). This shift away from

calcifying to non-calcifying primary producers would in-turn reduce the ratio of inorganic to organic carbon (PIC:POC) of particulate carbon sinking to the seafloor, and therefore have a net lowering effect on atmospheric CO_2 levels (Matsumoto et al., 2002; Archer, 1991). Crosta et al. (2007) show that changes in the production of SAMW can complicate the effect of SALH on low latitude diatom productivity. For example if intervals of low surface Southern Ocean Si:Nitrate ratio coincide with intervals of enhanced SAMW subduction, the increase in absolute silicic acid supply would continue to support diatom productivity in spite of a lower nutrient ratio. In this chapter, I have shown that the production of SAMW may have varied on long, climatically-relevant timescales, highlighting the need for studies testing these the role for these hypotheses over climate transitions such as the MPT to consider variations in SAMW production, in addition to the ratio of nutrients in SAMW. The $\Delta\delta^{13}C$ record presented here is alone limited in its ability to test how changes in the Southern Ocean chemocline and SAMW dynamics on long eccentricity timescales influenced phytoplankton community structure and productivity elsewhere in the ocean; further investigation would benefit from reconstructions of coccolith versus diatom accumulation in conjunction with reconstructions of mode water circulation from sites spanning various regimes in the mid- to low-latitude ocean.

5.7.2 Conclusion

In conclusion, in this Chapter I propose that whilst glacial-interglacial variations in $\Delta\delta^{13}C_{(SAMW-CDW)}$ likely result predominantly from changes in biological productivity integrated over a large area of the Southern Ocean, there is a clear amplitude modulation by long eccentricity cycles (~400 kyr period). A similar signal in the record of $\Delta\delta^{18}O$ suggests that this response is related to changes in the formation or thermohaline properties of SAMW, although a role for thermodynamic effects on $\delta^{13}C$ or metabolic disequilibrium of $\delta^{13}C_{trunc}$ cannot be ruled out. Evidence for such a link between eccentricity and $\Delta\delta^{13}C_{(SAMW-CDW)}$ holds interesting implications for explaining records of carbonate production and dissolution in the ocean, however more work is required to elucidate the role of Southern Ocean mode water formation in low latitude carbonate production.

6 | Changes in Physical and Chemical Ventilation of Deep-Water in the SW Indian Ocean across Climate Transitions of the past 1.9 Million Years

6.1 Introduction

The role of ocean circulation in the global carbon cycle is well-documented. Perhaps the clearest demonstration of this can be seen during the last glacial cycle when lower atmospheric CO_2 levels were likely balanced by higher carbon storage in the deep ocean (Broecker, 1982). Paleoceanographic reconstructions reveal a 'chemical divide' at around 2000-2500m in the glacial ocean (Hodell et al., 2003; Mccorkle and Heggie, 1998), reflecting a build-up of respired carbon below this depth. The development of a chemocline in the glacial ocean corroborates a shift of nutrients and CO_2 from the shallow to the deep ocean, proposed in early studies to result from enhanced biological productivity (Broecker, 1982; Boyle, 1988). For this deep storage to persist, however, physical mechanisms acting to isolate the deep ocean from the surface (and atmosphere) must also be called upon (Toggweiler, 1999; Sigman and Boyle, 2000). In the modern ocean, deep water-masses (i.e. below around 2500m) are mostly exposed to the surface in the Southern Ocean by upwelling around Antarctica, the result of the predominantly wind-driven Antarctic Circumpolar Current* (ACC; Toggweiler and Samuels, 1993). The extent to which carbon entrained in this

*while classically considered a wind-driven current (e.g. Gill, 1968), an increased role for buoyancy forcing has been recognised in recent studies (Hogg, 2010)

upwelled water is released into the atmosphere depends on the thermodynamic and biological processes which follow (as discussed in Chapter 5), as well as physical processes impacting the exposure of deep-water to the surface.

Toggweiler et al. (2006) proposed that during glacial intervals, upwelling around Antarctica was reduced as a result of an equatorward displacement of the Southern Hemisphere westerly wind belt (hereafter referred to as SWWB). This coupling is also implicated in driving a surge of respired carbon out of the deep ocean during deglaciations (Anderson et al., 2009), possibly signifying the breakdown of the deep chemocline, although the timing of chemical and physical stratification changes paint a more complex deglacial picture (Roberts et al., 2016). Moreover, expanded sea-ice around Antarctica may have physically limited air-sea exchange in the high-latitude Southern Ocean during glacials (Stephens and Keeling, 2000), and may even have driven an expansion in the volume of Southern Ocean deep-waters at the expense of a shallower North Atlantic Deep Water (NADW) (Ferrari et al., 2014). In the modern Southern Ocean, the position and variability of sea-ice and the SWWB are intimately linked to the position of the ACC and the associated oceanic fronts (Orsi et al., 1995) along which the major flow-lines occur[†]. This emphasises the importance of complementing reconstructions of past ACC dynamics with reconstructions of Southern Ocean front and sea-ice evolution, although building a coherent interpretation from records of each component is often complex (e.g. Kohfeld et al., 2013) as the relationship between ocean flow, surface hydrography and sea-floor topography varies between different regions of the Southern Ocean (Graham et al., 2012).

Untangling the drivers of oceanic CO_2 storage on glacial-interglacial timescales requires a multitude of paleoceanographic reconstructions spanning a range of locations and water depths. Indeed, connecting physical drivers (e.g. SWWB, sea ice) to chemical (e.g. carbon and nutrient distributions) and physical (e.g. density stratification and flow speed) ocean properties continues to motivate research. Studies of this nature have thus far been limited on timescales spanning multiple glacial cycles and climate transitions. For example, evidence exists for a deep chemocline during most glacial periods of at least the last 1.5 Ma (Hodell et al., 2003), how-

[†]much of the ACC transport occurs in narrow jets along oceanic fronts (Sokolov and Rintoul, 2009)

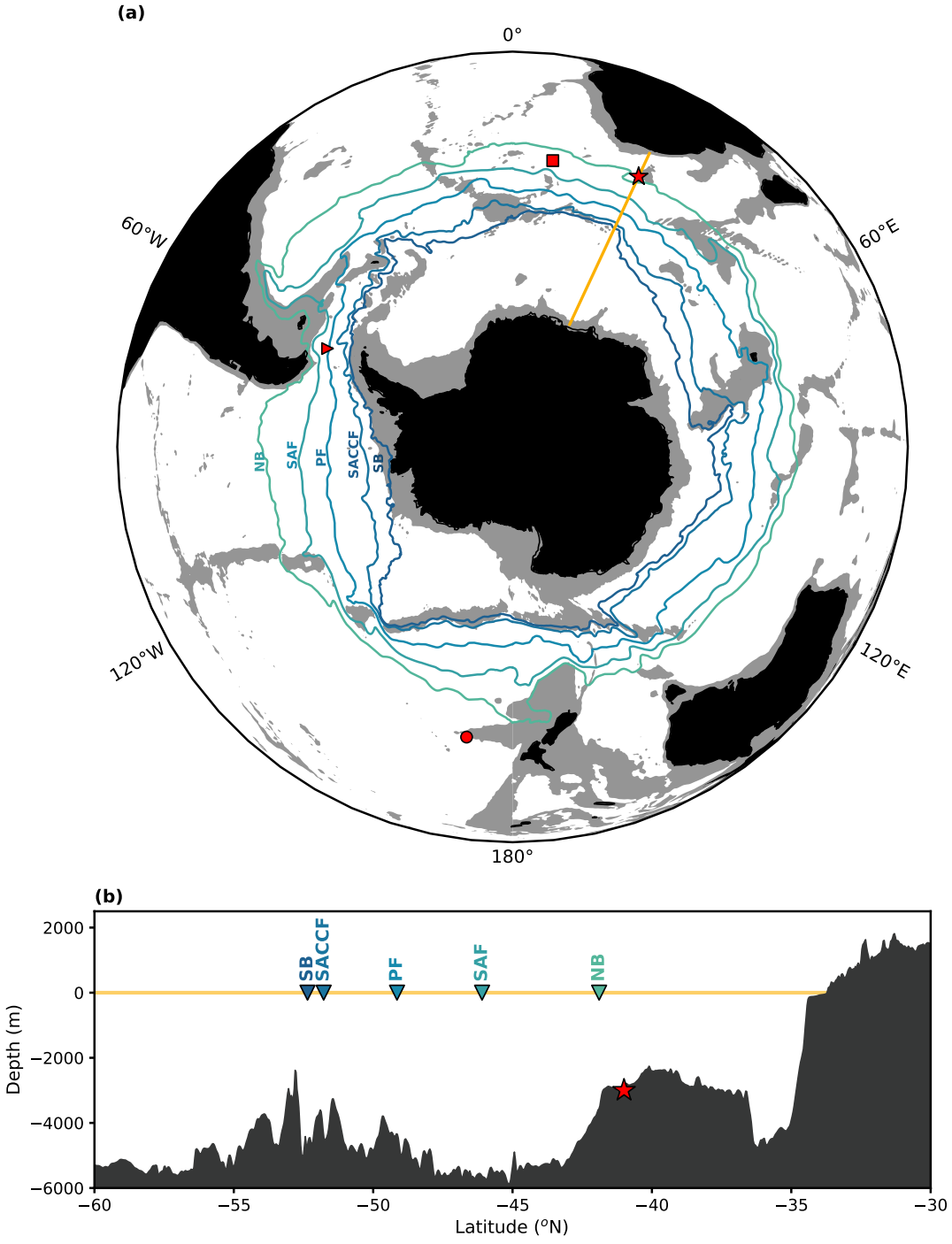

Figure 6.1: **(a)** Circum-Antarctic ocean fronts associated with the ACC as defined by Park et al. (2019): NB = Northern Boundary; SAF = Subantarctic Front; PF = Polar Front; SACCF = southern ACC Front; SB = southern Boundary. A selection of core sites discussed in this Chapter are shown as red markers. Star = AP_{comp}; Square = ODP 1090; Triangle = PS97/093-2; Circle = ODP 1123. The sea-floor shallower than 3000m is shaded (data from ETOPO1 1 Arc-Minute Global Relief Model, Geophysical Data Center, 2009). **(b)** Bathymetric profile at 26^{o}E with the AP_{comp} position shown (red star) and the ACC fronts from (a) at this longitude shown as triangles.

ever understanding of the origin of this phenomenon is limited by the sparsity of long, continuous records of potential physical drivers. To address this, this Chapter presents an extended near-bottom flow speed record from the Agulhas Plateau spanning the past 1.9 Ma, combining previous measurements from core MD02-2588 (Charidemou, 2018, *Ian R. Hall, unpublished data;*) with new measurements from International Ocean Discovery (IODP) Site U1475, presented as a continuous record on the Agulhas Plateau Composite (AP_{comp}; see Chapter 2).

6.1.1 Agulhas Plateau Deep Paleoceanography

Hydrographic surveys of the modern Agulhas Plateau region (Arhan et al., 2003) reveal a deep water column characterised by the competing presence of NADW and deep/bottom waters of Southern Ocean origin (Lower Circumpolar Deep Water and Antarctic Bottom Water; LCDW and AABW), hereafter referred to collectively as Southern Sourced Waters (SSW). These water masses constitute key players in the two 'cells' composing the Global Overturning Circulation (Talley, 2013). The Agulhas Plateau therefore represents an important intersection between these upper and lower cells; NADW exits the Atlantic basin and flows into either the Indian Ocean north of the Agulhas Plateau, or the Southern Ocean to the south, where it is sits above SSW, joining the eastward flowing Antarctic Circumpolar Current (ACC). The position of Agulhas Plateau means that paleoceanographic proxies from the region are highly sensitive to shifts in the presence of NADW (or glacial analogues referred to as Northern Sourced Waters; NSW) versus SSW (Starr et al., 2021; Molyneux et al., 2007). In addition, the southern Agulhas Plateau is currently situated within the influence of the most equatorward ACC jets (Drouin and Lozier, 2019; Orsi et al., 1995), and regional changes in deep flow vigour have been tightly linked to changes in the strength or position of the ACC (Molyneux et al., 2007).

Figure 2 shows selected reconstructions of deep hydrography from sediments cores recovered from the Agulhas Plateau. Firstly, the Sortable Silt mean grain size ($\overline{\mathbf{SS}}$; see Chapter 2) proxy implies higher near-bottom flow speeds at 2500m – 3000m water depths during glacial and cold intervals (Figure 6.2 c-d; Martínez-Méndez et al.,

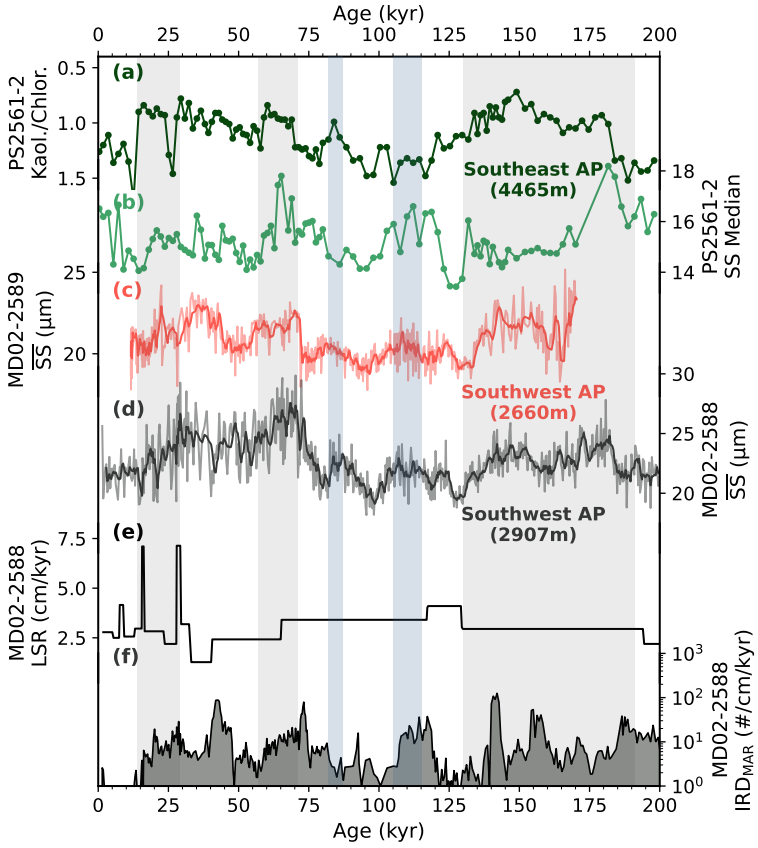

Figure 6.2: Paleoceanography of the southern Agulhas Plateau for the past 200 kyr. Kaolinite/Chlorite (a; Krueger et al., 2008) and SS_{Median} (b; Krueger et al., 2012) from PS2561-2. **c)** $\overline{SS}$ from MD02-2589 (Molyneux et al., 2007) and $\overline{SS}$ (d; Charidemou, 2018), Linear Sedimentation Rate (e; Ziegler et al., 2013) and IRD accumulation (f; Marino et al., 2013) from MD02-2588

2008; Molyneux et al., 2007). This likely reflects a strengthening or equatorward shift in the deep-reaching ACC at this longitude. High glacial flow-speeds are mirrored by reduced NSW presence, indicated by nutrient and water-mass provenance proxies such as Ca/Cd (Martínez-Méndez et al., 2008), $\delta^{13}C_{benthic}$ (Molyneux et al., 2007) and ϵNd (Rutberg et al., 2000). Furthermore, clay mineralogies of sediments from the Agulhas Plateau (Figure 6.2 a; Krueger et al., 2008) and the Cape Basin (Diekmann and Kuhn, 2002) show a similar pattern, with glacial (interglacial) intervals characterised by increased (decreased) presence of chlorite- (kaolinite-) bearing high (low) latitude water-masses. Interestingly, $\overline{SS}$ from the deep (>4400m) Agulhas Plateau (Figure 6.2 b Krueger et al., 2012) shows less distinct glacial-interglacial variability, possibly reflecting the diminished reach of ACC jets at abyssal depths.

A compelling story emerges from this region over the last glacial cycle, whereby glacial conditions are linked to an equatorward shift or strengthening of circumpolar flow associated with the ACC. Moreover, an apparent coupling between physical flow vigour and chemical ventilation hints at a mechanistic link between wind-driven Southern Ocean circulation and the isolation of the deep ocean (*á la* Toggweiler et al., 2006). However, a wider perspective must be taken, for example by considering the flow-speed evolution at other locations within reach of the ACC system. $\overline{\mathbf{SS}}$ reconstructions from the Drake Passage region and south-west Atlantic reveal lower flow-speeds during the last glacial maximum compared to the Holocene (Lamy et al., 2015; Wu et al., 2021; Roberts et al., 2017), although results from the Scotia Sea are less clear (McCave et al., 2013). Moreover, lower glacial flow speeds in the south-east Indian Ocean (Williams et al., 2021) contrast the generally higher glacial flow-speeds reconstructed in the south-west Pacific (Hall et al., 2001), central South Atlantic (Beny et al., 2020), and Agulhas Plateau region (this chapter; Martínez-Méndez et al., 2008). To accommodate these spatially heterogeneous results, a model relating glacial-interglacial ACC change and deep ventilation requires a more complex explanation than a linear response to stronger/weaker SWWB, for example one which accounts for the topographic control on flow and different Southern Ocean fronts in different regions.

Finally, the evolution of surface-deep ocean coupling further back in time remains unresolved. For example, proxy records related to biological productivity and sea surface temperature suggest that the position of Southern Ocean fronts were highly variable through the Pleistocene (Kemp et al., 2010; Becquey and Gersonde, 2002; Civel-Mazens et al., 2021), yet it is unclear how these relate to changes in the strength and geometry of the ACC and the ventilation of deep waters. In this chapter, I investigate how major climate transitions such as the Mid-Pleistocene Transition (MPT) and Mid-Brunhes Transition (MBT) manifest in this system, and whether such a physical-chemical coupling occurs across Early Pleistocene glacial cycles.

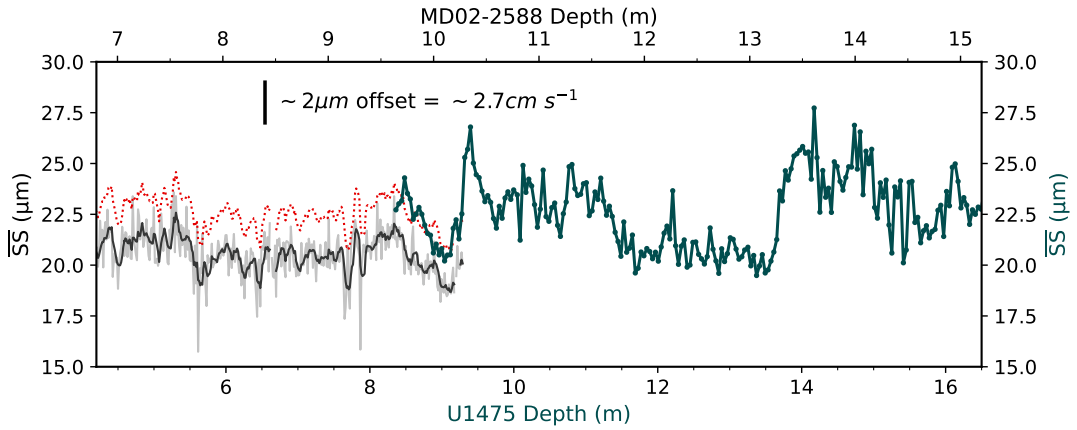

Figure 6.3: $\overline{SS}$ for the overlapping section of MD02-2588 and U1475. MD02-2588 is shown in grey (5-point moving-average in dark grey), and U1475 in teal. The red dashed line is the MD02-2588 data offset by +2μm. U1475 depth is given on the Shipboard Splice scale

6.2 Methods Summary

6.2.1 MD02-2588 - Site U1475 Continuity

To present a continuous record of near-bottom flow speed through the Mid- to Late-Pleistocene, the new Site U1475 $\overline{SS}$ data is combined with new and previously presented $\overline{SS}$ data from nearby sediment core MD02-2588 (Charidemou, 2018, data collected by I.R. Hall, Cardiff University). The two sites are geographically close, within 0.2 degrees of latitude and 0.6 degrees of longitude of each other, and are separated by around 250 m water depth. Whilst the two locations should therefore be influenced by the same local hydrographic conditions, the difference in depth as well as topographic features such as sediment waves and mounds on the south-west Agulhas Plateau (Uenzelmann-Neben, 2001) may result in hydrodynamic differences between the two sites. Figure 3 shows $\overline{SS}$ data across the stratigraphic overlap between the two sites. Although only covering a single glacial-interglacial transition (aligned via $\delta^{18}O_{benthic}$; see Chapter 3), a distinct offset is observable between the two records. $\overline{SS}$ from Site U1475 (the shallower site) is ~2μm higher than MD02-2588, which would equate to a vertical flow speed gradient of ~1.4 cm s^{-1} per 100 m according to the calibration of McCave et al. (2017).

To determine how pervasive this $\overline{SS}$ offset is a comparison to the nearby core site

MD02-2589 (water depth 2660m; Molyneux et al., 2007) is made. No core-top $\overline{\mathbf{SS}}$ data is available for MD02-2589, however the time-averaged $\overline{\mathbf{SS}}$ for the 11-170 ka interval is 20.6μm, around 2μm lower than the same time interval average in MD02-2588 (water depth 2900m). Interestingly, the depth-gradient between the two sites is of the opposite trend to the U1475 – MD02-2588 gradient. This may be due to the interaction of ocean flow and sedimentary features, or the downstream fining effect on $\overline{\mathbf{SS}}$ (McCave and Hall, 2006); MD02-2589 is located to the east of MD02-2588 and U1475, making it 'downstream' with respect to NADW and the ACC flow. With regards to combining the records of MD02-2588 and U1475, it is ultimately not possible to determine whether this offset would be constant across other time intervals. Therefore, instead of adjusting one of the records by a constant offset, both series are instead standardised to zero-mean and standard deviation of 1 ('unit variance') before being 'spliced' together. An exception applies to Figures 6.8 and 6.12 where the mean is subtracted from the MD02-2588 and U1475 intervals separately before conversion to flow speed anomaly (cm s^{-1}) using the slope of 1.36 cm s^{-1}/ μm (McCave et al., 2017).

6.2.2 Frequency-domain analysis

To identify the periodicities present in the AP_{comp} $\overline{\mathbf{SS}}$ record, auto-spectral density, cross-spectral density, and spectral coherence are estimated against an orbital curve product (ETP) using the Lomb-Scargle periodogram approach (REDFIT; see Chapter 2 for full description). The significance of the results, shown in Figure 6.4, is determined using 'Monte Carlo' red noise and chi^2 confidence levels (Ólafsdóttir et al., 2016). Peaks in the auto-spectrum which exceed the 99% confidence level are identified with a local-maxima ('peak finder') algorithm. Figure 6.4 shows that significant spectral peaks are present at 1/700, 1/120, 1/95, and 1/41 kyr. Similarly, strong cross-spectral peaks and significant coherency are present at ~1/100 and 1/41 kyr, with additional significant coherency at 1/55 and 1/21 kyr.

Furthermore, to test the phasing of $\overline{\mathbf{SS}}$ at different frequencies relative to the time series presented in Chapters 4 and 5, Blackman-Tukey phase estimates are calculated

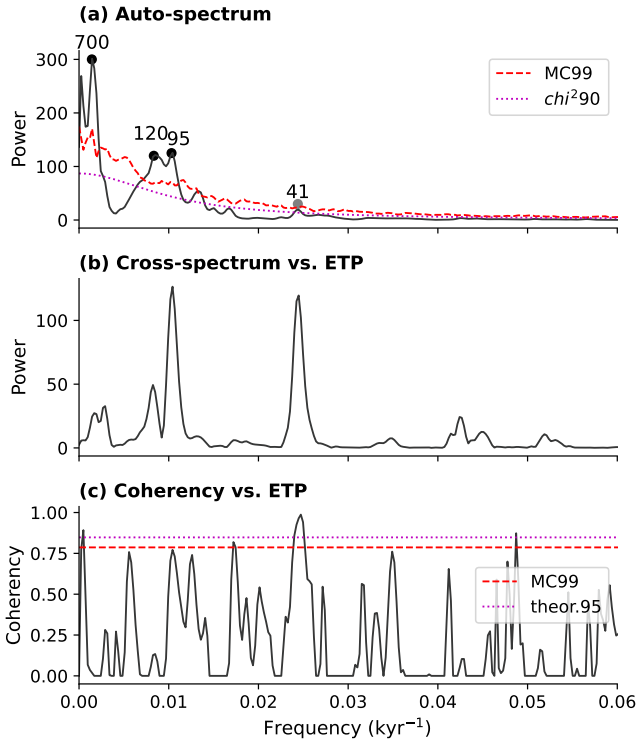

Figure 6.4: Spectral density estimate and cross-spectral analysis for $\overline{\mathbf{SS}}$ against ETP (sum of normalized eccentricity, precession and obliquity (Laskar et al., 2004)). **(a)** Auto-spectrum for $\overline{\mathbf{SS}}$, significant peaks are labelled as periods in kyr (grey indicates significant with respect to the *chi*^{2} 90% false alarm limit but not exceeding the 99% red noise level (Monte Carlo; MC99). **(b)** Cross-spectrum against ETP. **(c)** Coherency against ETP with Monte Carlo 99% and theoretical 95% confidence intervals. *Analysis were performed using 'REDFIT-x' software with 'ofac' of 5, 'hifac' of 2 and 'n50' of 3. 6dB bandwidth is 2 x 10*$^-$*3 kyr*$^{-1}$.

against AP_{comp} $\delta^{18}O_{benthic}$. These results are shown in Figure 7.3 for the 1/23 kyr (panel a), 1/41 kyr (panel b) and 1/100 kyr (panel c) bands. As expected from the absence of auto-spectral peaks around the precession-band frequencies (Figure 6.4a), the coherence of $\overline{\mathbf{SS}}$ to $\delta^{18}O_{benthic}$ is too weak to determine phase confidently. For 1/41 kyr, $\overline{\mathbf{SS}}$ is in-phase with $\Delta\delta^{13}C_{SAMW-CDW}$ and leads IRD_{MAR}, $\delta^{18}O_{benthic}$ and $\delta^{13}C_{benthic}$. In the 1/100 kyr band, $\overline{\mathbf{SS}}$ lags behind $\Delta\delta^{13}C_{SAMW-CDW}$ and IRD_{MAR}, slightly leading (though within uncertainty) $\delta^{13}C_{benthic}$ and $\delta^{18}O_{benthic}$.

6.2.3 Change-Point Detection

In order to assess how stationary trends and variability in $\overline{\mathbf{SS}}$ are over time, the record is divided into sections separated by events or transitions in the data. To do so

(quasi-) objectively, a suite of offline Change-Point Detection (CPD) algorithms are applied to the standardized data after first interpolating to a linear age scale (δt = maximum spacing between raw data points). CPD is a signal-processing technique which considers the time series to be 'piecewise non-stationary', meaning some characteristic changes at one or more unknown points in time, and has been previously utilized to detect changes in paleoclimate time series (Ruggieri et al., 2009; Kylander et al., 2007). The goal is to find a number of change-points which minimize a cost function; in other words to fit a model in which each segment is as statistically homogeneous as possible. The four algorithms used here are a Pruned Exact Linear Time (PELT) search, a Dynamic Programming search, Binary Segmentation search, and Window-Based Search (Figure 6.6). An exhaustive review of change-point detection approaches is beyond the scope of this thesis (see Truong et al., 2020 for a detailed description of the algorithms employed here), and I note that the result of no single approach is taken to be absolute or 'true'. Instead, transitions that are identified by multiple approaches and could also be identified by visual inspection are used to approximate segments in the time series. As shown in Figure 6.6a, multiple change-points can be assigned to the time-series, and the CPD algorithm results are not always unanimous.

6.3 Results

6.3.1 Pleistocene $\overline{\mathbf{SS}}$ Variability

The SS record (Figure 6.5a) displays distinct variations over glacial-interglacial and longer timescales. As previously observed at the Agulhas Plateau (Molyneux et al., 2007), glacial intervals are generally characterised by high near-bottom flow speeds with minima occurring during interglacial intervals. This pattern is observable for the much of the record back to around 1.6 Ma, becoming less clear in older glacial cycles. Notable exceptions occur during glacial intervals MIS 22 and MIS 28 where $\overline{\mathbf{SS}}$ maxima are absent or heavily muted. Furthermore, the timing of glacial $\overline{\mathbf{SS}}$ maxima relative to glacial maxima (in the context of peaks in $\delta^{18}O_{benthic}$) is non-stationary

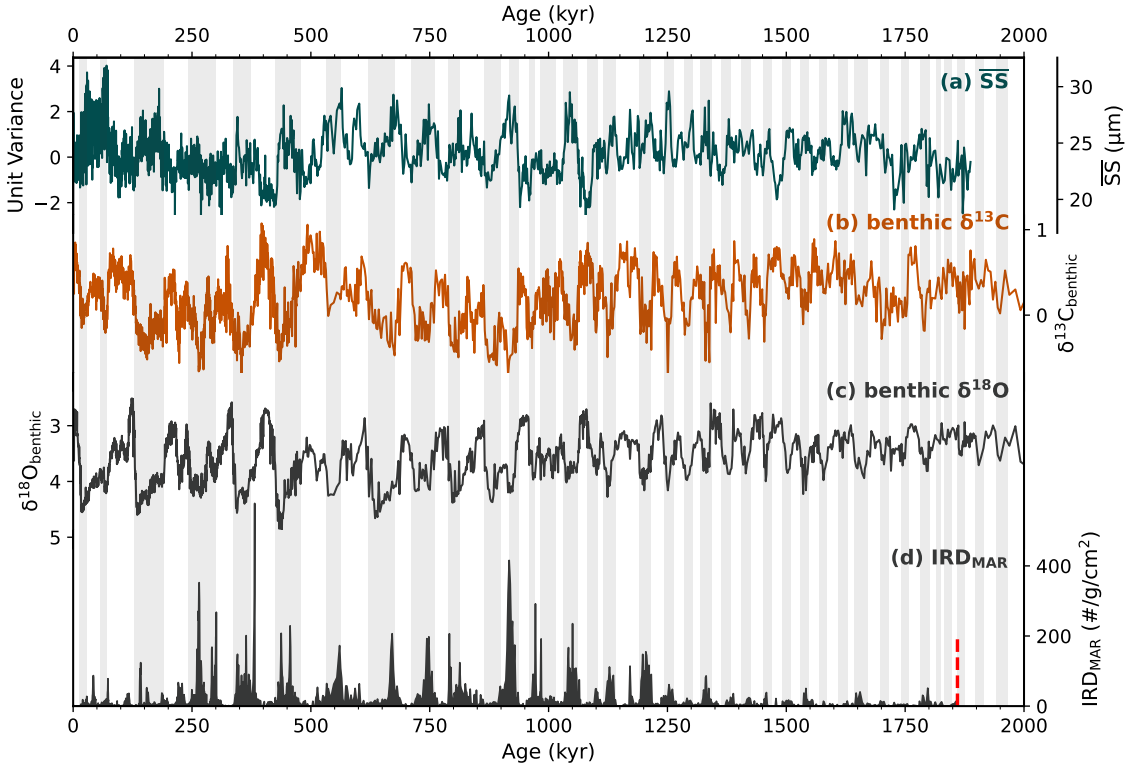

Figure 6.5: Results from the AP_{comp} for 0 - 1.85 Ma. **(a)** The full $\overline{SS}$ record is plotted as unit variance (see text) with a secondary axis provided for μm units (MD02-2588 is offset by 2μm on this axis). $\delta^{13}C_{benthic}$ (b), $\delta^{18}O$ (c), and IRD accumulation (d) are also shown (see Chapter 4). Glacial intervals (following Lisiecki and Raymo, 2005) are shaded grey. The red dashed line indicates the base of the IRD dataset.

through time. This is most striking in the 0-800 ka interval, where $\overline{SS}$ peaks appear to occur relatively early in the glacial sequence, returning to interglacial levels before the deglacial transition in $\delta^{18}O_{benthic}$. Furthermore, on top of the background glacial-interglacial variability there are a number of state changes evident which might be of paleoclimatic significance:

- **71 ka.** All four CPD algorithms identify a change-point around the MIS 5/4 transition, supported by a stepwise increase in the rolling standard deviation of the time series (Figure 6.6c). This transition is characterised by an abrupt increase in $\overline{SS}$ which persists into MIS 2, and is described in detail by Molyneux et al. (2007) in site MD02-2589. In that study, they demonstrate a decoupling between global ice-volume, chemical ventilation and flow vigour across this transition.

- **430 ka.** 3 of the 4 algorithms detect a change-point between 400 and 500 ka, which I assign to 430 ka based on a peak in rolling-standard deviation. This transition displays a sharp decrease in $\overline{\mathbf{SS}}$ from MIS 11 into MIS 10.
- **930 ka and 1060 ka.** Thirdly, 3 of the 4 methods identify two transitions aligning roughly with the Mid-Pleistocene Transition (MPT; e.g. Clark et al., 2006); one at 930 ka (MIS 25/24) and another at around 1060 ka (MIS 31/30). These are characterised by increased glacial-interglacial variance separating lower (higher) frequency glacial cycles after (before) the MPT. Between these transitions, $\overline{\mathbf{SS}}$ is low with little glacial-interglacial variability, mirroring the suppressed cycles in $\delta^{18}O_{benthic}$.
- **Pre-MPT.** Additional change-points are identified in the >1060 ka section (notably around 1600 ka), however these are less clear by eye and less obvious in the rolling standard deviation, and no change-point are formally defined before the MPT.

In this chapter I will explore the nature of each of these transitions, in particular with consideration of regional and global climatic changes recorded in other proxy records. First, however, it is important to evaluate the fidelity of the $\overline{\mathbf{SS}}$ proxy to record near-bottom flow vigour at this location, acknowledging any caveats that might influence interpretations made.

6.4 Discussion

6.4.1 Influences on the $\overline{\mathbf{SS}}$ proxy

The utility of $\overline{\mathbf{SS}}$ to reconstruct near-bottom flow speed (and hence ACC proximity/strength) at the Agulhas Plateau relies on the assumption that hydraulic sorting is the dominant control on grain size (atleast in the 10-63μm 'Sortable Silt' fraction). More precisely, it depends on the dominance of selective deposition in the sorting of this size fraction (McCave et al., 1995b). Encouragingly, seismic data provide evidence for a sedimentary environment which interacts extensively with current pat-

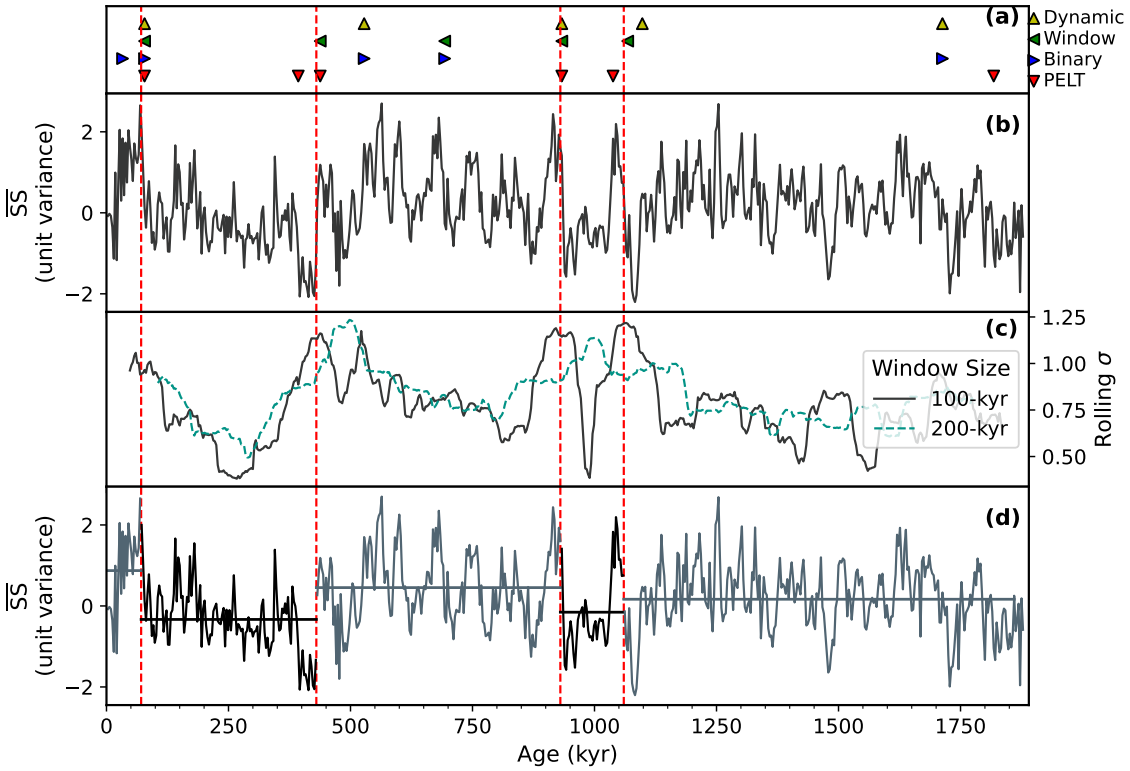

Figure 6.6: Change-Point Detection. **(a)** Transitions detected by the 4 algorithms described in the text (see the key). The AP_{comp} $\overline{\mathbf{SS}}$ record **(b)** and its rolling-window standard deviation (σ; **c**) are also shown. The bottom panel **(d)** shows the $\overline{\mathbf{SS}}$ record segmented at the transitions denoted by vertical red dashed lines, as discussed in the text. Solid horizontal lines represent the segment average.

terns on the Agulhas Plateau (Uenzelmann-Neben, 2002). Moreover, the irregularity of benthic storms in the region (Cronin et al., 2013) and the range of flow-speeds observed at nearby moored-current meters (Pollard and Read, 2001) support the assumptions above. However, mean grain size through time can also be influenced by changes in the supply of sediment, and any attempt to directly relate $\overline{\mathbf{SS}}$ to absolute flow speed must also consider the effect of 'downstream fining' along a flow path (McCave and Hall, 2006).

Furthermore, suspicion has be cast as to whether sediments containing ice-rafted debris (IRD) deposits are sufficiently current-sorted for the application of paleo-flow speed proxies (Hass, 2002; Jonkers et al., 2015). This is because IRD, whilst often practically defined as a coarse fraction percent (e.g. >150μm; Chapter 4), in reality consists of a broad grain size spectra. McCave and Andrews (2019) provide a test for the influence of ice-rafting on current-sorting, by computing the running correlation

between $\overline{\mathbf{SS}}$ and the percentage of fine material in the 10-63μm range (SS%), whereby if the correlation falls below some threshold the sediment is considered unsuitable for application of the $\overline{\mathbf{SS}}$ proxy. The presence of IRD in Pleistocene AP_{comp} sediments (Chapter 4) means that a potential relationship must be considered here. Whilst the test of McCave and Andrews (2019) can not be used in this instance (the approach employed here only measures grains within the 10-63μm fraction), it is reassuring that they go on to find no consistent relationship between fine-fraction sorting and the amount of coarse IRD present in North Atlantic sediments. Provided that flow speeds remain relatively high and the deposition of IRD is neither too high or abrupt, McCave and Andrews (2019) argue that sediment will be current-sorted regardless of its origin (ice-rafted or otherwise). In the Drake Passage region, where IRD deposition is higher than at the Agulhas Plateau due to the proximity to Antarctica, no correlation between IRD and $\overline{\mathbf{SS}}$ is evident, nor is an influence of IRD peaks on the correlation between $\overline{\mathbf{SS}}$ and SS% (Roberts et al., 2017; Wu et al., 2021). Finally, there is only a weak correlation between IRD concentration and $\overline{\mathbf{SS}}$ at the AP_{comp} ($r^2 = 0.24$). A relationship between the two proxies would likely be exaggerated by complementary environmental conditions favouring both IRD deposition and higher flow speed, such as a northward expansion of the ACC with the associated Southern Ocean fronts (Starr et al., 2021). To summarise, it is likely that the dominant control on $\overline{\mathbf{SS}}$ presented here is near-bottom flow speed.

6.4.2 Physical – Chemical Coupling

As reasoned above, the AP_{comp} $\overline{\mathbf{SS}}$ record provides a reconstruction of near-bottom flow speed at this location. In combination with other proxies for changes in water-mass chemistry or provenance, an opportunity arises to investigate the link between Southern Ocean wind-forcing, ACC dynamics, and deep chemical ventilation. For example, taking $\delta^{13}C_{benthic}$ as a record of the contribution of canonically well-ventilated NSW (e.g. Broecker, 1979) versus the 'older' SSW (Chapter 3; Molyneux et al., 2007), it is possible to assess the coupling between ACC strength/extent and deep ventilation at the Agulhas Plateau. In Figure 6.7, the AP_{comp} $\overline{\mathbf{SS}}$ and $\delta^{13}C$ records are shown, along with a sliding-window correlation coefficient between the two. This reveals in-

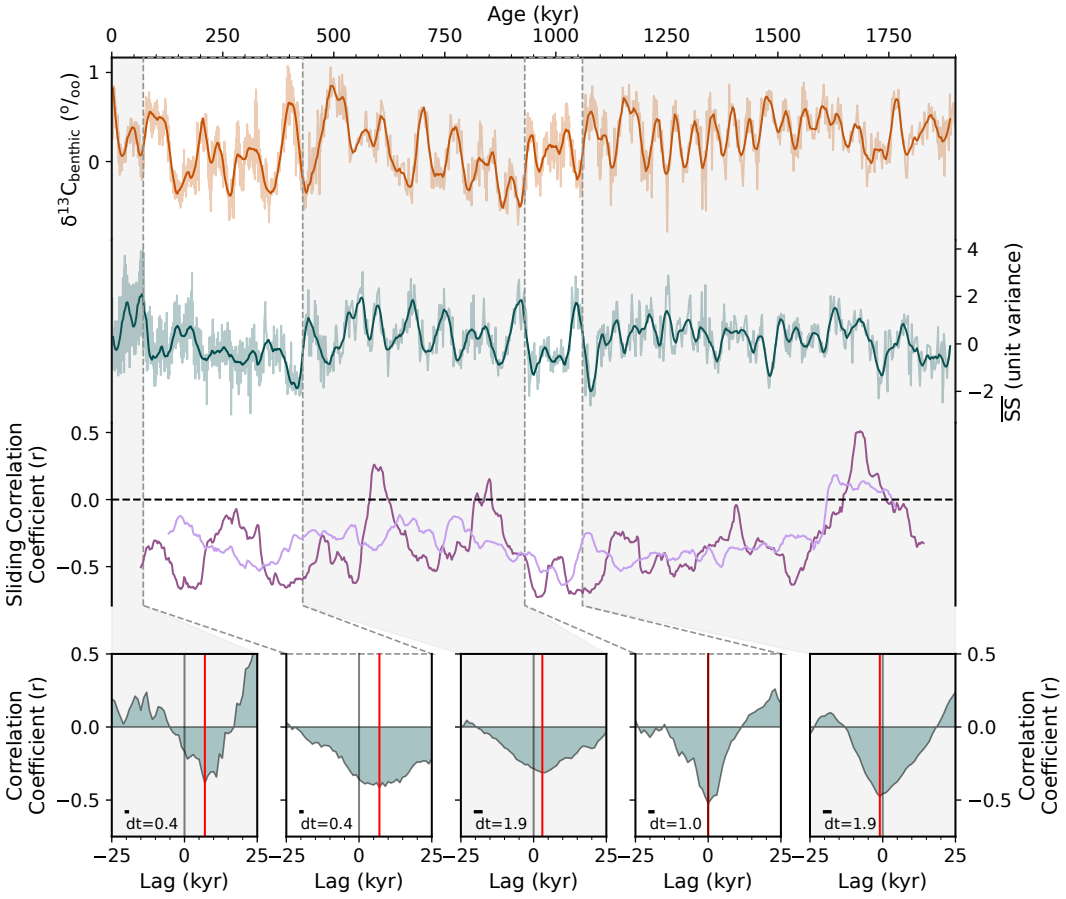

Figure 6.7: AP_{comp} Physical - Chemical Coupling The top two panels show $\delta^{13}C_{benthic}$ and $\overline{SS}$ (semi-transparent = raw data; solid line = 15-point 3rd order Savitsky-Golay smoothing filter). The next panel shows the sliding correlation coefficient (r) between $\overline{SS}$ and $\delta^{13}C_{benthic}$ (dark purple = 150-ka; light purple = 300-ka). The lower panel shows the cross-correlation results for $\overline{SS}$ versus $\delta^{13}C_{benthic}$ for each segment identified above using the algorithm of Rehfeld et al. (2011). The average temporal resolution for each interval is given in the bottom left of each sub-plot and the lag corresponding to maximum negative correlation is indicated by the vertical red lines. A positive lag corresponds to $\overline{SS}$ leading $\delta^{13}C_{benthic}$

tervals of pronounced coupling (strong negative correlation) where high near-bottom flow speeds accompany depleted $\delta^{13}C$. Interestingly, transient intervals of weak and even positive correlation are evident at times, which might indicate periodic decoupling between ACC strength/position and relative NSW vs SSW ventilation. It is important to note that the timing and regularity of these intervals is somewhat sensitive to the window size used for the sliding correlation. For example, a 150-kyr window (dark purple in Figure 6.7) reveals brief intervals of weak positive correlation around MIS 15, MIS 20, and ~MIS 54. A correlation switch around MIS 54 is also revealed with a 300-kyr window, and appears to coincide with a large-scale transition in overturning circulation and Northern Hemisphere ice sheet behaviour (Hodell and Channell, 2016).

Coupling after 1.6 Ma

A transition in the relationship between $\overline{\mathbf{SS}}$ and $\delta^{13}C$ is evident at ~1.6 Ma (roughly corresponding to MIS 54; Figure 6.7). Before this, a weak positive correlation results from suppressed glacial-interglacial variability, in addition to a gradual increase in both $\overline{\mathbf{SS}}$ and $\delta^{13}C$ between MIS 61 and MIS 56. Interestingly, this interval has been suggested to exhibit maxima in NADW formation (Bell et al., 2015; Venz and Hodell, 2002) and is followed by a stepwise decrease in NADW formation (Raymo et al., 1990; Lang et al., 2016) and an increase in the glacial chemocline between the intermediate and deep Atlantic (Hodell and Venz-Curtis, 2006; Lisiecki, 2014). The onset of a clear (negative) coupling after 1.6 Ma might be related to a transition in the nature (Khélifi and Frank, 2014) and orbital phase (Lisiecki, 2014) of overturning circulation coincident with an intensification in Northern Hemisphere glacial cycles (Hodell and Channell, 2016) and surface cooling in the North Atlantic (Naafs et al., 2012). Moreover, this interval marks an apparent 'synchronization' between the high latitude North and South Atlantic (Hodell and Channell, 2016), marked by regular 41-kyr^{-1} cyclicity in the respective Polar Fronts (Hodell and Venz, 2013). Such an inter-hemispheric synchronization could explain the onset of clear coupling between $\overline{\mathbf{SS}}$ and $\delta^{13}C_{benthic}$, as the ACC position is intrinsically linked to the position of the Southern Ocean Polar Front (Orsi et al., 1995) and $\delta^{13}C$ is heavily influenced by the export of NADW from

the Atlantic.

6.4.3 The Mid-Pleistocene Transition

Following the onset of clear negative coupling after ~1.6 Ma, the next notable transition occurs during the MPT. Here, maxima during MIS 24 and MIS 30 bound an interval of low $\overline{\mathbf{SS}}$ with minimal variability (Figure 6.8). The first indication of the transition is a distinct minimum during the MIS 31 interglacial, where $\overline{\mathbf{SS}}$ is ~5μm lower than during earlier interglacials (with the exception of MIS 49). The relatively rapid transition from MIS 31 to MIS 30 is characterised by a flow-speed change of nearly 10 cm/s at the AP_{comp}, followed by a sustained high during the glacial MIS 30. This pattern is also evident at a similar latitude in the south-west Pacific (ODP 1123; Hall et al., 2001), where a ~7 cm/s rise across the MIS 31/30 transition occurs. This seemingly abrupt shift punctuates a long-term transition in global climate conditions around this time, marking a shift in the periodicity (41-kyr^{-1} to ~100-kyr^{-1}), intensity (transition to colder, icier conditions) and shape (symmetrical to asymmetrical) of glacial-interglacial cycles (Clark et al., 2006). The nature and timing of the MPT varies between archives, and depending on the statistical method applied (Clark et al., 2006). In the AP_{comp} $\overline{\mathbf{SS}}$ record, it appears to manifest as a series of acute minima and maxima beginning at MIS 31.

MIS 31

MIS 31 is considered to be an exceptional interglacial in the circum-Antarctic region, characterised by anomalously warm temperatures at high latitudes and an extreme retreat of the West Antarctic Ice Sheet (Beltran et al., 2020) with a corresponding ~20 m sea level rise (Raymo, 2006). Higher-than-Holocene sea surface temperatures around the Antarctic Margin (5 to 9^{o}C warmer) (Scherer et al., 2008; Beltran et al., 2020) and the modern Polar Frontal Zone (3^{o}C warmer) (ODP Site 1094; Beltran et al., 2020), the appearance of calcareous sediments around the Antarctic Margin (Scherer et al., 2008; Villa et al., 2012), and high coccolith accumulation at Site 1094 (Flores and Sierro, 2007) likely reflect a southward shift in the Polar Front. A southward

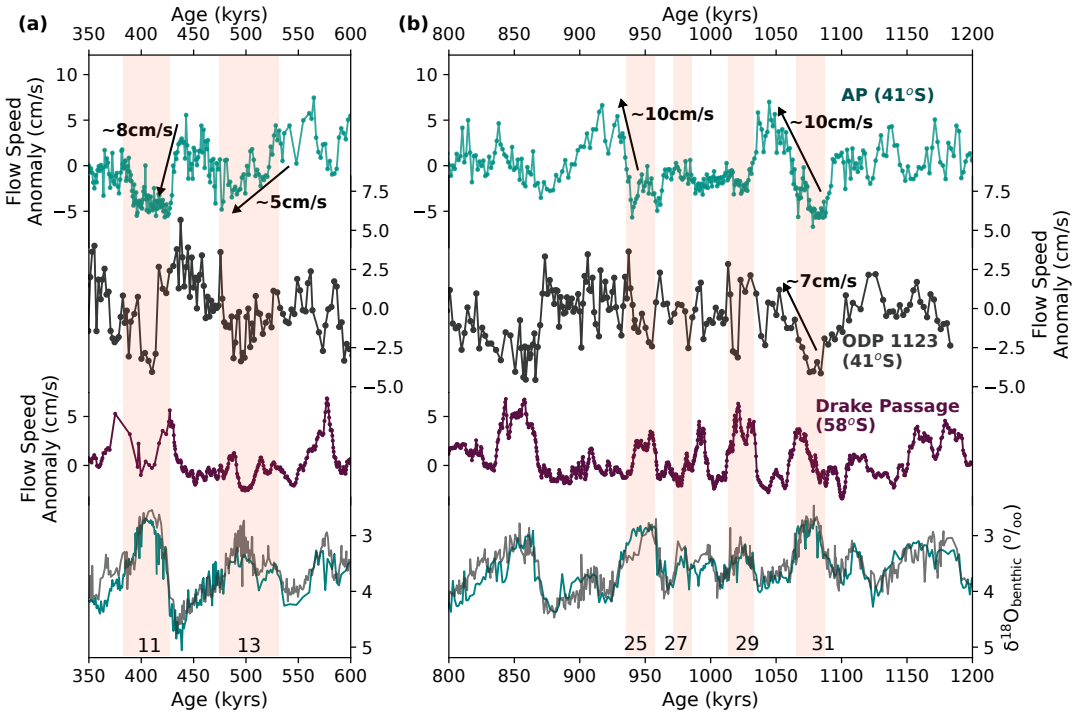

Figure 6.8: $\overline{\mathbf{SS}}$ derived near bottom flow speed anomaly records from the AP_{comp} (top), ODP 1123 (middle Hall et al., 2001), and PS97/093-2 (bottom Toyos et al., 2020). **(1)** Shows the Mid-Brunhes Transition and **(b)** shows the Mid-Pleistocene Transition. Selected interglacial intervals are shaded red. Flow speed anomaly is calculated as $\overline{\mathbf{SS}}$ difference from mean, converted using the slope of McCave et al. (2017). AP = Agulhas Plateau

shift in the Subantarctic and Subtropical Fronts is also indicated by calcareous nannofossil assemblages (Maiorano et al., 2009) and low wind-blown dust deposition (Martínez-Garcia et al., 2011) in the modern Subantarctic Zone (ODP Site 1090), and high sea surface temperatures at the Agulhas Plateau (Cartagena-Sierra et al., 2021). Finally, a minima in the percentage of tetra-unsaturated alkenones relative to the total abundance of unsaturated C_{37} alkenones ($\%C_{37:4}$; Figure 6.9e) and more saline surface conditions at ODP 1090 (Rodríguez-Sanz et al., 2012) further support more subtropical conditions at this time (Martinez-Garcia et al., 2010).

This suggests that a poleward contraction of the Southern Ocean frontal system is concurrent with the diminished influence of the ACC on near-bottom flow vigour on the Agulhas Plateau, with flow speeds around 5 cm/s lower than during the previous interglacials MIS 33 and 35. Whether this is driven by an orbital configuration which favours warm Southern Hemisphere summers (Scherer et al., 2008) or some internal climate feedback is unclear, however a scenario whereby warm interglacial condi-

tions coincide with a poleward ACC (and associated frontal system) might provide an interesting analogue for future warming.

MIS 30 to MIS 25

Following MIS 31, $\overline{\mathbf{SS}}$ increased rapidly to a maximum during the MIS 30 glacial. This sharp transition is mirrored in a marked surface freshening (Rodríguez-Sanz et al., 2012) and increase in polar water advection (Martinez-Garcia et al., 2010) at Site 1090 (Figure 6.9 d and e). This likely reflected a northward expansion of the SAF and STF, bringing fresher, more nutrient-rich surface waters to the Agulhas Plateau, stimulating a rise in biological productivity (Figure 6.9 f; Cartagena-Sierra et al., 2021). Anomalously high $\overline{\mathbf{SS}}$ suggests a strong and/or proximal ACC, which may be related to a step-wise increase in lithogenic sediment accumulation at Site 1090 (Diekmann and Kuhn, 2002) and in IRD deposition at the Agulhas Plateau (Chapter 4; Starr et al., 2021). There is less evidence available to support a substantial shift in deep ocean conditions at this time, either in the proportion of NADW (Kim et al., 2021) or accumulation of DIC (Farmer et al., 2019) in the deep Atlantic (Figure 6.10). However, a negative correlation between $\overline{\mathbf{SS}}$ and $\delta^{13}C$ persists in this interval, which does exhibit a negative $\delta^{13}C$ excursion characteristic of SSW presence; this suggests that some level of physical - chemical ventilation coupling is at play.

The interval that follows is characterised by a prolonged interval of low $\overline{\mathbf{SS}}$ with little orbital-scale variability. These low flow-speed, low variance glacial cycles are mirrored somewhat by summer sea surface temperatures in the South Atlantic (Becquey and Gersonde, 2002), but are contrasted by highly variable sea surface temperatures (Crundwell et al., 2008) and near-bottom flow speeds (Hall et al., 2001) in the south-west Pacific. Furthermore, the high Agulhas Plateau productivity during MIS 30 continues through this interval (Cartagena-Sierra et al., 2021) and large amplitude fluctuations occur in the $\%C_{37:4}$ record from ODP 1090 (Martinez-Garcia et al., 2010). These results provide a seemingly disparate picture of the ACC and associated fronts. For example, the low and relatively stable $\overline{\mathbf{SS}}$ implies a prolonged distal or weak ACC, whilst the continued biological productivity at the Agulhas Plateau and advection of

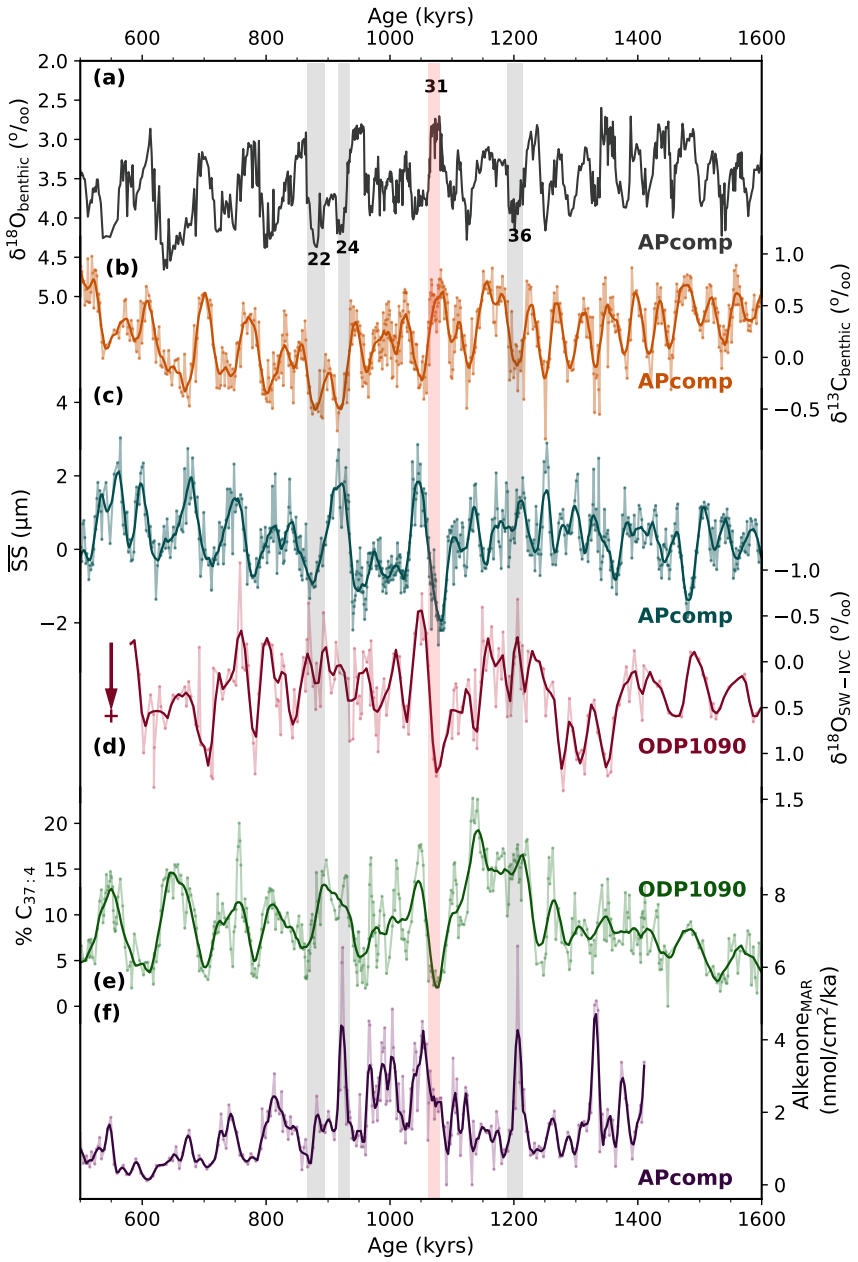

Figure 6.9: Surface Paleoceanography across the MPT. **(a)** AP_{comp} $\delta^{18}O_{benthic}$ record (this thesis). **(b)** AP_{comp} $\delta^{13}C_{benthic}$ (this thesis). **(c)** AP_{comp} $\overline{SS}$ (this chapter). **(d)** $\delta^{18}O$ of surface seawater at ODP Site 1090 (note reversed scale Rodríguez-Sanz et al., 2012). **(e)** Percentage of tetra-unsaturated alkenones relative to the total abundance of unsaturated C37 alkenones from ODP Site 1090 ($\%C_{37:4}$; Martinez-Garcia et al., 2010). **(f)** AP_{comp} alkenone accumulation rate (Cartagena-Sierra et al., 2021).

polar waters at ODP 1090 imply a northerly SAF or STF, although the controls on productivity in the Agulhas Plateau region are obviously more complex than this simplified model (Read et al., 2000). A possible explanation for this apparent paradox could be that a northerly STF was not mirrored by a northerly PF, allowing the incursion of cold, nutrient-rich waters at the Agulhas Plateau whilst ACC jets associated with the PF remained distal. Graham and Boer (2013) show that jets associated with the STF, particularly in the Agulhas region, are confined to the surface due to the more stratified water column and more baroclinic flow. This suggests that changes in the STF position, which result in strong hydrographic changes at the surface, can be decoupled from changes in deep flow vigour. Alternatively, an equatorward yet weaker SWWB might have the same effect on decoupling productivity from flow speed.

MIS 24 to MIS 22 and the '900 ka Event'

Similarly to MIS 30, the MIS 24 glacial is associated with a rapid increase in $\overline{\mathbf{SS}}$, although the latter coincides with a suite of evidence from multiple proxies and locations describing a substantial, large-scale shift in climate. In the context of the MPT, this shift represents an abrupt event punctuating a background of long-term global cooling and intensified glacials (Clark et al., 2006; Elderfield et al., 2012; McClymont et al., 2013). At this time, NSW abruptly gave way to SSW in the deep Atlantic (Figure 6.10; Pena and Goldstein, 2014; Tachikawa et al., 2021), accompanying an accumulation of DIC in the deep ocean (Farmer et al., 2019), and possibly coincident with a shift in the nature of the East Antarctic Ice Sheet (Raymo, 2006; Elderfield et al., 2012). Closer inspection of the anatomy of this '900 ka event' reveals that many of these perturbations climax during MIS 22, whereas the Agulhas Plateau $\overline{\mathbf{SS}}$ record peaks at MIS 24 before gradually declining across MIS 23 and MIS 22 into the interglacial MIS 21. Similarly, AP_{comp} IRD accumulation reaches a long-term maxima (the second highest of all glacial intervals recorded) during MIS 24, yet returns to interglacial levels during MIS 22, as does biomarker accumulation (Cartagena-Sierra et al., 2021). An equatorward and/or stronger ACC is therefore implied during MIS 24, with a substantial supply of icebergs across the Southern Ocean which, following Chapter 4 and Starr et al. (2021) would lead changes in overturning circulation

through the 'southern escape' mechanism. However, the offset between this Southern Ocean surface expansion and the overturning circulation 'crisis' peak at MIS 22 (>20 kyr) is too long to be attributed to this mechanism (which works on the scale of 1 - 2 kyr).

Alternatively, sea ice expansion during MIS 22 could have reduced the strength of the ACC by acting as a frictional barrier between the sea surface and westerly winds (Wu et al., 2021; Martin et al., 2014). Such an anomalously large sea-ice extent would have a profound impact not just on ACC strength, but also on air-sea exchange (Stephens and Keeling, 2000) and possibly deep water mass geometry (Ferrari et al., 2014). In the absence of a direct Southern Ocean sea-ice reconstruction at this time this is purely conjecture, however it provides a plausible explanation for the patterns observed. *But why might sea-ice expand so much during this interval?* One possibility is that subdued summer insolation, due to low orbital eccentricity (Laskar et al., 2004), facilitated cooling across MIS 23 (Kemp et al., 2010), with regional Southern Ocean cooling amplified further by the sea-ice albedo effect (*X. Zhang, personal communication, 2021*). Support for this mechanism might be found in comparing flow speed records from the Drake Passage (Toyos et al., 2020) and the Agulhas Plateau (Figure 6.8). This comparison shows that the anti-correlated glacial-interglacial trend usually observed between $\overline{\mathbf{SS}}$ at the two locations breaks down during MIS 22. The latitudinal heterogeneity in ACC-related flow speed changes (discussed in more detail below) would not apply if shifts in the SWWB were disconnected from the ACC flow by extended (and thick) sea ice.

To summarize, the MPT manifests in the AP_{comp} $\overline{\mathbf{SS}}$ record as a series of maxima and minima of higher amplitude than the preceding glacial and interglacial intervals. More specifically, a marked flow-speed minimum during the anomalously warm (Scherer et al., 2008) MIS 31 is followed by a strong and/or proximal ACC during MIS 30. Little variability is evident during the following cycles, and an apparent disparity between biological and physical proxies may indicate a decoupling of the ACC and STF (although more work is needed to elucidate this). Finally, a sharp transition into a flow-speed maxima during MIS 24 marks the beginning of a large-scale reorganization of ocean circulation (Pena and Goldstein, 2014), deep ocean chemistry (Farmer

et al., 2019), and ice sheet dynamics (Raymo, 2006). Whilst these perturbations continue and 'peak' during MIS 22, $\overline{\mathbf{SS}}$ decreases gradually towards interglacial levels. I propose that this is the result of anomalously widespread sea-ice in the Atlantic Southern Ocean through MIS 23 and 22, reducing the exchange of momentum from the SWWB to the the ACC.

6.4.4 The Mid-Brunhes Transition

Following the MPT, orbital modulation of $\overline{\mathbf{SS}}$ continues with periodic glacial highs and interglacial lows of slightly higher amplitude than pre-MPT cycles. This is superimposed on a gradual trend of increasing $\overline{\mathbf{SS}}$ which terminates in distinct lows during MIS 13 and MIS 11. All 4 CPD algorithms identify a transition between 500 and 400 ka and a peak in the rolling standard deviation centres this shift at around 430 ka. In the context of global climate, this marks a shift in the amplitude of glacial-interglacial cycles known as the Mid-Brunhes Transition (MBT; also known as the Mid-Brunhes Event). In ice-core records, the MBT corresponds to a stepwise increase in interglacial CO_2 and temperature (Jouzel et al., 2007), whilst marine sediment cores document a decrease in interglacial ice-volume (Lisiecki and Raymo, 2005). Whilst the MBT was originally described as an abrupt shift centred on MIS 11 (Jansen et al., 1986), recent work has suggested a more gradual transition (Yin, 2013), and evaluation of the preceding interglacial MIS 13 reveals that changes in the global carbon cycle were already set in motion around 500 ka (Ao et al., 2020; Barth et al., 2018).

The relatively low $\overline{\mathbf{SS}}$ during MIS 13 (Figure 6.6) supports the concept of a two-step MBT. This interglacial coincides with a whole-ocean $\delta^{13}C$ maxima (Barth et al., 2018), as well as distinct shifts towards drier conditions in southern Africa (Caley et al., 2018; Ivory et al., 2016), intense monsoonal precipitation in North Africa (Zhao et al., 2012) and South Asia (Ziegler et al., 2010), and wetter conditions recorded by East Asian loess sequences (Ao et al., 2020). However, whilst both MIS 13 and MIS 11 were exceptional relative to earlier interglacials, the two also exhibit distinct differences. For example, MIS 13 is characterised by inter-hemispheric differences in temperature (Guo et al., 2009), with muted sea surface temperature peaks in the South Atlantic

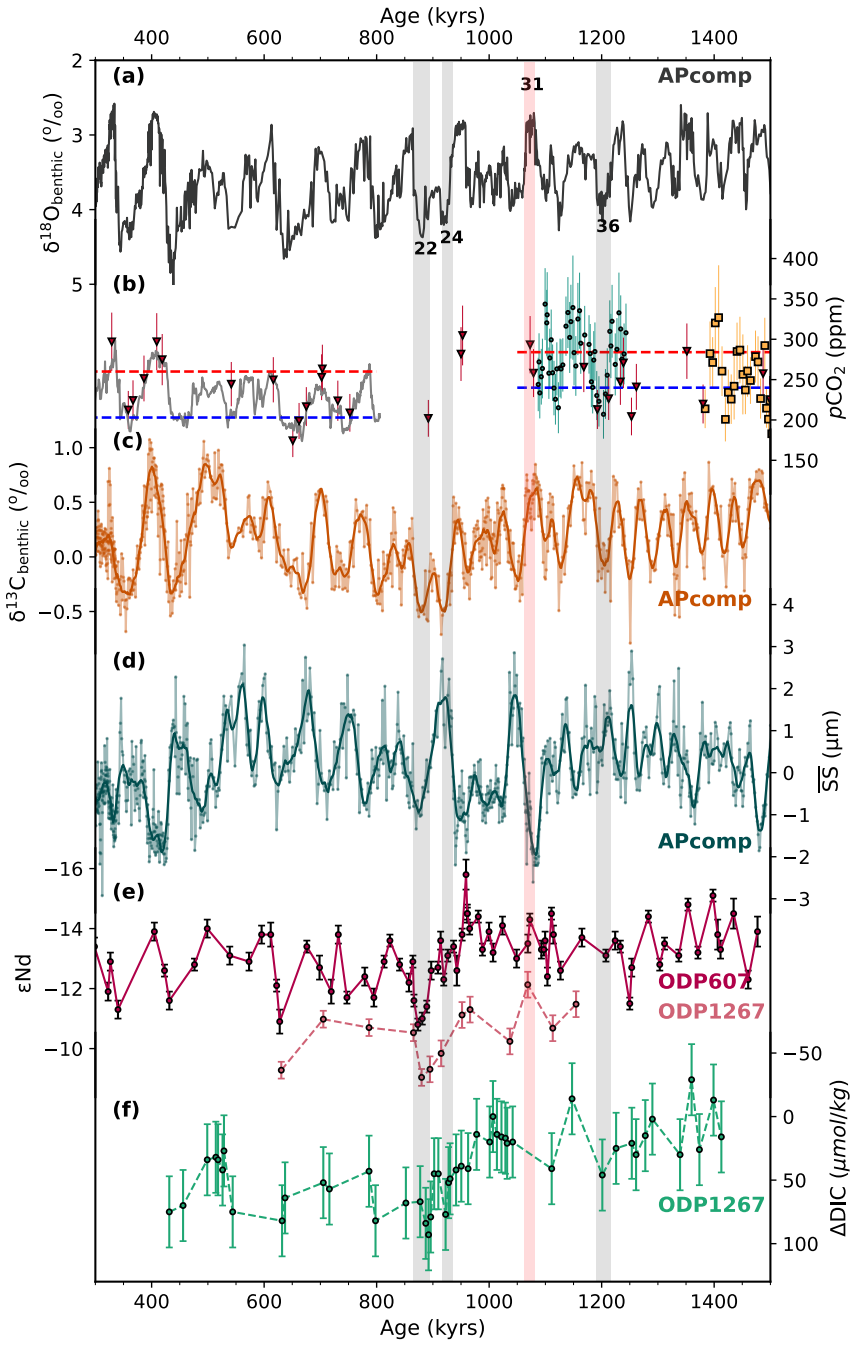

Figure 6.10: Deep paleoceanography across the MPT (a) AP_{comp} $\delta^{18}O_{benthic}$ record (this thesis). **(b)** Ice core (black line; Masson-Delmotte et al., 2010, and references therein) and boron-isotope based sediment core (markers; Chalk et al., 2017; Dyez et al., 2018; Foster, 2008; Henehan et al., 2013; Honisch et al., 2009) reconstructions of pCO_2. **(c)** AP_{comp} $\delta^{13}C_{benthic}$ (this thesis). **(d)** AP_{comp} $\overline{SS}$ (this chapter). **(e)** εNd records from ODP Site 607 (Kim et al., 2021) and ODP Site 1267 (Farmer et al., 2019). **(f)** Change in Dissolved Inorganic Carbon (DIC) concentration in bottom water at ODP Site 1267 (Farmer et al., 2019)

(Martínez-Garcia et al., 2009) and wider Southern Ocean (Ao et al., 2020), and lower pCO_2 and Antarctic temperature relative to MIS 11 (Jouzel et al., 2007). Cool (for interglacial standards) Southern Ocean conditions during MIS 13 are seemingly at odds with $\overline{\mathbf{SS}}$ minima, which suggests a poleward or weakened ACC. Indeed, $\overline{\mathbf{SS}}$ in the Drake Passage is relatively low compared to MIS 11. It may be the case that whilst the MIS 13 climate exhibited inter-hemispheric asymmetry, the low- to high-latitude Southern Hemisphere temperature (and thus pressure) gradient may have been weak. For example, sea surface temperatures were low during MIS 13 in the tropical South Atlantic (Schefuss et al., 2004), however a better understanding the complexities of atmospheric circulation and tele-connections during this interval is required to explain the differences observed between regions (Muri et al., 2011).

MIS 11: Another remarkable interglacial?

The interglacial MIS 11 is characterised by a pronounced $\overline{\mathbf{SS}}$ low, similar in amplitude to MIS 31. Compared to the relatively gradual onset of the preceding MIS 13 $\overline{\mathbf{SS}}$ minimum, the MIS 12/11 transition is remarkably abrupt (Figure 6.8), occurring across only 2 or 3 samples (with δt around 1 kyr). The rapid termination of MIS 12 is reflected in a 'massive and prolonged' terminal ice-rafting event in the North Atlantic (Riveiros et al., 2013). MIS 11 is characterised by a sea-level high-stand up to 20 m above modern (Rohling et al., 1998) and a (partial) collapse of the West Antarctic Ice Sheet (Scherer, 1998). In the Southern Ocean, summer sea surface temperatures were over 2^oC warmer-than-Holocene in the modern Polar Frontal Zone (ODP 1094; Kunz-Pirrung et al., 2002) and Subantarctic Zone (Cortese et al., 2007). As with MIS 31, these results are coherent with poleward shifted Southern Ocean fronts, linked to a poleward migration of the SWWB (Tapia et al., 2021). The circum-Antarctic extent of this shift (Figure 6.8) is reflected in a similarly abrupt flow-speed minimum in the south-west Pacific (Hall et al., 2001) and a coincident spike in Drake Passage flow-speeds (Toyos et al., 2020).

Considering the MIS 11 and MIS 31 interglacials together, a picture emerges where an intense poleward shift in the SWWB appears to drive a poleward shift in the reach of

the ACC; evident in anomalously low $\overline{\mathbf{SS}}$ at the Agulhas Plateau and SW Pacific Ocean and high $\overline{\mathbf{SS}}$ in the Drake Passage. In the context of anthropogenic climate change, a poleward intensification of the SWWB has been attributed to anthropogenic forcing (Cai, 2006; Böning et al., 2008), however in the past (during the last deglaciation for example) shifting SWWB and Southern Ocean fronts appear to either lead (Anderson et al., 2009) or coincide with Riveiros et al. (2010) changes in CO_2. Anderson et al. (2009) suggest that this is due to the upwelling of carbon-rich SSW in response to the SWWB aligning with the ACC at the Drake Passage latitude-band (Toggweiler et al., 2006), although a synergistic increase in Agulhas Leakage in response to movement of the zero wind-stress curl latitude south of Africa (Bard and Rickaby, 2009; Peeters et al., 2004) may also occur. During MIS 31, the configuration of the ACC and PF is suggested to have warmed the Antarctic margin by enhancing the upwelling of relatively warm CDW and initiating a retreat of the West Antarctic Ice Sheet which further warmed the Southern Ocean, pulling the SWWB and ACC poleward (Beltran et al., 2020).

6.4.5 Surface-Deep Phasing

Interestingly, Riveiros et al. (2010) also find that changes in surface hydrography in the South Atlantic during the MIS 10/11 transition leads changes in the deep ocean during this transition by 2±1 kyr. Applying cross-correlation analysis to the intervals identified Figure 6.7 reveals a similar, though slightly larger temporal offset (4-6 kyr) between $\overline{\mathbf{SS}}$ and $\delta^{13}C$ following the MPT (<930 ka). Before this time, the maximum negative correlation occurs at a lag of 0 kyr (within the intervals average sampling resolutions of 1 - 1.9 ka). Blackman-Tukey phase estimates for the full time series (Figure 7.3) show that a lead for $\overline{\mathbf{SS}}$ over $\delta^{13}C$ is most clear in the obliquity frequency band (1/41 kyr), with a slight lead in the eccentricity band (1/100 kyr). This corroborates the observation that $\overline{\mathbf{SS}}$ maxima during Mid- to Late-Pleistocene glacials occurs relatively early in the glacial sequence, particularly during the transition from interglacial to glacial conditions, strongly influenced by obliquity in the Southern Hemisphere (Fogwill et al., 2015, ; Chapter 4).

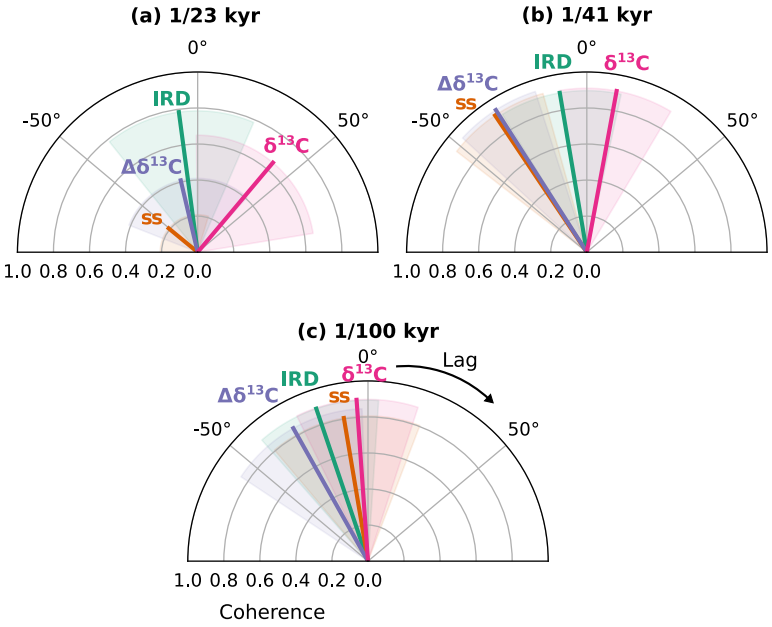

Figure 6.11: Blackman-Tukey phase estimates for AP_{comp} records against $\delta^{18}O_{benthic}$. The records are $\delta^{13}C_{benthic}$ (multiplied by -1; labelled $\delta^{13}C$; pink), log-transformed IRD_{MAR} (labelled IRD; green), $\Delta\delta^{13}C_{SAMW-CDW}$ (labelled $\Delta\delta^{13}C_{SAMW-CDW}$; purple) and $\overline{\mathbf{SS}}$ (orange). Phases are given in degrees relative to maximum $\delta^{18}O_{benthic}$ (0^o is in phase with $\delta^{18}O$ maximum, 90^o represents a half-cycle lag relative to $\delta^{18}O_{benthic}$ and 180^o equates to anti-phase). Shading represents the 95% confidence interval. *Performed with the Analyseries software (Paillard et al., 1996) after linearly interpolating (δt=3 kyr) and standardizing (mean = 0, standard deviation = 1) the data.*

A consistent lead-lag phasing is also present between IRD accumulation and $\delta^{13}C_{benthic}$ at this location (see Chapter 4; Starr et al., 2021), whereby IRD accumulation generally increases 1-2 kyr before $\delta^{13}C_{benthic}$ begins to decrease (i.e. SSW presence increases as NSW shoals). In Chapter 4, this temporal phasing is attributed to an early equatorward shift in the meltwater distribution of Antarctic icebergs, in response to a change in Southern Ocean surface hydrography, resulting in the 'escape' of positive buoyancy anomalies into the upper Atlantic circulation. This then perturbs the formation and/or density of NADW, thus reorganizing deep water-mass geometry at the Agulhas Plateau. The equatorward shift in iceberg trajectories is likely the result of some combination of changes in sea ice, Southern Ocean surface cooling and circulation patterns, and shifts in the SWWB; each of which can also be related to movement of the ACC (where not bathymetrically constrained; Sokolov and Rintoul, 2009). Therefore, a lead for Southern Ocean surface conditions over deep ocean hydrography during the transition from interglacial to glacial conditions is apparent in both the IRD - $\delta^{13}C$ and $\overline{\mathbf{SS}}$- $\delta^{13}C$ relationships at the Agulhas $Plateau_{comp}$.

Whilst this temporal phasing is present since atleast 1.5 Ma between IRD and $\delta^{13}C$, it only emerges after the MPT between $\overline{\mathbf{SS}}$ and $\delta^{13}C$. This might be attributed to differences in the dominant factors controlling ACC strength/position and iceberg trajectories. For example, sedimentological records from the Atlantic Southern Ocean sector suggest that northward shifts in the glacial Polar Front position increased after ~1.1 Ma (Diekmann and Kuhn, 2002) or ~0.9 Ma (Kemp et al., 2010), whereas the Subtropical Front south of Africa, north of which waters are too warm to sustain substantial iceberg drift, may have already reached its northernmost position by ~1.4 Ma (Cartagena-Sierra et al., 2021). Such a diachronous evolution of different Southern Ocean fronts would carry important implications for nutrient dynamics and possibly export productivity across the MPT, due to the contrasting response of the Antarctic and Subantarctic Zones to different boundary conditions (Jaccard et al., 2013).

6.5 Concluding Remarks: The circum-Antarctic View

The Agulhas Plateau flow speed record shows distinct variations across globally-significant climate transitions of the past 1.9 Ma (e.g the MPT and MBT). To summarize, exceptionally warm intervals such as MIS 31 and MIS 11 correspond to flow speed minima. On the other hand, maxima correlate to glacial conditions, with a notable peak at the onset of the '900 ka event' from MIS 24 to MIS 22. The onset of a pervasive negative correlation between $\overline{\mathbf{SS}}$ and $\delta^{13}C_{benthic}$ at ~1.6 Ma coincides with a state change in the glacial-interglacial overturning behaviour of overturning circulation at this time, and the development of distinct intermediate-deep chemocline during glacials. Generally, high flow speed during glacial intervals is associated with indications of an equatorward displacement of the STF (Cartagena-Sierra et al., 2021; Bard and Rickaby, 2009; Schaefer et al., 2005; Sikes et al., 2009), SAF (Becquey and Gersonde, 2002; Ho et al., 2012), and PF (Gersonde et al., 2005; Weaver et al., 1998), although decoupling between the STF and ACC is apparent during some intervals (i.e. MIS 30 to MIS 25). As discussed above, this might reflect additional influences on the SWWB - ACC - Southern Ocean fronts relationship (such as anomalously high sea-ice, as proposed for MIS 22). It may also reflect additional influences on the $\overline{\mathbf{SS}}$

record, such as local hydraulic or sediment dynamics, or on the records of frontal position utilized. Kohfeld et al. (2013) demonstrate that connecting reconstructions of frontal positions with changes in the SWWB and the ACC is not straightforward, relying on assumptions regarding the definition of fronts and their relationship with wind forcing. Much of the discussion in this chapter has applied the assumption that the position of the ACC is directly dependent on the position of the SWWB, and is intimately connected with Southern Ocean fronts, however this assumption may break down under certain conditions.

For example, in several regions of the Southern Ocean the position of ACC jets are tightly constrained by the topography of the sea-floor (Graham et al., 2012). One way to untangle the influence of shifting SWWB on the ACC is to compare records from different regions. For example, in contrast to the Agulhas Plateau, flow speed in the Drake Passage region generally decreased during glacial intervals (though results are not unanimous, and it is dependent on where sites are positioned relative to major flow paths; McCave et al., 2013). The ACC is constrained by the South American continent in the Drake Passage, and an equatorward shift in the SWWB and the SAF would disconnect the ACC from the ocean surface in this region (Lamy et al., 2015). This is supported by records tracking the SWWB position over South America (Herman and Brandon, 2015), and (indirectly) the south-east Pacific Ocean (Mohtadi and Hebbeln, 2004; Ho et al., 2012). Furthermore, $\overline{\mathbf{SS}}$ from a site in the south-east Indian Ocean also reveals lower glacial flow-speeds (Figure 6.12; Williams et al., 2021). The ACC here is highly constrained by bathymetry (notably the Kerguelen - Ile St Paul Passage) and so a similar response in the Drake Passage might be expected. Recent micropaleontological work from this region suggests that the PF was positioned north of the Kerguelen Plateau during the last glacial maximum (Figure 6.12; Civel-Mazens et al., 2021). This might suggest that the SAF ACC jets were displaced north of the Ile St Paul plateau. Further work is required to elucidate circulation changes in this region.

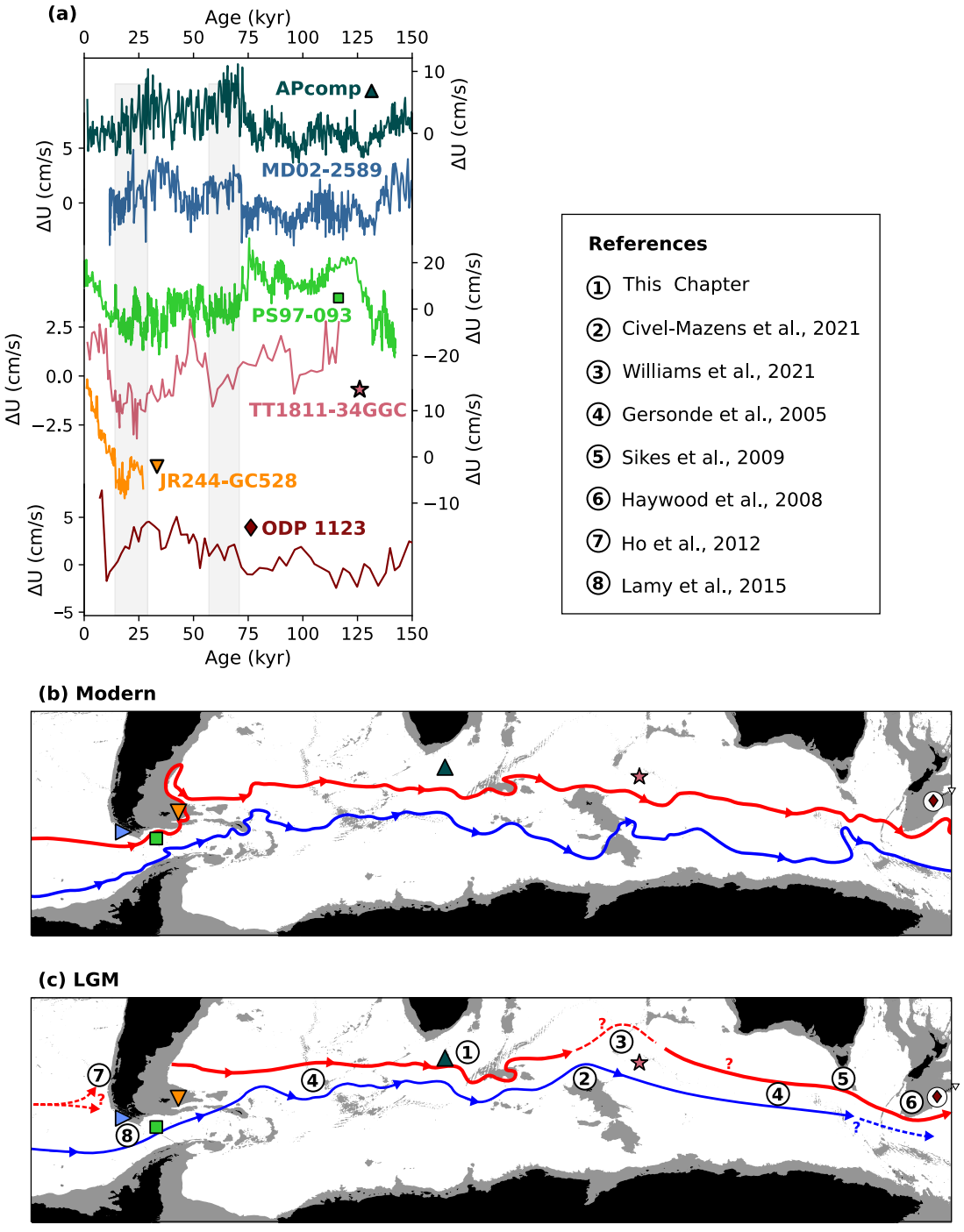

Figure 6.12: Circum-Antarctic view of glacial ACC and frontal positions. **(a)** from top to bottom: $\overline{\mathbf{SS}}$ time series from the AP_{comp} (this chapter), MD02-2589 (Molyneux et al., 2007), PS97-093 (Wu et al., 2021), TT1811-34GGC (Williams et al., 2021), JR244-GC528 (Roberts et al., 2017), ODP Site 1123 (Hall et al., 2001). $\overline{\mathbf{SS}}$ is converted to ΔU by subtracting the mean and applying the slope of McCave et al. (2017). **(b-c)** Schematic showing modern (b) and proposed Last Glacial Maximum (c) position of SAF (red) and PF (blue). Modern position is from Park et al. (2019) and LGM position is predicted from the references given in the key (question marks and dashed lines represent particularly uncertain predictions). Bathymetry is from the ETOPO2 dataset; shading is <2000m.

The ACC, Deep Upwelling, and the Southern Ocean Chemocline: A case not closed?

The heterogeneous results from the Drake Passage, Agulhas region, and south-east Indian Ocean emphasize the spatially non-uniform behaviour of the ACC (Figure 6.12a). Figure 6.12c synthesizes the available reconstructions of the ACC frontal positions during the Last Glacial Maximum. It shows that the PF and SAF migrate to varying degrees in different Southern Ocean sectors. For example, both fronts may have shifted by several degrees in the south-west Indian Ocean, whilst around the Campbell Plateau there was minimal change in the SAF but possibly an equatorward migration of the PF. What are the implications of this glacial ACC configuration in terms of the deep ocean? Firstly, if it reflects an equatorward migration of the SWWB, the work of Toggweiler et al. (2006) suggests a corresponding decrease in the upwelling of deep (>2500m) in the Southern Ocean. Furthermore, the results presented here for the most-part support an ACC - deep ventilation coupling, which developed after ~1.6 Ma and was coincident with the intensification of the glacial chemocline (Lisiecki, 2014; Hodell and Venz-Curtis, 2006). Major climate transitions manifest clearly in near-bottom flow speed at the Agulhas Plateau, suggesting an ACC which is highly responsive to particularly warm (MIS 31, MIS 11) periods as well as state changes in global glacial conditions (the '900 ka Event'). Supporting previous work (Chapter 4), an early response for Southern Ocean conditions relative to the deep ocean and global climate is observed; this might reflect the importance of feedbacks in the Southern Ocean such as the 'southern escape' of meltwater during glacials or the poleward ACC contraction during warm interglacials. However, it is not clear whether Southern Ocean upwelling and overturning circulation are driven primarily by SWWB forcing; Such a forcing has been questioned by some models (Hallberg and Gnanadesikan, 2006) and a combination of wind and buoyancy forcing is likely required to explain past changes in this system (Anderson et al., 2009).

7 | Synthesis: The Evolution of Glacial Cycles as viewed from the Agulhas Plateau and Proposed Future Work

7.1 Introduction

In the previous chapters, new and existing sediment core records from the Agulhas Plateau have been used to build a picture of of surface and deep paleoceanography over the past 2 million years (myr). These records cover a range of time-scales, from glacial-interglacial cycles to transitions and long-term trends which pervade the Pleistocene climate system. By comparing and contrasting each record, an opportunity arises to understand how different components of the climate system evolved with respect to each other across cycles and transitions. The availability of multiple co-registered proxy records from a single sediment core site (here, the Agulhas Plateau Composite; AP_{comp}) provides insights into the coupling between different environmental processes free from uncertainties which arise from comparing across different stratigraphic sequences.

Located at the junction between the Indian, Atlantic and Southern Ocean, the Agulhas Plateau is situated in a complex and globally-significant oceanographic region (e.g. Lutjeharms and Ansorge, 2001). At the Agulhas Retroflection to the north-west of the Agulhas Plateau, inter-basin exchange of warm, saline Indian Ocean waters into the Atlantic via the 'Agulhas Leakage' represents a key component in the return of shallow waters to the North Atlantic. This exchange balances the export of NADW from the Atlantic basin into the Indian and Southern Oceans, an important pathway

in the spread of North Atlantic Deep Water (NADW) across the globe (Bower et al., 2019). This deep-water export is intimately linked to the sedimentary environment on the Agulhas Plateau (Uenzelmann-Neben, 2002). Furthermore, multiple hydrographic fronts are present in the region, as cool and relatively fresh Southern Ocean surface waters meet the warmer, more saline subtropical Indian and Atlantic waters. This results in complex biogeochemical dynamics in the region. Stark gradients exist in the distributions of nutrients, phytoplankton, and primary productivity (Read et al., 2000), and further complexities are introduced by the influence of mesoscale eddies in the region (Gordon et al., 1987). Finally, the location of the southern-most Agulhas Plateau at the extreme equator-ward reach of far-travelled Antarctic icebergs (Chapter 4; Starr et al., 2021) makes it a useful location for studying iceberg drift across the Southern Ocean in the past.

In this chapter, I briefly review the results from previous chapters, considering how they build on previous work from the region, before synthesising the new records and discussing their evolution through the Pleistocene. Finally, I propose directions for future work which would build upon the results presented in this thesis, towards the goal of better understanding the role that surface-deep ocean coupling plays in the climate system.

7.2 The Agulhas Plateau Sediment Record

The combination of complex and globally significant surface dynamics (i.e. Agulhas Leakage; Beal et al., 2011), and a deep water column which is highly sensitive to changes in the Atlantic and Southern Ocean overturning circulation cells, makes the Agulhas Region* a prime target for paleoceanographic reconstructions. Sediment core records produced over the past decades have revealed a number of valuable insights into the Agulhas Region's role in the climate system, regionally and globally (e.g. Martínez-Méndez et al., 2010; Ziegler et al., 2013; Simon et al., 2013; Peeters et al., 2004; Bard and Rickaby, 2009; Franzese et al., 2009; Caley et al., 2012, 2018;

*'Agulhas Region' here refers to the area between the southern African continent and the Southern Ocean, under the influence of the Agulhas Current and it's successors.

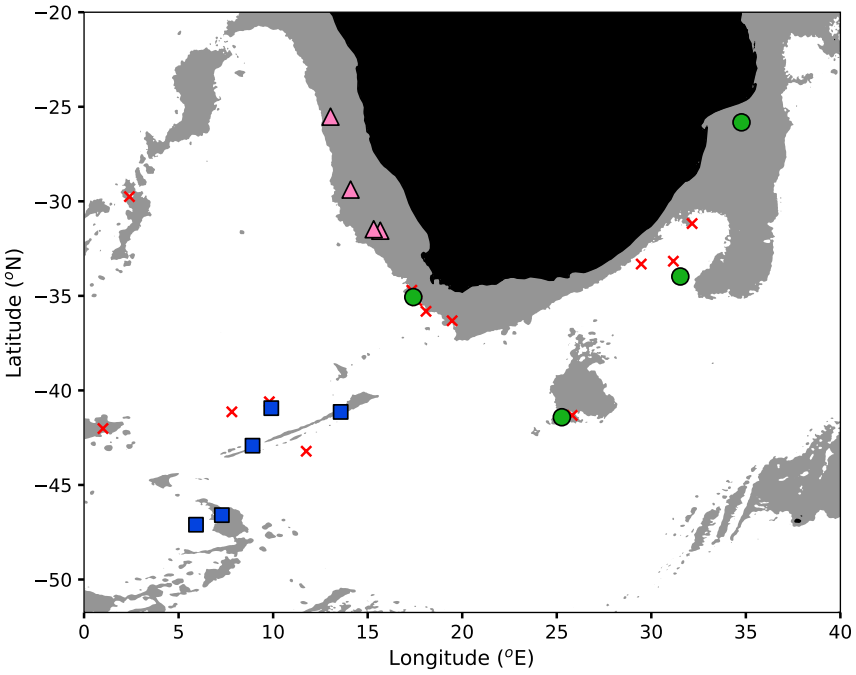

Figure 7.1: The distribution of selected sediment core locations in the Greater Agulhas Region. Red crosses represent 'short' gravity or piston core sites generally spanning the Late Pleistocene interval. Green circles are core sites drilled during IODP Expedition 361 (Hall et al., 2017b), pink triangles are sites drilled during ODP Leg 175 (Wefer et al., 1998) and blue squares are sites drilled during ODP Leg 177 (Hodell, 1999). The sea-floor shallower than 3000m is shaded (data from ETOPO1 1 Arc-Minute Global Relief Model, Geophysical Data Center, 2009))

Flores et al., 1999; Taylor et al., 2021; Cartagena-Sierra et al., 2021). Figure 7.1 shows the distribution of selected sediment core locations in the region, including 'short' piston and gravity cores (red crosses) as well as longer archives recovered during Ocean Drilling Program (ODP) Leg 175 (Wefer et al., 1998) and Leg 177 (Hodell, 1999) and International Ocean Discovery Program (IODP) Expedition 361 (Hall et al., 2017b).

7.2.1 Agulhas Leakage

An important aim for paleoceanographic studies in the region has been understanding how Agulhas Leakage has changed in the past. Faunal assemblage studies have revealed a dynamic history for the Agulhas Leakage, seemingly reduced during glacial intervals with abrupt peaks in inter-ocean exchange during deglaciations (Peeters et al., 2004; Caley et al., 2014). This pattern extends back through much of the Mid- to

Proxy	Range	Reference
$\delta^{18}O_{benthic}$	0-3200	0-350 Ziegler13; 350-3200*
$\delta^{13}C_{benthic}$	0-3200	0-350 Ziegler13; 350-3200*
$\delta^{13}C_{G.trunc.\cdot}$	0-1550	0-350 Ziegler13; 350-1550*
$\delta^{18}O_{G.trunc.}$	0-1550	0-350 Ziegler13; 350-1550*
IRD_{MAR}	0-1700	0-350 Simon13, Marino13; 350-1700*
$\overline{SS}$	0-1950	0-150 Charidemou18; 150-1950*
$U_{37}^{K'}$	0-1450	0-350 Romero15; 350-1450 Cartagena21
Alkenone AR	0-1450	0-350 Romero15; 350-1450 Cartagena21

Table 7.1: Records used in this chapter. Range is given in ka, and references are given after the interval across which the proxy record was published. References refer to: Ziegler13 = Ziegler et al. (2013), Simon13 = Simon et al. (2013), Marino13 = Marino et al. (2013), Charidemou18 = Charidemou (2018), Romero15 = Romero et al. (2015), Cartagena21 = Cartagena-Sierra et al. (2021). * refers to new data presented in this thesis.

Late-Pleistocene (Caley et al., 2012), and has been causally linked to the resumption of a strong AMOC mode during deglaciations (Knorr and Lohmann, 2003; Peeters et al., 2004; Chiessi et al., 2008; Dyez et al., 2014). Records of surface conditions suggest that during glacial intervals, diminished Agulhas Leakage coincided with an equatorward shift in the Subtropical Frontal Zone (STFZ) (Peeters et al., 2004; Flores et al., 1999; Bard and Rickaby, 2009; Caley et al., 2012; Marino et al., 2013). Modelling studies have investigated this connection, however the dominant control on Agulhas Leakage remains unresolved. Candidates for this mechanism include the latitude of zero wind-stress curl (Biastoch et al., 2009), the strength of the Southern Hemisphere westerly wind belt (Durgadoo et al., 2013), or other factors such as the strength of the upstream Agulhas Current (van Sebille et al., 2009). Times in the past during which Agulhas Leakage was weaker or stronger than today therefore provide natural experiments from which paleoclimate studies might gain a better understanding of these potential drivers.

Agulhas Leakage impacts overturning circulation and hence global climate in a number of ways, most notably by altering the thermohaline conditions and thus deep-water formation in the Atlantic Ocean (Knorr and Lohmann, 2003; Biastoch et al., 2008). Essentially, an increase in the exchange of positive density anomalies from the Indian Ocean leads to a more saline Atlantic, and subsequently a stronger and more stable AMOC (Beal et al., 2011). Whilst the magnitude of Agulhas Leakage can

therefore modify the density field in the Atlantic Ocean, it follows that so too could changes in the 'upstream' properties of Agulhas waters (Simon et al., 2013). Reconstructions of surface temperature and salinity in the region have shown that salinity changes in the Southeast Atlantic over the Late Pleistocene (Kasper et al., 2014; Marino et al., 2013; Dickson et al., 2010) might be linked to changes in the salinity of the Agulhas Current (Simon et al., 2013), influenced by the cross-frontal incursion of relatively fresh Southern Ocean surface waters into the Southwest Indian Ocean gyre (Marino et al., 2013; Simon et al., 2013, 2020).

7.2.2 The Southern Escape of buoyancy forcing

In Chapter 4, this concept was developed further by extending the existing 350 kyr-long record of IRD_{MAR} from the AP_{comp} back to 1.65 Ma. This record (Figure 7.2c) revealed the quasi-periodic presence of Antarctic icebergs at the Agulhas Plateau since at least the latter part of the Early Pleistocene, superimposed over long-term trends linked to the Mid-Pleistocene Transiton (MPT). Furthermore, the co-registered $\delta^{13}C_{benthic}$ record allowed a direct analysis of the phasing between surface conditions (IRD_{MAR}) and deep water-mass dynamics ($\delta^{13}C_{benthic}$). A combination of statistical approaches testing the phasing between IRD_{MAR} and $\delta^{13}C_{benthic}$ revealed a persistent 1-2 kyr lead for changes in iceberg presence over changes in deep ventilation during glacial intervals. By comparing the IRD_{MAR} proxy record to iceberg trajectory model experiments, it was shown that a glacial shift in iceberg trajectories and hence meltwater across the Atlantic-Indian Southern Ocean could result in a substantial redistribution of freshwater, with positive buoyancy anomalies moving further from regions of AABW formation and towards the subtropical AMOC return limb.

Simon et al. (2013) proposed that changes in cross-frontal exchange altered the thermohaline properties transmitted into the Atlantic by Agulhas Leakage. The results in Chapter 4 took this further, suggesting that an equator-ward shift in Antarctic iceberg melt-water would amplify this effect, facilitating the 'escape' of buoyancy anomalies from the Southern Ocean, freshening the Indian Ocean gyre and hence Agulhas Leakage, as well as plausibly entering the South Atlantic by cross-frontal exchange

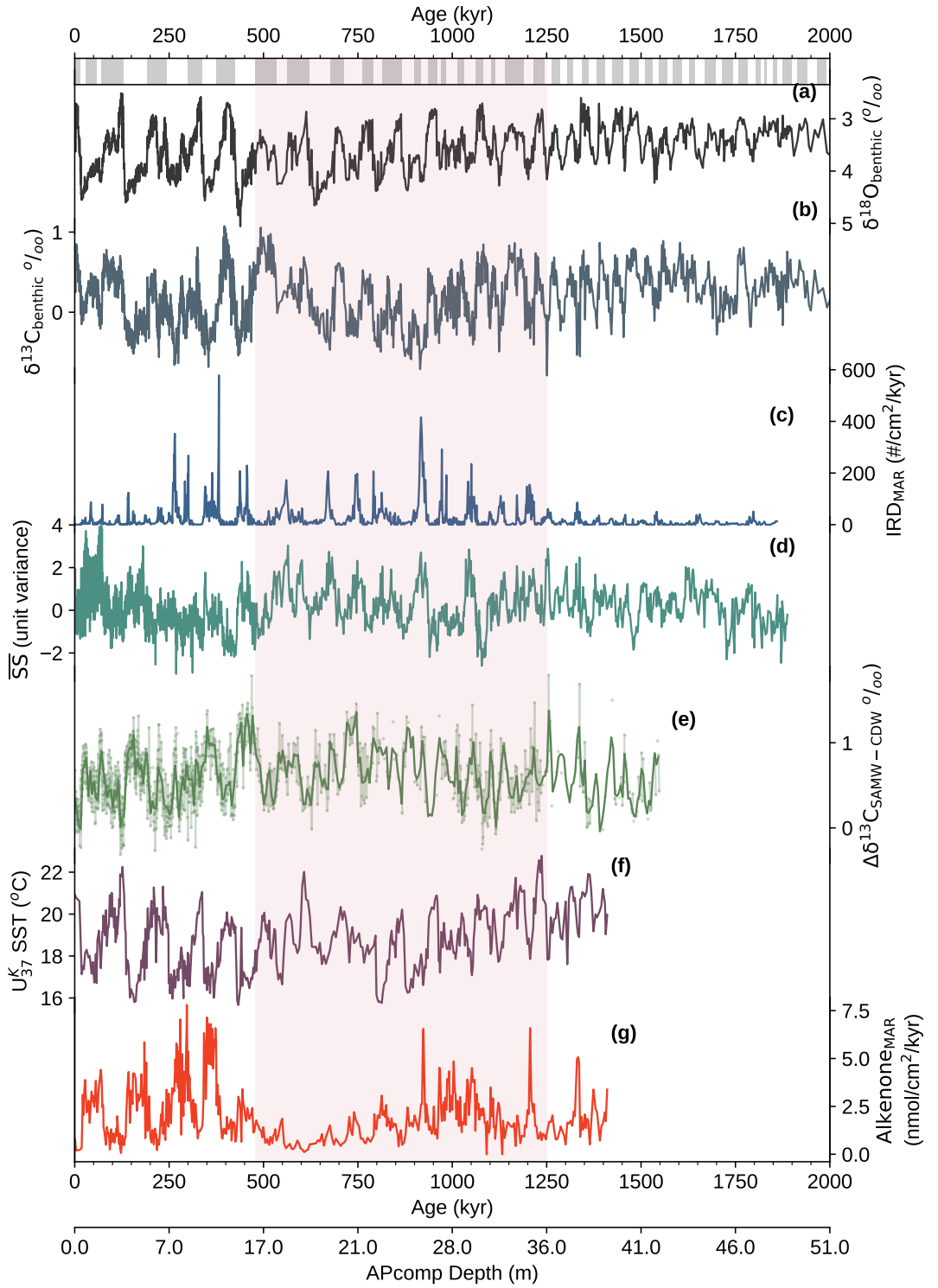

Figure 7.2: A compilation of new and published records spanning the Middle to Late Pleistocene from the AP_{comp}. **(a)** $\delta^{18}O_{benthic}$, **(b)** $\delta^{13}C_{benthic}$, **(c)** Ice-Rafted Debris (IRD) Mass Accumulation Rate (MAR), **(d)** Sortable Silt mean grain size (standardized to mean = 0 and standard deviation = 1), **(e)** The carbon isotope gradient between *G. truncatulinoides (s)* and *C. wuellerstorfi*, **(f)** $U^{K'}_{37}$ sea surface temperature from Romero et al. (2015) and Cartagena-Sierra et al. (2021), **(g)** alkenone accumulation rate from Romero et al. (2015) and Cartagena-Sierra et al. (2021). A secondary x-axis is given showing the AP_{comp} depth scale. The pink shading indicates the MPT interval and the grey bars at the top indicate glacial Marine Isotope Stages following Lisiecki and Raymo (2005).

to the west of the Agulhas Plateau. This mechanism was then linked to an inter-hemispheric teleconnection, operating between the 'Southern Escape' of freshwater and the changes in NADW formation.

7.2.3 Biogeochemistry and the deep chemical divide in the Agulhas Region

Moreover, reconstructions of surface conditions around the Agulhas Plateau have provided insights into nutrient dynamics, primary productivity, and carbon export in the past (e.g. Romero et al., 2015; Tangunan et al., 2021; Cartagena-Sierra et al., 2021; Diz et al., 2007). The proximity of the Agulhas Plateau to steep hydrographic fronts and highly dynamic surface circulation means that biological processes in the upper water column varied considerably in the Pleistocene. For example, distinct glacial-interglacial variations in primary productivity (Romero et al., 2015; Tangunan et al., 2021; Cartagena-Sierra et al., 2021), coccolithophore (Tangunan et al., 2021), diatom (Romero et al., 2015), and benthic foraminifera community structure (Diz et al., 2007) likely reflect frontal migrations and the injection of nutrients from Southern Ocean waters and deep mixing at the fronts (Read et al., 2000). Superimposed on these glacial-interglacial cycles are more complex ecological responses to additional drivers such as local insolation cycles (Tangunan et al., 2021; Romero et al., 2015). Records of biomarker accumulation over the past 1.4 myr (Figure 7.2g; Cartagena-Sierra et al., 2021) highlight the complexity of regional biogeochemistry.

While records of surface biogeochemistry from the Agulhas Plateau provide information regarding regional dynamics in fronts and insolation forcing, the sub-surface water column in the region is composed of mode and intermediate waters integrating biogeochemical signals over a much wider area. Ziegler et al. (2013) showed that the carbon isotope gradient between Subantarctic Mode Water (SAMW) and Circumpolar Deep Waters (CDW) reconstructed at the Agulhas Plateau from sub-surface and bottom dwelling foraminifera was closely tied to changes in Southern Ocean productivity and dust fluxes, as well as atmospheric CO_2 levels during glacial and millennial-scale cold periods of the past 350 kyr. The development of a chemical

gradient between intermediate and deep waters is an established phenomenon in the glacial ocean (Hodell et al., 2003; Charles et al., 2010; Ninnemann and Charles, 1997), reflecting the export of isotopically-light carbon from the surface to the deep ocean likely due to some combination of high surface productivity and reduced deep water ventilation.

In Chapter 5, new and previously published stable isotope records of the deep-dwelling planktic foraminifer *G. truncatulinoides* (s) (0-350 kyr published in Ziegler et al., 2013) and the benthic *C. wuellerstorfi* (0-350 kyr published in Ziegler et al., 2013) were combined to extend the record of $\Delta\delta^{13}C_{(SAMW-CDW)}$ back to the Early Pleistocene. This new data provides an insight into how the vertical fractionation of carbon between ocean layers evolved across longer intervals, for example spanning the MPT (Figure 7.2e). Two key insights were gained from this dataset: 1) the magnitude of glacial $\Delta\delta^{13}C_{(SAMW-CDW)}$ does not change across the MPT, suggesting that either export productivity in the Subantarctic Zone did not evolve substantially (c.f. Chalk et al., 2017), or that additional factors operate on these longer timescales which may mask the export productivity signal identified by Ziegler et al. (2013). 2) There are clear long-term fluctuations in $\Delta\delta^{13}C_{(SAMW-CDW)}$, which seemingly align with 400-kyr cycles in Earth's orbital eccentricity. This low frequency variance is expressed most clearly in the modulation of glacial values and might therefore provide insights into similar (though not identical) secular variations in other records of the marine carbon cycle (Rickaby et al., 2007; Barker et al., 2006; Wang et al., 2010). Furthermore the modulation of glacial $\Delta\delta^{13}C_{(SAMW-CDW)}$ is linked to a decoupling from records of atmospheric CO_2, apparently at odds with findings from the Late Pleistocene (Ziegler et al., 2013).

In Chapter 5, a mechanism is put forward connecting this 400 kyr periodicity to changes in the formation of SAMW (ventilation of the sub-surface water column), driven by changes in meridional atmospheric circulation patterns and the meridional insolation gradient. Evidence for such a link can be found in the 400-kyr periodicity of several records of African hydroclimate (e.g. Caley et al., 2018), however further work is required to provide more direct evidence supporting this mechanism. Furthermore the implications of this mechanism in the context of the oceanic carbon

cycle remain unresolved; *does the 400-kyr carbon isotope gradient cycle relate to ~500-kyr cycles which pervade other records of ocean productivity, carbonate dissolution, and Southeast Asian monsoon proxies?*

7.2.4 Pleistocene deep hydrography at the Agulhas Plateau

The deep water column over the modern Agulhas Plateau is characterised by the competing presence of NADW and deep/bottom waters of Southern Ocean origin (Arhan et al., 2003), representing a junction between the upper (NADW) and lower (Southern Ocean waters) overturning circulation cells (Talley, 2013). Deep hydrography at the Agulhas Plateau is therefore highly sensitive to shifts in the presence of NADW (Molyneux et al., 2007), making it an ideal location to test hypotheses regarding the strength, depth and export of NADW from the Atlantic basin in the past, thought to exert an important influence on global climate (e.g. Sikes et al., 2017).

Furthermore, near-bottom flow speeds in the region are closely linked to regional and circum-Antarctic circulation dynamics. Records of 'Sortable Silt' mean grain size proxy ($\overline{\mathbf{SS}}$; see Chapter 2) reveal relatively vigorous bottom-currents at 2500m – 3000m water depths during glacial intervals (Martínez-Méndez et al., 2008; Molyneux et al., 2007), reflecting the strengthening and/or equator-ward migration of deep-reaching Antarctic Circumpolar Current (ACC) jets. Generally, flow-speed changes mirror NSW presence, as indicated by nutrient and water-mass provenance proxies such as Ca/Cd (Martínez-Méndez et al., 2008), $\delta^{13}C_{benthic}$ (Molyneux et al., 2007) and ϵNd (Rutberg et al., 2000), however intervals of decoupling between flow vigour and chemical ventilation have been identified (e.g. the MIS 6/5 transition; Molyneux et al., 2007).

In Chapter 6, a 1.9 myr-long record of $\overline{\mathbf{SS}}$ is presented from the AP_{comp}, providing one of the longest continuous near-bottom flow speed records in the Southern Hemisphere. This record shows that high near-bottom flow speeds prevailed consistently during glacial intervals of the Middle and Late Pleistocene, mirroring reduced chemical ventilation (low $\delta^{13}C_{benthic}$) and high IRD_{MAR} deposition. Some exceptions to this pattern are evident during MIS 28 and MIS 22, where $\overline{\mathbf{SS}}$ remained at interglacial

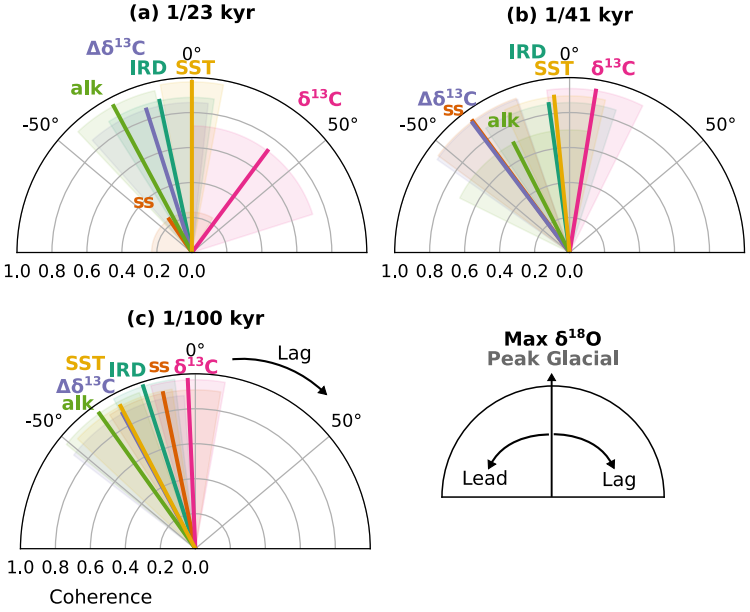

Figure 7.3: Phase wheels showing the phase of AP_{comp} proxy records relative to $\delta^{18}O_{benthic}$; All records are limited to 0 to 1400 ka for a more direct comparison. SST is sea surface temperature, $\Delta\delta^{13}C$ is $\Delta\delta^{13}C_{SAMW-CDW}$, IRD is IRD_{MAR}, alk is Alkenone accumulation rate, $\delta^{13}C$ is $\delta^{13}C_{benthic}$. **(a)** 1/23 kyr band, **(b)** 1/41 kyr band, **(c)** 1/100 kyr band. SST and alkenone accumulation rate data are from Romero et al. (2015) and Cartagena-Sierra et al. (2021)

levels. In Chapter 6, at least 4 transitions are identified in the $\overline{\mathbf{SS}}$ record, marking changes in either the variance, mean, or trend in the data (and identified using an array of 'change-point detection' algorithms). Two of these transitions correspond to distinct maxima and minima between 1.1 Ma and 0.9 Ma, coinciding with an acme of global changes linked to the MPT (Clark et al., 2006), and signifying the transition from shorter, lower amplitude pre-MPT $\overline{\mathbf{SS}}$ cycles, into longer, higher amplitude cycles after the MPT. As previously hypothesised, the MPT is characterised by dramatic fluctuations in Southern Ocean conditions (Martínez-Garcia et al., 2011; Rodríguez-Sanz et al., 2012), possibly relating to the migration of oceanic fronts (Kemp et al., 2010) or swings in the Southern Hemisphere westerly wind belt. This hypothesis finds support in the AP_{comp} flow speed record, which in particular highlights the significance of interglacial and well as glacial intervals through the transition. For example, exceptionally low flow speed anomalies during the warm MIS 31 imply an anomalous weakening or poleward shift in the ACC. *What are the implications of this for circulation and the upwelling of carbon-rich deep waters in the Southern Ocean during this interval?*

7.3 Synthesis: Phasing and the glacial sequence of events

Figure 7.3 shows a synthesis of the relative phasing of Pleistocene AP_{comp} records (Table 7.1). Expanding on analysis from the previous chapters, these 'phase wheels' provide a summary of the timing of peaks and troughs at different periodicities, relative to the AP_{comp} $\delta^{18}O_{benthic}$ record. Only data collected from the AP_{comp} is included in this analysis, to avoid the potential for spurious lead-lag relationships introduce by tuning across records. For example, Skinner and Shackleton (2005) show that offsets on the order of 4 kyr are present between deep Pacific and Atlantic Ocean $\delta^{18}O_{benthic}$ records across the last glacial termination.

7.3.1 1/23 kyr band

Figure 7.3a shows the phase in the 1/23 kyr 'precession' band. All records apart from SST and $\delta^{13}C_{benthic}$ lead relative to maximum $\delta^{18}O_{benthic}$ at this frequency. As demonstrated in Chapter 4, IRD_{MAR} leads relative to $\delta^{13}C_{benthic}$ (possibly an indication of the 'Southern Escape' mechanism), and interestingly so too do alkenone accumulation rate and $\Delta\delta^{13}C_{SAMW-CDW}$. This suggests that there may be a common mechanism linking productivity, mode water formation and IRD deposition at the Agulhas Plateau in this frequency-band, such as meridional shifts in Southern Ocean fronts or the intensity/position of the Southern Hemisphere westerly wind belt (SWWB). Interestingly, SST is in-phase with $\delta^{18}O_{benthic}$, suggesting that global, rather than regional controls dominate the SST signal at this frequency (in other words, the coldest temperatures occur at maximum ice volume and vice versa). A similar in-phase relationship between SST and ice volume has been shown in the South Indian Ocean (Howard and Prell, 1994) and the equatorial Atlantic (Villanueva et al., 1998), however it contrasts the substantial lag for SST found in the North Atlantic at this frequency (Lisiecki et al., 2008; Ruddiman and McIntyre, 1981). The North Atlantic lag has been attributed to a moisture feedback imposing a time constant on North Atlantic temperatures or a tight link between SST and the 'upper' overturning circulation cell (Lisiecki et al., 2008; Lisiecki, 2014; Ruddiman and McIntyre, 1981).

Interestingly, $\overline{\mathbf{SS}}$ and $\delta^{18}O_{benthic}$ are not significantly coherent at this band, due to the absence of precession-band power in the $\overline{\mathbf{SS}}$ auto-spectrum (Chapter 6).

7.3.2 1/41 kyr band

Figure 7.3b shows the same as panel 7.3a, but for the 1/41 kyr 'obliquity' band. Similarly to the precession band, all but $\delta^{13}C_{benthic}$ lead $\delta^{18}O_{benthic}$ at this frequency. SST and IRD_{MAR} both lead $\delta^{18}O_{benthic}$ by a similar magnitude, and a larger lead is seen for $\overline{\mathbf{SS}}$, $\Delta\delta^{13}C_{SAMW-CDW}$, and alkenone accumulation. Once again the lead for surface conditions over global ice volume and $\delta^{13}C_{benthic}$ imply an 'early' response to glacial cycles in the Southern Ocean, perhaps reminiscent of the 'early-LGM' which characterises Southern Hemisphere mid-latitude terrestrial records and glacial extent (Vandergoes et al., 2005; Newnham et al., 2007) and has been theorised to result from obliquity forcing of the SWWB and storm tracks (Fogwill et al., 2015; Rother et al., 2014; Timmermann et al., 2014). One plausible explanation for the $\sim 40 \pm 12^{o}$ lead for $\Delta\delta^{13}C_{SAMW-CDW}$ and $\overline{\mathbf{SS}}$ over $\delta^{18}O_{benthic}$ would be through a strengthening or equatorward shift in the SWWB (and hence ACC) early in the glacial sequence of events, paced by the enhancement of meridional heat transport at times of low obliquity (Timmermann et al., 2014). In this framework, changes in $\Delta\delta^{13}C_{SAMW-CDW}$ might be intimately linked to $\overline{\mathbf{SS}}$ on obliquity time-scales through the invigoration of mode-water formation (i.e. intensified deep winter convection in the mid-latitude Southern Ocean), as outlined in Chapter 5.

7.3.3 1/100 kyr band

Figure 7.3c shows the results in the 1/100 kyr 'eccentricity' band. Phasing at this frequency with respect to orbital forcing is perhaps the most difficult to interpret due to the near-absence of direct 1/100-kyr forcing of insolation cycles. With the exception of $\delta^{13}C_{benthic}$ which is roughly in-phase, all the records lead $\delta^{18}O_{benthic}$ at this frequency. This is coherent with the findings of Shackleton (2000), who shows that the $\sim$1/100 kyr cyclicity in global ice volume appears to originate from changes in the global carbon cycle, rather than ice-sheet dynamics as per earlier theories (e.g.

Imbrie et al., 1984). It is important to note here that Shackleton (2000) questions the fidelity of the phase of $\delta^{18}O_{benthic}$ as a proxy for the phase of global ice volume due to the 'contamination' by deep ocean temperature changes. The confounding impacts of temperature versus ice volume changes in $\delta^{18}O_{benthic}$ records has been shown to manifest as a rapid deep ocean cooling during the more gradual built up of ice (Bintanja et al., 2005; Elderfield et al., 2012). This means that the observed lag of $\delta^{18}O_{benthic}$ in Figure 7.3 may make for conservative estimates of ice volume lag when isolated from temperature.

Across all three frequency bands a common pattern prevails: changes in SST, IRD deposition, productivity, intermediate-deep chemical gradient and near-bottom flow vigour all generally lead relative to $\delta^{18}O_{benthic}$. If $\delta^{18}O_{benthic}$ is taken as an approximation of global ice volume, this suggests that the response of surface and subsurface conditions at the Agulhas Plateau to Pleistocene climate cycles is an early one, coherent with the idea of asynchronous glacial dynamics between the Northern and Southern Hemispheres. The consistent lag for $\delta^{13}C_{benthic}$ over the other records carries interesting implications for the sequence of events which characterise glacial cycles. For example, the Imbrie et al. (1992) and Imbrie et al. (1993) model of glacial cycles proposes that Northern Hemisphere summer insolation forcing triggers a 'train of responses' with cooling transmitted from the Arctic/Nordic Seas to the Southern Ocean via NADW. By cooling the surface Southern Ocean and triggering changes in Antarctic sea-ice, for example, the response is globalised by lowering atmospheric CO_2 levels. In this model, one might expect a relatively early signal in $\delta^{13}C_{benthic}$ due to the potential role of Antarctic sea ice and Southern Ocean surface conditions in setting AABW formation and glacial water-mass geometry (Ferrari et al., 2014). However, the delayed response of $\delta^{13}C_{benthic}$ at the AP_{comp} might instead implicate a 'northern pull' mechanism where changes in the depth and/or export of NADW at the Agulhas Plateau are driven by changes in the North Atlantic, for example through feedbacks such as the 'southern escape' of meltwater outlined in Chapter 4 or the 'train of responses' returning to the North Atlantic through to Southern Ocean-driven atmospheric CO_2 forcing. Govin et al. (2009) showed that the expansion of AABW (inferred from $\delta^{13}C_{benthic}$ at deep Southern Ocean sites, >3400m) during the MIS 5e/5d transition preceded changes in $\delta^{13}C_{benthic}$ at the shallower Agulhas Plateau

core site MD02-2589 (2660m; Molyneux et al., 2007) by several kyr, suggesting a decoupling between Southern Ocean bottom water formation and NADW presence in the mid-depth Southern Ocean. This is fitting with the proposed effect of early Southern Ocean cooling and/or sea ice expansion on timing of AABW changes and a delayed response of NADW formation tied to the subsequent response of Northern Hemisphere ice sheets (*à la* Imbrie et al., 1992).

7.4 Synthesis: Manifestations of the MPT in AP_{comp} records

In addition to investigating the phasing between proxy records from the AP_{comp}, it is also possible to identify the emergence of low-frequency (~1/100 kyr) power associated with the MPT (Clark et al., 2006). In this respect, changes in IRD_{MAR}, SST, and alkenone MAR can provide insights into surface hydrography evolution. Changes in the carbon isotope composition of *G. truncatulinoides* and, to an extent (see Chapter 5), $\Delta\delta^{13}C_{SAMW-CDW}$ reflects the evolution of the subsurface water column. Benthic stable isotopes and near-bottom flow speed ($\overline{\mathbf{SS}}$) on the other hand predominantly reflect changes in deep hydrography. Comparing the frequency-domain evolution of the available AP_{comp} records (Figure 7.2) offers an insight into the time-transgressive nature of the MPT in different climate system components (i.e. proxies for different properties), all presented on the same stratigraphic framework. Figure 7.4 shows Continuous Wavelet Transforms for each record (Table 7.1), with statistically significant (at 95%) power highlighted by black contours. Each record shows a transition from predominantly ~1/41 kyr power towards ~1/100 kyr power over the past 1.4 myr, however the timing and nature of these transitions is highly variable.

The three surface proxies all in some way reflect the position of the STFZ relative to the AP_{comp}, however they will each also represent unique responses to additional factors. For example, the survivability of icebergs and hence deposition of IRD at the AP_{comp} is influenced by the position of the STFZ (as the boundary between cool, iceberg-laden Subantarctic waters and warm Subtropical waters), however it is also sensitive to the affect of Southern Ocean surface currents and the SWWB on iceberg drift across the Southern Ocean. Organic biomarker proxies such as the $U^{K'}_{37}$ paleo-

thermometer and the mass accumulation of alkenones are similarly complex to interpret. For example, changes in the population of alkenone-producing haptophyte plankton might be driven by changes in nutrient dynamics (e.g. Read et al., 2000) and insolation cycles (e.g. Tangunan et al., 2017). Moreover, the deposition and preservation of organic biomarkers may introduce signals independent of changes in surface productivity (e.g. Sachs et al., 2000).

The longest of the three surface records, IRD_{MAR}, provides perhaps the best insight into the emergence of ~1/100-kyr power in surface conditions at the Agulhas Plateau. Figure 7.4c shows that statistically significant spectral power at a frequency lower than 1/41-kyr first appears around 1.3 Ma. Interestingly, this variance is centred at ~1/80-kyr, and significant power in the 1/95 to 1/110 kyr bands does not emergence until much later at around 700 ka. Another notable observation, made also in Chapter 4, is the re-emergence of significant obliquity-band variance in the Late Pleistocene. The wavelet results show that no significant 100-kyr variance is present after 250 ka, with obliquity and precession-band power dominating.

The emergence of lower-than-obliquity frequency power at around 1.2 Ma is mirrored in the SST spectra (Figure 7.4f). Similarly to IRD_{MAR}, the transition towards lower-frequency power is a gradual one, and statistically significant 1/100-kyr power does not appear until around 1 Ma. This transition is reflected also in a decrease of obliquity-band power around 1.2 Ma, however as with IRD_{MAR} this power returns in the Late Pleistocene. The records differ, however, in the continued dominance of ~1/100-kyr power in SST throughout the Late Pleistocene which may reflect a more global surface temperature signal associated with Late Pleistocene glacial cycles (Snyder, 2016). In this respect, the SST spectra follows the $\delta^{18}O_{benthic}$, $\delta^{13}C_{benthic}$, and Alkenone MAR records.

McClymont et al. (2013) analysed several globally-distributed records of sea surface temperature, finding that ~1/100-kyr spectral power emerged amid a background trend of long-term cooling beginning in the Early Pleistocene. This long-term cooling trend is clearly visible in the AP_{comp} SST record (Figure 7.2f; Cartagena-Sierra et al., 2021; Romero et al., 2015), and is also reflected in a long-term increase in glacial-time IRD_{MAR} (Figure 7.2c. Whilst the SST record is not long enough to assess when

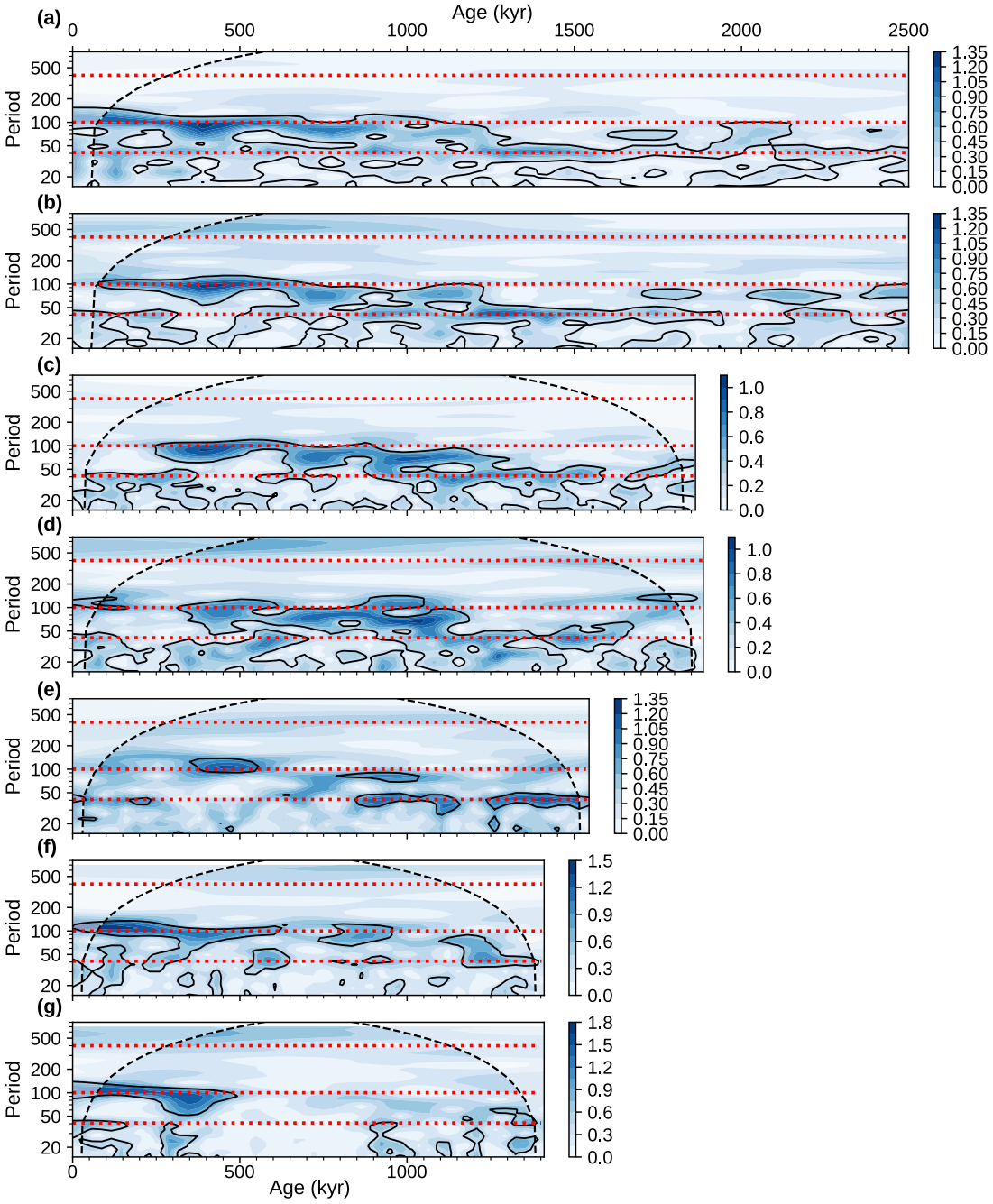

Figure 7.4: Continuous Wavelet Transform of AP_{comp} records across the MPT. **(a)** $\delta^{18}O_{benthic}$, **(b)** $\delta^{13}C_{benthic}$, **(c)** IRD_{MAR}, **(d)** $\overline{SS}$, **(e)** $\Delta\delta^{13}C_{SAMW-CDW}$, **(f)** SST from Romero et al. (2015) and Cartagena-Sierra et al. (2021), **(g)** alkenone accumulation from Romero et al. (2015) and Cartagena-Sierra et al. (2021). Data are standardized, interpolated to a 5 kyr time step and de-de-trended before Continuous Wavelet Transform using a Morlet mother wavelet. The red dashed lines represent (from top to bottom) 1/400 kyr, 1/100 kyr, and 1/41 kyr frequencies. Colour-bars are given in units of relative power (darker blue = higher power at that frequency)

this trend began, glacial IRD_{MAR} increases in a step-wise fashion first at around 1.2 Ma, and again at 1 Ma. A long-term trend is less clear in the alkenone accumulation record (Figure 7.2g), however intervals of high accumulation between 1.2 and 0.9 Ma do coincide with increasingly high IRD_{MAR}. This may reflect a common driver such as progressive expansions of the Subantarctic Zone bringing nutrient-rich and iceberg-laden surface waters from the Southern Ocean over the Agulhas Plateau. A decoupling between the MPT trend in $\overline{\mathbf{SS}}$ and alkenone accumulation might relate to the varying degrees to which both proxies are influenced by regional/local conditions, as well as the influence of the STFZ versus the Subantarctic Front on each record (Cartagena-Sierra et al., 2021). The onset of statistically-significant 1/100-kyr power is relatively late in the AP_{comp} alkenone MAR record (~500 ka) likely relating to the subdued glacial-interglacial variability between ~900 and ~500 ka.

Emergence of statistically significant ~1/100 kyr power in the records for subsurface ($\Delta\delta^{13}C_{SAMW-CDW}$) and deep ($\overline{\mathbf{SS}}$, $\delta^{13}C_{benthic}$, $\delta^{18}O_{benthic}$) conditions across the MPT generally occurs later than in the surface. With the exception of a brief appearance of ~1/100 kyr power around 2 Ma, $\delta^{18}O_{benthic}$ remains dominated by obliquity-band power until around 1.2 Ma, where the prevailing power transitions towards the eccentricity band.

Mudelsee and Schulz (1997) proposed that the increase in 1/100 kyr variance in global ice volume cycles lagged a substantial build-up of ice during the MPT by around 280 kyr. In this view, the '100-kyr World' became fully established only after around 650 ka, much later than is observed, for example, in records of tropical SST (Liu et al., 2008) and in all but the alkenone accumulation wavelet spectra presented here (Figure 7.4g). Further analysis of global $\delta^{18}O_{benthic}$ records (notably the LR04 Stack (Lisiecki and Raymo, 2005)) demonstrated that a substantial increase in ~1/100 kyr power occurred around 1.2 Ma (Lisiecki, 2010; Clark et al., 2006). Analysis of sea-level reconstructions (i.e. independent on the temperature component in $\delta^{18}O_{benthic}$) suggests a slightly later emergence of ~1/100-kyr power at around 900 ka (Elderfield et al., 2012; Maslin and Brierley, 2015), coinciding with a step-wise increase in (likely Antarctic) ice volume (Elderfield et al., 2012) and a major perturbation to overturning circulation (Pena and Goldstein, 2014).

The so-called '900 ka event' manifests at the Agulhas Plateau in the step-wise increase in IRD accumulation (Figure 7.2c) and a minimum in $\delta^{13}C_{benthic}$ (Figure 7.2b). Interestingly, when viewed with the $\overline{\mathbf{SS}}$ record, 'the 900 ka event' appears to represent the terminal event in a series of distinct swings in the position or intensity of deep ACC jets between glacial and interglacial conditions beginning at MIS 31. This same interval is characterised by prolonged high productivity (Figure 7.2d) and long-term minima in $\Delta\delta^{13}C_{SAMW-CDW}$. For example, during MIS 31, near-bottom flow is at it's lowest, suggesting a marked poleward contraction or weakening of the ACC, coinciding with a nearly complete breakdown of the intermediate-deep carbon isotope gradient. The nature of the '100-kyr World' continues to stimulate debate, particularly around whether the ~1/100 climate cycles are a response to the ~1/100 kyr eccentricity cycles (Lisiecki, 2010; Ridgwell et al., 1999), a harmonic of the ~400 kyr eccentricity cycle (Rial et al., 2013), or not 100 kyr cycles at all (Maslin and Brierley, 2015; Ruddiman, 2003; Huybers and Wunsch, 2005).

7.5 Future Work

7.5.1 Inter-hemispheric Coupling and the Pliocene

The work presented in this thesis provides a view of surface and deep hydrographic change across Pleistocene glacial cycles. This approach is valuable in that the controls on surface conditions are predominantly 'Southern Ocean' processes, whilst the drivers of deep chemical ventilation and near-bottom flow speed are additionally influenced by the export of NADW from the Atlantic basin. In a way, these records provide inter-hemispheric insights into climate evolution under different boundary conditions. Whilst this approach is independent of cross-site stratigraphic correlation, and the associated caveats, it is also limited because deep-water conditions are not purely a Northern Hemisphere signal. For example, a negative excursion in $\delta^{13}C_{benthic}$ might reflect an expansion of Southern Ocean deep waters driven by changes in Southern Ocean conditions, a contraction of NADW driven by North Atlantic conditions, or some combination. As discussed in Chapter 4, lead-lag relation-

ships between surface and deep hydrography at the Agulhas Plateau can not simply be interpreted as purely a Northern - Southern Hemisphere phasing.

One way to better test inter-hemispheric linkages at the Agulhas Plateau would be through comparisons to sediment cores from other regions, such as the North Atlantic. The major obstacle here would be developing a robust stratigraphic framework tying the AP_{comp} to the chosen comparison site, for example by tuning to a common orbital/insolation cycle.That being said, a candidate tuning target might be orbital precession, as cyclic variations in the sediment colour of sites recovered by IODP Expedition 361, including Site U1475, have been noted as containing a strong precession component (personal communication from Christopher C. Charles; Koutsodendris et al., 2021). Interestingly, sediment cores from the Northeast Atlantic continental margin also show a strong precession response (Hodell et al., 2013b,a), and a robust precession-tuned chronology has been shown to be viable at least during the Middle to Late Pleistocene (Hodell et al., 2015). Furthermore, the sensitivity of this region to Northern Hemisphere (manifesting in the surface hydrography) and Southern Hemisphere (manifesting in the deep hydrography) climates on sub-orbital timescales means a comparison between the two regions would allow further examination of processes identified in this thesis, such as the coupling between near-bottom flow speed and deep chemical ventilation and the 'Southern Escape' of buoyancy forcing.

Finally, a preliminary age model for the Middle to Late Pliocene section of the AP_{comp} (Figure 7.5) suggests that that sedimentation rates are relatively high between ~2.8 and ~3.7 Ma (averaging 6 cm/kyr, up to 7.5 cm/kyr in places). High sedimentation rates during the Pliocene (9.6 cm/kyr from 3.9 to 5.3 Ma) are also implied by the shipboard age model (Hall et al., 2017a). Pliocene sections of the AP_{comp} therefore present an exciting opportunity to examine inter-hemispheric connections during warmer-than present periods in the Pliocene, wherein many questions regarding orbital forcing, deep ocean circulation and ocean carbon cycling remain unresolved. Furthermore, the possibility of developing a precession-tuned age model would allow direct comparisons to be made to existing and future sediment core records from the Northeast Atlantic Ocean, ultimately providing insights into the evolution of North-

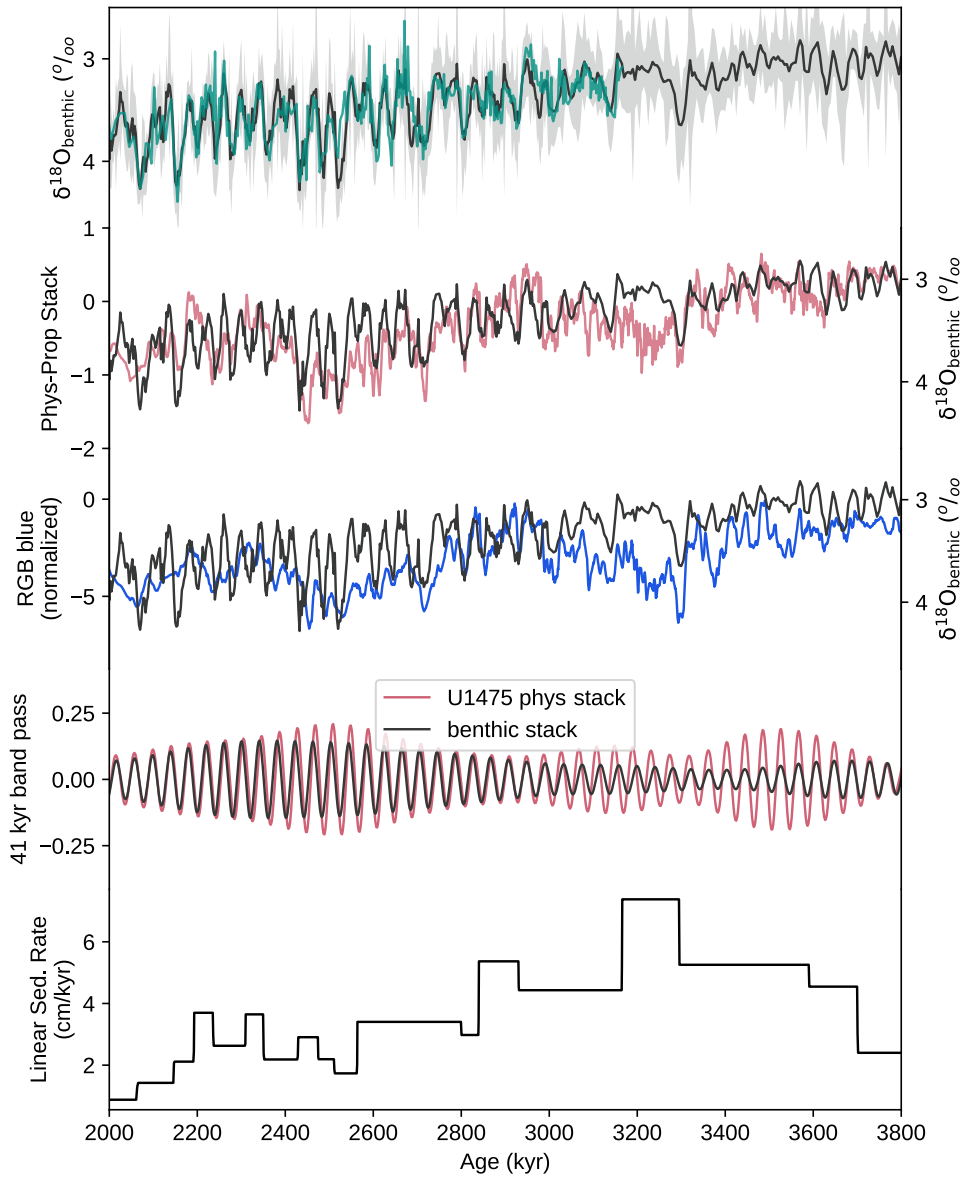

Figure 7.5: Preliminary age-depth model for the Mid-Pliocene AP_{comp}, obtained by tuning the AP_{comp} $\delta^{18}O_{benthic}$ record (<3.2 Ma; top) and a stack of physical properties (L*, RGB Blue, RGB Red, bulk K%; second row) and blue reflectance (RGB Blue; third row) to the $\delta^{18}O_{benthic}$ stack of Ahn et al. (2017) (dark grey; top three rows). The second from bottom row shows the AP_{comp} physical properties stack and the $\delta^{18}O_{benthic}$ stack with an obliquity-band (1/41-kyr) bandpass filter. The bottom panel shows linear sediment rate implied for this preliminary age model. *Physical properties data were obtained from the International Ocean Discovery Program data repository 'LIMS'*

ern and Southern Hemisphere climates at timescales not previously possible.

7.5.2 Elucidating the Southern Escape

Moreover, a key finding from the work presented in this thesis is the mechanism connecting Southern Ocean iceberg melt to overturning circulation patterns. This connection might be central in triggering a chain of feedbacks ultimately effecting the sequestration or release of vast quantities of carbon and heat through changes in the density and geometry of key water masses. Such a previously unrecognised feedback between the spatial distribution of Antarctic iceberg melt and the formation of NADW may have helped to facilitate the periodic development of global glacial conditions over the past 1.5 myr. Whilst this study highlighted how sensitive global ocean circulation is to Antarctic iceberg melt-water, the behaviour of this mechanism during times of abrupt climate change, for example the rapid temperature swings associated with Dansgaard-Oeschger cycles over the last glacial cycle, remains unresolved. To this end, future work might focus on reconstructing Southern Ocean iceberg drift and deep circulation at higher temporal resolutions, from high-accumulation sediment core locations in the South Atlantic, South Indian and South Pacific Oceans.

By following the approach of measuring multiple proxies on single sediment cores, and by attempting to develop robust, consistent chronologies across the Southern Ocean (e.g. Waelbroeck et al., 2019), exciting opportunities arise to explore the timing and nature of how abrupt climate changes manifest in the Southern Ocean and Antarctic region. Moreover, a systematic study of the provenance of IRD deposited in the Subantarctic Region using a suite of petrological/geochemical techniques such as U/Pb, $^{40}Ar/^{39}Ar$, and K/Ar dating (see review of techniques by Licht and Hemming, 2017), Pb, Sr and Nd isotope analysis (Cook et al., 2013) or determining minor and trace element compositions (Nielsen et al., 2007a), holds the potential to further our understanding of the Antarctic Ice Sheet under different boundary conditions.

In addition, an array of consistently-dated sediment cores across North and South Atlantic might allow one to track buoyancy anomalies related to the 'southern escape' of Antarctic meltwater or pulses in Agulhas Leakage as they propagate across the Atlantic. Multi-proxy studies combining surface hydrography (for example us-

ing Mg/Ca and $\delta^{18}O$ of planktic foraminifera to isolate surface salinity) and deep circulation (for example $\delta^{13}C_{benthic}$, ϵNd and $\overline{\mathbf{SS}}$) would provide a framework to further test and constrain the timing and nature of buoyancy-driven inter-hemispheric tele-connections.

7.5.3 Summary

To summarize, I propose two complimentary directions for future work. Firstly, extending the study of inter-hemispheric and surface-deep ocean coupling beyond the Pleistocene, and secondly 'zooming in' on shorter time-scales at higher temporal resolution. Both of these objectives would require comparing sediment core records from multiple locations, and a heavy emphasis must be put on establishing robust and precise chronologies. Understanding how different components of the ocean-climate system force and respond to each other during times of abrupt climate change (such as sub-orbital cycles during the Late Pleistocene) and under boundary conditions more similar to those of today (such as warm intervals in the Middle and Early Pliocene) may ultimately shed light on the complexities of the climate system with relevance to ongoing and future change.

References

Adhèmar, j. (1842). *Rèvolutions De La Mer, Dèluges Pèriodiques*. Carilian-Goeury & V. Dalmont, Paris, France.

Adkins, J. (2013). The role of deep ocean circulation in setting glacial climates. *Paleoceanography*, 28(3):539–561.

Adkins, j. F. (2002). The salinity, temperature, and delta 18o of the glacial deep ocean. *Science*, 298(5599):1769–1773.

Agassiz, L., Bettannier, J., and Nicolet, H. (1840). *E'tudes Sur Les Glaciers*. Aux frais de l' auteur.

Ahn, J. and Brook, E. J. (2008). Atmospheric CO 2 and Climate on Millennial Time Scales during the Last Glacial Period. *Science*, 322(5898):83–85.

Ahn, S. et al. (2017). A Probabilistic Pliocene/Pleistocene Stack of Benthic δ18O Using a Profile Hidden Markov Model. *Dynamics and Statistics of the Climate System*, 2(1).

Ai, X., Studer, A. S., Sigman, D. M., Martínez-garcía, A., Fripiat, F., Thöle, L. M., Michel, E., Gottschalk, J., Arnold, L., Moretti, S., Schmitt, M., Oleynik, S., Jaccard, S. L., and Haug, G. H. (2020). Southern ocean upwelling, earth's obliquity, and glacial-interglacial atmospheric CO 2 change. *Science*, 370(6522):1348–1352.

Allen, C. and Warnke, D. (1991). History of ice rafting at leg 114 sites, subantarctic/-south atlantic. In *Proceedings of the Ocean Drilling Program, 114 Scientific Reports*. Ocean Drilling Program.

Allen, C. S., Pike, J., and Pudsey, C. J. (2011). Last glacial–interglacial sea-ice cover in the SW atlantic and its potential role in global deglaciation. *Quaternary Science Reviews*, 30(19-20):2446–2458.

Anderson, R., Bacon, M., and Brewer, P. (1983). Removal of230th and231pa from the open ocean. *Earth and Planetary Science Letters*, 62(1):7–23.

Anderson, R. F., Ali, S., Bradtmiller, L. I., Nielsen, S. H. H., Fleisher, M., Anderson, B. E., and Burckle, L. H. (2009). Wind-Driven upwelling in theRise in Atmospheric CO2. *Science*, 323(March):1443–1448.

Anderson, R. F., Barker, S., Fleisher, M., Gersonde, R., Goldstein, S. L., Kuhn, G., Mortyn, P. G., Pahnke, K., and Sachs, J. P. (2014). Biological response to millennial variability of dust and nutrient supply in the Subantarctic South Atlantic Ocean. *Philos. Trans. R. Soc. A Math. Phys. Eng. Sci.*, 372(2019).

Anderson, R. F., Chase, Z., Fleisher, M. Q., and Sachs, J. (2002). The southern ocean's biological pump during the last glacial maximum. *Deep Sea Research Part II*, 49(9-10):1909–1938.

Anderson, R. F. and Winckler, G. (2005). Problems with paleoproductivity proxies. *Paleoceanography*, 20(3):n/a–n/a.

Ao, H., Rohling, E. J., Stringer, C., Roberts, A. P., Dekkers, M. J., Dupont-Nivet, G., Yu, J., Liu, Q., Zhang, P., Liu, Z., Ma, X., Zhou, W., Jin, Z., Xiao, G., Wang, H., Sun, Q., Yang, P., Peng, X., Shi, Z., Qiang, X., and An, Z. (2020). Two-stage Mid-brunhes Climate Transition and Mid-pleistocene Human Diversification. *Earth-Science Reviews*, 210:103354.

Archer, D. (1991). Modeling the Calcite Lysocline. *Journal of Geophysical Research: Oceans*, 96(C9):17037.

Archer, D. E. (1996). An atlas of the distribution of calcium carbonate in sediments of the deep sea. *Global Biogeochemical Cycles*, 10(1):159–174.

Arhan, M., Mercier, H., and Park, Y. H. (2003). On the deep water circulation of the eastern South Atlantic Ocean. *Deep. Res. Part I Oceanogr. Res. Pap.*, 50(7):889–916.

Arz, H. W., Pätzold, J., and Wefer, G. (1998). Correlated millennial-scale changes in surface hydrography and terrigenous sediment yield inferred from last-glacial marine deposits off northeastern brazil. *Quaternary Research*, 50(2):157–166.

Bajo, P., Drysdale, R. N., Woodhead, J. D., Hellstrom, J. C., Hodell, D., Ferretti, P., Voelker, A. H. L., Zanchetta, G., Rodrigues, T., Wolff, E., Tyler, J., Frisia, S., Spötl, C., and Fallick, A. E. (2020). Persistent influence of obliquity on ice age terminations since the middle pleistocene transition. *Science*, 367(6483):1235–1239.

Bard, E. and Rickaby, R. E. (2009). Migration of the subtropical front as a modulator of glacial climate. *Nature*, 460(7253):380–383.

Barker, S., Archer, D., Booth, L., Elderfield, H., Henderiks, J., and Rickaby, R. E. M. (2006). Globally increased pelagic carbonate production during the Mid-Brunhes dissolution interval and the CO2 paradox of MIS 11. *Quat. Sci. Rev.*, 25(23-24):3278–3293.

Barker, S., Chen, J., Gong, X., Jonkers, L., Knorr, G., and Thornalley, D. (2015). Icebergs not the trigger for north atlantic cold events. *Nature*, 520(7547):333–336.

Barker, S., Starr, A., van der Lubbe, H., et al. (in review). Persistent influence of precession on northern ice sheet variability since the early Pleistocene. In Review (Science).

Barth, A. M., Clark, P. U., Bill, N. S., He, F., and Pisias, N. G. (2018). Climate evolution across the mid-brunhes transition. *Climate of the Past*, 14(12):2071–2087.

Bassinot, F. C., Beaufort, L., Vincent, E., Labeyrie, L. D., Rostek, F., Müller, P. J., Quidelleur, X., and Lancelot, Y. (1994). Coarse fraction fluctuations in pelagic carbonate sediments from the tropical Indian Ocean: A 1500-kyr record of carbonate dissolution. *Paleoceanography*, 9(4):579–600.

Beal, L. M., , Ruijter, W. P. M. D., Biastoch, A., and Zahn, R. (2011). On the role of the agulhas system in ocean circulation and climate. *Nature*, 472(7344):429–436.

Beaufort, L., Lancelot, Y., Camberlin, P., Cayre, O., Vincent, E., Bassinot, F., and Labeyrie, L. (1997). Insolation cycles as a major control of equatorial Indian Ocean primary production. *Science*, 278(5342):1451–1454.

Becker, K., , Austin, J., Exon, N., Humphris, S., Kastner, M., McKenzie, J., Miller, K., Suyehiro, K., and Taira, A. (2019). Fifty Years of Scientific Ocean Drilling. *Oceanography*, 32(1):17–21.

Becquey, S. and Gersonde, R. (2002). Past hydrographic and climatic changes in the subantarctic zone of the south atlantic – the pleistocene record from ODP site 1090. *Palaeogeography, Palaeoclimatology, Palaeoecology*, 182(3-4):221–239.

Belanger, P., Curry, W., and Matthews, R. (1981). Core-top evaluation of benthic foraminiferal isotopic ratios for paleo-oceanographic interpretations. *Palaeogeography, Palaeoclimatology, Palaeoecology*, 33(1-3):205–220.

Bell, D. B., Jung, S. J., and Kroon, D. (2015). The plio-pleistocene development of atlantic deep-water circulation and its influence on climate trends. *Quaternary Science Reviews*, 123:265–282.

Beltran, C., Golledge, N. R., Ohneiser, C., Kowalewski, D. E., Sicre, M.-A., Hageman, K. J., Smith, R., Wilson, G. S., and Mainié, F. (2020). Southern ocean temperature records and ice-sheet models demonstrate rapid antarctic ice sheet retreat under low atmospheric CO2 during marine isotope stage 31. *Quaternary Science Reviews*, 228:106069.

Bemis, B. E., Spero, H. J., Lea, D. W., and Bijma, J. (2000). Temperature influence on the carbon isotopic composition of Globigerina bulloides and Orbulina universa (planktonic foraminifera). *Mar. Micropaleontol.*, 38(3-4):213–228.

Beny, F., Bout-Roumazeilles, V., Davies, G., Waelbroeck, C., Bory, A., Tribovillard, N., Delattre, M., and Abraham, R. (2020). Radiogenic isotopic and clay mineralogical signatures of terrigenous particles as water-mass tracers: New insights into south atlantic deep circulation during the last termination. *Quaternary Science Reviews*, 228:106089.

Berends, C. J., Köhler, P., Lourens, L. J., and Wal, R. S. W. (2021). On the cause of the mid-pleistocene transition. *Reviews of Geophysics*, 59(2).

Berger, A. (1977). Long-term variations of the earth's orbital elements. *Celestial Mechanics*, 15(1):53–74.

Berger, A. and Loutre, M. (1991). Insolation values for the climate of the last 10 million years. *Quaternary Science Reviews*, 10(4):297–317.

Berger, A., Loutre, M.-F., and Mélice, J. L. (2006). Equatorial insolation: from precession harmonics to eccentricity frequencies. *Clim. Past*, 2(2):131–136.

Bianchi, G., Hall, I. R., McCave, I. N., and Joseph, L. (1999). Measurement of the sortable silt current speed proxy using the Sedigraph 5100 and Coulter Multisizer IIe: precision and accuracy. *https://www.scopus.com/sourceid/26320*, 46(6):1001–1014.

Bianchi, G. G. and McCave, I. N. (1999). Holocene periodicity in north atlantic climate and deep-ocean flow south of iceland. *Nature*, 397(6719):515–517.

Biastoch, A., Böning, C. W., and Lutjeharms, J. R. E. (2008). Agulhas leakage dynamics affects decadal variability in atlantic overturning circulation. *Nature*, 456(7221):489–492.

Biastoch, A., Böning, C. W., Schwarzkopf, F. U., and Lutjeharms, J. R. E. (2009). Increase in agulhas leakage due to poleward shift of southern hemisphere westerlies. *Nature*, 462(7272):495–498.

Bigg, G. R. (2020). The impact of icebergs of sub-Antarctic origin on Southern Ocean ice-rafted debris distributions. *Quat. Sci. Rev.*, 232:106204.

Bigg, G. R., Wadley, M. R., Stevens, D. P., and Johnson, J. A. (1997). Modelling the dynamics and thermodynamics of icebergs. *Cold Reg. Sci. Technol.*, 26(2):113–135.

Bintanja, R., van de Wal, R. S., and Oerlemans, J. (2005). Modelled atmospheric temperatures and global sea levels over the past million years. *Nature*, 437(7055):125–128.

Biscaye, P. E. (1965). Mineralogy and sedimentation of recent deep-sea clay in the atlantic ocean and adjacent seas and oceans. *Geological Society of America Bulletin*, 76(7):803.

Boebel, O., Rossby, T., Lutjeharms, J., Zenk, W., and Barron, C. (2003). Path and variability of the agulhas return current. *Deep Sea Research Part II: Topical Studies in Oceanography*, 50(1):35–56.

Bolton, C. T., Chang, L., Clemens, S. C., Kodama, K., Ikehara, M., Medina-Elizalde, M., Paterson, G. A., Roberts, A. P., Rohling, E. J., Yamamoto, Y., and Zhao, X. (2013). A 500,000 year record of indian summer monsoon dynamics recorded by eastern equatorial indian ocean upper water-column structure. *Quaternary Science Reviews*, 77:167–180.

Bower, A., Lozier, S., Biastoch, A., Drouin, K., Foukal, N., Furey, H., Lankhorst, M., Rühs, S., and Zou, S. (2019). Lagrangian views of the pathways of the atlantic meridional overturning circulation. *Journal of Geophysical Research: Oceans*, 124(8):5313–5335.

Boyd, P. W., Watson, A. J., Law, C. S., Abraham, E. R., Trull, T., Murdoch, R., Bakker, D. C. E., Bowie, A. R., Buesseler, K. O., Chang, H., Charette, M., Croot, P., Downing, K., Frew, R., Gall, M., Hadfield, M., Hall, J., Harvey, M., Jameson, G., LaRoche, J., Liddicoat, M., Ling, R., Maldonado, M. T., McKay, R. M., Nodder, S., Pickmere, S., Pridmore, R., Rintoul, S., Safi, K., Sutton, P., Strzepek, R., Tanneberger, K., Turner, S., Waite, A., and Zeldis, J. (2000). A mesoscale phytoplankton bloom in the polar southern ocean stimulated by iron fertilization. *Nature*, 407(6805):695–702.

Boyle, E. A. (1981). Cadmium, zinc, copper, and barium in foraminifera tests. *Earth and Planetary Science Letters*, 53(1):11–35.

Boyle, E. A. (1988). Vertical oceanic nutrient fractionation and glacial/interglacial CO2cycles. *Nature*, 331(6151):55–56.

Boyle, E. A. and Keigwin, L. (1987). North atlantic thermohaline circulation during the past 20,000 years linked to high-latitude surface temperature. *Nature*, 330(6143):35–40.

Brathauer, U. and Abelmann, A. (1999). Late quaternary variations in sea surface temperatures and their relationship to orbital forcing recorded in the Southern Ocean (Atlantic sector). *Paleoceanography*, 14(2):135–148.

Broecker, W. S. (1979). A revised estimate for the radiocarbon age of North Atlantic deep water. *J. Geophys. Res.*, 84(C6):3218.

Broecker, W. S. (1982). Glacial to interglacial changes in ocean chemistry. *Prog. Oceanogr.*, 11(2):151–197.

Broecker, W. S., Andree, M., Bonani, G., Wolfli, W., Klas, M., Mix, A., and Oeschger, H. (1988). Comparison between Radiocarbon Ages Obtained on Coexisting Planktonic Foraminifera. *Paleoceanography*, 3(6):647–657.

Broecker, W. S. and Peng, T.-H. (1987). The Role of CaCO3compensation in the Glacial to Interglacial Atmospheric CO2change. *Global Biogeochemical Cycles*, 1(1):15–29.

Broecker, W. S., Peng, T.-H., Trumbore, S., Bonani, G., and Wolfli, W. (1990). The distribution of radiocarbon in the glacial ocean. *Global Biogeochemical Cycles*, 4(1):103–117.

Broecker, W. S., Peteet, D. M., and Rind, D. (1985). Does the Ocean–atmosphere System Have More Than One Stable Mode of Operation? *Nature*, 315(6014):21–26.

Broecker, W. S. and van Donk, J. (1970). Insolation Changes, Ice Volumes, and the O18record in Deep-sea Cores. *Reviews of Geophysics*, 8(1):169.

Brovkin, V., Ganopolski, A., Archer, D., and Rahmstorf, S. (2007). Lowering of glacial atmospheric CO2in response to changes in oceanic circulation and marine biogeochemistry. *Paleoceanography*, 22(4):n/a–n/a.

Budge, J. S. and Long, D. G. (2018). A Comprehensive Database for Antarctic Iceberg Tracking Using Scatterometer Data. *IEEE J. Sel. Top. Appl. Earth Obs. Remote Sens.*, 11(2):434–442.

Buitenhuis, E. T., Hashioka, T., and Quéré, C. L. (2013). Combined constraints on global ocean primary production using observations and models. *Global Biogeochemical Cycles*, 27(3):847–858.

Buitenhuis, E. T., van der Wal, P., and de Baar, H. J. W. (2001). Blooms ofEmiliania Huxleyiare Sinks of Atmospheric Carbon Dioxide: A Field and Mesocosm Study Derived Simulation. *Global Biogeochemical Cycles*, 15(3):577–587.

Burton, K. W., Ling, H.-F., and O'Nions, R. K. (1997). Closure of the Central American Isthmus and Its Effect on Deep-water Formation in the North Atlantic. *Nature*, 386(6623):382–385.

Böhm, E., Lippold, J., Gutjahr, M., Frank, M., Blaser, P., Antz, B., Fohlmeister, J., Frank, N., Andersen, M. B., and Deininger, M. (2014). Strong and deep atlantic meridional overturning circulation during the last glacial cycle. *Nature*, 517(7532):73–76.

Böning, C. W., Dispert, A., Visbeck, M., Rintoul, S. R., and Schwarzkopf, F. U. (2008). The response of the antarctic circumpolar current to recent climate change. *Nature Geoscience*, 1(12):864–869.

Cai, W. (2006). Antarctic ozone depletion causes an intensification of the southern ocean super-gyre circulation. *Geophysical Research Letters*, 33(3).

Caley, T., Extier, T., Collins, J. A., Schefu**SS**, E., Dupont, L., Malaizé, B., Rossignol, L., Souron, A., McClymont, E. L., Jimenez-Espejo, F. J., García-Comas, C., Eynaud, F., Martinez, P., Roche, D. M., Jorry, S. J., Charlier, K., Wary, M., Gourves, P.-Y., Billy, I., and Giraudeau, J. (2018). A Two-million-year-long Hydroclimatic Context for Hominin Evolution in Southeastern Africa. *Nature*, 560(7716):76–79.

Caley, T., Giraudeau, J., Malaizé, B., Rossignol, L., and Pierre, C. (2012). Agulhas leakage as a key process in the modes of Quaternary climate changes. *Proc. Natl. Acad. Sci. U. S. A.*, 109(18):6835–6839.

Caley, T., Malaizé, B., Zaragosi, S., Rossignol, L., Bourget, J., Eynaud, F., Martinez, P., Giraudeau, J., Charlier, K., and Ellouz-Zimmermann, N. (2011). New Arabian Sea Records Help Decipher Orbital Timing of Indo-asian Monsoon. *Earth and Planetary Science Letters*, 308(3-4):433–444.

Caley, T., Peeters, F. J. C., Biastoch, A., Rossignol, L., van Sebille, E., Durgadoo, J., Malaizé, B., Giraudeau, J., Arthur, K., and Zahn, R. (2014). Quantitative estimate of the paleo-agulhas leakage. *Geophysical Research Letters*, 41(4):1238–1246.

Campin, J.-M., Fichefet, T., and Duplessy, J.-C. (1999). Problems with Using Radio-

carbon to Infer Ocean Ventilation Rates for Past and Present Climates. *Earth and Planetary Science Letters*, 165(1):17–24.

Cartagena-Sierra, A., Berke, M. A., Robinson, R. S., Marcks, B., Castañeda, I. S., Starr, A., Hall, I. R., Hemming, S. R., and and, L. J. L. (2021). Latitudinal migrations of the subtropical front at the agulhas plateau through the mid-pleistocene transition. *Paleoceanography and Paleoclimatology*, 36(7):1–17.

Cessi, P. (2019). The global overturning circulation. *Annual Review of Marine Science*, 11(1):249–270.

Chalk, T. B., Hain, M. P., Foster, G. L., Rohling, E. J., Sexton, P. F., Badger, M. P. S., Cherry, S. G., Hasenfratz, A. P., Haug, G. H., Jaccard, S. L., Martínez-García, A., Pälike, H., Pancost, R. D., and Wilson, P. A. (2017). Causes of ice age intensification across the mid-pleistocene transition. *Proceedings of the National Academy of Sciences*, 114(50):13114–13119.

Channell, J., Singer, B., and Jicha, B. (2020). Timing of Quaternary Geomagnetic Reversals and Excursions in Volcanic and Sedimentary Archives. *Quaternary Science Reviews*, 228:106114.

Channell, J., Xuan, C., and Hodell, D. (2009). Stacking paleointensity and oxygen isotope data for the last 1.5 myr (PISO-1500). *Earth and Planetary Science Letters*, 283(1-4):14–23.

Charidemou, M. S. J. (2018). *Paleoceanographic variability on the Agulhas Plateau during the past 150 kyr BP*. PhD thesis, Cardiff University.

Charles, C. D., Pahnke, K., Zahn, R., Mortyn, P. G., Ninnemann, U., and Hodell, D. A. (2010). Millennial scale evolution of the Southern Ocean chemical divide. *Quat. Sci. Rev.*, 29(3-4):399–409.

Charles, C. D., Wright, J. D., and Fairbanks, R. G. (1993). Thermodynamic influences on the marine carbon isotope record. *Paleoceanography*, 8(6):691–697.

Chase, B. M. (2021). Orbital Forcing in Southern Africa: Towards a Conceptual Model for Predicting Deep Time Environmental Change from an Incomplete Proxy Record. *Quaternary Science Reviews*, 265:107050.

Chase, Z., Anderson, R. F., Fleisher, M. Q., and Kubik, P. W. (2002). The Influence of Particle Composition and Particle Flux on Scavenging of Th, Pa and Be in the Ocean. *Earth and Planetary Science Letters*, 204(1-2):215–229.

Cheng, H., Edwards, R. L., Broecker, W. S., Denton, G. H., Kong, X., Wang, Y., Zhang, R., and Wang, X. (2009). Ice Age Terminations. *Science*, 326(5950):248–252.

Cheng, H., Edwards, R. L., Sinha, A., Spötl, C., Yi, L., Chen, S., Kelly, M., Kathayat, G., Wang, X., Li, X., Kong, X., Wang, Y., Ning, Y., and Zhang, H. (2016). The asian monsoon over the past 640,000 years and ice age terminations. *Nature*, 534(7609):640–646.

Chiessi, C. M., Mulitza, S., Paul, A., Pätzold, J., Groeneveld, J., and Wefer, G. (2008). South atlantic interocean exchange as the trigger for the bølling warm event. *Geology*, 36(12):919.

Chiessi, C. M., Ulrich, S., Mulitza, S., Pätzold, J., and Wefer, G. (2007). Signature of the Brazil-Malvinas Confluence (Argentine Basin) in the isotopic composition of planktonic foraminifera from surface sediments. *Mar. Micropaleontol.*, 64(1-2):52–66.

Chow, T. J. and Patterson, C. (1962). The Occurrence and Significance of Lead Isotopes in Pelagic Sediments. *Geochimica et Cosmochimica Acta*, 26(2):263–308.

Civel-Mazens, M., Crosta, X., Cortese, G., Michel, E., Mazaud, A., Ther, O., Ikehara, M., and Itaki, T. (2021). Antarctic polar front migrations in the kerguelen plateau region, southern ocean, over the past 360 kyrs. *Global and Planetary Change*, 202:103526.

Clark, P. U., Archer, D., Pollard, D., Blum, J. D., Rial, J. A., Brovkin, V., Mix, A. C., Pisias, N. G., and Roy, M. (2006). The middle pleistocene transition: Characteristics, mechanisms, and implications for long-term changes in atmospheric pCO2. *Quaternary Science Reviews*, 25(23-24):3150–3184.

Clark, P. U. and Pollard, D. (1998). Origin of the middle pleistocene transition by ice sheet erosion of regolith. *Paleoceanography*, 13(1):1–9.

Cléroux, C., Cortijo, E., Duplessy, J. C., and Zahn, R. (2007). Deep-dwelling foraminifera as thermocline temperature recorders. *Geochemistry, Geophys. Geosystems*, 8(4).

CLIMAP Project Members (1976). The surface of the ice-age earth. *Science*, 191(4232):1131–1137.

Cofaigh, C. Ó., Dowdeswell, J. A., and Pudsey, C. J. (2001). Late quaternary iceberg rafting along the antarctic peninsula continental rise and in the weddell and scotia seas. *Quaternary Research*, 56(3):308–321.

Conolly, J. R. and Ewing, M. (1965). Pleistocene glacial-marine zones in north atlantic deep-sea sediments. *Nature*, 208(5006):135–138.

Cook, C. P., van de Flierdt, T., Williams, T., Hemming, S. R., Iwai, M., Kobayashi, M., Jimenez-Espejo, F. J., Escutia, C., González, J. J., Khim, B.-K., McKay, R. M., Passchier, S., Bohaty, S. M., Riesselman, C. R., Tauxe, L., Sugisaki, S., Galindo, A. L., Patterson, M. O., Sangiorgi, F., Pierce, E. L., Brinkhuis, H., Klaus, A., Fehr, A., Bendle, J. A. P., Bijl, P. K., Carr, S. A., Dunbar, R. B., Flores, J. A., Hayden, T. G., Katsuki, K., Kong, G. S., Nakai, M., Olney, M. P., Pekar, S. F., Pross, J., Röhl, U., Sakai, T., Shrivastava, P. K., Stickley, C. E., Tuo, S., Welsh, K., and Yamane, M. (2013). Dynamic behaviour of the east antarctic ice sheet during pliocene warmth. *Nature Geoscience*, 6(9):765–769.

Corliss, B. H., McCorkle, D. C., and Higdon, D. M. (2002). A time series study of the carbon isotopic composition of deep-sea benthic foraminifera. *Paleoceanography*, 17(3):8–1–8–27.

Cortese, G., Abelmann, A., and Gersonde, R. (2007). The last five glacial-interglacial transitions: A high-resolution 450,000-year record from the subantarctic atlantic. *Paleoceanography*, 22(4):n/a–n/a.

Croll, J. (1867). LV. on the change in the obliquity of the ecliptic, its influence on the climate of the polar regions and on the level of the sea. *The London, Edinburgh, and Dublin Philosophical Magazine and Journal of Science*, 33(225):426–445.

Cronin, M. F., Tozuka, T., Biastoch, A., Durgadoo, J. V., and Beal, L. M. (2013). Prevalence of strong bottom currents in the greater agulhas system. *Geophysical Research Letters*, 40(9):1772–1776.

Crosta, X., Beucher, C., Pahnke, K., and Brzezinski, M. A. (2007). Silicic acid leakage from the southern ocean: Opposing effects of nutrient uptake and oceanic circulation. *Geophysical Research Letters*, 34(13):n/a–n/a.

Croudace, I. W. and Rothwell, R. G., editors (2015). *Micro-XRF Studies of Sediment Cores*. Springer Netherlands.

Crowley, T. J. and Häkkinen, S. (1988). A new mechanism for decreasing north atlantic deep water production rates during the pleistocene. *Paleoceanography*, 3(3):249–258.

Crundwell, M., Scott, G., Naish, T., and Carter, L. (2008). Glacial-interglacial ocean climate variability from planktonic foraminifera during the Mid-Pleistocene transition in the temperate Southwest Pacific, ODP Site 1123. *Palaeogeogr. Palaeoclimatol. Palaeoecol.*, 260(1-2):202–229.

Curry, W. B. and Oppo, D. W. (2005). Glacial water mass geometry and the distribution of δ13c of σco2 in the western atlantic ocean. *Paleoceanography*.

de Baar, H. J. W., de Jong, J. T. M., Bakker, D. C. E., Löscher, B. M., Veth, C., Bathmann, U., and Smetacek, V. (1995). Importance of iron for plankton blooms and carbon dioxide drawdown in the southern ocean. *Nature*, 373(6513):412–415.

de Boer, B., Lourens, L. J., and van de Wal, R. S. (2014). Persistent 400,000-year variability of antarctic ice volume and the carbon cycle is revealed throughout the plio-pleistocene. *Nature Communications*, 5(1).

de Ruijter, W. P. M., Biastoch, A., Drijfhout, S. S., Lutjeharms, J. R. E., Matano, R. P., Pichevin, T., van Leeuwen, P. J., and Weijer, W. (1999). Indian-atlantic interocean exchange: Dynamics, estimation and impact. *Journal of Geophysical Research: Oceans*, 104(C9):20885–20910.

de Vargas, C., Renaud, S., Hilbrecht, H., and Pawlowski, J. (2001). Pleistocene adaptive radiation in globorotalia truncatulinoides: Genetic, morphologic, and environmental evidence. *Paleobiology*, 27(1):104–125.

deMenocal, P. B., Oppo, D. W., Fairbanks, R. G., and Prell, W. L. (1992). Pleistocene δ13c variability of north atlantic intermediate water. *Paleoceanography*, 7(2):229–250.

Dickson, A. J., Leng, M. J., Maslin, M. A., Sloane, H. J., Green, J., Bendle, J. A., McClymont, E. L., and Pancost, R. D. (2010). Atlantic overturning circulation and agulhas leakage influences on southeast atlantic upper ocean hydrography during marine isotope stage 11. *Paleoceanography*, 25(3).

Dickson, R. R. and Brown, J. (1994). The production of north atlantic deep water: Sources, rates, and pathways. *Journal of Geophysical Research*, 99(C6):12319.

Diekmann, B. (2007). Sedimentary patterns in the late Quaternary Southern Ocean. *Deep. Res. Part II Top. Stud. Oceanogr.*, 54(21-22):2350–2366.

Diekmann, B., Fälker, M., and Kuhn, G. (2003a). Environmental history of the southeastern South Atlantic since the Middle Miocene: Evidence from the sedimentological records of ODP sites 1088 and 1092. *Sedimentology*, 50(3):511–529.

Diekmann, B., Fütterer, D. K., Grobe, H., Hillenbrand, C. D., Kuhn, G., Michels, K., Petschick, R., and Pirrung, M. (2003b). Terrigenous sediment supply in the polar to temperate south atlantic: Land-ocean links of environmental changes during the late quaternary. In *The South Atlantic in the Late Quaternary*, pages 375–399. Springer Berlin Heidelberg.

Diekmann, B. and Kuhn, G. (1999). Provenance and dispersal of glacial–marine surface sediments in the weddell sea and adjoining areas, antarctica: Ice-rafting versus current transport. *Marine Geology*, 158(1-4):209–231.

Diekmann, B. and Kuhn, G. (2002). Sedimentary record of the mid-pleistocene climate transition in the southeastern south atlantic (ODP site 1090). *Palaeogeography, Palaeoclimatology, Palaeoecology*, 182(3-4):241–258.

Diz, P., Hall, I. R., Zahn, R., and Molyneux, E. G. (2007). Paleoceanography of the southern agulhas plateau during the last 150 ka: Inferences from benthic foraminiferal assemblages and multispecies epifaunal carbon isotopes. *Paleoceanography*, 22(4):n/a–n/a.

Donahue, J. G. (1965). Diatoms as indicators of pleistocene climatic fluctuations in the pacific sector of the southern ocean. *Progress in Oceanography*, 4:133–140.

Dong, S., Sprintall, J., Gille, S. T., and Talley, L. (2008). Southern Ocean mixed-layer depth from Argo float profiles. *Journal of Geophysical Research Oceans*, 113(C6).

Drouin, K. L. and Lozier, M. S. (2019). The Surface Pathways of the South Atlantic: Revisiting the Cold and Warm Water Routes Using Observational Data. *J. Geophys. Res. Ocean.*, 124(10):7082–7103.

Du, J., Haley, B. A., and Mix, A. C. (2020). Evolution of the global overturning circulation since the last glacial maximum based on marine authigenic neodymium isotopes. *Quaternary Science Reviews*, 241:106396.

Duchamp-Alphonse, S., Siani, G., Michel, E., Beaufort, L., Gally, Y., and Jaccard, S. L. (2018). Enhanced ocean-atmosphere carbon partitioning via the carbonate counter pump during the last deglacial. *Nature Communications*, 9(1).

Duplessy, J. C., Shackleton, N. J., Fairbanks, R. G., Labeyrie, L., Oppo, D., and Kallel, N. (1988). Deepwater Source Variations during the Last Climatic Cycle and Their Impact on the Global Deepwater Circulation. *Paleoceanography*, 3(3):343–360.

Duplessy, J.-C., Shackleton, N. J., Matthews, R. K., Prell, W., Ruddiman, W. F., Caralp, M., and Hendy, C. H. (1984). 13c Record of Benthic Foraminifera in the Last Interglacial Ocean: Implications for the Carbon Cycle and the Global Deep Water Circulation. *Quaternary Research*, 21(2):225–243.

Durgadoo, J. V., Loveday, B. R., Reason, C. J. C., Penven, P., and Biastoch, A. (2013). Agulhas leakage predominantly responds to the southern hemisphere westerlies. *Journal of Physical Oceanography*, 43(10):2113–2131.

Dutkiewicz, A., Müller, R. D., O'Callaghan, S., and Jónasson, H. (2015). Census of seafloor sediments in the world's ocean. *Geology*, 43(9):795–798.

Dyez, K. A., Hönisch, B., and Schmidt, G. A. (2018). Early pleistocene obliquity-scale pCO 2 variability at ~1.5 million years ago. *Paleoceanography and Paleoclimatology*, 33(11):1270–1291.

Dyez, K. A., Zahn, R., and Hall, I. R. (2014). Multicentennial Agulhas leakage variability and links to North Atlantic climate during the past 80,000-years. *Paleoceanography*, 29(12):1238–1248.

Edwards, L. E., Mudie, P. J., and de Vernal, A. (1991). Pliocene Paleoclimatic Reconstruction Using Dinoflagellate Cysts: Comparison of Methods. *Quaternary Science Reviews*, 10(2-3):259–274.

Eide, M., Olsen, A., Ninnemann, U. S., and Johannessen, T. (2017). A global ocean climatology of preindustrial and modern ocean δ13C. *Global Biogeochem. Cycles*, 31(3):515–534.

Elderfield, H., Ferretti, P., Greaves, M., Crowhurst, S., McCave, I. N., Hodell, D., and Piotrowski, A. M. (2012). Evolution of ocean temperature and ice volume through the mid-pleistocene climate transition. *Science*, 337(6095):704–709.

Emiliani, C. (1955). Pleistocene temperatures. *The Journal of Geology*, 63(6):538–578.

Emiliani, C. (1971). The last interglacial: Paleotemperatures and chronology. *Science*, 171(3971):571–573.

Epstein, S. and Lowenstam, H. A. (1953). Temperature-shell-growth relations of recent and interglacial pleistocene shoal-water biota from bermuda. *The Journal of Geology*, 61(5):424–438.

Farmer, G., Barber, D., and Andrews, J. (2003). Provenance of Late Quaternary Ice-proximal Sediments in the North Atlantic: Nd, Sr and Pb Isotopic Evidence. *Earth and Planetary Science Letters*, 209(1-2):227–243.

Farmer, J. R., Hönisch, B., Haynes, L. L., Kroon, D., Jung, S., Ford, H. L., Raymo, M. E., Jaume-Seguí, M., Bell, D. B., Goldstein, S. L., Pena, L. D., Yehudai, M., and Kim, J. (2019). Deep atlantic ocean carbon storage and the rise of 100,000-year glacial cycles. *Nature Geoscience*, 12(5):355–360.

Ferrari, R., Jansen, M. F., Adkins, J. F., Burke, A., Stewart, A. L., and Thompson, A. F. (2014). Antarctic sea ice control on ocean circulation in present and glacial climates. *Proc. Natl. Acad. Sci. U. S. A.*, 111(24):8753–8758.

Fischer, H., Schmitt, J., Lüthi, D., Stocker, T. F., Tschumi, T., Parekh, P., Joos, F., Köhler, P., Völker, C., Gersonde, R., Barbante, C., Floch, M. L., Raynaud, D., and Wolff, E. (2010). The role of southern ocean processes in orbital and millennial CO2 variations – a synthesis. *Quaternary Science Reviews*, 29(1-2):193–205.

Flores, J. A., Gersonde, R., and Sierro, F. J. (1999). Pleistocene fluctuations in the Agulhas Current Retroflection based on the calcareous plankton record. *Mar. Micropaleontol.*, 37(1):1–22.

Flores, J.-A. and Sierro, F. J. (2007). Pronounced mid-pleistocene southward shift of the polar front in the atlantic sector of the southern ocean. *Deep Sea Research Part II: Topical Studies in Oceanography*, 54(21-22):2432–2442.

Flower, B. P., Oppo, D. W., McManus, J. F., Venz, K. A., Hodell, D. A., and Cullen, J. L. (2000). North atlantic intermediate to deep water circulation and chemical stratification during the past 1 myr. *Paleoceanography*, 15(4):388–403.

Fogwill, C., Turney, C., Hutchinson, D., Taschetto, A., and England, M. (2015). Obliquity control on southern hemisphere climate during the last glacial. *Scientific Reports*, 5(1).

Ford, H. L. and Raymo, M. E. (2019). Regional and global signals in seawater δ18o records across the mid-pleistocene transition. *Geology*, 48(2):113–117.

Foster, G. (2008). Seawater pH, pCO2 and [CO2-3] variations in the caribbean sea over the last 130 kyr: A boron isotope and b/ca study of planktic foraminifera. *Earth and Planetary Science Letters*, 271(1-4):254–266.

Foster, T. D. and Carmack, E. C. (1976). Frontal zone mixing and antarctic bottom water formation in the southern weddell sea. *Deep Sea Research and Oceanographic Abstracts*, 23(4):301–317.

Fraass, A. J. and Lowery, C. M. (2017). Defining uncertainty and error in planktic foraminiferal oxygen isotope measurements. *Paleoceanography*, 32(2):104–122.

François, R., Altabet, M. A., Yu, E.-F., Sigman, D. M., Bacon, M. P., Frank, M., Bohrmann, G., Bareille, G., and Labeyrie, L. D. (1997). Contribution of southern ocean surface-water stratification to low atmospheric CO2 concentrations during the last glacial period. *Nature*, 389(6654):929–935.

Frank, M. (1996). Reconstruction of Late Quaternary Environmental Conditions Applying the Natural Radionuclides 230th, 10be, 231pa and 238u: A Study of Deep-sea Sediments from the Eastern Sector of the Antarctic Circumpolar Current System (rekonstruktion Von Spätquartären Umweltbedingungen Mit Den Natürlichen Radionukliden 230th, 10be 231pa Und 238u: Eine Untersuchung Von Tiefseesedimenten Aus Dem Östlichen Sektor Des Antarktischen Zirkumpolarstromsystems). Technical report, Berichte zur Polarforschung.

Frank, M. (2002). RADIOGENIC ISOTOPES: TRACERS OF PAST OCEAN CIRCULATION AND EROSIONAL INPUT. *Reviews of Geophysics*, 40(1):1–1–1–38.

Frankignoulle, M., Canon, C., and Gattuso, J.-P. (1994). Marine calcification as a source of carbon dioxide: Positive feedback of increasing atmospheric CO2. *Limnology and Oceanography*, 39(2):458–462.

Franzese, A. M. et al. (2009). Use of strontium isotopes in detrital sediments to constrain the glacial position of the agulhas retroflection. *Paleoceanography*, 24(2):n/a–n/a.

Friedrich, O., Schiebel, R., Wilson, P. A., Weldeab, S., Beer, C. J., Cooper, M. J., and Fiebig, J. (2012). Influence of test size, water depth, and ecology on mg/ca, sr/ca, δ18o and δ13c in nine modern species of planktic foraminifers. *Earth and Planetary Science Letters*, 319-320:133–145.

Fritsch, F. N. and Butland, J. (1984). A Method for Constructing Local Monotone Piecewise Cubic Interpolants. *SIAM J. Sci. Stat. Comput.*, 5(2):300–304.

Galbraith, E. D. and Skinner, L. C. (2020). The biological pump during the last glacial maximum. *Annual Review of Marine Science*, 12(1):559–586.

Gebbie, G. (2014). How much did glacial north atlantic water shoal? *Paleoceanography*, 29(3):190–209.

Gebbie, G. and Huybers, P. (2012). The mean age of ocean waters inferred from radiocarbon observations: Sensitivity to surface sources and accounting for mixing histories. *Journal of Physical Oceanography*, 42(2):291–305.

Gebhardt, H., Sarnthein, M., Grootes, P. M., Kiefer, T., Kuehn, H., Schmieder, F., and Röhl, U. (2008). Paleonutrient and productivity records from the subarctic north pacific for pleistocene glacial terminations i to v. *Paleoceanography*, 23(4):n/a–n/a.

Gersonde, R., Crosta, X., Abelmann, A., and Armand, L. (2005). Sea-surface temperature and sea ice distribution of the southern ocean at the EPILOG last glacial maximum—a circum-antarctic view based on siliceous microfossil records. *Quaternary Science Reviews*, 24(7-9):869–896.

Gibbard, P. L., Head, M. J., and and, M. J. C. W. (2010). Formal ratification of the quaternary system/period and the pleistocene series/epoch with a base at 2.58 ma. *Journal of Quaternary Science*, 25(2):96–102.

Gill, A. E. (1968). A linear model of the antarctic circumpolar current. *Journal of Fluid Mechanics*, 32(3):465–488.

Gladstone, R. M., Bigg, G. R., and Nicholls, K. W. (2001). Iceberg trajectory modeling and meltwater injection in the Southern Ocean. *J. Geophys. Res. Ocean.*, 106(C9):19903–19915.

Goldstein, R. M., Zebker, H. A., and Barnett, T. P. (1989). Remote sensing of ocean currents. *Science*, 246(4935):1282–1285.

González-Dávila, M., Santana-Casiano, J. M., Fine, R. A., Happell, J., Delille, B., and Speich, S. (2011). Carbonate system in the water masses of the southeast atlantic sector of the southern ocean during february and march 2008. *Biogeosciences*, 8(5):1401–1413.

Gordon, A. L. (1986). Interocean exchange of thermocline water. *Journal of Geophysical Research*, 91(C4):5037.

Gordon, A. L., Lutjeharms, J. R., and Gründlingh, M. L. (1987). Stratification and circulation at the agulhas retroflection. *Deep Sea Research Part A. Oceanographic Research Papers*, 34(4):565–599.

Gottschalk, J., Skinner, L. C., Lippold, J., Vogel, H., Frank, N., Jaccard, S. L., and Waelbroeck, C. (2016). Biological and physical controls in the Southern Ocean on past millennial-scale atmospheric CO2 changes. *Nat. Commun.*, 7(May).

Gouretski, V. (2018). World ocean circulation experiment–argo global hydrographic climatology. *Ocean Science*.

Govin, A., Michel, E., Labeyrie, L., Waelbroeck, C., Dewilde, F., and Jansen, E. (2009). Evidence for northward expansion of antarctic bottom water mass in the southern ocean during the last glacial inception. *Paleoceanography*, 24(1):n/a–n/a.

Graham, R. M. and Boer, A. M. D. (2013). The dynamical subtropical front. *Journal of Geophysical Research: Oceans*, 118(10):5676–5685.

Graham, R. M., de Boer, A. M., Heywood, K. J., Chapman, M. R., and Stevens, D. P. (2012). Southern ocean fronts: Controlled by wind or topography? *Journal of Geophysical Research: Oceans*, 117(C8):n/a–n/a.

Grant, K. M., Rohling, E. J., Westerhold, T., Zabel, M., Heslop, D., Konijnendijk, T., and Lourens, L. (2017). A 3 million year index for north african humidity/aridity and the implication of potential pan-african humid periods. *Quaternary Science Reviews*, 171:100–118.

Grinsted, A., Moore, J. C., and Jevrejeva, S. (2004). Application of the cross wavelet transform and wavelet coherence to geophysical time series. *Nonlinear Processes in Geophysics*, 11(5/6):561–566.

Gruetzner, J., Espejo, F. J. J., Lathika, N., Uenzelmann-Neben, G., Hall, I. R., Hemming, S. R., and and, L. J. L. (2019). A new seismic stratigraphy in the indian-atlantic ocean gateway resembles major paleo-oceanographic changes of the last 7 ma. *Geochemistry, Geophysics, Geosystems*, 20(1):339–358.

Gröger, M., Henrich, R., and Bickert, T. (2003). Glacial–interglacial Variability in Lower North Atlantic Deep Water: Inference from Silt Grain-size Analysis and Carbonate Preservation in the Western Equatorial Atlantic. *Marine Geology,*, 201(4):321–332.

Guo, Z. T., Berger, A., Yin, Q. Z., and Qin, L. (2009). Strong asymmetry of hemispheric climates during MIS-13 inferred from correlating china loess and antarctica ice records. *Climate of the Past*, 5(1):21–31.

Hall, I. et al. (2017a). Site u1475. In *Proceedings of the International Ocean Discovery Program*. International Ocean Discovery Program.

Hall, I., Hemming, S., LeVay, L., Barker, S., Berke, M., Brentegani, L., Caley, T., Cartagena-Sierra, A., Charles, C., Coenen, J., Crespin, J., Franzese, A., Gruetzner, J., Han, X., Hines, S., Espejo, F. J., Just, J., Koutsodendris, A., Kubota, K., Lathika, N., Norris, R., dos Santos, T. P., Robinson, R., Rolinson, J., Simon, M., Tangunan, D., van der Lubbe, J., Yamane, M., and Zhang, H. (2017b). Expedition 361 summary. In *Proceedings of the International Ocean Discovery Program*. International Ocean Discovery Program.

Hall, I. R., McCave, I. N., Shackleton, N. J., Weedon, G. P., and Harris, S. E. (2001). Intensified deep pacific inflow and ventilation in pleistocene glacial times. *Nature*, 412(6849):809–812.

Hall, I. R., McCave, I. N., Zahn, R., Carter, L., Knutz, P. C., and Weedon, G. P. (2003). Paleocurrent reconstruction of the deep pacific inflow during the middle miocene: Reflections of east antarctic ice sheet growth. *Paleoceanography*, 18(2):n/a–n/a.

Hall, I. R., Moran, S. B., Zahn, R., Knutz, P. C., Shen, C.-C., and Edwards, R. L. (2006). Accelerated Drawdown of Meridional Overturning in the Late-glacial Atlantic Triggered by Transient Pre-h Event Freshwater Perturbation. *Geophysical Research Letters*, 33(16).

Hallberg, R. and Gnanadesikan, A. (2006). The role of eddies in determining the structure and response of the wind-driven southern hemisphere overturning: Results from the modeling eddies in the southern ocean (MESO) project. *Journal of Physical Oceanography*, 36(12):2232–2252.

Harms, N. C., Lahajnar, N., Gaye, B., Rixen, T., Schwarz-Schampera, U., and Emeis, K.-C. (2021). Sediment trap-derived particulate matter fluxes in the oligotrophic subtropical gyre of the South Indian Ocean. *Deep Sea Research Part II Top. Stud. Oceanogr.*, 183:104924.

Hasenfratz, A. P., Jaccard, S. L., Martínez-García, A., Sigman, D. M., Hodell, D. A., Vance, D., Bernasconi, S. M., Kleiven, H. K. F., Haumann, F. A., and Haug, G. H. (2019). The residence time of southern ocean surface waters and the 100,000-year ice age cycle. *Science*, 363(6431):1080–1084.

Hass, H. C. (2002). A method to reduce the influence of ice-rafted debris on a grain size record from northern fram strait, arctic ocean. *Polar Research*, 21(2):299–306.

Haug, G. H. and Tiedemann, R. (1998). Effect of the formation of the isthmus of panama on atlantic ocean thermohaline circulation. *Nature*, 393(6686):673–676.

Hays, J. D., Imbrie, J., and Shackleton, N. J. (1976). Variations in the Earth's Orbit: Pacemaker of the Ice Ages. *Science*, 194(4270):1121–1132.

Hayward, B. W., Kawagata, S., Grenfell, H. R., Sabaa, A. T., and O'Neill, T. (2007). Last global extinction in the deep sea during the mid-Pleistocene climate transition. *Paleoceanography*, 22(3).

Heinrich, H. (1988). Origin and consequences of cyclic ice rafting in the northeast atlantic ocean during the past 130,000 years. *Quaternary Research*, 29(2):142–152.

Heinze, C., Maier-Reimer, E., and Winn, K. (1991). Glacial pCO2reduction by the world ocean: Experiments with the hamburg carbon cycle model. *Paleoceanography*, 6(4):395–430.

Hemleben, C., Spindler, M., Breitinger, I., and Deuser, W. G. (1985). Field and laboratory studies on the ontogeny and ecology of some globorotaliid species from the Sargasso Sea off Bermuda. *J. Foraminifer. Res.*, 15(4):254–272.

Hemming, N. and Hanson, G. (1992). Boron isotopic composition and concentration in modern marine carbonates. *Geochimica et Cosmochimica Acta*, 56(1):537–543.

Hemming, S., Broecker, W., Sharp, W., Bond, G., Gwiazda, R., McManus, J., Klas, M., and Hajdas, I. (1998). Provenance of Heinrich Layers in Core V28-82, Northeastern Atlantic: 40ar/39ar Ages of Ice-rafted Hornblende, Pb Isotopes in Feldspar Grains, and Nd–sr–pb Isotopes in the Fine Sediment Fraction. *Earth and Planetary Science Letters*, 164(1-2):317–333.

Hemming, S. R. (2004). Heinrich events: Massive late pleistocene detritus layers of the north atlantic and their global climate imprint. *Reviews of Geophysics*, 42(1).

Henderson, G. M., Heinze, C., Anderson, R. F., and Winguth, A. M. (1999). Global distribution of the flux to ocean sediments constrained by GCM modelling. *Deep Sea Research Part I: Oceanographic Research Papers*, 46(11):1861–1893.

Henehan, M. J., Rae, J. W., Foster, G. L., Erez, J., Prentice, K. C., Kucera, M., Bostock, H. C., Martínez-Botí, M. A., Milton, J. A., Wilson, P. A., Marshall, B. J., and Elliott, T. (2013). Calibration of the boron isotope proxy in the planktonic foraminifera globigerinoides ruber for use in palaeo-CO2 reconstruction. *Earth and Planetary Science Letters*, 364:111–122.

Herbert, T. D., Peterson, L. C., Lawrence, K. T., and Liu, Z. (2010). Tropical ocean temperatures over the past 3.5 million years. *Science*, 328(5985):1530–1534.

Herman, F. and Brandon, M. (2015). Mid-latitude glacial erosion hotspot related to equatorial shifts in southern westerlies. *Geology*, 43(11):987–990.

Hesse, T., Butzin, M., Bickert, T., and Lohmann, G. (2011). A model-data comparison ofδ13c in the glacial atlantic ocean. *Paleoceanography*, 26(3):n/a–n/a.

Hillenbrand, C. D., Kuhn, G., and Frederichs, T. (2009). Record of a Mid-Pleistocene depositional anomaly in West Antarctic continental margin sediments: an indicator for ice-sheet collapse? *Quat. Sci. Rev.*, 28(13-14):1147–1159.

Ho, S. L., Mollenhauer, G., Lamy, F., Martínez-Garcia, A., Mohtadi, M., Gersonde, R., Hebbeln, D., Nunez-Ricardo, S., Rosell-Melé, A., and Tiedemann, R. (2012). Sea surface temperature variability in the pacific sector of the southern ocean over the past 700 kyr. *Paleoceanography*, 27(4).

Hodell, D. (1999). Leg 177 summary: Southern ocean paleoceanography. In *Proceedings of the Ocean Drilling Program, 177 Initial Reports*. Ocean Drilling Program.

Hodell, D., Crowhurst, S., Skinner, L., Tzedakis, P. C., Margari, V., Channell, J. E., Kamenov, G., Maclachlan, S., and Rothwell, G. (2013a). Response of iberian margin sediments to orbital and suborbital forcing over the past 420 ka. *Paleoceanography*, 28(1):185–199.

Hodell, D., Lourens, L., Crowhurst, S., Konijnendijk, T., Tjallingii, R., Jiménez-Espejo, F., Skinner, L., Tzedakis, P., Abrantes, F., Acton, G. D., Zarikian, C. A. A., Bahr, A., Balestra, B., Barranco, E. L., Carrara, G., Ducassou, E., Flood, R. D., Flores, J.-A., Furota, S., Grimalt, J., Grunert, P., Hernández-Molina, J., Kim, J. K., Krissek, L. A., Kuroda, J., Li, B., Lofi, J., Margari, V., Martrat, B., Miller, M. D., Nanayama, F., Nishida, N., Richter, C., Rodrigues, T., Rodríguez-Tovar, F. J., Roque, A. C. F., Goñi, M. F. S., Sánchez, F. J. S., Singh, A. D., Sloss, C. R., Stow, D. A., Takashimizu, Y., Tzanova, A., Voelker, A., Xuan, C., and Williams, T. (2015). A reference time scale for site u1385 (shackleton site) on the SW iberian margin. *Global and Planetary Change*, 133:49–64.

Hodell, D. A. and Channell, J. E. T. (2016). Mode transitions in northern hemisphere glaciation: Co-evolution of millennial and orbital variability in quaternary climate. *Climate of the Past*, 12(9):1805–1828.

Hodell, D. A., Channell, J. E. T., Curtis, J. H., Romero, O. E., and Röhl, U. (2008). Onset of Hudson Strait Heinrich Events in the Eastern North Atlantic at the End of the Middle Pleistocene Transition (~640 Ka)? *Paleoceanography and Paleoclimatology*, 23(4):n/a–n/a.

Hodell, D. A., Charles, C. D., and Sierro, F. J. (2001). Late Pleistocene evolution of the ocean's carbonate system. *Earth Planet. Sci. Lett.*, 192(2):109–124.

Hodell, D. A., Lourens, L., Stow, D. A. V., Hernández-Molina, J., and and, C. A. A. Z. (2013b). The 'shackleton site' (iodp site u1385) on the iberian margin. *Scientific Drilling*, 16:13–19.

Hodell, D. A. and Venz, K. (2013). Toward a high-resolution stable isotopic record of the southern ocean during the pliocene-pleistocene (4.8 to 0.8 MA). In *The Antarctic Paleoenvironment: A Perspective on Global Change: Part One*, volume 56, pages 265–310. American Geophysical Union.

Hodell, D. A., Venz, K. A., Charles, C. D., and Ninnemann, U. S. (2003). Pleistocene vertical carbon isotope and carbonate gradients in the South Atlantic sector of the Southern Ocean. *Geochemistry, Geophys. Geosystems*, 4(1):1–19.

Hodell, D. A. and Venz-Curtis, K. A. (2006). Late Neogene history of deepwater ventilation in the Southern Ocean. *Geochemistry, Geophysics, Geosystems*, 7(9).

Hoffmann, S. S., Dalsing, R. E., and Murphy, S. C. (2019). Sortable Silt Records of Intermediate-depth Circulation and Sedimentation in the Southwest Labrador Sea since the Last Glacial Maximum. *Quaternary Science Reviews*, 206:99–110.

Hogg, A. M. (2010). An antarctic circumpolar current driven by surface buoyancy forcing. *Geophysical Research Letters*, 37(23):n/a–n/a.

Holbourn, A., Kuhnt, W., Schulz, M., Flores, J.-A., and Andersen, N. (2007). Orbitally-paced climate evolution during the middle Miocene 'Monterey' carbon-isotope excursion. *Earth Planet. Sci. Lett.*, 261(3-4):534–550.

Honisch, B., Hemming, N. G., Archer, D., Siddall, M., and McManus, J. F. (2009). Atmospheric carbon dioxide concentration across the mid-pleistocene transition. *Science*, 324(5934):1551–1554.

Hoogakker, B. A., Rohling, E. J., Palmer, M. R., Tyrrell, T., and Rothwell, R. G. (2006). Underlying causes for long-term global ocean δ13C fluctuations over the last 1.20 Myr. *Earth Planet. Sci. Lett.*, 248(1-2):15–29.

Hough, J. L. (1950). Pleistocene lithology of antarctic ocean-bottom sediments. *The Journal of Geology*, 58(3):254–260.

Howard, W. R. and Prell, W. L. (1992). Late quaternary surface circulation of the southern indian ocean and its relationship to orbital variations. *Paleoceanography*, 7(1):79–117.

Howard, W. R. and Prell, W. L. (1994). Late quaternary CaCO3production and preservation in the southern ocean: Implications for oceanic and atmospheric carbon cycling. *Paleoceanography*, 9(3):453–482.

Howe, J. N. W. and Piotrowski, A. M. (2017). Atlantic deep water provenance decoupled from atmospheric CO2 concentration during the lukewarm interglacials. *Nature Communications*, 8(1).

Howe, J. N. W., Piotrowski, A. M., Noble, T. L., Mulitza, S., Chiessi, C. M., and Bayon, G. (2016). North atlantic deep water production during the last glacial maximum. *Nature Communications*, 7(1).

Hu, R., Bostock, H. C., Greaves, M., Piotrowski, A. M., and McCave, I. N. (2020). Coupled evolution of stable carbon isotopes between the southern ocean and the atmosphere over the last 260 ka. *Earth and Planetary Science Letters*, 538:116215.

Huybers, P. (2007). Glacial variability over the last two million years: An extended depth-derived agemodel, continuous obliquity pacing, and the pleistocene progression. *Quaternary Science Reviews*, 26(1-2):37–55.

Huybers, P. (2011). Combined obliquity and precession pacing of late pleistocene deglaciations. *Nature*, 480(7376):229–232.

Huybers, P. and Wunsch, C. (2004). A Depth-derived Pleistocene Age Model: Uncertainty Estimates, Sedimentation Variability, and Nonlinear Climate Change. *Paleoceanography*, 19(1):n/a–n/a.

Huybers, P. and Wunsch, C. (2005). Obliquity pacing of the late pleistocene glacial terminations. *Nature*, 434(7032):491–494.

Ikehara, M., Kawamura, K., Ohkouchi, N., Murayama, M., Nakamura, T., and Taira, A. (2000). Variations of terrestrial input and marine productivity in the southern ocean (48°s) during the last two deglaciations. *Paleoceanography*, 15(2):170–180.

Imbrie, J. (1971). A New Micropaleontological Method for Quantitative Paleoclimatology : Application to a Late Pleistocene Caribbean Core. *The late Cenozoic glacial ages*.

Imbrie, J., Berger, A., Boyle, E. A., Clemens, S. C., Duffy, A., Howard, W. R., Kukla, G., Kutzbach, J., Martinson, D. G., McIntyre, A., Mix, A. C., Molfino, B., Morley, J. J., Peterson, L. C., Pisias, N. G., Prell, W. L., Raymo, M. E., Shackleton, N. J., and Toggweiler, J. R. (1993). On the Structure and Origin of Major Glaciation Cycles 2. The 100,000-year Cycle. *Paleoceanography*, 8(6):699–735.

Imbrie, J., Boyle, E. A., Clemens, S. C., Duffy, A., Howard, W. R., Kukla, G., Kutzbach, J., Martinson, D. G., McIntyre, A., Mix, A. C., Molfino, B., Morley, J. J., Peterson,

L. C., Pisias, N. G., Prell, W. L., Raymo, M. E., Shackleton, N. J., and Toggweiler, J. R. (1992). On the Structure and Origin of Major Glaciation Cycles 1. Linear Responses to Milankovitch Forcing. *Paleoceanography*, 7(6):701–738.

Imbrie, J., Hays, J. D., Martinson, D. G., McIntyre, A., Mix, A. C., Morley, J. J., Pisias, N. G., Prell, W. L., and Shackleton, N. J. (1984). *Milankovitch And Climate, Part 1*, chapter The orbital theory of Pleistocene climate: support from a revised chronology of the marine d18O record, pages 269–305. D. Reidel Publishing Company.

IPCC (2021). *Climate Change 2021: The Physical Science Basis. Contribution of Working Group I to the Sixthassessment Report of the Intergovernmental Panel on Climate Change*. Cambridge University Press.

Ito, T. and Follows, M. J. (2005). Preformed phosphate, soft tissue pump and atmospheric co_2. *Journal of Marine Research*, 63(4):813–839.

Ivory, S. J., Blome, M. W., King, J. W., McGlue, M. M., Cole, J. E., and Cohen, A. S. (2016). Environmental change explains cichlid adaptive radiation at lake malawi over the past 1.2 million years. *Proceedings of the National Academy of Sciences*, 113(42):11895–11900.

Jaccard, S. L. (2005). Glacial/interglacial changes in subarctic north pacific stratification. *Science*, 308(5724):1003–1006.

Jaccard, S. L. and Galbraith, E. D. (2011). Large climate-driven changes of oceanic oxygen concentrations during the last deglaciation. *Nature Geoscience*, 5(2):151–156.

Jaccard, S. L., Hayes, C. T., Martínez-García, A., Hodell, D. A., Anderson, R. F., Sigman, D. M., and Haug, G. H. (2013). Two modes of change in Southern Ocean productivity over the past million years. *Science*, 339(6126):1419–1423.

Jacobs, S. S., Amos, A. F., and Bruchhausen, P. M. (1970). Ross sea oceanography and antarctic bottom water formation. *Deep Sea Research and Oceanographic Abstracts*, 17(6):935–962.

Jansen, J. H. F., Kuijpers, A., and Troelstra, S. R. (1986). A mid-brunhes climatic

event: Long-term changes in global atmosphere and ocean circulation. *Science*, 232(4750):619–622.

John, K. S., Passchier, S., TantillO, B., Darby, D., and Kearns, L. (2015). Microfeatures of modern sea-ice-rafted sediment and implications for paleo-sea-ice reconstructions. *Annals of Glaciology*, 56(69):83–93.

Jonkers, L., Barker, S., Hall, I. R., and Prins, M. A. (2015). Correcting for the influence of ice-rafted detritus on grain size-based paleocurrent speed estimates. *Paleoceanography*, 30(10):1347–1357.

Joos, F. and Spahni, R. (2008). Rates of change in natural and anthropogenic radiative forcing over the past 20,000 years. *Proceedings of the National Academy of Sciences*, 105(5):1425–1430.

Jouzel, J., Masson-Delmotte, V., Cattani, O., Dreyfus, G., Falourd, S., Hoffmann, G., Minster, B., Nouet, J., Barnola, J. M., Chappellaz, J., Fischer, H., Gallet, J. C., Johnsen, S., Leuenberger, M., Loulergue, L., Luethi, D., Oerter, H., Parrenin, F., Raisbeck, G., Raynaud, D., Schilt, A., Schwander, J., Selmo, E., Souchez, R., Spahni, R., Stauffer, B., Steffensen, J. P., Stenni, B., Stocker, T. F., Tison, J. L., Werner, M., and Wolff, E. W. (2007). Orbital and millennial antarctic climate variability over the past 800,000 years. *Science*, 317(5839):793–796.

Kageyama, M., Harrison, S. P., Kapsch, M.-L., Lofverstrom, M., Lora, J. M., Mikolajewicz, U., Sherriff-Tadano, S., Vadsaria, T., Abe-Ouchi, A., Bouttes, N., Chandan, D., Gregoire, L. J., Ivanovic, R. F., Izumi, K., LeGrande, A. N., Lhardy, F., Lohmann, G., Morozova, P. A., Ohgaito, R., Paul, A., Peltier, W. R., Poulsen, C. J., Quiquet, A., Roche, D. M., Shi, X., Tierney, J. E., Valdes, P. J., Volodin, E., and Zhu, J. (2021). The PMIP4 last glacial maximum experiments: Preliminary results and comparison with the PMIP3 simulations. *Climate of the Past*, 17(3):1065–1089.

Kaiser, E. A., Caldwell, A., and Billups, K. (2019). North Atlantic Upper-Ocean Hydrography During the Mid-Pleistocene Transition Evidenced by Globorotalia truncatulinoides Coiling Ratios. *Paleoceanogr. Paleoclimatology*, 34(4):658–671.

Kanfoush, S. L. (2000). Millennial-scale instability of the antarctic ice sheet during the last glaciation. *Science*, 288(5472):1815–1819.

Kanfoush, S. L., Hodell, D. A., Charles, C. D., Janecek, T. R., and Rack, F. R. (2002). Comparison of ice-rafted debris and physical properties in ODP site 1094 (south atlantic) with the vostok ice core over the last four climatic cycles. *Palaeogeography, Palaeoclimatology, Palaeoecology*, 182(3-4):329–349.

Karsten, R. H. and Marshall, J. (2002). Constructing the residual circulation of the ACC from observations. *Journal of Physical Oceanography*, 32(12):3315–3327.

Kasper, S., van der Meer, M. T. J., Mets, A., Zahn, R., Damsté, J. S. S., and Schouten, S. (2014). Salinity changes in the agulhas leakage area recorded by stable hydrogen isotopes of c alkenones during termination i and II. *Climate of the Past*, 10(1):251–260.

Keany, J., Ledbetter, M., Watkins, N., and Huang, T.-C. (1976). Diachronous deposition of ice-rafted debris in sub-antarctic deep-sea sediments. *Geological Society of America Bulletin*, 87(6):873.

Keigwin, L. (1982). Isotopic paleoceanography of the caribbean and east pacific: Role of panama uplift in late neogene time. *Science*, 217(4557):350–353.

Kemp, A., Grigorov, I., Pearce, R., and Garabato, A. N. (2010). Migration of the antarctic polar front through the mid-pleistocene transition: Evidence and climatic implications. *Quaternary Science Reviews*, 29(17-18):1993–2009.

Kender, S., McClymont, E. L., Elmore, A. C., Emanuele, D., Leng, M. J., and Elderfield, H. (2016). Mid Pleistocene foraminiferal mass extinction coupled with phytoplankton evolution. *Nat. Commun.*, 7(May).

Key, R. M., Kozyr, A., Sabine, C. L., Lee, K., Wanninkhof, R., Bullister, J. L., Feely, R. A., Millero, F. J., Mordy, C., and Peng, T.-H. (2004). A global ocean carbon climatology: Results from global data analysis project (GLODAP). *Global Biogeochemical Cycles*, 18(4):n/a–n/a.

Khatiwala, S., Primeau, F., and Hall, T. (2009). Reconstruction of the history of anthropogenic CO2 concentrations in the ocean. *Nature*, 462(7271):346–349.

Khatiwala, S., Primeau, F., and Holzer, M. (2012). Ventilation of the deep ocean

constrained with tracer observations and implications for radiocarbon estimates of ideal mean age. *Earth Planet. Sci. Lett.*, 325-326:116–125.

Khélifi, N. and Frank, M. (2014). A major change in north atlantic deep water circulation 1.6 million years ago. *Climate of the Past*, 10(4):1441–1451.

Killingley, J., Johnson, R., and Berger, W. (1981). Oxygen and carbon isotopes of individual shells of planktonic foraminifera from Ontong-Java plateau, equatorial pacific. *Palaeogeogr. Palaeoclimatol. Palaeoecol.*, 33(1-3):193–204.

Kim, J., Goldstein, S. L., Pena, L. D., Jaume-Seguí, M., Knudson, K. P., Yehudai, M., and Bolge, L. (2021). North atlantic deep water during pleistocene interglacials and glacials. *Quaternary Science Reviews*, 269:107146.

Kim, S. T. and O'Neil, J. R. (1997). Equilibrium and nonequilibrium oxygen isotope effects in synthetic carbonates. *Geochim. Cosmochim. Acta*, 61(16):3461–3475.

Kleiven, H. F., Hall, I. R., McCave, I. N., Knorr, G., and Jansen, E. (2011). Coupled deep-water flow and climate variability in the middle pleistocene north atlantic. *Geology*, 39(4):343–346.

Kleiven, H. F., Jansen, E., Curry, W. B., Hodell, D. A., and Venz, K. (2003). Atlantic ocean thermohaline circulation changes on orbital to suborbital timescales during the mid-pleistocene. *Paleoceanography*, 18(1):n/a–n/a.

Knorr, G. and Lohmann, G. (2003). Southern ocean origin for the resumption of atlantic thermohaline circulation during deglaciation. *Nature*, 424(6948):532–536.

Knox, F. and McElroy, M. B. (1984). Changes in atmospheric CO2: Influence of the marine biota at high latitude. *Journal of Geophysical Research*, 89(D3):4629.

Koch-Larrouy, A., Morrow, R., Penduff, T., and Juza, M. (2010). Origin and mechanism of subantarctic mode water formation and transformation in the southern indian ocean. *Ocean Dynamics*, 60(3):563–583.

Kohfeld, K., Graham, R., de Boer, A., Sime, L., Wolff, E., Quéré, C. L., and Bopp, L. (2013). Southern hemisphere westerly wind changes during the last glacial maximum: Paleo-data synthesis. *Quaternary Science Reviews*, 68:76–95.

Kohfeld, K. E., Anderson, R. F., and Lynch-Stieglitz, J. (2000). Carbon isotopic disequilibrium in polar planktonic foraminifera and its impact on modern and Last Glacial Maximum reconstructions. *Paleoceanography*, 15(1):53–64.

Kohfeld, K. E., Le Quéré, C., Harrison, S. P., and Anderson, R. F. (2005). Role of marine biology in glacial-interglacial CO2 cycles. *Science*, 308(5718):74–78.

Konfirst, M. A., Kuhn, G., Monien, D., and Scherer, R. P. (2011). Correlation of Early Pliocene Diatomite to Low Amplitude Milankovitch Cycles in the ANDRILL AND-1b Drill Core. *Marine Micropaleontology*, 80(3-4):114–124.

Koutsodendris, A., Nakajima, K., Kaboth-Bahr, S., Berke, M. A., Franzese, A. M., Hall, I. R., Hemming, S. R., Just, J., LeVay, L. J., Pross, J., and Robinson, R. (2021). A pliopleistocene (c. 0–4 ma) cyclostratigraphy for IODP site u1478 (mozambique channel, SW indian ocean): Exploring an offshore record of paleoclimate and ecosystem variability in SE africa. *Newsletters on Stratigraphy*, 54(2):159–181.

Kroopnick, P. M. (1985). The distribution of 13C of ΣCO2 in the world oceans. *Deep Sea Res. Part A, Oceanogr. Res. Pap.*, 32(1):57–84.

Krueger, S., Leuschner, D., Ehrmann, W., Schmiedl, G., and Mackensen, A. (2012). North atlantic deep water and antarctic bottom water variability during the last 200ka recorded in an abyssal sediment core off south africa. *Global and Planetary Change*, 80-81:180–189.

Krueger, S., Leuschner, D. C., Ehrmann, W., Schmiedl, G., Mackensen, A., and Diekmann, B. (2008). Ocean circulation patterns and dust supply into the South Atlantic during the last glacial cycle revealed by statistical analysis of kaolinite/chlorite ratios. *Mar. Geol.*, 253(3-4):82–91.

Kumar, N., Anderson, R. F., Mortlock, R. A., Froelich, P. N., Kubik, P., Dittrich-Hannen, B., and Suter, M. (1995). Increased biological productivity and export production in the glacial southern ocean. *Nature*, 378(6558):675–680.

Kunz-Pirrung, M., Gersonde, R., and Hodell, D. A. (2002). Mid-brunhes century-scale diatom sea surface temperature and sea ice records from the atlantic sector of

the southern ocean (ODP leg 177, sites 1093, 1094 and core PS2089-2). *Palaeogeography, Palaeoclimatology, Palaeoecology*, 182(3-4):305–328.

Kurahashi-Nakamura, T., Paul, A., and Losch, M. (2017). Dynamical Reconstruction of the Global Ocean State during the Last Glacial Maximum. *Paleoceanography*, 32(4):326–350.

Kwon, E. Y., Hain, M. P., Sigman, D. M., Galbraith, E. D., Sarmiento, J. L., and Toggweiler, J. R. (2012). North atlantic ventilation of southern-sourced deep water in the glacial ocean. *Paleoceanography*, 27(2):n/a–n/a.

Kylander, M. E., Muller, J., Wüst, R. A., Gallagher, K., Garcia-Sanchez, R., Coles, B. J., and Weiss, D. J. (2007). Rare earth element and Pb isotope variations in a 52 kyr peat core from Lynch's Crater (NE Queensland, Australia): Proxy development and application to paleoclimate in the Southern Hemisphere. *Geochim. Cosmochim. Acta*, 71(4):942–960.

Köhler, P. and Bintanja, R. (2008). The carbon cycle during the mid pleistocene transition: The southern ocean decoupling hypothesis. *Climate of the Past*, 4(4):311–332.

Köhler, P., Fischer, H., Munhoven, G., and Zeebe, R. E. (2005). Quantitative interpretation of atmospheric carbon records over the last glacial termination. *Global Biogeochemical Cycles*, 19(4):n/a–n/a.

Labeyrie, L. D., Pichon, J. J., Labracherie, M., Ippolito, P., Duprat, J., and Duplessy, J. C. (1986). Melting History of Antarctica during the Past 60,000 Years. *Nature*, 322(6081):701–706.

Laepple, T. and Lohmann, G. (2009). Seasonal cycle as template for climate variability on astronomical timescales. *Paleoceanography*, 24(4).

Lamy, F., Arz, H. W., Kilian, R., Lange, C. B., Lembke-Jene, L., Wengler, M., Kaiser, J., Baeza-Urrea, O., Hall, I. R., Harada, N., and Tiedemann, R. (2015). Glacial reduction and millennial-scale variations in drake passage throughflow. *Proceedings of the National Academy of Sciences*, 112(44):13496–13501.

Lamy, F., Gersonde, R., Winckler, G., Esper, O., Jaeschke, A., Kuhn, G., Ullermann, J.,

Martinez-Garcia, A., Lambert, F., and Kilian, R. (2014). Increased dust deposition in the pacific southern ocean during glacial periods. *Science*, 343(6169):403–407.

Lamy, F., Winckler, G., and Zarikian, C. A. (2021). *Volume 383: Dynamics of the Pacific Antarctic Circumpolar Current (DYNAPACC)*. International Ocean Discovery Program.

Lang, D. C., Bailey, I., Wilson, P. A., Chalk, T. B., Foster, G. L., and Gutjahr, M. (2016). Incursions of southern-sourced water into the deep North Atlantic during late Pliocene glacial intensification. *Nat. Geosci.*, 9(5):375–379.

Lang, N. and Wolff, E. W. (2011). Interglacial and glacial variability from the last 800 ka in marine, ice and terrestrial archives. *Clim. Past*, 7(2):361–380.

Larrasoaña, J. C., Roberts, A. P., Rohling, E. J., Winklhofer, M., and Wehausen, R. (2003). Three million years of monsoon variability over the northern sahara. *Climate Dynamics*, 21(7-8):689–698.

Laskar, J., Robutel, P., Joutel, F., Gastineau, M., Correia, A. C. M., and Levrard, B. (2004). A long-term numerical solution for the insolation quantities of the Earth. *Astron. \& Astrophys.*, 428(1):261–285.

Latimer, J. C. and Filippelli, G. M. (2001). Terrigenous input and paleoproductivity in the Southern Ocean. *Paleoceanography*, 16(6):627–643.

Lazarus, D., Hilbrecht, H., Spencer-Cervato, C., and Thierstein, H. (1995). Sympatric speciation and phyletic change in globorotalia truncatulinoides. *Paleobiology*, 21(1):28–51.

Lear, C. H., Bailey, T. R., Pearson, P. N., Coxall, H. K., and Rosenthal, Y. (2008). Cooling and ice growth across the eocene-oligocene transition. *Geology*, 36(3):251.

Lear, C. H., Billups, K., Rickaby, R. E., Diester-Haass, L., Mawbey, E. M., and Sosdian, S. M. (2016). Breathing more deeply: Deep ocean carbon storage during the mid-pleistocene climate transition. *Geology*, 44(12):1035–1038.

LeGrand, P. and Wunsch, C. (1995). Constraints from Paleotracer Data on the North Atlantic Circulation during the Last Glacial Maximum. *Paleoceanography*, 10(6):1011–1045.

LeGrande, A. N., Lynch-Stieglitz, J., and Farmer, E. C. (2004). Oxygen isotopic composition of Globorotalia truncatulinoides as a proxy for intermediate depth density. *Paleoceanography*, 19(4):1–7.

Li, C., Le Roux, G., Sonke, J., van Beek, P., Souhaut, M., Van der Putten, N., and De Vleeschouwer, F. (2017). Recent 210Pb, 137Cs and 241Am accumulation in an ombrotrophic peatland from Amsterdam Island (Southern Indian Ocean). *J. Environ. Radioact.*, 175-176:164–169.

Lichey, C. and Hellmer, H. H. (2001). Modeling giant-iceberg drift under the influence of sea ice in the weddell sea, antarctica. *Journal of Glaciology*, 47(158):452–460.

Licht, K. J. and Hemming, S. R. (2017). Analysis of antarctic glacigenic sediment provenance through geochemical and petrologic applications. *Quaternary Science Reviews*, 164:1–24.

Lisiecki, L. E. (2010). A benthicδ13c-based proxy for atmospheric pCO_2 over the last 1.5 myr. *Geophysical Research Letters*, 37(21):n/a–n/a.

Lisiecki, L. E. (2014). Atlantic overturning responses to obliquity and precession over the last 3 Myr. *Paleoceanography*, 29(2):71–86.

Lisiecki, L. E. and Raymo, M. E. (2005). A pliocene-pleistocene stack of 57 globally distributed benthic δ18o records. *Paleoceanography*, 20(1):n/a–n/a.

Lisiecki, L. E., Raymo, M. E., and Curry, W. B. (2008). Atlantic overturning responses to late pleistocene climate forcings. *Nature*, 456(7218):85–88.

Lisitzin, A. (1960). Bottom Sediments of the Eastern Antarctic and the Southern Indian Ocean. *Deep Sea Research (1953)*, 7(2):89–99.

Liu, Z. and Alexander, M. (2007). Atmospheric bridge, oceanic tunnel, and global climatic teleconnections. *Rev. Geophys.*, 45(2):1–34.

Liu, Z., Cleaveland, L. C., and Herbert, T. D. (2008). Early onset and origin of 100-kyr cycles in pleistocene tropical SST records. *Earth and Planetary Science Letters*, 265(3-4):703–715.

Lohmann, G. P. and Schweitzer, P. N. (1990). Globorotalia truncatulinoides' Growth and chemistry as probes of the past thermocline: 1. Shell Size. *Paleoceanography*, 5(1):55–75.

Lomb, N. R. (1976). Least-squares frequency analysis of unequally spaced data. *Astrophys. Space Sci.*, 39(2):447–462.

Lončarić, N., Peeters, F. J., Kroon, D., and Brummer, G. J. A. (2006). Oxygen isotope ecology of recent planktic foraminifera at the central Walvis Ridge (SE Atlantic). *Paleoceanography*, 21(3):1–18.

Lougheed, B. C. and Obrochta, S. P. (2019). A rapid, deterministic age-depth modeling routine for geological sequences with inherent depth uncertainty. *Paleoceanography and Paleoclimatology*, 34(1):122–133.

Lund, D. C., Adkins, J. F., and Ferrari, R. (2011). Abyssal atlantic circulation during the last glacial maximum: Constraining the ratio between transport and vertical mixing. *Paleoceanography*, 26(1).

Lutjeharms, J. and Ansorge, I. (2001). The agulhas return current. *Journal of Marine Systems*, 30(1-2):115–138.

Lutjeharms, J. R. E. and Ballegooyen, R. C. V. (1988). The retroflection of the agulhas current. *Journal of Physical Oceanography*, 18(11):1570–1583.

Lynch-Stieglitz, J., Adkins, J. F., Curry, W. B., Dokken, T., Hall, I. R., Herguera, J. C., Hirschi, J. J.-M., Ivanova, E. V., Kissel, C., Marchal, O., Marchitto, T. M., McCave, I. N., McManus, J. F., Mulitza, S., Ninnemann, U., Peeters, F., Yu, E.-F., and Zahn, R. (2007). Atlantic meridional overturning circulation during the last glacial maximum. *Science*, 316(5821):66–69.

Lynch-Stieglitz, J., Stocker, T. F., Broecker, W. S., and Fairbanks, R. G. (1995). The influence of air-sea exchange on the isotopic composition of oceanic carbon: Observations and modeling. *Global Biogeochemical Cycles*, 9(4):653–665.

Lynch-Stieglitz, J., Valley, S. G., and Schmidt, M. W. (2019). Temperature-dependent ocean–atmosphere equilibration of carbon isotopes in surface and intermediate waters over the deglaciation. *Earth Planet. Sci. Lett.*, 506:466–475.

Löwemark, L., Hong, W.-L., Yui, T.-F., and Hung, G.-W. (2005). A test of different factors influencing the isotopic signal of planktonic foraminifera in surface sediments from the northern south china sea. *Marine Micropaleontology*, 55(1-2):49–62.

Lüthi, D., Floch, M. L., Bereiter, B., Blunier, T., Barnola, J.-M., Siegenthaler, U., Raynaud, D., Jouzel, J., Fischer, H., Kawamura, K., and Stocker, T. F. (2008). High-resolution carbon dioxide concentration record 650,000–800,000 years before present. *Nature*, 453(7193):379–382.

Mackensen, A., Grobe, H., Hubberten, H.-W., Spiess, V., and Fütterer, D. (1989). Stable isotope stratigraphy from the antarctic continental margin during the last one million years. *Marine Geology*, 87(2-4):315–321.

Mackensen, A. and Licari, L. (2003). Carbon isotopes of live benthic foraminifera from the south atlantic: Sensitivity to bottom water carbonate saturation state and organic matter rain rates. In *The South Atlantic in the Late Quaternary*, pages 623–644. Springer Berlin Heidelberg.

Mahaney, W. C. (2002). *Atlas of Sand Grain Surface Textures and Applications*. Oxford University Press, Oxford New York.

Maiorano, P., Marino, M., and Flores, J.-A. (2009). The warm interglacial marine isotope stage 31: Evidences from the calcareous nannofossil assemblages at site 1090 (southern ocean). *Marine Micropaleontology*, 71(3-4):166–175.

Manabe, S. and Stouffer, R. J. (1988). Two stable equilibria of a coupled ocean-atmosphere model. *Journal of Climate*, 1(9):841–866.

Mancin, N., Hayward, B. W., Trattenero, I., Cobianchi, M., and Lupi, C. (2013). Can the morphology of deep-sea benthic foraminifera reveal what caused their extinction during the mid-Pleistocene Climate Transition? *Mar. Micropaleontol.*, 104:53–70.

Manoj, M. C., Thambam, M., Sahana, A., Mohan, R., and Mahender, K. (2013). Provenance and temporal variability of ice rafted debris in the indian sector of the southern ocean during the last 22,000 years. *Journal of Earth System Science*, 122(2):491–501.

Marchitto, T. M. and Broecker, W. S. (2006). Deep Water Mass Geometry in the Glacial Atlantic Ocean: A Review of Constraints from the Paleonutrient Proxy Cd/ca. *Geochemistry, Geophysics, Geosystems*, 7(12):n/a–n/a.

Marchitto, T. M., Lehman, S. J., Ortiz, J. D., Fluckiger, J., and van Geen, A. (2007). Marine radiocarbon evidence for the mechanism of deglacial atmospheric CO2 rise. *Science*, 316(5830):1456–1459.

Margolis, S. V., Kroopnick, P. M., Goodney, D. E., Dudley, W. C., and Mahoney, M. E. (1975). Oxygen and Carbon Isotopes from Calcareous Nannofossils As Paleoceanographic Indicators. *Science*, 189(4202):555–557.

Marino, G. et al. (2013). Agulhas Salt-leakage Oscillations during Abrupt Climate Changes of the Late Pleistocene. *Paleoceanography*, 28(3):599–606.

Marino, M., Maiorano, P., Lirer, F., and Pelosi, N. (2009). Response of calcareous nannofossil assemblages to paleoenvironmental changes through the mid-Pleistocene revolution at Site 1090 (Southern Ocean). *Palaeogeogr. Palaeoclimatol. Palaeoecol.*, 280(3-4):333–349.

Marinov, I., Gnanadesikan, A., Sarmiento, J. L., Toggweiler, J. R., Follows, M., and Mignone, B. K. (2008). Impact of oceanic circulation on biological carbon storage in the ocean and atmosphericpCO2. *Global Biogeochemical Cycles*, 22(3):n/a–n/a.

Marinov, I., Gnanadesikan, A., Toggweiler, J. R., and Sarmiento, J. L. (2006). The Southern Ocean biogeochemical divide. *Nature*, 441(7096):964–967.

Marshall, J. and Speer, K. (2012). Closure of the meridional overturning circulation through southern ocean upwelling. *Nature Geoscience*, 5(3):171–180.

Martin, J. H. (1990). Glacial-interglacial CO 2 change: The Iron Hypothesis. *Paleoceanography*, 5(1):1–13.

Martin, T., Steele, M., and Zhang, J. (2014). Seasonality and long-term trend of arctic ocean surface stress in a model. *Journal of Geophysical Research: Oceans*, 119(3):1723–1738.

Martínez, J. I. (1997). Decreasing influence of Subantarctic Mode Water north of the Tasman Front over the past 150 kyr. *Palaeogeogr. Palaeoclimatol. Palaeoecol.*, 131(3-4):355–364.

Martínez-Garcia, A., Rosell-Melé, A., Geibert, W., Gersonde, R., Masqué, P., Gaspari, V., and Barbante, C. (2009). Links between iron supply, marine productivity, sea surface temperature, and CO2over the last 1.1 ma. *Paleoceanography*, 24(1):n/a–n/a.

Martínez-Garcia, A., Rosell-Melé, A., Jaccard, S. L., Geibert, W., Sigman, D. M., and Haug, G. H. (2011). Southern Ocean dust-climate coupling over the past four million years. *Nature*, 476(7360):312–315.

Martinez-Garcia, A., Rosell-Mele, A., McClymont, E. L., Gersonde, R., and Haug, G. H. (2010). Subpolar link to the emergence of the modern equatorial pacific cold tongue. *Science*, 328(5985):1550–1553.

Martínez-García, A., Sigman, D. M., Ren, H., Anderson, R. F., Straub, M., Hodell, D. A., Jaccard, S. L., Eglinton, T. I., and Haug, G. H. (2014). Iron fertilization of the subantarctic ocean during the last ice age. *Science*, 343(6177):1347–1350.

Martínez-Méndez, G., Zahn, R., Hall, I. R., Peeters, F. J. C., Pena, L. D., Cacho, I., and Negre, C. (2010). Contrasting multiproxy reconstructions of surface ocean hydrography in the agulhas corridor and implications for the agulhas leakage during the last 345,000 years. *Paleoceanography*, 25(4):n/a–n/a.

Martínez-Méndez, G., Zahn, R., Hall, I. R., Pena, L. D., and Cacho, I. (2008). 345,000-year-long multi-proxy records off south africa document variable contributions of northern versus southern component water to the deep south atlantic. *Earth and Planetary Science Letters*, 267(1-2):309–321.

Maslin, M. A. and Brierley, C. M. (2015). The role of orbital forcing in the early middle pleistocene transition. *Quaternary International*, 389:47–55.

Masson-Delmotte, V., Stenni, B., Pol, K., Braconnot, P., Cattani, O., Falourd, S., Kageyama, M., Jouzel, J., Landais, A., Minster, B., Barnola, J., Chappellaz, J., Krinner, G., Johnsen, S., Röthlisberger, R., Hansen, J., Mikolajewicz, U., and Otto-

Bliesner, B. (2010). EPICA dome c record of glacial and interglacial intensities. *Quaternary Science Reviews*, 29(1-2):113–128.

Matsumoto, K. and Lynch-Stieglitz, J. (1999). Similar glacial and holocene deep water circulation inferred from southeast pacific benthic foraminiferal carbon isotope composition. *Paleoceanography*, 14(2):149–163.

Matsumoto, K., Sarmiento, J. L., and Brzezinski, M. A. (2002). Silicic Acid Leakage from the Southern Ocean: A Possible Explanation for Glacial atmosphericpCO2. *Global Biogeochemical Cycles*, 16(3):5–1–5–23.

McCave, I. (2008). Chapter 8 size sorting during transport and deposition of fine sediments. In *Developments in Sedimentology*, pages 121–142. Elsevier.

McCave, I. and Andrews, J. (2019). Distinguishing current effects in sediments delivered to the ocean by ice. i. principles, methods and examples. *Quaternary Science Reviews*, 212:92–107.

McCave, I., Thornalley, D., and Hall, I. (2017). Relation of Sortable Silt Grain-size to Deep-sea Current Speeds: Calibration of the 'mud Current Meter'. *Deep Sea Research Part I: Oceanographic Research Papers*, 127:1–12.

McCave, I. N., Crowhurst, S. J., Kuhn, G., Hillenbrand, C.-D., and Meredith, M. P. (2013). Minimal change in antarctic circumpolar current flow speed between the last glacial and holocene. *Nature Geoscience*, 7(2):113–116.

McCave, I. N. and Hall, I. R. (2006). Size sorting in marine muds: Processes, pitfalls, and prospects for paleoflow-speed proxies. *Geochemistry, Geophysics, Geosystems*, 7(10):n/a–n/a.

McCave, I. N., Manighetti, B., and Beveridge, N. A. S. (1995a). Circulation in the Glacial North Atlantic Inferred from Grain-size Measurements. *Nature*, 374(6518):149–152.

McCave, I. N., Manighetti, B., and Robinson, S. G. (1995b). Sortable silt and fine sediment size/composition slicing: Parameters for palaeocurrent speed and palaeoceanography. *Paleoceanography*, 10(3):593–610.

McClymont, E. L., Elmore, A. C., Kender, S., Leng, M. J., Greaves, M., and Elderfield, H. (2016). Pliocene-Pleistocene evolution of sea surface and intermediate water temperatures from the southwest Pacific. *Paleoceanography*, 31(6):895–913.

McClymont, E. L., Sosdian, S. M., Rosell-Melé, A., and Rosenthal, Y. (2013). Pleistocene sea-surface temperature evolution: Early cooling, delayed glacial intensification, and implications for the mid-pleistocene climate transition. *Earth-Science Reviews*, 123:173–193.

Mccorkle, D. C. and Heggie, D. T. (1998). Glacial and Holocene stable isotope distributions in the southeastern We have variations in Cibicidoides wuellerstorfi using depth transects of cores firore and We compare these new restfits stable isotope records changes in Indian Ocean The strong last g. *Holocene*, 13(1):20–34.

McCorkle, D. C. and Keigwin, L. D. (1994). Depth Profiles of δ13c in Bottom Water and Core Top C.wuellerstorfion the Ontong Java Plateau and Emperor Seamounts. *Paleoceanography*, 9(2):197–208.

McManus, J. F., Francois, R., Gherardi, J.-M., Keigwin, L. D., and Brown-Leger, S. (2004). Collapse and Rapid Resumption of Atlantic Meridional Circulation Linked to Deglacial Climate Changes. *Nature*, 428(6985):834–837.

McManus, J. F., Oppo, D. W., and Cullen, J. L. (1999). A 0.5-million-year record of millennial-scale climate variability in the north atlantic. *Science*, 283(5404):971–975.

Melles, M., Brigham-Grette, J., Minyuk, P. S., Nowaczyk, N. R., Wennrich, V., DeConto, R. M., Anderson, P. M., Andreev, A. A., Coletti, A., Cook, T. L., Haltia-Hovi, E., Kukkonen, M., Lozhkin, A. V., Rosen, P., Tarasov, P., Vogel, H., and Wagner, B. (2012). 2.8 Million Years of Arctic Climate Change from Lake El'gygytgyn, NE Russia. *Science*, 337(6092):315–320.

Menviel, L., Yu, J., Joos, F., Mouchet, A., Meissner, K. J., and England, M. H. (2017). Poorly ventilated deep ocean at the last glacial maximum inferred from carbon isotopes: A data-model comparison study. *Paleoceanography*, 32(1):2–17.

Menviel, L. C., Skinner, L. C., Tarasov, L., and Tzedakis, P. C. (2020). An ice–climate oscillatory framework for dansgaard–oeschger cycles. *Nature Reviews Earth & Environment*, 1(12):677–693.

Merino, N., Sommer, J. L., Durand, G., Jourdain, N. C., Madec, G., Mathiot, P., and Tournadre, J. (2016). Antarctic icebergs melt over the southern ocean: Climatology and impact on sea ice. *Ocean Modelling*, 104:99–110.

Meskhidze, N., Nenes, A., Chameides, W. L., Luo, C., and Mahowald, N. (2007). Atlantic southern ocean productivity: Fertilization from above or below? *Global Biogeochemical Cycles*, 21(2):n/a–n/a.

Meyers, S. R. (2012). Seeing red in cyclic stratigraphy: Spectral noise estimation for astrochronology. *Paleoceanography*, 27(3):1–12.

Milankovič, M. (1940). *Canon of Insolation and the Ice-age Problem*. Zavod za udžzbenike i nastavna sredstva, Beograd.

Miller, M. C., McCave, I. N., and Komar, P. D. (1977). Threshold of sediment motion under unidirectional currents. *Sedimentology*, 24(4):507–527.

Mix, A., Pisias, N., Rugh, W., Wilson, J., Morey, A., and Hagelberg, T. (1995). Benthic foraminifer stable isotope record from site 849 (0-5 ma): Local and global climate changes. In *Proceedings of the Ocean Drilling Program, 138 Scientific Results*. Ocean Drilling Program.

Mix, A. C. and Fairbanks, R. G. (1985). North atlantic surface-ocean control of pleistocene deep-ocean circulation. *Earth and Planetary Science Letters*, 73(2-4):231–243.

Mohtadi, M. and Hebbeln, D. (2004). Mechanisms and variations of the paleoproductivity off northern chile (24°s-33°s) during the last 40,000 years. *Paleoceanography*, 19(2):n/a–n/a.

Møller, H. S., Jensen, K. G., Kuijpers, A., Aagaard-Sørensen, S., Seidenkrantz, M.-S., Prins, M., Endler, R., and Mikkelsen, N. (2006). Late-holocene Environment and Climatic Changes in Ameralik Fjord, Southwest Greenland: Evidence from the Sedimentary Record. *The Holocene*, 16(5):685–695.

Molyneux, E. G. et al. (2007). Deep water variability on the southern Agulhas Plateau: Interhemispheric links over the past 170 ka. *Paleoceanography*, 22(4):1–14.

Monien, D., Kuhn, G., von Eynatten, H., and Talarico, F. M. (2012). Geochemical Provenance Analysis of Fine-grained Sediment Revealing Late Miocene to Recent Paleo-environmental Changes in the Western Ross Sea, Antarctica. *Global and Planetary Change*, 96-97:41–58.

Mook, W. G., Bommerson, J. C., and Staverman, W. H. (1974). Carbon isotope fractionation between dissolved bicarbonate and gaseous carbon dioxide. *Earth Planet. Sci. Lett.*, 22(2):169–176.

Morée, A. L., Schwinger, J., and Heinze, C. (2018). Southern ocean controls of the vertical marine c gradient – a modelling study. *Biogeosciences*, 15(23):7205–7223.

Moriarty, K. C. (1977). Clay minerals in southeast indian ocean sediments, transport mechanisms and depositional environments. *Marine Geology*, 25(1-3):149–174.

Mudelsee, M. and Schulz, M. (1997). The mid-pleistocene climate transition: Onset of 100 ka cycle lags ice volume build-up by 280 ka. *Earth and Planetary Science Letters*, 151(1-2):117–123.

Muglia, J. and Schmittner, A. (2015). Glacial Atlantic overturning increased by wind stress in climate models. *Geophys. Res. Lett.*, 42(22):9862–9869.

Muglia, J. and Schmittner, A. (2021). Carbon isotope constraints on glacial atlantic meridional overturning: Strength vs depth. *Quaternary Science Reviews*, 257:106844.

Muglia, J., Skinner, L. C., and Schmittner, A. (2018). Weak overturning circulation and high Southern Ocean nutrient utilization maximized glacial ocean carbon. *Earth Planet. Sci. Lett.*, 496:47–56.

Mulitza, S., Rühlemann, C., Bickert, T., Hale, W., Pätzold, J., and Wefer, G. (1998). Late Quaternary δ13C gradients and carbonate accumulation in the western equatorial Atlantic. *Earth Planet. Sci. Lett.*, 155(3-4):237–249.

Muri, H., Berger, A., Yin, Q., Voldoire, A., Mélia, D. S. Y., and Sundaram, S. (2011). SST and ice sheet impacts on the MIS–13 climate. *Climate Dynamics*, 39(7-8):1739–1761.

Naafs, B. D. A., Hefter, J., Acton, G., Haug, G. H., Martínez-Garcia, A., Pancost, R., and Stein, R. (2012). Strengthening of north american dust sources during the late pliocene (2.7ma). *Earth and Planetary Science Letters*, 317-318:8–19.

Newnham, R. M., Lowe, D. J., Giles, T., and Alloway, B. V. (2007). Vegetation and climate of auckland, new zealand, since ca. 32 000 cal. yr ago: Support for an extended LGM. *Journal of Quaternary Science*, 22(5):517–534.

Niebler, H.-S. (1995). *Rekonstruktionen Von Paläo-umweltparametern Anhand Von Stabilen Isotopen Und Faunen-vergesellschaftungen Planktischer Foraminiferen Im Südatlantik= Reconstruction of Paleo-environmental Parameters Using Stable Isotopes and Faunal Assemblages of Planktonic Foraminifera in the South Atlantic Ocean*. PhD thesis, Alfred Wegener Institute for Polar and Marine Research.

Nielsen, S. H. H., Hodell, D. A., editor Raymond, C., and International Symposium on Antarctic Earth, S. (2007a). Antarctic ice-rafted detritus (IRD) in the South Atlantic; Indicators of Iceshelf Dynamics or Ocean Surface Conditions? *Open-File Rep. - U. S. Geol. Surv.*, 4(1999):Short Research Paper 020.

Nielsen, S. H. H., Hodell, D. A., Kamenov, G., Guilderson, T., and Perfit, M. R. (2007b). Origin and significance of ice-rafted detritus in the atlantic sector of the southern ocean. *Geochemistry, Geophysics, Geosystems*, 8(12):n/a–n/a.

Ninnemann, U. S. and Charles, C. D. (1997). Regional differences in Quaternary Subantarctic nutrient cycling: Link to intermediate and deep water ventilation. *Paleoceanography*, 12(4):560–567.

Noble, T. L., Piotrowski, A. M., Robinson, L. F., McManus, J. F., Hillenbrand, C.-D., and Bory, A. J.-M. (2012). Greater supply of patagonian-sourced detritus and transport by the ACC to the atlantic sector of the southern ocean during the last glacial period. *Earth and Planetary Science Letters*, 317-318:374–385.

Ólafsdóttir, K. B., Schulz, M., and Mudelsee, M. (2016). REDFIT-x: Cross-spectral analysis of unevenly spaced paleoclimate time series. *Computers & Geosciences*, 91(December 2010):11–18.

Olsen, A., Key, R. M., van Heuven, S., Lauvset, S. K., Velo, A., Lin, X., Schirnick, C., Kozyr, A., Tanhua, T., Hoppema, M., Jutterström, S., Steinfeldt, R., Jeansson, E., Ishii, M., Pérez, F. F., and Suzuki, T. (2016). The Global Ocean Data Analysis Project version 2 (GLODAPv2) – an internally consistent data product for the world ocean. *Earth Syst. Sci. Data*, 8(2):297–323.

Oppo, D. W. and Fairbanks, R. G. (1987). Variability in the deep and intermediate water circulation of the Atlantic Ocean during the past 25,000 years: Northern Hemisphere modulation of the Southern Ocean. *Earth Planet. Sci. Lett.*, 86(1):1–15.

Oppo, D. W. and Fairbanks, R. G. (1989). Carbon isotope composition of tropical surface water during the past 22,000 years. *Paleoceanography*, 4(4):333–351.

Oppo, D. W., Gebbie, G., Huang, K.-F., Curry, W. B., Marchitto, T. M., and Pietro, K. R. (2018). Data constraints on glacial atlantic water mass geometry and properties. *Paleoceanography and Paleoclimatology*, 33(9):1013–1034.

Oppo, D. W. and Lehman, S. J. (1993). Mid-depth circulation of the subpolar north atlantic during the last glacial maximum. *Science*, 259(5098):1148–1152.

Oppo, D. W., McManus, J. F., and Cullen, J. L. (1998). Abrupt climate events 500,000 to 340,000 years ago: Evidence from subpolar north atlantic sediments. *Science*, 279(5355):1335–1338.

Orsi, A. H., Whitworth, T., and Nowlin, W. D. (1995). On the meridional extent and fronts of the Antarctic Circumpolar Current. *Deep. Res. Part I*, 42(5):641–673.

Paillard, D., Labeyrie, L., and Yiou, P. (1996). Macintosh program performs time-series analysis. *Eos, Transactions American Geophysical Union*, 77(39):379–379.

Palmer, M. and Elderfield, H. (1986). Rare Earth Elements and Neodymium Isotopes in Ferromanganese Oxide Coatings of Cenozoic Foraminifera from the Atlantic Ocean. *Geochimica et Cosmochimica Acta*, 50(3):409–417.

Park, Y.-H., Park, T., Kim, T.-W., Lee, S.-H., Hong, C.-S., Lee, J.-H., Rio, M.-H., Pujol, M.-I., Ballarotta, M., Durand, I., and Provost, C. (2019). Observations of the antarctic circumpolar current over the udintsev fracture zone, the narrowest choke point in the southern ocean. *Journal of Geophysical Research: Oceans*, 124(7):4511–4528.

Past Interglacials Working Group of PAGES (2016). Interglacials of the last 800,000 years. *Reviews of Geophysics*, 54(1):162–219.

Peeters, F. J., Acheson, R., Brummer, G. J. A., De Ruijter, W. P., Schneider, R. R., Ganssen, G. M., Ufkes, E., and Kroon, D. (2004). Vigorous exchange between the Indian and Atlantic oceans at the end of the past five glacial periods. *Nature*, 430(7000):661–665.

Pena, L. D. and Goldstein, S. L. (2014). Thermohaline circulation crisis and impacts during the mid-pleistocene transition. *Science*, 345(6194):318–322.

Peterson, C. D. and Lisiecki, L. E. (2018). Deglacial whole-ocean δ^{13}c change estimated from 480 benthic foraminiferal records. *Climate of the Past*, 14(8):1229–1252.

Petit, J. R., Jouzel, J., Raynaud, D., Barkov, N. I., Barnola, J.-M., Basile, I., Bender, M., Chappellaz, J., Davis, M., Delaygue, G., Delmotte, M., Kotlyakov, V. M., Legrand, M., Lipenkov, V. Y., Lorius, C., PÉpin, L., Ritz, C., Saltzman, E., and Stievenard, M. (1999). Climate and atmospheric history of the past 420,000 years from the vostok ice core, antarctica. *Nature*, 399(6735):429–436.

Petschick, R., Kuhn, G., and Gingele, F. (1996). Clay mineral distribution in surface sediments of the south atlantic: Sources, transport, and relation to oceanography. *Marine Geology*, 130(3-4):203–229.

Pettersson, H. (1948). The swedish deep-sea expedition. *Nature*, 162(4113):324–325.

Philander, S. G. H. (1983). El niño southern oscillation phenomena. *Nature*, 302(5906):295–301.

Piotrowski, A. M., Lee, D.-C., Christensen, J. N., Burton, K. W., Halliday, A. N., Hein, J. R., and Günther, D. (2000). Changes in Erosion and Ocean Circulation Recorded in the Hf Isotopic Compositions of North Atlantic and Indian Ocean Ferromanganese Crusts. *Earth and Planetary Science Letters*, 181(3):315–325.

Pisias, N. G., Mix, A. C., and Zahn, R. (1990). Nonlinear response in the global climate system: Evidence from benthic oxygen isotopic record in core RC13-110. *Paleoceanography*, 5(2):147–160.

Poirier, R. K. and Billups, K. (2014). Pleistocene climate transition. *Paleoceanography*, 29:1046–1061.

Pollard, D. and DeConto, R. M. (2009). Modelling west antarctic ice sheet growth and collapse through the past five million years. *Nature*, 458(7236):329–332.

Pollard, R. T. and Read, J. F. (2001). Circulation pathways and transports of the southern ocean in the vicinity of the southwest indian ridge. *Journal of Geophysical Research: Oceans*, 106(C2):2881–2898.

Poore, R. Z. and Berggren, W. A. (1975). Late cenozoic planktonic foraminiferal biostratigraphy and paleoclimatology of hatton-rockall basin; DSDP site 116. *The Journal of Foraminiferal Research*, 5(4):270–293.

Praetorius, S. K., McManus, J. F., Oppo, D. W., and Curry, W. B. (2008). Episodic Reductions in Bottom-water Currents since the Last Ice Age. *Nature Geoscience*, 1(7):449–452.

Prell, W. L., Imbrie, J., Martinson, D. G., Morley, J. J., Pisias, N. G., Shackleton, N. J., and Streeter, H. F. (1986). Graphic Correlation of Oxygen Isotope Stratigraphy Application to the Late Quaternary. *Paleoceanography*, 1(2):137–162.

Pugh, R., McCave, I., Hillenbrand, C.-D., and Kuhn, G. (2009). Circum-antarctic age modelling of quaternary marine cores under the antarctic circumpolar current: Ice-core dust–magnetic correlation. *Earth and Planetary Science Letters*, 284(1-2):113–123.

Quillévéré, F., Morard, R., Escarguel, G., Douady, C. J., Ujiié, Y., de Garidel-Thoron, T., and de Vargas, C. (2013). Global scale same-specimen morpho-genetic analysis of truncorotalia truncatulinoides: A perspective on the morphological species concept in planktonic foraminifera. *Palaeogeography, Palaeoclimatology, Palaeoecology*, 391:2–12.

Rackow, T., Wesche, C., Timmermann, R., Hellmer, H. H., Juricke, S., and Jung, T. (2017). A simulation of small to giant Antarctic iceberg evolution: Differential impact on climatology estimates. *J. Geophys. Res. Ocean.*, 122(4):3170–3190.

Rahmstorf, S. (2000). The thermohaline ocean circulation: A system with dangerous thresholds? *Climatic Change*, 46(3):247–256.

Rahmstorf, S. (2002). Ocean circulation and climate during the past 120,000 years. *Nature*, 419(6903):207–214.

Railsback, L. B., Gibbard, P. L., Head, M. J., Voarintsoa, N. R. G., and Toucanne, S. (2015). An optimized scheme of lettered marine isotope substages for the last 1.0 million years, and the climatostratigraphic nature of isotope stages and substages. *Quaternary Science Reviews*, 111:94–106.

Raiswell, R., Benning, L. G., Tranter, M., and Tulaczyk, S. (2008). Bioavailable iron in the Southern Ocean: The significance of the iceberg conveyor belt. *Geochem. Trans.*, 9:1–9.

Raymo, M. E. (2006). Plio-pleistocene ice volume, antarctic climate, and the global 18o record. *Science*, 313(5786):492–495.

Raymo, M. E., Ganley, K., Carter, S., Oppo, D. W., and McManus, J. (1998). Millennial-scale climate instability during the early pleistocene epoch. *Nature*, 392(6677):699–702.

Raymo, M. E. and Mitrovica, J. X. (2012). Collapse of polar ice sheets during the stage 11 interglacial. *Nature*, 483(7390):453–456.

Raymo, M. E., Oppo, D. W., and Curry, W. (1997). The mid-Pleistocene climate transition: A deep sea carbon isotopic perspective. *Paleoceanography*, 12(4):546–559.

Raymo, M. E., Oppo, D. W., Flower, B. P., Hodell, D. A., McManus, J. F., Venz, K. A., Kleiven, K. F., and McIntyre, K. (2004). Stability of North Atlantic water masses in face of pronounced climate variability during the Pleistocene. *Paleoceanography*, 19(2):1–13.

Raymo, M. E., Ruddiman, W. F., Backman, J., Clement, B. M., and Martinson, D. G. (1989). Late pliocene variation in northern hemisphere ice sheets and north atlantic deep water circulation. *Paleoceanography*, 4(4):413–446.

Raymo, M. E., Ruddiman, W. F., Shackleton, N. J., and Oppo, D. W. (1990). Evolution of Atlantic-Pacific δ13C gradients over the last 2.5 m.y. *Earth Planet. Sci. Lett.*, 97(3-4):353–368.

Read, J., Lucas, M., Holley, S., and Pollard, R. (2000). Phytoplankton, nutrients and hydrography in the frontal zone between the southwest indian subtropical gyre and the southern ocean. *Deep Sea Research Part I: Oceanographic Research Papers*, 47(12):2341–2367.

Read, J. F. and Pollard, R. T. (1993). Structure and transport of the antarctic circumpolar current and agulhas return current at 40°e. *Journal of Geophysical Research*, 98(C7):12281.

Reason, C. J. C. and Rouault, M. (2006). Sea surface temperature variability in the tropical southeast atlantic ocean and west african rainfall. *Geophysical Research Letters*, 33(21).

Reed, S. J. B. (2005). *Electron Microprobe Analysis and Scanning Electron Microscopy in Geology*. Cambridge University Press.

Rehfeld, K. and Kurths, J. (2014). Similarity estimators for irregular and age-uncertain time series. *Climate of the Past*, 10(1):107–122.

Rehfeld, K., Marwan, N., Heitzig, J., and Kurths, J. (2011). Comparison of correlation analysis techniques for irregularly sampled time series. *Nonlinear Processes in Geophysics*, 18(3):389–404.

Reichart, G. J., Lourens, L. J., and Zachariasse, W. J. (1998). Temporal variability in the northern Arabian Sea oxygen minimum zone (OMZ) during the last 225,000 years. *Paleoceanography*, 13(6):607–621.

Reid, J. L. (2003). On the total geostrophic circulation of the Indian Ocean: Flow patterns, tracers, and transports. *Prog. Oceanogr.*, 56(1):137–186.

Reynolds, B., Frank, M., and O'Nions, R. (1999). Nd- and Pb-isotope Time Series from Atlantic Ferromanganese Crusts: Implications for Changes in Provenance and Paleocirculation Over the Last 8 Myr. *Earth and Planetary Science Letters*, 173(4):381–396.

Rial, J. A., Oh, J., and Reischmann, E. (2013). Synchronization of the climate system to eccentricity forcing and the 100,000-year problem. *Nature Geoscience*, 6(4):289–293.

Rickaby, R. E. M., Bard, E., Sonzogni, C., Rostek, F., Beaufort, L., Barker, S., Rees, G., and Schrag, D. P. (2007). Coccolith chemistry reveals secular variations in the global ocean carbon cycle? *Earth Planet. Sci. Lett.*, 253(1-2):83–95.

Ridgwell, A. J., Watson, A. J., and Raymo, M. E. (1999). Is the spectral signature of the 100 kyr glacial cycle consistent with a milankovitch origin? *Paleoceanography*, 14(4):437–440.

Rintoul, S. R. (1991). South atlantic interbasin exchange. *Journal of Geophysical Research: Oceans*, 96(C2):2675–2692.

Rintoul, S. R. and England, M. H. (2002). Ekman transport dominates local air–sea fluxes in driving variability of Subantarctic Mode Water. *J. Phys. Oceanogr.*, 32(5):1308–1321.

Riveiros, N. V., Waelbroeck, C., Skinner, L., Duplessy, J.-C., McManus, J. F., Kandiano, E. S., and Bauch, H. A. (2013). The "MIS 11 Paradox" and Ocean Circulation: Role of Millennial Scale Events. *Earth and Planetary Science Letters*, 371-372:258–268.

Riveiros, N. V., Waelbroeck, C., Skinner, L., Roche, D. M., Duplessy, J.-C., and Michel, E. (2010). Response of South Atlantic Deep Waters to Deglacial Warming during Terminations V and I. *Earth and Planetary Science Letters*, 298(3-4):323–333.

Roberts, J., Gottschalk, J., Skinner, L. C., Peck, V. L., Kender, S., Elderfield, H., Waelbroeck, C., Riveiros, N. V., and Hodell, D. A. (2016). Evolution of south atlantic density and chemical stratification across the last deglaciation. *Proceedings of the National Academy of Sciences*, 113(3):514–519.

Roberts, J., McCave, I., McClymont, E., Kender, S., Hillenbrand, C.-D., Matano, R., Hodell, D., and Peck, V. (2017). Deglacial changes in flow and frontal structure through the drake passage. *Earth and Planetary Science Letters*, 474:397–408.

Robinson, R. S., Sigman, D. M., DiFiore, P. J., Rohde, M. M., Mashiotta, T. A., and Lea, D. W. (2005). Diatom-bound15n/14n: New support for enhanced nutrient consumption in the ice age subantarctic. *Paleoceanography*, 20(3):n/a–n/a.

Rodríguez-Sanz, L., Mortyn, P. G., Martínez-Garcia, A., Rosell-Melé, A., and Hall, I. R. (2012). Glacial southern ocean freshening at the onset of the middle pleistocene climate transition. *Earth and Planetary Science Letters*, 345-348:194–202.

Rohling, E. J., Fenton, M., Jorissen, F. J., Bertrand, P., Ganssen, G., and Caulet, J. P. (1998). Magnitudes of sea-level lowstands of the past 500,000 years. *Nature*, 394(6689):162–165.

Romahn, S., MacKensen, A., Groeneveld, J., and Pätzold, J. (2014). Deglacial intermediate water reorganization: New evidence from the Indian Ocean. *Clim. Past*, 10(1):293–303.

Romero, O. E., Kim, J. H., Bárcena, M. A., Hall, I. R., Zahn, R., and Schneider, R. (2015). High-latitude forcing of diatom productivity in the southern Agulhas Plateau during the past 350 kyr. *Paleoceanography*, 30(2):118–132.

Rose, K. A., Sikes, E. L., Guilderson, T. P., Shane, P., Hill, T. M., Zahn, R., and Spero, H. J. (2010). Upper-ocean-to-atmosphere radiocarbon offsets imply fast deglacial carbon dioxide release. *Nature*, 466(7310):1093–1097.

Rosenthal, Y., Boyle, E. A., and Slowey, N. (1997). Temperature control on the incorporation of magnesium, strontium, fluorine, and cadmium into benthic foraminiferal shells from little bahama bank: Prospects for thermocline paleoceanography. *Geochimica et Cosmochimica Acta*, 61(17):3633–3643.

Rother, H., Fink, D., Shulmeister, J., Mifsud, C., Evans, M., and Pugh, J. (2014). The early rise and late demise of new zealand's last glacial maximum. *Proceedings of the National Academy of Sciences*, 111(32):11630–11635.

Ruddiman, W. F. (2003). Orbital insolation, ice volume, and greenhouse gases. *Quaternary Science Reviews*, 22(15-17):1597–1629.

Ruddiman, W. F. and McIntyre, A. (1981). Oceanic mechanisms for amplification of the 23,000-year ice-volume cycle. *Science*, 212(4495):617–627.

Ruddiman, W. F., Raymo, M. E., Martinson, D. G., Clement, B. M., and Backman, J. (1989). Pleistocene evolution: Northern hemisphere ice sheets and north atlantic ocean. *Paleoceanography*, 4(4):353–412.

Ruggieri, E., Herbert, T., Lawrence, K. T., and Lawrence, C. E. (2009). Change point method for detecting regime shifts in paleoclimatic time series: Application to δ18O time series of the Plio-Pleistocene. *Paleoceanography*, 24(1):1–15.

Russon, T., Elliot, M., Kissel, C., Cabioch, G., Deckker, P. D., and Corrège, T. (2009). Middle-late pleistocene deep water circulation in the southwest subtropical pacific. *Paleoceanography*, 24(4).

Rutberg, R. L., Hemming, S. R., and Goldstein, S. L. (2000). Reduced north atlantic deep water flux to the glacial southern ocean inferred from neodymium isotope ratios. *Nature*, 405(June):935–938.

Sachs, J. P., Schneider, R. R., Eglinton, T. I., Freeman, K. H., Ganssen, G., McManus, J. F., and Oppo, D. W. (2000). Alkenones as paleoceanographic proxies. *Geochemistry, Geophysics, Geosystems*, 1(11):n/a–n/a.

Sallée, J. B., Pellichero, V., Akhoudas, C., Pauthenet, E., Vignes, L., Schmidtko, S., Garabato, A. N., Sutherland, P., and Kuusela, M. (2021). Summertime increases in upper-ocean stratification and mixed-layer depth. *Nature*, 591(7851):592–598.

Sallée, J.-B., Wienders, N., Speer, K., and Morrow, R. (2006). Formation of subantarctic mode water in the southeastern indian ocean. *Ocean Dynamics*, 56(5-6):525–542.

Sarmiento, J. L., Gruber, N., Brzezinski, M. A., and Dunne, J. P. (2004). High-latitude controls of thermocline nutrients and low latitude biological productivity. *Nature*, 427(6969):56–60.

Sarmiento, J. L. and Toggweiler, J. R. (1984). A new model for the role of the oceans in determining atmospheric p CO2. *Nature*, 308(5960):621–624.

Sarnthein, M. and Tiedemann, R. (1989). Toward a high-resolution stable isotope stratigraphy of the last 3.4 million years: Sites 658 and 659 off northwest africa. In *Proceedings of the Ocean Drilling Program, 108 Scientific Results*. Ocean Drilling Program.

Scargle, J. D. (1982). Studies in astronomical time series analysis. Ii - Statistical Aspects of Spectral Analysis of Unevenly Spaced Data. *Astrophys. J.*, 263:835.

Schaefer, G., Rodger, J. S., Hayward, B. W., Kennett, J. P., Sabaa, A. T., and Scott, G. H. (2005). Planktic foraminiferal and sea surface temperature record during the last 1 myr across the subtropical front, southwest pacific. *Marine Micropaleontology*, 54(3-4):191–212.

Schefuss, E., Damsté, J. S. S., and Jansen, J. H. F. (2004). Forcing of tropical atlantic sea surface temperatures during the mid-pleistocene transition. *Paleoceanography*, 19(4):n/a–n/a.

Scherer, R. P. (1998). Pleistocene collapse of the west antarctic ice sheet. *Science*, 281(5373):82–85.

Scherer, R. P., Bohaty, S. M., Dunbar, R. B., Esper, O., Flores, J.-A., Gersonde, R., Harwood, D. M., Roberts, A. P., and Taviani, M. (2008). Antarctic records of precession-paced insolation-driven warming during early pleistocene marine isotope stage 31. *Geophysical Research Letters*, 35(3).

Schiffelbein, P. and Hills, S. (1984). Direct assessment of stable isotope variability in planktonic foraminifera populations. *Palaeogeography, Palaeoclimatology, Palaeoecology*, 48(2-4):197–213.

Schmidt, H., Berger, W. H., Bickert, T., and Wefer, G. (1993). Quaternary carbon isotope record of pelagic foraminifers: Site 806, Ontong Java Plateau. In *Proc. Ocean Drill. Progr. Sci. Results*, volume 130, pages 397–409.

Schmitt, J., Schneider, R., Elsig, J., Leuenberger, D., Lourantou, A., Chappellaz, J., Köhler, P., Joos, F., Stocker, T. F., Leuenberger, M., and Fischer, H. (2012). Carbon isotope constraints on the deglacial CO2 rise from ice cores. *Science*, 336(6082):711–714.

Schmittner, A. (2003). Southern ocean sea ice and radiocarbon ages of glacial bottom waters. *Earth and Planetary Science Letters*, 213(1-2):53–62.

Schmittner, A., Bostock, H. C., Cartapanis, O., Curry, W. B., Filipsson, H. L., Galbraith, E. D., Gottschalk, J., Herguera, J. C., Hoogakker, B., Jaccard, S. L., Lisiecki, L. E., Lund, D. C., Martínez-Méndez, G., Lynch-Stieglitz, J., Mackensen, A., Michel, E., Mix, A. C., Oppo, D. W., Peterson, C. D., Repschläger, J., Sikes, E. L., Spero, H. J., and Waelbroeck, C. (2017). Calibration of the carbon isotope composition (δ 13 C) of benthic foraminifera. *Paleoceanography*, 32(6):512–530.

Schmittner, A. and Galbraith, E. D. (2008). Glacial greenhouse-gas fluctuations controlled by ocean circulation changes. *Nature*, 456(7220):373–376.

Schodlok, M. P., Hellmer, H. H., Rohardt, G., and Fahrbach, E. (2006). Weddell Sea iceberg drift: Five years of observations. *J. Geophys. Res. Ocean.*, 111(6):1–14.

Scussolini, P., Marino, G., Brummer, G.-J. A., and Peeters, F. J. (2015). Saline indian ocean waters invaded the south atlantic thermocline during glacial termination II. *Geology*, 43(2):139–142.

Seidov, D., Stouffer, R. J., and Haupt, B. J. (2005). Is there a simple bi-polar ocean seesaw? *Global and Planetary Change*, 49(1-2):19–27.

Semtner, A. J. (1986). History and methodology of modelling the circulation of the world ocean. In *Advanced Physical Oceanographic Numerical Modelling*, pages 23–32. Springer Netherlands.

Sexton, P. F. and Norris, R. D. (2008). Dispersal and biogeography of marine plankton: Long-distance dispersal of the foraminifer Truncorotalia truncatulinoides. *Geology*, 36(11):899–902.

Shackleton, N., Le, J., Mix, A., and Hall, M. (1992). Carbon isotope records from pacific surface waters and atmospheric carbon dioxide. *Quaternary Science Reviews*, 11(4):387–400.

Shackleton, N. J. (1967). Oxygen isotope analyses and pleistocene temperatures reassessed. *Nature*, 215(5096):15–17.

Shackleton, N. J. (1977). The oxygen isotope stratigraphic record of the late pleistocene. *Philosophical Transactions of the Royal Society of London. B, Biological Sciences*, 280(972):169–182.

Shackleton, N. J. (2000). The 100,000-year ice-age cycle identified and found to lag temperature, carbon dioxide, and orbital eccentricity. *Science*, 289(5486):1897–1902.

Shackleton, N. J., Backman, J., Zimmerman, H., Kent, D. V., Hall, M. A., Roberts, D. G., Schnitker, D., Baldauf, J. G., Desprairies, A., Homrighausen, R., Huddlestun, P., Keene, J. B., Kaltenback, A. J., Krumsiek, K. A. O., Morton, A. C., Murray, J. W., and Westberg-Smith, J. (1984). Oxygen isotope calibration of the onset of ice-rafting and history of glaciation in the north atlantic region. *Nature*, 307(5952):620–623.

Shackleton, N. J., Berger, A., and Peltier, W. R. (1990). An alternative astronomical calibration of the lower pleistocene timescale based on ODP site 677. *Transactions of the Royal Society of Edinburgh: Earth Sciences*, 81(4):251–261.

Shackleton, N. J., Hall, M. A., Line, J., and Shuxi, C. (1983). Carbon isotope data in core v19-30 confirm reduced carbon dioxide concentration in the ice age atmosphere. *Nature*, 306(5941):319–322.

Shackleton, N. J. and Opdyke, N. D. (1973). Oxygen isotope and palaeomagnetic stratigraphy of equatorial pacific core v28-238: Oxygen isotope temperatures and ice volumes on a 105 year and 106 year scale. *Quaternary Research*, 3(1):39–55.

Shoenfelt, E. M., Winckler, G., Lamy, F., Anderson, R. F., and Bostick, B. C. (2018). Highly bioavailable dust-borne iron delivered to the Southern Ocean during glacial periods. *Proc. Natl. Acad. Sci. U. S. A.*, 115(44):11180–11185.

Siccha, M. and Kucera, M. (2017). Data Descriptor: ForCenS, a curated database of planktonic foraminifera census counts in marine surface sediment samples. *Sci. Data*, 4:1–12.

Sieber, M., Conway, T. M., de Souza, G. F., Hassler, C. S., Ellwood, M. J., and Vance,

D. (2021). Isotopic fingerprinting of biogeochemical processes and iron sources in the iron-limited surface Southern Ocean. *Earth Planet. Sci. Lett.*, 567:116967.

Siegenthaler, U. and Wenk, T. (1984). Rapid atmospheric CO2 variations and ocean circulation. *Nature*, 308(5960):624–626.

Sigman, D. M. and Boyle, E. A. (2000). Glacial/Interglacial changes in atmospheric carbon dioxide. *Nature*, 407(October):859–869.

Sigman, D. M., Hain, M. P., and Haug, G. H. (2010). The polar ocean and glacial cycles in atmospheric CO2 concentration. *Nature*, 466(7302):47–55.

Sikes, E. L., Allen, K. A., and Lund, D. C. (2017). Enhanced δ13c and δ18o differences between the south atlantic and south pacific during the last glaciation: The deep gateway hypothesis. *Paleoceanography*, 32(10):1000–1017.

Sikes, E. L., Howard, W. R., Samson, C. R., Mahan, T. S., Robertson, L. G., and Volkman, J. K. (2009). Southern ocean seasonal temperature and subtropical front movement on the south tasman rise in the late quaternary. *Paleoceanography*, 24(2):n/a–n/a.

Silva, T. A. M., Bigg, G. R., and Nicholls, K. W. (2006). Contribution of giant icebergs to the southern ocean freshwater flux. *Journal of Geophysical Research*, 111(C3).

Simon, M. H., Arthur, K. L., Hall, I. R., Peeters, F. J. C., Loveday, B. R., Barker, S., Ziegler, M., and Zahn, R. (2013). Millennial-scale Agulhas Current variability and its implications for salt-leakage through the Indian–Atlantic Ocean Gateway. *Earth Planet. Sci. Lett.*, 383:101–112.

Simon, M. H., Ziegler, M., Barker, S., van der Meer, M. T. J., Schouten, S., and Hall, I. R. (2020). A late pleistocene dataset of agulhas current variability. *Scientific Data*, 7(1).

Skinner, L. and Shackleton, N. (2005). An atlantic lead over pacific deep-water change across termination i: Implications for the application of the marine isotope stage stratigraphy. *Quaternary Science Reviews*, 24(5-6):571–580.

Skinner, L. C., Primeau, F., Freeman, E., de la Fuente, M., Goodwin, P. A., Gottschalk, J., Huang, E., McCave, I. N., Noble, T. L., and Scrivner, A. E. (2017). Radiocarbon Constraints on the Glacial Ocean Circulation and Its Impact on Atmospheric CO2. *Nature*, 8(1).

Sloyan, B. M. and Rintoul, S. R. (2001). Circulation, renewal, and modification of antarctic mode and intermediate water. *Journal of Physical Oceanography*, 31(4):1005–1030.

Sluijs, A., Röhl, U., Schouten, S., Brumsack, H.-J., Sangiorgi, F., Damsté, J. S. S., and Brinkhuis, H. (2008). Arctic Late Paleocene-early Eocene Paleoenvironments with Special Emphasis on the Paleocene-eocene Thermal Maximum (lomonosov Ridge, Integrated Ocean Drilling Program Expedition 302). *Paleoceanography*, 23(1):n/a–n/a.

Smith, D. G., Ledbetter, M. T., and Ciesielski, P. F. (1983). Ice-rafted volcanic ash in the south atlantic sector of the southern ocean during the last 100,000 years. *Marine Geology*, 53(4):291–312.

Snyder, C. W. (2016). Evolution of global temperature over the past two million years. *Nature*, 538(7624):226–228.

Sokolov, S. and Rintoul, S. R. (2009). Circumpolar structure and distribution of the antarctic circumpolar current fronts: 1. mean circumpolar paths. *Journal of Geophysical Research*, 114(C11).

Sosdian, S. and Rosenthal, Y. (2009). Deep-sea temperature and ice volume changes across the pliocene-pleistocene climate transitions. *Science*, 325(5938):306–310.

Speich, S., Blanke, B., and Cai, W. (2007). Atlantic meridional overturning circulation and the southern hemisphere supergyre. *Geophysical Research Letters*, 34(23):n/a–n/a.

Spero, H. J., Bijma, J., Lea, D. W., and Bernis, B. E. (1997). Effect of seawater carbonate concentration on foraminiferal carbon and oxygen isotopes. *Nature*, 390(6659):497–500.

Spero, H. J. and Lea, D. W. (2002). The cause of carbon isotope minimum events on glacial terminations. *Science*, 296(5567):522–525.

Spero, H. J., Lerche, I., and Williams, D. F. (1991). Opening the carbon isotope "vital effect" black box, 2, quantitative model for interpreting foraminiferal carbon isotope data. *Paleoceanography*, 6(6):639–655.

Spooner, P. T., Thornalley, D. J. R., and Ellis, P. (2018). Grain Size Constraints on Glacial Circulation in the Southwest Atlantic. *Paleoceanography and Paleoclimatology*, 33(1):21–30.

Starr, A. et al. (2021). Antarctic icebergs reorganize ocean circulation during pleistocene glacials. *Nature*, 589(7841):236–241.

Stephens, B. B. and Keeling, R. F. (2000). The influence of antarctic sea ice on glacial–interglacial CO2 variations. *Nature*, 404(6774):171–174.

Stommel, H. (1961). Thermohaline convection with two stable regimes of flow. *Tellus*, 13(2):224–230.

Stouffer, R. J., Seidov, D., and Haupt, B. J. (2007). Climate response to external sources of freshwater: North atlantic versus the southern ocean. *Journal of Climate*, 20(3):436–448.

Straub, M., Tremblay, M. M., Sigman, D. M., Studer, A. S., Ren, H., Toggweiler, J. R., and Haug, G. H. (2013). Nutrient conditions in the subpolar north atlantic during the last glacial period reconstructed from foraminifera-bound nitrogen isotopes. *Paleoceanography*, 28(1):79–90.

Stuut, J.-B. W., Prins, M. A., Schneider, R. R., Weltje, G. J., Jansen, J., and Postma, G. (2002). A 300-kyr Record of Aridity and Wind Strength in Southwestern Africa: Inferences from Grain-size Distributions of Sediments on Walvis Ridge, SE Atlantic. *Marine Geology*, 180(1-4):221–233.

Sun, S., Eisenman, I., and Stewart, A. L. (2018). Does southern ocean surface forcing shape the global ocean overturning circulation? *Geophysical Research Letters*, 45(5):2413–2423.

Sun, Y., An, Z., Clemens, S. C., Bloemendal, J., and Vandenberghe, J. (2010). Seven Million Years of Wind and Precipitation Variability on the Chinese Loess Plateau. *Earth and Planetary Science Letters*, 297(3-4):525–535.

Tabor, C. R. and Poulsen, C. J. (2016). Simulating the mid-Pleistocene transition through regolith removal. *Earth Planet. Sci. Lett.*, 434:231–240.

Tachikawa, K., Rapuc, W., Vidal, L., Dubois-Dauphin, Q., Westerhold, T., Guihou, A., Bickert, T., Pérez-Asensio, J. N., Deschamps, P., and Skonieczny, C. (2021). Eastern Atlantic deep-water circulation and carbon storage inferred from neodymium and carbon isotopic compositions over the past 1.1 million years. *Quat. Sci. Rev.*, 252.

Tagliabue, A., Sallée, J.-B., Bowie, A. R., Lévy, M., Swart, S., and Boyd, P. W. (2014). Surface-water iron supplies in the southern ocean sustained by deep winter mixing. *Nature Geoscience*, 7(4):314–320.

Talley, L. (2013). Closure of the global overturning circulation through the indian, pacific, and southern oceans: Schematics and transports. *Oceanography*, 26(1):80–97.

Talley, L. D. and McCartney, M. S. (1982). Distribution and circulation of labrador sea water. *Journal of Physical Oceanography*, 12(11):1189–1205.

Tangunan, D., Baumann, K.-H., Pätzold, J., Henrich, R., Kucera, M., De Pol-Holz, R., and Groeneveld, J. (2017). Insolation forcing of coccolithophore productivity in the western tropical Indian Ocean over the last two glacial-interglacial cycles. *Paleoceanography*, 32(7):692–709.

Tangunan, D., Berke, M. A., Cartagena-Sierra, A., Flores, J. A., Gruetzner, J., Jiménez-Espejo, F., LeVay, L. J., Baumann, K.-H., Romero, O., Saavedra-Pellitero, M., Coenen, J. J., Starr, A., Hemming, S. R., and Hall, I. R. (2021). Strong glacial-interglacial variability in upper ocean hydrodynamics, biogeochemistry, and productivity in the southern Indian Ocean. *Commun. Earth Environ.*, 2(1):80.

Tapia, R., Ho, S. L., Núñez-Ricardo, S., Marchant, M., Lamy, F., and Hebbeln, D. (2021). Increased Marine Productivity in the Southern Humboldt Current System During MIS 2–4 and 10–11. *Paleoceanogr. Paleoclimatology*, 36(4):1–18.

Taylor, A. K., Berke, M. A., Castañeda, I. S., Koutsodendris, A., Campos, H., Hall, I. R., Hemming, S. R., LeVay, L. J., Sierra, A. C., and and, K. O. (2021). Plio-pleistocene continental hydroclimate and indian ocean sea surface temperatures at the south-east african margin. *Paleoceanography and Paleoclimatology*, 36(3).

Teitler, L., Florindo, F., Warnke, D. A., Filippelli, G. M., Kupp, G., and Taylor, B. (2015). Antarctic ice sheet response to a long warm interval across marine isotope stage 31: A cross-latitudinal study of iceberg-rafted debris. *Earth and Planetary Science Letters*, 409:109–119.

Teitler, L., Warnke, D. A., Venz, K. A., Hodell, D. A., Becquey, S., Gersonde, R., and Teitler, W. (2010). Determination of antarctic ice sheet stability over the last ~500 ka through a study of iceberg-rafted debris. *Paleoceanography*, 25(1).

Thornalley, D. J. R., Oppo, D. W., Ortega, P., Robson, J. I., Brierley, C. M., Davis, R., Hall, I. R., Moffa-Sanchez, P., Rose, N. L., Spooner, P. T., Yashayaev, I., and Keigwin, L. D. (2018). Anomalously weak labrador sea convection and atlantic overturning during the past 150 years. *Nature*, 556(7700):227–230.

Timmermann, A., Friedrich, T., Timm, O. E., Chikamoto, M. O., Abe-Ouchi, A., and Ganopolski, A. (2014). Modeling obliquity and CO2 effects on southern hemisphere climate during the past 408 ka. *Journal of Climate*, 27(5):1863–1875.

Toggweiler, J. and Samuels, B. (1995). Effect of drake passage on the global thermohaline circulation. *Deep Sea Research Part I: Oceanographic Research Papers*, 42(4):477–500.

Toggweiler, J. R. (1999). Variation of atmospheric CO2by ventilation of the ocean's deepest water. *Paleoceanography*, 14(5):571–588.

Toggweiler, J. R., Russell, J. L., and Carson, S. R. (2006). Midlatitude westerlies, atmospheric CO2, and climate change during the ice ages. *Paleoceanography*, 21(2):1–15.

Toggweiler, J. R. and Samuels, B. (1993). Is the magnitude of the deep outflow from the atlantic ocean actually governed by southern hemisphere winds? In *The Global Carbon Cycle*, pages 303–331. Springer Berlin Heidelberg.

Torrence, C. and Compo, G. P. (1998). A practical guide to wavelet analysis. *Bulletin of the American Meteorological Society*, 79(1):61–78.

Tournadre, J., Bouhier, N., Girard-Ardhuin, F., and Rémy, F. (2016). Antarctic icebergs distributions 1992–2014. *Journal of Geophysical Research: Oceans*, 121(1):327–349.

Toyos, M. H., Lamy, F., Lange, C. B., Lembke-Jene, L., Saavedra-Pellitero, M., Esper, O., and Arz, H. W. (2020). Antarctic Circumpolar Current Dynamics at the Pacific Entrance to the Drake Passage Over the Past 1.3 Million Years. *Paleoceanogr. Paleoclimatology*, 35(7):0–3.

Trauth, M. H., Larrasoaña, J. C., and Mudelsee, M. (2009). Trends, rhythms and events in plio-pleistocene african climate. *Quaternary Science Reviews*, 28(5-6):399–411.

Tzedakis, P. C., Raynaud, D., McManus, J. F., Berger, A., Brovkin, V., and Kiefer, T. (2009). Interglacial diversity. *Nat. Geosci.*, 2(11):751–755.

Tziperman, E. and Gildor, H. (2003). On the mid-pleistocene transition to 100-kyr glacial cycles and the asymmetry between glaciation and deglaciation times. *Paleoceanography*, 18(1):1–1–1–8.

Uenzelmann-Neben, G. (2001). Seismic characteristics of sediment drifts: An example from the Agulhas Plateau, southwest Indian Ocean. *Marine Geophysical Researches*, 22(5/6):323–343.

Uenzelmann-Neben, G. (2002). Contourites on the agulhas plateau, SW indian ocean: Indications for the evolution of currents since palaeogene times. *Geological Society, London, Memoirs*, 22(1):271–288.

Ufkes, E. and Kroon, D. (2012). Sensitivity of south-east Atlantic planktonic foraminifera to mid-Pleistocene climate change. *Palaeontology*, 55(1):183–204.

van Aken, H. M. (2000). The hydrography of the mid-latitude northeast atlantic ocean. *Deep Sea Research Part I: Oceanographic Research Papers*, 47(5):789–824.

van de Flierdt, T., Frank, M., Lee, D.-C., and Halliday, A. N. (2002). Glacial Weathering and the Hafnium Isotope Composition of Seawater. *Earth and Planetary Science Letters*, 201(3-4):639–647.

van Sebille, E., Biastoch, A., van Leeuwen, P. J., and de Ruijter, W. P. M. (2009). A weaker agulhas current leads to more agulhas leakage. *Geophysical Research Letters*, 36(3):n/a–n/a.

Vandergoes, M. J., Newnham, R. M., Preusser, F., Hendy, C. H., Lowell, T. V., Fitzsimons, S. J., Hogg, A. G., Kasper, H. U., and Schlüchter, C. (2005). Regional insolation forcing of late quaternary climate change in the southern hemisphere. *Nature*, 436(7048):242–245.

Venz, K. A. and Hodell, D. A. (2002). New evidence for changes in plio–pleistocene deep water circulation from southern ocean ODP leg 177 site 1090. *Palaeogeography, Palaeoclimatology, Palaeoecology*, 182(3-4):197–220.

Venz, K. A., Hodell, D. A., Stanton, C., and Warnke, D. A. (1999). A 1.0 myr record of glacial north atlantic intermediate water variability from ODP site 982 in the northeast atlantic. *Paleoceanography*, 14(1):42–52.

Villa, G., Persico, D., Wise, S. W., and Gadaleta, A. (2012). Calcareous nannofossil evidence for marine isotope stage 31 (1ma) in core AND-1b, ANDRILL McMurdo ice shelf project (antarctica). *Global and Planetary Change*, 96-97:75–86.

Villanueva, J., Grimalt, J. O., Labeyrie, L. D., Cortijo, E., Vidal, L., and Louis-Turon, J. (1998). Precessional forcing of productivity in the north atlantic ocean. *Paleoceanography*, 13(6):561–571.

Vleeschouwer, D. D., Dunlea, A. G., Auer, G., Anderson, C. H., Brumsack, H., de Loach, A., Gurnis, M., Huh, Y., Ishiwa, T., Jang, K., Kominz, M. A., März, C., Schnetger, B., Murray, R. W., and and, H. P. (2017). Quantifying k, u, and th contents of marine sediments using shipboard natural gamma radiation spectra measured on DVJOIDESResolution. *Geochemistry, Geophysics, Geosystems*, 18(3):1053–1064.

Waelbroeck, C., Lougheed, B. C., Riveiros, N. V., Missiaen, L., Pedro, J., Dokken, T., Hajdas, I., Wacker, L., Abbott, P., Dumoulin, J.-P., Thil, F., Eynaud, F., Rossignol, L., Fersi, W., Albuquerque, A. L., Arz, H., Austin, W. E. N., Came, R., Carlson, A. E., Collins, J. A., Dennielou, B., Desprat, S., Dickson, A., Elliot, M., Farmer, C.,

Giraudeau, J., Gottschalk, J., Henderiks, J., Hughen, K., Jung, S., Knutz, P., Lebreiro, S., Lund, D. C., Lynch-Stieglitz, J., Malaizé, B., Marchitto, T., Martínez-Méndez, G., Mollenhauer, G., Naughton, F., Nave, S., Nürnberg, D., Oppo, D., Peck, V., Peeters, F. J. C., Penaud, A., da Costa Portilho-Ramos, R., Repschläger, J., Roberts, J., Rühlemann, C., Salgueiro, E., Goni, M. F. S., Schönfeld, J., Scussolini, P., Skinner, L. C., Skonieczny, C., Thornalley, D., Toucanne, S., Rooij, D. V., Vidal, L., Voelker, A. H. L., Wary, M., Weldeab, S., and Ziegler, M. (2019). Consistently dated atlantic sediment cores over the last 40 thousand years. *Scientific Data*, 6(1).

Waelbroeck, C., Paul, A., Kucera, M., Rosell-Melé, A., Weinelt, M., Schneider, R., Mix, A. C., Abelmann, A., Armand, L., Bard, E., Barker, S., Barrows, T. T., Benway, H., Cacho, I., Chen, M. T., Cortijo, E., Crosta, X., De Vernal, A., Dokken, T., Duprat, J., Elderfield, H., Eynaud, F., Gersonde, R., Hayes, A., Henry, M., Hillaire-Marcel, C., Huang, C. C., Jansen, E., Juggins, S., Kallel, N., Kiefer, T., Kienast, M., Labeyrie, L., Leclaire, H., Londeix, L., Mangin, S., Matthiessen, J., Marret, F., Meland, M., Morey, A. E., Mulitza, S., Pflaumann, U., Pisias, N. G., Radi, T., Rochon, A., Rohling, E. J., Sbaffi, L., Schäfer-Neth, C., Solignac, S., Spero, H., Tachikawa, K., and Turon, J. L. (2009). Constraints on the magnitude and patterns of ocean cooling at the Last Glacial Maximum. *Nat. Geosci.*, 2(2):127–132.

Wagner, T. J., Dell, R. W., Eisenman, I., Keeling, R. F., Padman, L., and Severinghaus, J. P. (2018). Wave inhibition by sea ice enables trans-atlantic ice rafting of debris during heinrich events. *Earth and Planetary Science Letters*, 495:157–163.

Wang, P., Tian, J., Cheng, X., Liu, C., and Xu, J. (2004). Major Pleistocene stages in a carbon perspective: The South China Sea record and its global comparison. *Paleoceanography*, 19(4).

Wang, P., Tian, J., and Lourens, L. J. (2010). Obscuring of long eccentricity cyclicity in Pleistocene oceanic carbon isotope records. *Earth Planet. Sci. Lett.*, 290(3-4):319–330.

Watkins, N. D., Keany, J., Ledbetter, M. T., and Huang, T.-C. (1974). Antarctic glacial history from analyses of ice-rafted deposits in marine sediments: New model and initial tests. *Science*, 186(4163):533–536.

Watson, A. J., Bakker, D. C. E., Ridgwell, A. J., Boyd, P. W., and Law, C. S. (2000). Effect of iron supply on Southern Ocean CO 2 uptake and implications for glacial atmospheric CO 2. *Nature*, 407(6805):730–733.

Watson, A. J. and Garabato, A. C. N. (2006). The role of southern ocean mixing and upwelling in glacial-interglacial atmospheric CO2 change. *Tellus B: Chemical and Physical Meteorology*, 58(1):73–87.

Watson, A. J., Vallis, G. K., and Nikurashin, M. (2015). Southern Ocean buoyancy forcing of ocean ventilation and glacial atmospheric CO2. *Nat. Geosci.*, 8(11):861–864.

Weaver, P. P. E., Carter, L., and Neil, H. L. (1998). Response of surface water masses and circulation to late quaternary climate change east of new zealand. *Paleoceanography*, 13(1):70–83.

Weber, M., Kuhn, G., Sprenk, D., Rolf, C., Ohlwein, C., and Ricken, W. (2012). Dust transport from patagonia to antarctica – a new stratigraphic approach from the scotia sea and its implications for the last glacial cycle. *Quaternary Science Reviews*, 36:177–188.

Weber, M., Raymo, M., Peck, V., and Williams, T. (2021). *Volume 382: Iceberg Alley and Subantarctic Ice and Ocean Dynamics*. International Ocean Discovery Program.

Weber, M. E., Clark, P. U., Kuhn, G., Timmermann, A., Sprenk, D., Gladstone, R., Zhang, X., Lohmann, G., Menviel, L., Chikamoto, M. O., Friedrich, T., and Ohlwein, C. (2014). Millennial-scale variability in antarctic ice-sheet discharge during the last deglaciation. *Nature*, 510(7503):134–138.

Weber, T., Cram, J. A., Leung, S. W., DeVries, T., and Deutsch, C. (2016). Deep ocean nutrients imply large latitudinal variation in particle transfer efficiency. *Proceedings of the National Academy of Sciences*, 113(31):8606–8611.

Weedon, G. P. (2003). *Time-series Analysis and Cyclostratigraphy*. Cambridge University Press.

Wefer, G., Berger, W., and and, C. R., editors (1998). *Proceedings of the Ocean Drilling Program 175 Initial Reports*. Ocean Drilling Program.

Wesche, C. and Dierking, W. (2015). Near-coastal circum-antarctic iceberg size distributions determined from synthetic aperture radar images. *Remote Sensing of Environment*, 156:561–569.

Westerhold, T., Marwan, N., Drury, A. J., Liebrand, D., Agnini, C., Anagnostou, E., Barnet, J. S., Bohaty, S. M., De Vleeschouwer, D., Florindo, F., Frederichs, T., Hodell, D. A., Holbourn, A. E., Kroon, D., Lauretano, V., Littler, K., Lourens, L. J., Lyle, M., Pälike, H., Röhl, U., Tian, J., Wilkens, R. H., Wilson, P. A., and Zachos, J. C. (2020). An astronomically dated record of Earth's climate and its predictability over the last 66 million years. *Science*, 369(6509):1383–1388.

Wilkens, R. H., Westerhold, T., Drury, A. J., Lyle, M., Gorgas, T., and Tian, J. (2017). Revisiting the ceara rise, equatorial atlantic ocean: Isotope stratigraphy of odp leg 154 from 0 to 5 ma. *Climate of the Past*, 13(7):779–793.

Willeit, M., Ganopolski, A., Calov, R., and Brovkin, V. (2019). Mid-pleistocene transition in glacial cycles explained by declining CO2and regolith removal. *Science Advances*, 5(4):eaav7337.

Williams, D. F., Sommer II, M. A., and Bender, M. L. (1977). Carbon isotopic compositions of recent planktonic foraminifera of the Indian Ocean. *Earth Planet. Sci. Lett.*, 36(3):391–403.

Williams, T. J., Martin, E. E., Sikes, E., Starr, A., Umling, N. E., and Glaubke, R. (2021). Neodymium isotope evidence for coupled Southern Ocean circulation and Antarctic climate throughout the last 118,000 years. *Quat. Sci. Rev.*, 260.

Wilmes, S.-B., Green, J. A. M., and Schmittner, A. (2021). Enhanced vertical mixing in the glacial ocean inferred from sedimentary carbon isotopes. *Communications Earth & Environment*, 2(1).

Wolff, E. W., Fischer, H., Fundel, F., Ruth, U., Twarloh, B., Littot, G. C., Mulvaney, R., Röthlisberger, R., de Angelis, M., Boutron, C. F., Hansson, M., Jonsell, U., Hutterli, M. A., Lambert, F., Kaufmann, P., Stauffer, B., Stocker, T. F., Steffensen, J. P., Bigler, M., Siggaard-Andersen, M. L., Udisti, R., Becagli, S., Castellano, E., Severi, M., Wagenbach, D., Barbante, C., Gabrielli, P., and Gaspari, V. (2006). Southern ocean

sea-ice extent, productivity and iron flux over the past eight glacial cycles. *Nature*, 440(7083):491–496.

Woodruff, F., Savin, S. M., and Douglas, R. G. (1980). Biological Fractionation of Oxygen and Carbon Isotopes by Recent Benthic Foraminifera. *Marine Micropaleontology*, 5:3–11.

Wu, S., Lembke-Jene, L., Lamy, F., Arz, H. W., Nowaczyk, N., Xiao, W., Zhang, X., Hass, H. C., Titschack, J., Zheng, X., Liu, J., Dumm, L., Diekmann, B., Nürnberg, D., Tiedemann, R., and Kuhn, G. (2021). Orbital- and millennial-scale antarctic circumpolar current variability in drake passage over the past 140,000 years. *Nature Communications*, 12(1).

Wu, Z., Yin, Q., Guo, Z., and Berger, A. (2020). Hemisphere differences in response of sea surface temperature and sea ice to precession and obliquity. *Glob. Planet. Change*, 192(December 2019):103223.

Wunsch, C. (2003). Determining Paleoceanographic Circulations, with Emphasis on the Last Glacial Maximum. *Quaternary Science Review*, 22(2-4):371–385.

Yin, Q. (2013). Insolation-induced mid-Brunhes transition in Southern Ocean ventilation and deep-ocean temperature. *Nature*, 494(7436):222–225.

Yiou, P., Baert, E., and Loutre, M. F. (1996). Spectral analysis of climate data. *Surv. Geophys.*, 17(6):619–663.

You, Y. (1998). Intermediate water circulation and ventilation of the Indian Ocean derived from water-mass contributions. *J. Mar. Res.*, 56(5):1029–1067.

Yu, J., Anderson, R. F., Jin, Z., Rae, J. W., Opdyke, B. N., and Eggins, S. M. (2013). Responses of the deep ocean carbonate system to carbon reorganization during the last glacial–interglacial cycle. *Quaternary Science Reviews*, 76:39–52.

Yu, J. and Elderfield, H. (2007). Benthic foraminiferal b/ca ratios reflect deep water carbonate saturation state. *Earth and Planetary Science Letters*, 258(1-2):73–86.

Yu, J., Menviel, L., Jin, Z. D., Anderson, R. F., Jian, Z., Piotrowski, A. M., Ma, X., Rohling, E. J., Zhang, F., Marino, G., and McManus, J. F. (2020). Last glacial at-

mospheric CO2 decline due to widespread pacific deep-water expansion. *Nature Geoscience*, 13(9):628–633.

Yu, J., Menviel, L., Jin, Z. D., Thornalley, D. J. R., Foster, G. L., Rohling, E. J., McCave, I. N., McManus, J. F., Dai, Y., Ren, H., He, F., Zhang, F., Chen, P. J., and Roberts, A. P. (2019). More efficient north atlantic carbon pump during the last glacial maximum. *Nature Communications*, 10(1).

Zachos, J., Pagani, M., Sloan, L., Thomas, E., and Billups, K. (2001). Trends, rhythms, and aberrations in global climate 65 ma to present. *Science*, 292(5517):686–693.

Zanna, L., Khatiwala, S., Gregory, J. M., Ison, J., and Heimbach, P. (2019). Global reconstruction of historical ocean heat storage and transport. *Proc. Natl. Acad. Sci. U. S. A.*, 116(4):1126–1131.

Zhang, X., Lohmann, G., Knorr, G., and Xu, X. (2013). Different ocean states and transient characteristics in last glacial maximum simulations and implications for deglaciation. *Climate of the Past*, 9(5):2319–2333.

Zhao, Y., Colin, C., Liu, Z., Paterne, M., Siani, G., and Xie, X. (2012). Reconstructing precipitation changes in northeastern africa during the quaternary by clay mineralogical and geochemical investigations of nile deep-sea fan sediments. *Quaternary Science Reviews*, 57:58–70.

Zheng, Y., Anderson, R. F., Froelich, P. N., Beck, W., McNichol, A. P., and Guilderson, T. (2002). Challenges in radiocarbon dating organic carbon in opal-rich marine sediments. *Radiocarbon*, 44(1):123–136.

Ziegler, M. et al. (2013). Millennial-scale changes in atmospheric CO2 levels linked to the Southern Ocean carbon isotope gradient and dust flux. *Nat. Geosci.*, 6(6):457–461.

Ziegler, M., Jilbert, T., de Lange, G. J., Lourens, L. J., and Reichart, G.-J. (2008). Bromine counts from XRF scanning as an estimate of the marine organic carbon content of sediment cores. *Geochemistry, Geophys. Geosystems*, 9(5):n/a–n/a.

Ziegler, M., Lourens, L. J., Tuenter, E., and Reichart, G.-J. (2010). High arabian sea productivity conditions during MIS 13 – odd monsoon event or intensified over-

turning circulation at the end of the mid-pleistocene transition? *Climate of the Past*, 6(1):63–76.

Zweng, M., Seidov, D., Boyer, T., Locarnini, M., Garcia, H., Mishonov, A., Baranova, O., Weathers, K., Paver, C., Smolyar, I., et al. (2019). World ocean atlas 2018, volume 2: Salinity. Technical report.

8 | Appendix

8.1 Appendix Figures

Figure A1: Aligning benthic $\delta^{18}O$ to LR04 for sites used in the carbon isotope gradient compilation. Site name is given above each subplot; see Chapter 2 for table with references and metadata for each record. The LR04 sack (red) is from Lisiecki and Raymo (2005)

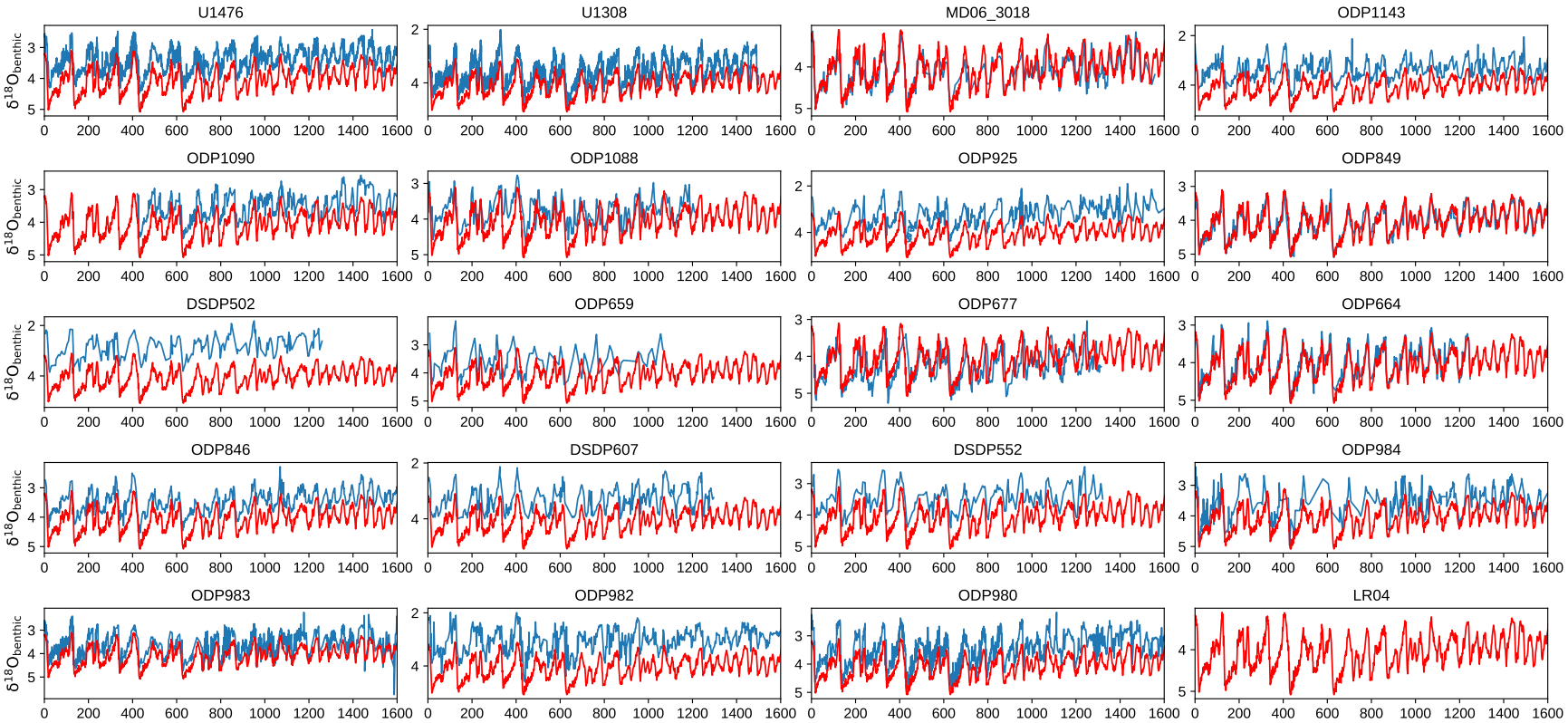

8.2 Appendix Tables

Table A1: Element oxide % of Ice-Rafted Debris from IODP Site U1475, determined by EDS point analysis of single grains. Successive rows for each sample represent measurement of different grains from that sample.

Sample	Site	Na	Mg	Al	Si	P	S	K	Ca	Ti	Fe	Zn	Rb	In	Sn	La	Ce	Nd	W
E-2H-3-76	1	0	0	0.74	99.26	0	0	0	0	0	0	0	0	0	0	0	0	0	0
E-2H-3-76	2	0	0	0	100	0	0	0	0	0	0	0	0	0	0	0	0	0	0
E-2H-3-76	2	0	0	0	69.91	0	0	0	30.09	0	0	0	0	0	0	0	0	0	0
E-2H-3-76	3	0	0	0	100	0	0	0	0	0	0	0	0	0	0	0	0	0	0
E-2H-3-76	3	0	0	1.73	3.97	0	0	0	0	93.44	0.86	0	0	0	0	0	0	0	0
C-2H-3-130	1	0	0	0	100	0	0	0	0	0	0	0	0	0	0	0	0	0	0
C-2H-3-130	1	0	0	2.7	33.43	0	0	0	28	34.84	1.04	0	0	0	0	0	0	0	0
C-2H-3-130	1	2.05	0	4.75	25.38	0	0	37.34	1.49	0	0.39	0	0	0	0	0	0	0	0
C-2H-3-130	1	0.61	0	0.83	66.7	0	0	0.26	30.72	0	0.29	0	0	0	0	0	0	0	0
C-2H-3-130	1	0	0	18.68	65.45	0	0	15.86	0	0	0	0	0	0	0	0	0	0	0
C-2H-3-130	1	0	0	18.36	65.21	0	0	16.43	0	0	0	0	0	0	0	0	0	0	0
C-2H-3-130	2	0	0	0	100	0	0	0	0	0	0	0	0	0	0	0	0	0	0
C-2H-3-130	2	0.46	0	0.81	86.98	0	1.25	0	0	0	0	0	0	0	0	0	0	0	5.87
C-2H-3-130	2	0	0	0	78.55	0	0	0	21.45	0	0	0	0	0	0	0	0	0	0
C-2H-3-130	2	0	0	0	100	0	0	0	0	0	0	0	0	0	0	0	0	0	0
C-2H-3-130	3	0	0	0	99.47	0	0	0	0	0	0.3	0	0	0.23	0	0	0	0	0

Table A1 continued from previous page

Sample	Site	Na	Mg	Al	Si	P	S	K	Ca	Ti	Fe	Zn	Rb	In	Sn	La	Ce	Nd	W
C-2H-3-130	3	0.66	0	18.43	64.43	0	0	15.5	0	0	0.32	0	0	0	0	0	0	0	0
C-2H-3-130	3	0	0	2.79	95.75	0	0	0.25	0.3	0	0.91	0	0	0	0	0	0	0	0
C-2H-3-130	3	1.79	0	19.04	66.92	0	0	12.25	0	0	0	0	0	0	0	0	0	0	0
C-2H-3-130	4	0	0	2.11	96.72	0	0	0.29	0	0	0.88	0	0	0	0	0	0	0	0
C-2H-3-130	4	0	0.59	2.71	33.71	0	0	0.39	0.4	0	3.18	0	0	0	0	0	0	0	3.42
C-2H-3-130	4	0	0	0.35	1.02	0	0	0	0	53.51	41.92	0	0	0	0	0	0	0	0
C-2H-3-130	4	0	0.72	4.23	9.77	0	0	0.32	0	44.23	39.75	0	0	0	0	0	0	0	0
E-3H-2-58	1	0.88	0	18.1	63.99	0	0	17.03	0	0	0	0	0	0	0	0	0	0	0
E-3H-2-58	1	1.16	0	6.03	84.63	0	1.1	3.13	1.14	0	0.38	0	0	0	0	0	0	0	0
E-3H-2-58	1	0	0.91	38.01	52.92	0	0	1.88	3.54	0.8	1.93	0	0	0	0	0	0	0	0
E-3H-2-58	1	0	0	7.05	20.35	0	0	4.06	68.55	0	0	0	0	0	0	0	0	0	0
E-3H-2-58	2	0.83	0	18.18	64.37	0	0	16.62	0	0	0	0	0	0	0	0	0	0	0
E-3H-2-58	2	0.97	0.58	5.82	87.14	0	0.74	3.1	1.02	0	0.27	0	0	0	0	0	0	0	0
E-3H-2-58	2	0	0.68	1.49	3.33	0	0	1.13	93.36	0	0	0	0	0	0	0	0	0	0
E-3H-2-90	1	0	0	0	100	0	0	0	0	0	0	0	0	0	0	0	0	0	0
E-3H-2-90	1	15.48	1.81	7.09	13.32	1.69	16.25	5.52	11.08	0	1.17	11.66	0	0	0	0	0	0	0
E-3H-2-90	1	3.23	0	29.43	45.66	0	1.05	11.12	2.51	0	6.47	0	0	0	0	0	0	0	0

Table A1 continued from previous page

Sample	Site	Na	Mg	Al	Si	P	S	K	Ca	Ti	Fe	Zn	Rb	In	Sn	La	Ce	Nd	W
E-3H-2-90	1	0	0	0	97.93	0	0	0.18	1.5	0	0.39	0	0	0	0	0	0	0	0
E-3H-2-90	1	16.11	2.24	5.77	36.39	0	3.57	1.04	18.28	0	0.98	0	0	0	0	0	0	0	0
E-3H-2-90	1	0.46	1.03	5.97	86.55	0	0	0.5	0	0	4.07	0	0	1.43	0	0	0	0	0
E-3H-2-90	1	0	0	0	48.27	0	0	0	51.73	0	0	0	0	0	0	0	0	0	0
B-5H-2-134	1	0	0	0	100	0	0	0	0	0	0	0	0	0	0	0	0	0	0
B-5H-2-134	1	1.02	2.55	19.17	61.89	0	0	6.41	1.13	0.49	6.87	0	0	0	0	0	0	0	0
B-5H-2-134	1	0	11.15	14.64	44.53	0	0	7.42	0	3.19	18.82	0	0	0	0	0	0	0	0
B-5H-2-134	1	0	0	0	7.95	0	0	0	92.05	0	0	0	0	0	0	0	0	0	0
B-5H-2-134	1	0	1.08	0.79	9.73	0	0	0	86.88	0	0.47	0	0	0	0	0	0	0	1.05
B-5H-2-134	2	0	0	0	99.38	0	0	0	0	0	0	0	0	0.34	0.28	0	0	0	0
B-5H-2-134	2	0	0	0	100	0	0	0	0	0	0	0	0	0	0	0	0	0	0
B-5H-2-134	2	0	0	0	3.73	0	0.64	0	95.62	0	0	0	0	0	0	0	0	0	0
B-5H-2-134	2	0	0.6	0.54	21.68	0	0	0	75.41	0	0	0	0	0	0	0	0	0	1.78
B-5H-2-134	2	6.35	5.02	2.47	21.8	0	14.61	0	48.4	0	0	0	0	0	0	0	0	0	0
B-5H-2-134	2	4.31	0	0	91.61	0	0	0	1.32	0	0	0	0	0	0	0	0	0	0
B-5H-2-134	4	0	0	0	100	0	0	0	0	0	0	0	0	0	0	0	0	0	0
B-5H-2-134	4	11.34	0	22.75	62.6	0	0	0	3.31	0	0	0	0	0	0	0	0	0	0

Table A1 continued from previous page

Sample	Site	Na	Mg	Al	Si	P	S	K	Ca	Ti	Fe	Zn	Rb	In	Sn	La	Ce	Nd	W
B-5H-2-134	4	0	0	0	10.09	0	0	0	89.91	0	0	0	0	0	0	0	0	0	0
B-5H-2-134	4	0.5	0.7	4.41	91.08	0	0	1.43	0.39	0	1.49	0	0	0	0	0	0	0	0
B-5H-2-134	4	3.22	2.03	13.84	66.66	0	0	3.69	1.73	0.49	8.33	0	0	0	0	0	0	0	0
B-5H-2-134	4	1.68	1.26	14.51	69.67	0	0	4.08	2.05	0.73	5.84	0	0	0	0	0	0	0	0
B-5H-2-134	4	0	0	0	5.52	0	0	0	94.48	0	0	0	0	0	0	0	0	0	0
B-5H-2-134	5	0	0	0	100	0	0	0	0	0	0	0	0	0	0	0	0	0	0
B-5H-2-134	5	0	0	0	100	0	0	0	0	0	0	0	0	0	0	0	0	0	0
B-5H-2-134	5	0	0.53	0.82	16.61	0	0	0	80.36	0	0.46	0	0	0	0	0	0	0	1.22
B-5H-2-134	5	2.56	0	1.45	78.82	0	2.65	0.52	7.43	0	0.5	0	0	0	0	0	0	0	0
B-5H-2-134	6	0	0	18.49	64.76	0	0	16.75	0	0	0	0	0	0	0	0	0	0	0
B-5H-2-134	6	0	0	0	98.76	0	0	0	0	0	0	0	0	0.66	0.59	0	0	0	0
B-5H-2-134	6	2.16	0	19.18	66.58	0	0	12.08	0	0	0	0	0	0	0	0	0	0	0
B-5H-2-134	6	0	0	4.28	13.49	0	0	2.23	66.84	0	0	12.63	0	0	0	0	0	0	0
B-5H-2-134	6	0	0	18.93	65.16	0	0	15.91	0	0	0	0	0	0	0	0	0	0	0
B-5H-2-134	7	0	0	0	100	0	0	0	0	0	0	0	0	0	0	0	0	0	0
B-5H-2-134	7	0	0	0.87	4.73	0	2.1	0	86.52	0	0	2.56	0	0	0	0	0	0	0
B-5H-2-134	7	0	7.93	19.4	51.44	0	0	5.81	0.62	2.8	12.01	0	0	0	0	0	0	0	0

Table A1 continued from previous page

Sample	Site	Na	Mg	Al	Si	P	S	K	Ca	Ti	Fe	Zn	Rb	In	Sn	La	Ce	Nd	W
B-5H-2-134	7	0	0	0	38.47	0	0	0	61.53	0	0	0	0	0	0	0	0	0	0
B-5H-2-134	7	0	0	0	100	0	0	0	0	0	0	0	0	0	0	0	0	0	0
B-5H-2-134	8	0	12.8	23.2	28.52	0	0	0.2	1.6	0	32.93	0	0	0	0	0	0	0	0
B-5H-2-134	8	13.29	0	20.38	66.33	0	0	0	0	0	0	0	0	0	0	0	0	0	0
B-5H-2-134	8	7.77	0	24.03	58.76	0	0	0.15	8.04	0	1.25	0	0	0	0	0	0	0	0
B-5H-2-134	8	0.44	0	26.89	36.24	3.25	0	0.46	26.75	0	4.48	0	0	0	0	0	0	0	0
B-5H-2-134	8	12.31	0	21.32	64.24	0	0	0	2.13	0	0	0	0	0	0	0	0	0	0
B-5H-2-134	8	0.33	0	25.3	38.15	0	0	0	25.22	0	10.69	0	0	0	0	0	0	0	0
B-5H-2-134	8	0	0	26.89	38.66	0	0	0	22.54	0	11.91	0	0	0	0	0	0	0	0
B-5H-2-134	8	0.62	1.77	30.33	48.81	0	0	12.45	0	0.44	5.59	0	0	0	0	0	0	0	0
B-5H-2-134	8	0.23	0	25.61	37.41	0.8	0	0	25.16	0	10.79	0	0	0	0	0	0	0	0
B-5H-2-134	9	0	0	0	100	0	0	0	0	0	0	0	0	0	0	0	0	0	0
B-5H-2-134	9	0	0	0	99.4	0	0	0	0	0	0	0	0	0	0.6	0	0	0	0
B-5H-2-134	9	1.46	3.34	4.65	22.09	0	2.16	1.01	61.85	0	2.16	0	0	0	0	0	0	0	0
B-5H-2-134	9	0	0	0	100	0	0	0	0	0	0	0	0	0	0	0	0	0	0
E-3H-2-98	1	0	0	0	100	0	0	0	0	0	0	0	0	0	0	0	0	0	0
E-3H-2-98	1	0	0	0	95.91	0	0	0	0	0	2.36	0	0	1.73	0	0	0	0	0

Table A1 continued from previous page

Sample	Site	Na	Mg	Al	Si	P	S	K	Ca	Ti	Fe	Zn	Rb	In	Sn	La	Ce	Nd	W
E-3H-2-98	1	0	0	1.31	97.06	0	0	0.48	0	0	0.58	0	0	0	0.56	0	0	0	0
E-3H-2-98	1	1.35	0	0	8.22	0	0.78	0	89.11	0	0	0	0	0	0	0	0	0	0
E-3H-2-98	1	0	0	0	99.76	0	0	0	0	0	0.24	0	0	0	0	0	0	0	0
E-3H-2-98	2	0	0	0	99.1	0	0	0	0	0	0	0	0	0.51	0.39	0	0	0	0
E-3H-2-98	2	0	0	0	98.94	0	0	0	0	0	0	0	0	0.49	0.57	0	0	0	0
E-3H-2-98	2	0	0	0	71.7	0	0	0	0	0	0	0	10.17	0	0	0	0	0	18.13
E-3H-2-98	3	0	0	0	92.95	0	0	0	0	0	4.79	0	0	2.25	0	0	0	0	0
E-3H-2-98	3	0	0	4.32	93.76	0	0	1.67	0	0	0.24	0	0	0	0	0	0	0	0
E-3H-2-98	3	3.14	0	17.86	63.12	0	0	11.89	0	0	0.41	0	0	0	0	0	0	0	3.57
E-3H-2-98	3	20.89	0	6.11	7.36	1.71	14.75	17.84	6.69	0	0	0	0	0	0	0	0	0	0
E-3H-2-98	3	0	0	3.53	17.86	0	0	1.5	75.81	0	1.3	0	0	0	0	0	0	0	0
E-3H-3-68	1	0	0	0	100	0	0	0	0	0	0	0	0	0	0	0	0	0	0
E-3H-3-68	1	0	0	0	62.49	0	0	0	37.51	0	0	0	0	0	0	0	0	0	0
E-3H-3-68	1	0	0	0	95.37	0	0	0	0	0	0	0	0	0	0	0	0	0	4.63
E-3H-3-68	1	0	0	0.4	3.98	0	0.75	0	94.13	0	0	0	0	0	0	0	0	0	0.74
E-3H-3-68	1	0	0	0	34.77	0	0	0	65.23	0	0	0	0	0	0	0	0	0	0
E-3H-3-68	2	0.82	0	18.99	65.24	0	0	14.6	0	0	0.35	0	0	0	0	0	0	0	0

Table A1 continued from previous page

Sample	Site	Na	Mg	Al	Si	P	S	K	Ca	Ti	Fe	Zn	Rb	In	Sn	La	Ce	Nd	W
E-3H-3-68	2	0	0	32.14	58.27	0	0	2.42	0.45	0.76	5.97	0	0	0	0	0	0	0	0
E-3H-3-68	2	0	0	19.33	65.14	0	0	15.53	0	0	0	0	0	0	0	0	0	0	0
E-3H-3-68	2	1.36	0	4.63	11.78	0	0	2.52	78.11	0	0	0	0	0	0	0	0	0	1.59
E-3H-3-68	2	0.98	0	18.72	64.9	0	0	15.4	0	0	0	0	0	0	0	0	0	0	0
E-3H-3-68	3	0	0	17.88	57.64	0	0	13.9	0	0	0.51	0	0	0	0	0	0	0	10.07
E-3H-3-68	3	0	0	0.83	0.88	19.99	0	0.3	0.39	0	0	0	0	0	0	24.66	33.13	6.98	0
E-3H-3-68	3	0	0	1.76	3.99	15.88	0	0.4	0.94	0	0	0	0	0	0	28.33	33.01	7.05	0
E-3H-3-68	4	0	0	0	100	0	0	0	0	0	0	0	0	0	0	0	0	0	0
E-3H-3-68	4	9.71	0	0	59.43	0	24.96	0	2.66	0	0	0	0	0	0	0	0	0	0
E-3H-3-68	4	0	0	0	100	0	0	0	0	0	0	0	0	0	0	0	0	0	0
E-3H-3-68	4	0	0	16.7	65.47	0	0	13.49	2.37	0	1.24	0	0	0	0	0	0	0	0
E-3H-3-68	4	0	0	0	68.98	0	0	0	0	0	0	0	14.57	0	0	0	0	0	16.46
E-3H-3-68	5	0	9.52	21.05	35.96	0	0	0	1.02	0	32.44	0	0	0	0	0	0	0	0
E-3H-3-68	5	2	3.21	18.64	55.59	0	0	6.59	3.38	1.55	9.02	0	0	0	0	0	0	0	0
E-3H-3-68	5	0	9.21	20.97	36.14	0	0	0	1.16	0	31.91	0	0	0	0	0	0	0	0
E-3H-3-68	5	0	10.2	23.91	41.44	0	2.04	0	2.31	0	20.1	0	0	0	0	0	0	0	0
E-3H-3-68	5	0	9.28	20.71	36.3	0	0	0	1.26	0	32.45	0	0	0	0	0	0	0	0

Table A1 continued from previous page

Sample	Site	Na	Mg	Al	Si	P	S	K	Ca	Ti	Fe	Zn	Rb	In	Sn	La	Ce	Nd	W
E-3H-3-68	5	0	9.83	22.25	38.15	0	0	0	1.01	0	28.76	0	0	0	0	0	0	0	0
E-3H-3-68	5	0	10.92	23.5	40.19	0	0	0	0.85	0	24.55	0	0	0	0	0	0	0	0
E-3H-3-68	5	9.6	0	22.13	64.9	0	0	0	2.89	0	0.48	0	0	0	0	0	0	0	0
F-2H-3-56	1	0	0	0	100	0	0	0	0	0	0	0	0	0	0	0	0	0	0
F-2H-3-56	1	0	0	0	100	0	0	0	0	0	0	0	0	0	0	0	0	0	0
F-2H-3-56	1	0	0	0	98.7	0	0	0	0	0	0.74	0	0	0.56	0	0	0	0	0
F-2H-3-56	1	0	0	0	100	0	0	0	0	0	0	0	0	0	0	0	0	0	0
F-2H-3-56	1	0	0	0	100	0	0	0	0	0	0	0	0	0	0	0	0	0	0
F-2H-3-56	1	0	32.73	0	66.46	0	0	0	0.31	0	0.5	0	0	0	0	0	0	0	0
F-2H-3-56	1	0	0	0	9.19	0	0	0	90.64	0	0	0	0	0	0	0	0	0	0
F-2H-3-56	1	0	0	0	100	0	0	0	0	0	0	0	0	0	0	0	0	0	0
F-2H-3-56	2	0	0	0	100	0	0	0	0	0	0	0	0	0	0	0	0	0	0
F-2H-3-56	2	0	5.3	12.83	59.69	0	0	2.05	1.61	0.53	18	0	0	0	0	0	0	0	0
F-2H-3-56	2	0	2.11	4.61	85.32	0	0	0	0	0	5.39	0	0	2.56	0	0	0	0	0
F-2H-3-56	2	0	0	0	99.05	0	0	0	0	0	0.95	0	0	0	0	0	0	0	0
F-2H-3-56	3	0	0	0	100	0	0	0	0	0	0	0	0	0	0	0	0	0	0
F-2H-3-56	3	0	0	0	100	0	0	0	0	0	0	0	0	0	0	0	0	0	0

Table A1 continued from previous page

Sample	Site	Na	Mg	Al	Si	P	S	K	Ca	Ti	Fe	Zn	Rb	In	Sn	La	Ce	Nd	W
F-2H-3-56	3	0	1.67	2.12	5.4	0	0	0.16	0	43.19	47.45	0	0	0	0	0	0	0	0
F-2H-3-56	3	0	1.14	3.69	8.33	0	0	0.19	0	44.56	42.09	0	0	0	0	0	0	0	0
F-2H-3-56	3	1.1	6.59	19.5	45.79	0	0	1.26	0.86	2.32	22.57	0	0	0	0	0	0	0	0
F-2H-3-56	3	3.27	1.24	19.43	69.93	0	0	3.46	1.61	0	0	0	0	0	0	0	0	0	0
F-2H-3-56	3	0	0	0.88	11.9	0	0.68	0	85.29	0	0	0	0	0	0	0	0	0	1.25
F-2H-3-56	4	0	0	0	100	0	0	0	0	0	0	0	0	0	0	0	0	0	0
F-2H-3-56	4	0.64	4.25	18.46	55.3	0	0	5.81	0.69	1.33	13.53	0	0	0	0	0	0	0	0
F-2H-3-56	4	0	0	3.49	10.55	0	5.25	0	69.64	0	0	10.15	0	0	0	0	0	0	0
F-2H-3-56	4	0	2.55	17.09	55.34	0	0	5.45	1.5	3.92	10.75	0	0	0	0	0	0	0	3.39
F-2H-3-56	4	0	5.31	22.15	40.27	0	0	0.17	0.43	0	31.67	0	0	0	0	0	0	0	0
F-2H-3-56	4	0	0	3.3	23.51	0	0	0	72.22	0	0.97	0	0	0	0	0	0	0	0
F-2H-3-56	4	0	0	0	99.72	0	0	0	0	0	0.28	0	0	0	0	0	0	0	0
F-2H-3-56	4	0	0	1.75	73.7	0	16.65	0	7.89	0	0	0	0	0	0	0	0	0	0
F-2H-3-56	5	0	0	0	99.51	0	0	0	0	0	0.49	0	0	0	0	0	0	0	0
F-2H-3-56	5	0	3.12	10.84	74.75	0	0	1.71	0.72	0.39	8.46	0	0	0	0	0	0	0	0
F-2H-3-56	5	0	0	1.02	31.54	0	0	0	66.88	0	0.55	0	0	0	0	0	0	0	0
F-2H-3-56	5	0	0	0	100	0	0	0	0	0	0	0	0	0	0	0	0	0	0

Table A1 continued from previous page

Sample	Site	Na	Mg	Al	Si	P	S	K	Ca	Ti	Fe	Zn	Rb	In	Sn	La	Ce	Nd	W
F-2H-3-56	5	0	0	0	100	0	0	0	0	0	0	0	0	0	0	0	0	0	0
F-2H-3-56	5	0	2.75	15.95	54.3	0	0	3.91	0.74	1.71	17.39	0	0	0	0	0	0	0	3.24
F-2H-3-56	6	0	0	0	100	0	0	0	0	0	0	0	0	0	0	0	0	0	0
F-2H-3-56	6	0	0	0	100	0	0	0	0	0	0	0	0	0	0	0	0	0	0
F-2H-3-56	6	0	0	0	100	0	0	0	0	0	0	0	0	0	0	0	0	0	0
F-2H-3-56	6	0	3.5	16.02	58.68	0	0	4.14	0.94	0.62	12.25	0	0	0	0	0	0	0	3.85
F-2H-3-56	6	1.66	2.17	17.65	63	0	0	5.63	0.8	0.44	8.65	0	0	0	0	0	0	0	0
F-2H-3-56	7	0	0	0	99.03	0	0	0	0	0	0	0	0	0.61	0.36	0	0	0	0
F-2H-3-56	7	0	0	0	100	0	0	0	0	0	0	0	0	0	0	0	0	0	0
F-2H-3-56	7	0	0	0	100	0	0	0	0	0	0	0	0	0	0	0	0	0	0
F-2H-3-56	7	0	0.65	2.35	72.59	0	0	0.47	23.05	0	0.89	0	0	0	0	0	0	0	0
F-2H-3-56	7	0.52	0	0.33	2.48	0	0	0	95.23	0	0.47	0	0	0	0	0	0	0	0.98
F-2H-3-56	7	0	1.61	18.11	65.81	0	0	9.34	0	0	5.14	0	0	0	0	0	0	0	0
F-2H-3-56	7	0	1.52	2.13	7.22	0	0	0	0	61.56	26.47	0	0	0	0	0	0	0	0
F-2H-3-56	7	0	0	1.43	98.57	0	0	0	0	0	0	0	0	0	0	0	0	0	0

Table A2: Age-depth tie points for aligning the AP_{comp} to the the 'Probabilistic Stack' of Ahn et al. (2017). Depth uncertainty was estimated to be the width of the transition in metres. AMS dates are taken from Ziegler et al. (2013). Site U1475 tie points for the upper 300 kyr are presented in Tangunan et al. (2021). Polarity tie points (paleomagnetic reversals) are from Hall et al. (2017a).

Age (kyr)	σ (kyr)	Event	Method	U1475 Depth	MD02-2588 Depth	APcomp Depth	σ (m)	Core
3.23	0.045	SUERC-4618	14C AMS (G. inflata)	0.05	0.06	0.06	0.01	MD02-2588
5.03	0.079	SUERC-4619	14C AMS (G. inflata)	0.09	0.11	0.11	0.01	MD02-2588
7.43	0.015	SUERC-4620	14C AMS (G. inflata)	0.15	0.17	0.17	0.01	MD02-2588
8.88	0.09	SUERC-4623	14C AMS (G. inflata)	0.20	0.23	0.23	0.01	MD02-2588
12.78	0.069	SUERC-4624	14C AMS (G. inflata)	0.29	0.33	0.33	0.01	MD02-2588
15.48	0.119	SUERC-4625	14C AMS (G. inflata)	0.36	0.41	0.41	0.01	MD02-2588
16.18	0.134	SUERC-4626	14C AMS (G. inflata)	0.40	0.46	0.46	0.01	MD02-2588

Table A2 continued from previous page

Age (kyr)	Age Uncertainty (kyr)	Event	Method	U1475 Depth	MD02-2588 Depth	APcomp Depth	Uncertainty	Core
23.26	0.235	SUERC-4627	14C AMS (G. inflata)	0.58	0.66	0.66	0.01	MD02-2588
27.82	0.196	SUERC-4635	14C AMS (G. bulloides)	0.67	0.76	0.76	0.01	MD02-2588
29.22	0.312	SUERC-4636	14C AMS (G. bulloides)	0.76	0.86	0.86	0.01	MD02-2588
32.36	0.236	SUERC-4637	14C AMS (G. bulloides)	0.85	0.96	0.96	0.01	MD02-2588
40.21	0.884	SUERC-4638	14C AMS (G. bulloides)	0.94	1.06	1.06	0.01	MD02-2588
65.00	4	MIS 4/3	18O_cib to Prob-Stack (Starr et al 2021)	1.47	1.66	1.66	0.09	MD02-2588
117.00	4	MIS 5e/5d	18O_cib to Prob-Stack (Starr et al 2021)	3.05	3.43	3.43	0.05	MD02-2588
129.20	4	T II	18O_cib to Prob-Stack (Starr et al 2021)	3.57	3.93	3.93	0.04	MD02-2588

Table A2 continued from previous page

Age (kyr)	Age Uncertainty (kyr)	Event	Method	U1475 Depth	MD02-2588 Depth	APcomp Depth	Uncertainty	Core
194.00	4		18O_cib to Prob-Stack (Starr et al 2021)	4.73	5.84	5.84	0.03	MD02-2588
220.00	4		18O_cib to Prob-Stack (Starr et al 2021)	5.53	6.41	6.41	0.03	MD02-2588
244.00	4	T III	18O_cib to Prob-Stack (Starr et al 2021)	6.15	7.03	7.03	0.04	MD02-2588
280.00	4		18O_cib to Prob-Stack (Starr et al 2021)	7.39	8.45	8.10	0.04	MD02-2588
292.00	4	T IV	18O_cib to Prob-Stack (Starr et al 2021)	9.22	10.23	8.56	0.05	MD02-2588
337.00	4	T V	18O_cib to Prob-Stack (Starr et al 2021)	13.41		10.23	0.09	361-U1475
380.00	4		18O_cib to Prob-Stack (Starr et al 2021)	10.70		11.85	0.10	361-U1475
423.00	4	T VI	18O_cib to Prob-Stack (Starr et al 2021)	13.41		14.57	0.04	361-U1475

Table A2 continued from previous page

Age (kyr)	Age Uncertainty (kyr)	Event	Method	U1475 Depth	MD02-2588 Depth	APcomp Depth	Uncertainty	Core
472.00	4	T VII	18O_cib to Prob-Stack (Starr et al 2021)	15.30		16.45	0.08	361-U1475
537.00	4	T VIII (MIS 18/17)	18O_cib to Prob-Stack (Starr et al 2021)	16.91		18.06	0.04	361-U1475
560.00	4		18O_cib to Prob-Stack (Starr et al 2021)	17.05		18.20	0.02	361-U1475
620.00	4	MIS 20/19	18O_cib to Prob-Stack (Starr et al 2021)	18.15		19.30	0.06	361-U1475
710.00	4	MIS 22/21	18O_cib to Prob-Stack (Starr et al 2021)	19.55		20.70	0.03	361-U1475
744.00	4	MIS 24/23	18O_cib to Prob-Stack (Starr et al 2021)	20.18		21.34	0.04	361-U1475
788.00	4	MIS 26/25	18O_cib to Prob-Stack (Starr et al 2021)	21.01		22.16	0.03	361-U1475
866.00	4		18O_cib to Prob-Stack (Starr et al 2021)	23.15		24.30	0.25	361-U1475

Table A2 continued from previous page

Age (kyr)	Age Uncertainty (kyr)	Event	Method	U1475 Depth	MD02-2588 Depth	APcomp Depth	Uncertainty	Core
930.00	6	MIS 30/29	18O_cib to Prob-Stack (Starr et al 2021)	24.25		25.40	0.10	361-U1475
958.00	6	MIS 31/30	18O_cib to Prob-Stack (Starr et al 2021)	25.31		26.46	0.05	361-U1475
982.00	6	MIS 32/31	18O_cib to Prob-Stack (Starr et al 2021)	26.11		27.26	0.20	361-U1475
1,032.00	6	MIS 34/33	18O_cib to Prob-Stack (Starr et al 2021)	28.63		29.78	0.30	361-U1475
1,062.00	6	MIS 36/35	18O_cib to Prob-Stack (Starr et al 2021)	29.47		30.62	0.08	361-U1475
1,088.00	6		18O_cib to Prob-Stack (Starr et al 2021)	30.95		32.10	0.02	361-U1475
1,118.00	6		18O_cib to Prob-Stack (Starr et al 2021)	31.83		32.98	0.01	361-U1475
1,190.00	6		18O_cib to Prob-Stack (Starr et al 2021)	33.23		34.38	0.04	361-U1475

Table A2 continued from previous page

Age (kyr)	Age Uncertainty (kyr)	Event	Method	U1475 Depth	MD02-2588 Depth	APcomp Depth	Uncertainty	Core
1,244.00	6	MIS 46/45	18O_cib to Prob-Stack (Starr et al 2021)	34.55		35.70	0.04	361-U1475
1,322.00	6	MIS 47/46	18O_cib to Prob-Stack (Starr et al 2021)	35.86		37.02	0.10	361-U1475
1,364.00	6		18O_cib to Prob-Stack (Starr et al 2021)	37.11		38.26	0.12	361-U1475
1,404.00	6	MIS 52/51	18O_cib to Prob-Stack (Starr et al 2021)	37.95		39.10	0.04	361-U1475
1,428.00	6	MIS 54/53	18O_cib to Prob-Stack (Starr et al 2021)	38.30		39.45	0.04	361-U1475
1,452.00	6	MIS 54/53	18O_cib to Prob-Stack (Starr et al 2021)	39.00		40.15	0.08	361-U1475
1,494.00	6		18O_cib to Prob-Stack (Starr et al 2021)	40.09		41.24	0.10	361-U1475
1,530.00	6		18O_cib to Prob-Stack (Starr et al 2021)	40.73		41.88	0.09	361-U1475

Table A2 continued from previous page

Age (kyr)	Age Uncertainty (kyr)	Event	Method	U1475 Depth	MD02-2588 Depth	APcomp Depth	Uncertainty	Core
1,569.00		B C1r	Polarity	41.81		42.96	0.50	361-U1475
1,642.00	6	MIS 64/63	18O_cib to Prob-Stack	43.33		44.48	0.05	361-U1475
1,700.00	6		18O_cib to Prob-Stack	44.18		45.33	0.05	361-U1475
1,782.00	6		18O_cib to Prob-Stack	45.52		46.67	0.09	361-U1475
1,805.00	6		18O_cib to Prob-Stack	45.95		47.10	0.10	361-U1475
1,860.00	6		18O_cib to Prob-Stack	46.61		47.76	0.50	361-U1475
1,900.00	6		18O_cib to Prob-Stack	48.35		49.50	0.30	361-U1475
1,950.00	6		18O_cib to Prob-Stack	49.25		50.40	0.03	361-U1475
2,010.00	6		18O_cib to Prob-Stack	49.75		50.90	0.04	361-U1475
2,080.00	6		18O_cib to Prob-Stack	51.85		53.00	0.04	361-U1475
2,142.00	6		18O_cib to Prob-Stack	52.55		53.70	0.05	361-U1475
2,197.00	6		18O_cib to Prob-Stack	53.70		54.85		361-U1475
2,235.53	6		18O_cib to Prob-Stack	55.32		56.47		361-U1475
2,315.00	6		18O_cib to Prob-Stack	57.18		58.33		361-U1475
2,349.73	6		18O_cib to Prob-Stack	58.65		59.80		361-U1475
2,428.29	6		18O_cib to Prob-Stack	60.36		61.52		361-U1475

Table A2 continued from previous page

Age (kyr)	Age Uncertainty (kyr)	Event	Method	U1475 Depth	MD02-2588 Depth	APcomp Depth	Uncertainty	Core
2,480.00	6		18O_cib to Prob-Stack	61.70		62.85		361-U1475
2,510.78	6		18O_cib to Prob-Stack	62.50		63.65		361-U1475
2,540.00	6		18O_cib to Prob-Stack	62.85		64.00		361-U1475
2,620.00	6		18O_cib to Prob-Stack	65.40		66.55		361-U1475
2,640.00	6		18O_cib to Prob-Stack	65.85		67.00		361-U1475
2,680.00	6		18O_cib to Prob-Stack	67.85		69.00		361-U1475
2,736.00	6		18O_cib to Prob-Stack	69.05		70.20		361-U1475
2,798.00	6		18O_cib to Prob-Stack	71.40		72.55		361-U1475
2,839.31	6		18O_cib to Prob-Stack	72.60		73.75		361-U1475
2,930.00	6		18O_cib to Prob-Stack	77.50		78.66		361-U1475
3,000.00	6		18O_cib to Prob-Stack	82.35		83.50		361-U1475
3,030.00	6		18O_cib to Prob-Stack	83.15		84.30		361-U1475
3,090.00	6		18O_cib to Prob-Stack	84.85		86.00		361-U1475
3,150.00	6		18O_cib to Prob-Stack	87.35		88.50		361-U1475
3,207.00		B C2An.2n	Polarity	91.85		93.00		361-U1475

8.3 Appendix Code 1: Chapter 3 Matlab Files

```
%--- Master script for Starr et al. 2021 ---%
%
%- Corresponding Author*: Aidan Starr, StarrA1@Cardiff.ac.uk / aidan.m.starr@gmail.com
%
%- Dependencies: nexcf.m; ar1sur.m;
%- Calls: analysis_1.m; analysis_2.m; analysis_3.m; analysis_4.m;
%        load_data.m;  create_analyseries_files.m
%
% Note: each part of the analysis is designed as a function, figures are then
% generated seperately at the end of the script. Caution is advised when
% running some section as Monte Carlo simulations may be CPU intensive, to
% save some power, pre-run simulation .mat files are available on my github

%%%%--------- Preamble ---------%%%%%
% load the data available from pangaea.de (DOI xxx)
%path = 'https://github.com/AidanStarr/Southern_Ocean_Lead/raw';
data = readtable('raw/starr_et_al_2020_data.csv','header',1);
bd13c = data.C_WuellerstorfiD13C_vs_PDB_;
bd18o = data.C_WuellerstorfiD18O_vs_PDB_;
irdmar = data.IRDApparentMAR_grains_cm2_kyr_;
[age,n] = unique(data.MedianAge_kyr_);
irdmar = irdmar(n);
bd13c = bd13c(n);
bd18o = bd18o(n);

dt = 1.5; % set dt for linearly rescaled data (used later)
lt = [0 : dt : 1645]; % create linear time scale in kyrs

%%%%--------- Analysis 1: Cross-Correlation ---------%%%%%
[Cxy1, lag, Q1] = analysis_1(age,bd13c,log10(irdmar+1)); % --> analysis_1(time vector, variable 1, variable 2)
[Cxy2, ~, ~] = analysis_1(age,bd18o,log10(irdmar+1)); % --> analysis_1(time vector, variable 1, variable 2)

%%%%--------- Analysis 2: Frequency Analysis ---------%%%%%
```

```
% Get lags from Blackman-Tukey calculated in Analyseries
[ob_lag, ec_lag, pr_lag] = analysis_2('irdmar','bd13c'); % --> analysis_2('variable 1','variable 2');

%%%%--------- Analysis 3: Peak-Lag Algorithm ---------%%%%%
% USAGE: analysis_3(linear timescale, spacing, original time scale, variable 1, variable 2)
filtype = 1; % 1 means use Moving Average filter, 2 means use Savitsky-Golay Filter
filtdeg = 6; % if 1, this is moving average degree in dt
dif = 1; % use first difference?
max_dist = 10;
[bd13c_lags, Q, q] = analysis_3(lt,dt, age,log10(irdmar+1),-bd13c,filtype,filtdeg,dif,max_dist);


% Test sensitivity to filter degree
filtype = 1; % 1 means use Moving Average filter, 2 means use Savitsky-Golay Filter
for i = 1 : 11
    filtdeg = i; % if 1, this is moving average in kyrs, if 2, this is SGolay Degrees
    dif = 1; % Use First Difference of x1 and x2? 1 for yes, 0 for no
    temp = analysis_3(lt,dt, age,log10(irdmar+1),-bd13c,filtype,filtdeg,dif,max_dist);
    b_lag(i)=nanmean(temp);
end


%%%%--------- Analysis 3b: Red-Noise Peak-Lag Algorithm ---------%%%%%
% Create red-noise surrogates and run them through the peak-lag algorithm
 NoSur=1000; % number of surrogates for MC analysis. For most reliable results, set to 1000.
 XSur=ar1sur(age(~isnan(bd13c)),bd13c(~isnan(bd13c)),NoSur); % create AR1 Surrogates for bd13c
 filtype = 1; % 1 means use Moving Average filter, 2 means use Savitsky-Golay Filter
filtdeg = 6; % if 1, this is moving average degree in dt
dif = 1; % use first difference?
    for k=1:NoSur-1
```

```
64          temp = analysis_3(lt,dt,age(~isnan(bd13c)),XSur(:,1),XSur(:,k+1),
    filtype,filtdeg,dif,max_dist);
65          red_lags{k}=temp;
66          clear temp
67      end
68  for i = 1 : size(red_lags,2)
69      red_lag(i) = nanmean(red_lags{i});
70  end
71  % use a 2-sided t test to determine whether the ird vs 13C data are
72  % significantly different to the 'random' red noise surrogates
73  [h,p,ci] = ttest2(bd13c_lags,red_lag);
74
75  %%%%--------- Analysis 4: Glacial Accumulation ---------%%%%%
76  plt = 0; % plot the process? 1 for yes, 0 for no
77  [d18o_cum, ird_cum, time_cum, time_cum_norm, f3s, tl] = analysis_4(lt,dt,
    age,bd18o,irdmar,plt); % Divide d18O into glacials  and intergrate under
     curve
78  % split into intervals
79  enwx = 1:1:100';
80  for i = 1:23
81      newird_cum(:,i) = interp1(time_cum_norm{i},ird_cum{i},enwx,'linear');
82  end
83
84  for i = 1:23
85      newtime_cum(:,i) = interp1(time_cum_norm{i},time_cum_norm{i},enwx,'
    linear');
86  end
87
88  for i = 1:23
89      newd18o_cum(:,i) = interp1(time_cum_norm{i},d18o_cum{i},enwx,'linear');
90  end
91  % mean accumulation for IRD
92  A = newird_cum(:,1:12);
93  B = newird_cum(:,13:18);
94  C = newird_cum(:,19:23);
95  pre_mpt = mean(A,2);
96  mpt = mean(B,2);
97  post_mpt = mean(C,2);
98  % calculate confidence intervals for IRD
99  SEM_A = std(A,1,2)/sqrt(40); % get standard error of the mean
```

```
100 SEM_B = std(B,1,2)/sqrt(40);
101 SEM_C = std(C,1,2)/sqrt(40);
102 CI95_A = bsxfun(@plus, mean(A,2), bsxfun(@times, [-1  1]*1.96, SEM_A));   %
        95% Bootstrap Confidence Intervals
103 CI95_B = bsxfun(@plus, mean(B,2), bsxfun(@times, [-1  1]*1.96, SEM_B));
104 CI95_C = bsxfun(@plus, mean(C,2), bsxfun(@times, [-1  1]*1.96, SEM_C));   %
        95% Confidence Intervals
105 % mean accumulation for d18O
106 A2 = newd18o_cum(:,1:11);
107 B2 = newd18o_cum(:,2:18);
108 C2 = newd18o_cum(:,19:23);
109 pre_mptd = mean(A2,2);
110 mptd = mean(B2,2);
111 post_mptd = mean(C2,2);
112
113 % calculate confidence intervals for d18O
114 SEM_A2 = std(newd18o_cum(:,1:11),1,2)/sqrt(40);
115 SEM_B2 = std(newd18o_cum(:,12:18),1,2)/sqrt(40);
116 SEM_C2 = std(newd18o_cum(:,19:23),1,2)/sqrt(40);
117 CI95_A2 = bsxfun(@plus, mean(A2,2), bsxfun(@times, [-1  1]*1.96, SEM_A2));
        % 95% Confidence Intervals
118 CI95_B2 = bsxfun(@plus, mean(B2,2), bsxfun(@times, [-1  1]*1.96, SEM_B2));
        % 95% Confidence Intervals
119 CI95_C2 = bsxfun(@plus, mean(C2,2), bsxfun(@times, [-1  1]*1.96, SEM_C2));
        % 95% Confidence Intervals
120
121 % analysis_4 OUTPUT
122 output_cumtrap(:,1) = pre_mpt;
123 output_cumtrap(:,2) = mpt;
124 output_cumtrap(:,3) = post_mpt;
125
126 output_cumtrap(:,4) = CI95_A(:,1);
127 output_cumtrap(:,5) =  CI95_A(:,2);
128 output_cumtrap(:,6) =  CI95_B(:,1);
129 output_cumtrap(:,7) =  CI95_B(:,2);
130 output_cumtrap(:,8) =  CI95_C(:,1);
131 output_cumtrap(:,9) =  CI95_C(:,2);
132
133 output_cumtrap(:,10) = pre_mptd;
134 output_cumtrap(:,11) = mptd;
```

```
output_cumtrap(:,12) = post_mptd;

output_cumtrap(:,13) = CI95_A2(:,1);
output_cumtrap(:,14) =  CI95_A2(:,2);
output_cumtrap(:,15) =  CI95_B2(:,1);
output_cumtrap(:,16) =  CI95_B2(:,2);
output_cumtrap(:,17) =  CI95_C2(:,1);
output_cumtrap(:,18) =  CI95_C2(:,2);

output_cumtrap(:,19) = enwx';
output_4 = array2table(output_cumtrap,'variablenames',{'IRD_mean_pre','
    IRD_mean_mpt','IRD_mean_post','IRDu_pre','IRDl_pre','IRDu_mpt','IRDl_mpt
    ','IRDu_post','IRDl_post','d18o_mean_pre','d18o_mean_mpt','
    d18o_mean_post','d18ou_pre','d18ol_pre','d18ou_mpt','d18ol_mpt','
    d18ou_post','d18ol_post','time'});
writetable(output_4,'outputs/cumulative_glacials.csv')

%%%%--------- Output Table ---------%%%%
% column 1 is the peak-lag algorithm result
output{1,1} = nanmean(bd13c_lags); % mean
output{2,1} = ci(1); % upper confidence
output{3,1} = ci(2); % lower confidence
% columns 2,3,4 are the blackman-tukey phase estimates
output{1,2} = -1*pr_lag(1);
output{2,2} = -1*pr_lag(3);
output{3,2} = -1*pr_lag(2);
output{1,3} = -1*ob_lag(1);
output{2,3} = -1*ob_lag(3);
output{3,3} = -1*ob_lag(2);
output{1,4} = -1*ec_lag(1);
output{2,4} = -1*ec_lag(3);
output{3,4} = -1*ec_lag(2);
%column 5 is the cross-correlaion estimate
output{1,5} = lag(Cxy1==min(Cxy1));
output{2,5} = lag(Cxy1==min(Cxy1))-mean(diff(lag));
output{3,5} = lag(Cxy1==min(Cxy1))+mean(diff(lag));

output_table = cell2table(output,'variablenames',{'peak_lag','precession_BT
    ','obliquity_BT','eccentricity_BT','cross_correlation'});
writetable(output_table,'outputs/lag_results.csv')
```

```
170
171
172 function [Cxy, lag, Q1] = analysis_1(t,x1,x2);
173 % Cross-correlation
174 % This follows the work of Kira Rehfeld (2014). It utilises their NESTool
175 %toolbox http://tocsy.pik-potsdam.de/nest.php
176
177 tx = t(~isnan(x1)); % tx is age with only points sampled for d13C
178 x = x1(~isnan(x1)); %x is d13C without gaps
179 ty = t(~isnan(x2)); %ty is age with only points sampled for IRD_MAR
180 y = x2(~isnan(x2)); %y is IRD_MAR without gaps
181
182 h = 0.5; %this sets the kernel width in units of dt (Rehfeld 2011)
183 lag = [-50 : 1 : 50]; %this sets the lags at which we want to measure
      correlation
184 [Cxy] = nexcf(tx,x,ty,y,lag,h); %the NEXCF function uses gaussian kernel
      approach
185
186 % Monte Carlo routine on surrogate red noise data, this is time consuming
187 if ~exist('CSur1000.mat') % check to see if there is already a datafile for
       the surrogate
188     NoSur=1000; % number of surrogates for MC analysis. For most reliable
      results, set to 1000.
189     XSur=ar1sur(tx,x,NoSur); % create AR1 Surrogates for X/Y
190     YSur=ar1sur(ty,y,NoSur);
191
192     wa=waitbar(0,'Surrogate tests');
193     for k=1:NoSur
194         waitbar(k/NoSur)
195         %gXCF
196         [temp1] = nexcf(tx,XSur(:,k),ty,YSur(:,k),lag,h);
197         CSur1000(k,:,:)=temp1;
198         clear temp1 temp2
199     end
200     save('CSur1000.mat')
201     delete(wa)
202 else
203     load('CSur1000.mat'); %load a pre-run Monte Carlo series
204 end
205 % - quantiles for each point from Csur to obtain critical values
```

```
206 Q1=quantile(CSur1000,[.05 .95],1); %find the 5th and 95th percentile
207
208 end
209
210 function [x2lags, Q, q] = analysis_3(t,dt,age,x1,x2,filtype,filtdeg,dif,
      max_dist);
211
212 %---- preamble ----%
213 max_distance = max_dist; % maximum distance to search between x1 and x2
      peaks
214 pdist1 = 15; pdist2 = 15;% set minimum peak distance for x1 (1) and x2 (2)
215 pheight1 = 0.075; pheight2 = 0.01; % set min peak height for x1 and x2:
      reccomended 0.075 for irdmar and 0.01 for bd13c
216
217 %---- Step 1: linear interpolation ----%
218 tl = fliplr(t.*-1)';
219 age1 = age(~isnan(x1));
220 x1 = x1(~isnan(x1));
221 xl1 = interp1(-age1,x1,tl,'linear','extrap');
222 age2 = age(~isnan(x2));
223 x2 = x2(~isnan(x2));
224 xl2 = interp1(-age2,x2,tl,'linear','extrap');
225
226 xl1 = normalize(xl1); % zscore normalization
227 xl2 = normalize(xl2); % zscore normalization
228
229 %---- Step 2: Filter ----%
230 if filtype == 1
231     SM = filtdeg;
232     f1s = filtfilt (ones(1,round(SM/dt))/round(SM/dt),1,xl1); % Moving-
      average
233     f2s = filtfilt (ones(1,round(SM/dt))/round(SM/dt),1,xl2); % Moving
      average
234 end
235 if filtype == 2
236     sgolay_degree = filtdeg;
237     sgolay_len = 31; % Savitsky-Golay Filter Length
238     f1s = sgolayfilt(xl1,sgolay_degree,sgolay_len); % Savitsky-Golay method
239   f2s = sgolayfilt(xl2,sgolay_degree,sgolay_len); % Savitsky-Golay method
240 end
```

```
241 %---- Step 3: First Difference ----%
242 if dif == 1
243     tDiff = tl(1:length(tl)-1,:) + diff(tl)/2; % generic timescale for 1st
      differential
244     for i = 1 : length(tl)-1
245         x1diff(i) = (f1s(i+1) - f1s(i))./(tl(i+1)-tl(i));
246         x2diff(i) = (f2s(i+1) - f2s(i))./(tl(i+1)-tl(i));
247     end
248 end
249
250 %---- Step 4: findpeaks ----%
251 [pks1,lcs1]=findpeaks(x1diff,tDiff,'minpeakdistance',pdist1,'minpeakheight
      ',pheight1); % find x1 peaks
252 [pks2,lcs2]=findpeaks(x2diff,tDiff,'minpeakdistance',pdist2,'minpeakheight
      ',pheight2); % find x2 peaks
253
254 for i = 1:length(pks2)
255     l = lcs2(i);
256     l2 = find(lcs1 >= l-max_distance & lcs1 < l+max_distance,1,'first');
257     if isempty(l2)
258         bin1(i) = NaN; % this means there is not ird peak within the max
      distance of the 13c peak
259     else
260         bin1(i)=lcs2(i)-lcs1(l2);
261     end
262 end
263
264 %---- Step 5: checl with event synchronization (Rehfeld 2013) ----%
265 for i = 0:5
266 [Q(i+1),q(i+1)] = eventsynchro(tDiff,x1diff,tDiff,x2diff,i,0.9);
267 end
268
269 display(['Events Found: ',num2str(length(bin1))])
270 display(['Average Lag: ',num2str(nanmean(-bin1))])
271
272 x2lags = -bin1;
273 end
274
275
276 function [d18o_cum, ird_cum, time_cum, time_cum_norm, f3s, tl] = analysis_4
```

```
    (t,dt,age,d18o,x1,plt);
277
278 %---- Step 1: linear interpolation of bd18O ----%
279 tl = fliplr(t.*-1)';
280 age1 = age(~isnan(d18o));
281 x3 = d18o(~isnan(d18o));
282 x3l = interp1(-age1,x3,tl,'linear','extrap');
283 age2 = age(~isnan(x1));
284 x1 = x1(~isnan(x1));
285 x1l = interp1(-age2,x1,tl,'linear','extrap');
286
287 %---- Step 2: Filter bd18O ----%
288 SM = 10; % moving average filter degree
289 f3s = filtfilt (ones(1,round(SM/dt))/round(SM/dt),1,x3l); % Moving average
290
291 %---- Step 3: Divide d18O into Glacials ----%
292 % lcs = load('glac_load.mat');
293 % pk = lcs.glac_load;
294 [~,pk] = findpeaks(-f3s,tl,'minpeakheight',-3.37,'minpeakdistance',25);
295 pk = [pk; -496; -76];
296 pk=sort(pk);
297 pk = pk(2:end)
298 clear('cp','ircp','d18c','tp')
299 %---- Step 4: Integrate under d18O curve for each glacial ----%
300 for i = 1 : length(pk)
301     n1 = find(tl>=pk(i),1,'first');
302     if i == length(pk)
303         n2 = find((tl<=0) & (f3s>=(3.75-0.43)),1,'last'); % run between
      peak interglacial and the next time 18O crosses a threshold
304     else
305     n2 = find((tl<=pk(i+1)) & (f3s>=(3.75-0.43)),1,'last'); % run between
      peak interglacial and the next time 18O crosses a threshold
306     end
307     if isempty(n1)
308         cp{i} = [];
309         ircp{i} = [];
310         d18c{i} = [];
311     end
312     if isempty(n2)
313         cp{i} = [];
```

```
314         ircp{i} = [];
315         d18c{i} = [];
316     end
317     if (~isempty(n1)) && (~isempty(n2))
318         xx = normalize(x3l(n1:n2),'range',[0 1]);
319         cp{i} = cumtrapz(tl(n1:n2),xx); %cumtrapz integrates and records
        the results in cp
320         ircp{i} = cumtrapz(tl(n1:n2),x1l(n1:n2));
321         d18c{i} = x3l(n1:n2);
322     end
323     tp{i} = tl(n1:n2);
324 end
325
326 %---- Step 5: 'normalise' the results to percentages of total accumulation
        ----%
327 clear('cpp','ircpp','tpp')
328 for i = 1:length(cp)
329     cpp{i} = (cp{i}./(max(cp{i}))).*100;
330     ircpp{i} = (ircp{i}./(max(ircp{i}))).*100;
331 end
332 % do the same for time
333 for i = 1:length(tp)
334     tpp{i} = (tp{i}-min(tp{i}));
335     tpp{i} = (tpp{i}./(max(tpp{i}))).*100;
336 end
337
338 %---- Step 6: Prepare outputs ----%
339 d18o_cum = cpp;
340 ird_cum = ircpp;
341 time_cum = tp;
342 time_cum_norm = tpp;
343
344 end
```

Appendix Code 2: Chapter 5 Data Processing

8.4 Appendix Code 2

Overview

This notebook is split into 3 parts:

1. loading the single-specimen isotope data and calculating confidence intervals for *G. truncatulinoides*
2. applying confidence intervals to downcore data
3. cleaning and smoothing downcore data by various aproaches

Input

`data/raw/U1475_gtrunc_IFA.csv` <- raw Individual Foram. Analysis data of G. truncatulinoides (sin) in 4 samples from Site U1475
`data/raw/U1475_MPT_trunc.csv` <- the raw U1475 proxy data (partially published by *Starr et al., 2021* and *Ziegler et al., 2013*)
`data/raw/starr_et_al_2020_age_model.csv` <- Starr 2021 LR04 Age Model
`data/raw/U1475_Pmag_U1476_age_model.csv` <- U1476 pMag Age Model (Barker et al., 2021)

Output

`/data/interim/u1475_starr_CI.csv` <- the raw U1475 proxy data with 95% Confidence Intervals added for G. truncat. d13C and d18O
`/data/interim/u1475_smoothed_series.csv` <- the smoothed series (using PCHIP and LOWESS, detailed below)
`/data/interim/u1475_binned.csv` <- the binned series (detailed below)

In [2]:

```
# PREAMBLE - import dependencies (all depencies are available in the virtual enviro
import numpy as np
import matplotlib as mpl
import pandas as pd
import pyleoclim as pyl
import matplotlib.gridspec as gridspec

from matplotlib import pyplot as plt
from matplotlib.ticker import (MultipleLocator, AutoMinorLocator)
from scipy.interpolate import interp1d
from scipy.interpolate import PchipInterpolator
from scipy.stats import sem
from statsmodels.nonparametric.smoothers_lowess import lowess as  sm_lowess
```

In [3]:

```
### ---- Useful Functions to be called throughout --- ###

def age_model(depth_in,tie_points):
    """ Takes a depth scale and converts it to age using the tie_points specified""
    y = tie_points.iloc[:,1] # AGE POINTS in position 1; sample every 5
    y[0] = 0 # froce minimum age of 0
    x = tie_points.iloc[:,0] # DEPTH POINTS in position 0; sample every 5
    x[0] = 0 # force minimum depth of 0
    f = interp1d(x,y,fill_value="extrapolate")
    age_out = f(depth_in) # interpolate depth in onto age model defined by tie_poir
    return age_out
```

3 - Applying C.I for downcore data

- taking the sigma estimated from IFA in section 1aand using the standard error of the mean
- *possibly more sophisticated ways of doing this, especially as the IFA for d18O is not normal (fails Shapiro-Wilks test)*

$$\sigma_{\bar{x}} = \frac{\sigma}{\sqrt{n}}$$

where σ is the standard deviation of multiple individually-measured foram specimens from an individual sample.

In [10]:

```
n = (u1475_starr['trunc specimens']<=2) # all samples with n smaller than or equal
u1475_starr['d18Otrunca'].loc[n] = np.nan # set to nan (i.e. remove)
u1475_starr['d13Ctrunc'].loc[n] = np.nan

# sem = sigma / sqrt(n)
sem_13 = u1475_starr.apply(lambda x : (0.308/np.sqrt(x['trunc specimens']) if x['tr
u1475_starr['d13C_trunc_upper95'] = u1475_starr['d13Ctrunc'] + (1.96*sem_13)
u1475_starr['d13C_trunc_lower95'] = u1475_starr['d13Ctrunc'] - (1.96*sem_13)
sem_18 = u1475_starr.apply(lambda x : (0.404/np.sqrt(x['trunc specimens']) if x['tr
u1475_starr['d18O_trunc_upper95'] = u1475_starr['d18Otrunca'] + (1.96*sem_18)
u1475_starr['d18O_trunc_lower95'] = u1475_starr['d18Otrunca'] - (1.96*sem_18)
```

In [11]:

```
x = u1475_starr['Median Age (kyr)']
bin_size = 8 # 8-kyr bins

d18O_bin = bin_AS(x, u1475_starr['d18Otrunca'], bin_size=bin_size,start=0,stop=1540
d13C_bin = bin_AS(x, u1475_starr['d13Ctrunc'], bin_size=bin_size,start=0,stop=1540,
n_bin = bin_AS(x, u1475_starr['trunc specimens'], bin_size=bin_size,start=0,stop=15

u1475_binned = pd.DataFrame()
u1475_binned['Age_mid (kyr)'] = d18O_bin['age']
u1475_binned['d18O_ G. trunc'] = d18O_bin['values']
u1475_binned['d13C_ G. trunc'] = d13C_bin['values']
u1475_binned['n_bins'] = d18O_bin['n']
u1475_binned['n_samples'] = n_bin['values']
u1475_binned['d18O_stat_error'] = d18O_bin['stat_error']
u1475_binned['d13C_stat_error'] = d13C_bin['stat_error']

# apply error to the newly binned data (with sum(n) from samples in each bin)
u1475_binned['d18O_sys_error'] = (0.404/np.sqrt(u1475_binned['n_samples']))
u1475_binned['d13C_sys_error'] = (0.308/np.sqrt(u1475_binned['n_samples']))

# combine systematic and statistical error
u1475_binned['d18O_total_error'] = 1.96*(np.sqrt(u1475_binned['d18O_stat_error']**2
u1475_binned['d13C_total_error'] = 1.96*(np.sqrt(u1475_binned['d13C_stat_error']**2

# remove samples where n is still lower than 3
n = (u1475_binned['n_samples']<=2) # all samples with n smaller than 3
u1475_binned['d18O_ G. trunc'].loc[n] = np.nan
u1475_binned['d13C_ G. trunc'].loc[n] = np.nan
u1475_binned['d18O_total_error'].loc[n] = np.nan
u1475_binned['d13C_total_error'].loc[n] = np.nan
u1475_binned['n_samples'].loc[n] = np.nan
u1475_binned['n_bins'].loc[n] = np.nan


##### do benthics
u1475_starr.rename(columns={'Median Age (kyr)':'Age_mid (kyr)','C. wuellerstorfi d1

u1475_starr['Cwuel_d18O (+0.64)'] = u1475_starr['Cwuel_d18O']+0.64
u1475_starr['Dd18O'] = u1475_starr['d18Otrunca']-u1475_starr['Cwuel_d18O (+0.64)']
u1475_starr['Dd13C'] = u1475_starr['d13Ctrunc']-u1475_starr['Cwuel_d13C']

d18O_bin = pyl.utils.tsutils.bin(u1475_starr['Age_mid (kyr)'], u1475_starr['Cwuel_d
d13C_bin = pyl.utils.tsutils.bin(u1475_starr['Age_mid (kyr)'], u1475_starr['Cwuel_d

# Combine
u1475_binned['Cwuel_d18O'] = pd.Series(d18O_bin['binned_values'])
u1475_binned['Cwuel_d13C'] = pd.Series(d13C_bin['binned_values'])

u1475_binned['Dd13C'] = u1475_binned['d13C_ G. trunc']-u1475_binned['Cwuel_d13C']
u1475_binned['Dd18O'] = u1475_binned['d18O_ G. trunc']-u1475_binned['Cwuel_d18O']
u1475_binned['Dd13C_upper'] = (u1475_binned['d13C_ G. trunc']+u1475_binned['d13C_to
u1475_binned['Dd13C_lower'] = (u1475_binned['d13C_ G. trunc']-u1475_binned['d13C_to
u1475_binned['Dd18O_upper'] = (u1475_binned['d18O_ G. trunc']+u1475_binned['d18O_to
u1475_binned['Dd18O_lower'] = (u1475_binned['d18O_ G. trunc']-u1475_binned['d18O_to
#
```

In [16]:

```
# intialize empty dataframe with a linearly-spaced age scale from 1-1550 kyrs and a
x_new = np.arange(1,1550,5)
smoothed = pd.DataFrame()
smoothed['Age [linear]'] = x_new
K = 100000 # number of bootstrap iterations

def pre_process(x,y,yerr):
    x=x[y.notnull()]
    yerr=yerr[y.notnull()]
    y=y[y.notnull()]
    y=y[x.notnull()]
    yerr=yerr[x.notnull()]
    x=x[x.notnull()]
    y=y.drop([858])
    x=x.drop([858])
    yerr=yerr.drop([858])

    y = y[yerr.notnull()]
    x = x[yerr.notnull()]
    yerr=yerr[yerr.notnull()]

    if np.max(yerr)!=0:
        yerr=(yerr-y)/1.96 # convert into standard error of mean
    return x,y,yerr

def pchip_(x,y,x_new,yerr):

    # BOOTSTRAP ROUTINE
    x = x.reset_index(drop=True)
    y = y.reset_index(drop=True)
    if np.max(yerr)!=0:
        y = np.random.normal(y,yerr)
    samples = np.random.choice(len(x), round(len(x)*0.95), replace=True) # take 90%
    n = np.unique(samples)
    x_s = x[n]
    y_s = y[n]
    f = PchipInterpolator(x_s,y_s) # interpolate the subsample using the PCHIP appr
    ynew = f(x_new) # apply the interpolator to the new age scale
    return ynew


### PCHIP d18O
x,y,yerr = pre_process(u1475_starr['Age_mid (kyr)'],u1475_starr['d18Otrunca'],u1475
stk = np.stack([pchip_(x, y, x_new,yerr) for k in range(K)]).T
mean = np.nanmean(stk, axis=1)
c5 = np.nanpercentile(stk, 5, axis=1) # 5 percent
c95 = np.nanpercentile(stk, 95, axis=1) # 95 percent
# a 95% confidence interval
smoothed['d18O_PCHIP'] = mean
smoothed['d18O_95'] = c95
smoothed['d18O_5'] = c5


### PCHIP d13C
x,y,yerr = pre_process(u1475_starr['Age_mid (kyr)'],u1475_starr['d13Ctrunc'],u1475_
stk = np.stack([pchip_(x, y, x_new,yerr) for k in range(K)]).T
mean = np.nanmean(stk, axis=1)
c5 = np.nanpercentile(stk, 2.5, axis=1) #2.5 percent
c95 = np.nanpercentile(stk, 95, axis=1) # 95 percent
# a 95% confidence interval
```

```
smoothed['d13C_PCHIP'] = mean
smoothed['d13C_95'] = c95
smoothed['d13C_5'] = c5

###### DO BENTHICS AS WELL
### PCHIP d18O
yerr = pd.Series(np.zeros(len(u1475_starr['Age_mid (kyr)'])))
x,y,yerr = pre_process(u1475_starr['Age_mid (kyr)'],u1475_starr['Cwuel_d18O'],yerr)
stk = np.stack([pchip_(x, y, x_new,yerr) for k in range(K)]).T
mean = np.nanmean(stk, axis=1)
c5 = np.nanpercentile(stk, 2.5, axis=1) #2.5 percent
c95 = np.nanpercentile(stk, 95, axis=1) # 95 percent
# a 95% confidence interval
smoothed['c18O_PCHIP'] = mean
smoothed['c18O_95'] = c95
smoothed['c18O_5'] = c5

### PCHIP d13C
yerr = pd.Series(np.zeros(len(u1475_starr['Age_mid (kyr)'])))
x,y,yerr = pre_process(u1475_starr['Age_mid (kyr)'],u1475_starr['Cwuel_d13C'],yerr)
stk = np.stack([pchip_(x, y, x_new,yerr) for k in range(K)]).T
mean = np.nanmean(stk, axis=1)
c5 = np.nanpercentile(stk, 2.5, axis=1) #2.5 percent
c95 = np.nanpercentile(stk, 95, axis=1) # 95 percent
# a 95% confidence interval
smoothed['c13C_PCHIP'] = mean
smoothed['c13C_95'] = c95
smoothed['c13C_5'] = c5

## gradients
smoothed['Dd13C_PCHIP'] = smoothed['d13C_PCHIP'] - smoothed['c13C_PCHIP']
smoothed['Dd13C_5'] = smoothed['d13C_5'] - smoothed['c13C_PCHIP']
smoothed['Dd13C_95'] = smoothed['d13C_95'] - smoothed['c13C_PCHIP']
smoothed['Dd18O_PCHIP'] = smoothed['d18O_PCHIP'] - smoothed['c18O_PCHIP']
smoothed['Dd18O_5'] = smoothed['d18O_5'] - smoothed['c18O_PCHIP']
smoothed['Dd18O_95'] = smoothed['d18O_95'] - smoothed['c18O_PCHIP']
```

Appendix Code 3: Carbon Isotope Compilation

8.5 Appendix Code 3

In [1]:

```
cd '/home/aidan/Insync/StarrA1@cardiff.ac.uk/OneDrive Biz/Files/Projects/U1475/subp
```

```
/home/aidan/Insync/StarrA1@cardiff.ac.uk/OneDrive Biz/Files/Projects/
U1475/subproject_repos/Gtrunc_paper
```

In [2]:

```
# PREAMBLE
import numpy as np
import matplotlib as mpl
import pandas as pd
import pyleoclim as pyl
import matplotlib.gridspec as gridspec
import statsmodels.api as sm
from matplotlib import pyplot as plt
from matplotlib.ticker import (MultipleLocator, AutoMinorLocator)
from scipy.interpolate import interp1d
from scipy.ndimage import gaussian_filter1d
from scipy.stats import shapiro
import scipy.stats as stats
from sklearn.linear_model import LinearRegression
import seaborn as sns
import io
import requests
import xarray as xr
import cartopy.crs as ccrs
import os
from scipy.interpolate import PchipInterpolator
import warnings
warnings.filterwarnings("ignore")
# plotting style
pyl.utils.plotting.set_style(style={'matplotlib','_spines','_nogrid'})

mpl.rcParams.update({
    'font.family':'sans-serif',
    'font.size':12,
    'font.sans-serif':['Liberation Sans'],
    'lines.linewidth':1.2
    })


# Load LR04
url = 'http://www.lorraine-lisiecki.com/LR04stack.txt'
s=requests.get(url).content
c = pd.read_csv(io.StringIO(s.decode('utf-8')),header=3,sep='\t',nrows=1100)
LR04 = c.rename(columns={'Time (ka)':'Age [ka BP]','Benthic d18O (per mil)':'d18O'}
```

In [3]:

```
%matplotlib inline
```

In [4]:

```
### ---- Useful Functions to be called throughout --- ###

def age_model(depth_in,tie_points):
    """ Takes a depth scale and converts it to age using the tie_points specified"
    y = tie_points.iloc[::5,1] # AGE POINTS in position 1; sample every 5
    y[0] = 0 # froce minimum age of 0
    x = tie_points.iloc[::5,0] # DEPTH POINTS in position 0; sample every 5
    x[0] = 0 # force minimum depth of 0
    f = interp1d(x,y,fill_value="extrapolate")
    age_out = f(depth_in) # interpolate depth in onto age model defined by tie_poir
    return age_out

def load_site(site):
    s=requests.get(site['url']).content
    c = pd.read_csv(io.StringIO(s.decode('utf-8')),header=site['header'],sep='\t')
    return c
```

Part 1: Get Data

In [23]:

```
sites = ['U1475','U1476','U1308','MD06_3018','ODP1143','ODP1090','ODP1088','ODP925'
```

In [24]:

```
ODP980 = {}
ODP980['url'] = 'http://moraymo.us/wp-content/uploads/2014/04/s980-981ageSBP90isoci
ODP980['header'] = 0
ODP980['chron'] = 'LR04'
ODP980['data'] = pd.read_table('data/isotope_compilation_raw/ODP980_981.csv',sep=",
ODP980['meta'] = {'lat':55.485,
                  'lon':-14.701667,
                  'depth':2172,
                  'ref':"Oppo1998; Flower2000; McManus1999",
                 'offset':'none',
                 'basin':'Atl'}


ODP982 = {}
ODP982['url'] = 'http://moraymo.us/wp-content/uploads/2014/04/s982ageSBP90isocib.tx
ODP982['header'] = 0
ODP982['chron'] = 'S95'
ODP982['data'] = load_site(ODP982)
ODP982['data'].rename(columns={'depth (mcd)':'Depth [m]','982 O18':'d18O','982 C13'
ODP982['meta'] = {'lat':57.516667,
                  'lon':-15.866667,
                  'depth':1134,
                  'ref':"Venz1999; Venz2002",
                 'offset':'none',
                 'basin':'Atl'}

ODP983 = {}
ODP983['url'] = 'http://moraymo.us/wp-content/uploads/2014/04/s983ageSBP90isocib.tx
ODP983['header'] = 0
ODP983['chron'] = 'SBP90'
ODP983['data'] = load_site(ODP983)
ODP983['data'].rename(columns={'depth (mcd)':'Depth [m]','O18-983':'d18O','C13-983'
ODP983['meta'] = {'lat':60.4033333333333,
                  'lon':-23.6406666666667,
                  'depth':1983,
                 'ref':'Klieven2003; Raymo1998',
                 'offset':'none',
                 'basin':'Atl'}
ODP984 = {}
ODP984['url'] = 'http://moraymo.us/wp-content/uploads/2014/04/s984ageSBP90isocib.tx
ODP984['header'] = 0
ODP984['chron'] = 'SBP90'
ODP984['data'] = load_site(ODP984)
ODP984['data'].rename(columns={'depth (mcd)':'Depth [m]','984 O18 ':'d18O','984 C13
ODP984['meta'] = {'lat':61.4251166666667,
                  'lon':-24.0825,
                  'depth':1649,
                 'ref':'Raymo2004',
                 'offset':'none',
                 'basin':'Atl'}

DSDP552 = {}
DSDP552['url'] = 'http://moraymo.us/wp-content/uploads/2014/04/552iso_ageLR04_0-1.3
DSDP552['header'] = 0
DSDP552['chron'] = 'LR04'
DSDP552['data'] = load_site(DSDP552)
DSDP552['data'].rename(columns={'LR04 age (ka)':'Age [ka BP]','Depth (m)':'Depth [m
DSDP552['meta'] = {'lat':56.0427,
                  'lon':-23.2313,
                  'depth':2301,
```

```
                  'ref':'Shackleton1984',
                  'offset':'d18O+0.64',
                  'basin':'Atl'}

DSDP607 = {}
DSDP607['url'] = 'http://moraymo.us/wp-content/uploads/2014/04/607iso_ageLR04_0-1.3
DSDP607['header'] = 0
DSDP607['chron'] = 'LR04'
DSDP607['data'] = load_site(DSDP607)
DSDP607['data'].rename(columns={'LR04age(ka)':'Age [ka BP]','Depth':'Depth [m]'},in
DSDP607['data']['d18O'].values[DSDP607['data']['d18O']>4] = np.nan
DSDP607['data']['d13C'].values[DSDP607['data']['d13C']>4] = np.nan
DSDP607['meta'] = {'lat':41,
                   'lon':-32.2313,
                   'depth':3427,
                   'ref':"Ruddiman1989; Raymo1989",
                   'offset':'d18O+0.64',
                    'basin':'Atl'}

ODP846 = {}
ODP846['url'] = 'http://moraymo.us/wp-content/uploads/2014/04/s846ageSBP90isocib.tx
ODP846['header'] = 0
ODP846['chron'] = 'SBP90'
ODP846['data'] = load_site(ODP846)
ODP846['data'].rename(columns={'RMCDepth (m)':'Depth [m]','846 O18':'d18O','846 C13
ODP846['meta'] = {'lat':-3.09493333333333,
                   'lon':-90.8179666666667,
                   'depth':3296,
                  'ref':'Mix1995',
                  'offset':'none',
                  'basin':'Pac'}

ODP664 = {}
ODP664['url'] = 'http://moraymo.us/wp-content/uploads/2014/04/664iso_ageLR04_0-1.3m
ODP664['header'] = 0
ODP664['chron'] = 'LR04'
ODP664['data'] = load_site(ODP664)
ODP664['data'].rename(columns={'LR04 age (ka)':'Age [ka BP]','Comp. Depth':'Depth [
ODP664['meta'] = {'lat':0.1073,
                   'lon':-23.2275,
                   'depth':3806,
                  'ref':'Raymo1997',
                  'offset':'d18O+0.64',
                  'basin':'Atl'}

ODP677 = {}
ODP677['url'] = 'http://moraymo.us/wp-content/uploads/2014/04/677iso_ageLR04_0-1.3m
ODP677['header'] = 0
ODP677['chron'] = 'LR04'
ODP677['data'] = load_site(ODP677)
ODP677['data'].rename(columns={'LR04 age (ka)':'Age [ka BP]','Depth':'Depth [m]'},i
ODP677['meta'] = {'lat':1.2023,
                  'lon':-83.737,
                  'depth':3472}

DSDP502 = {}
DSDP502['url'] = 'https://doi.pangaea.de/10.1594/PANGAEA.52481?format=textfile'
DSDP502['header'] = 17
DSDP502['chron'] = 'TP607'
DSDP502['data'] = load_site(DSDP502)
DSDP502['data'].rename(columns={'C. wuellerstorfi δ18O [‰ PDB]':'d18O','C. wuellers
DSDP502['meta'] = {'lat': 11.491,
```

```
                'lon':-79.3797,
                'depth':3051,
                'sill':1800,
                    'ref':'deMenocal1992',
                   'offset':'d18O+0.64',
                   'basin':'Atl'}

ODP659 = {}
ODP659['url'] = 'https://doi.pangaea.de/10.1594/PANGAEA.746218?format=textfile'
ODP659['header'] = 18
ODP659['chron'] = 'nul'
ODP659['data'] = load_site(ODP659)
ODP659['data'].rename(columns={'C. wuellerstorfi δ18O [‰ PDB]':'d18O','C. wuellerst
ODP659['meta'] = {'lat':18.0772,
                  'lon':-21.0262,
                  'depth':3071,
                  'ref':'Sarnthein1989',
                  'offset':'none',
                  'basin':'Atl'}

ODP849={}
ODP849['url'] = 'https://doi.pangaea.de/10.1594/PANGAEA.60255?format=textfile'
ODP849['header']=22
ODP849['chron'] = 'SPB90'
ODP849['data'] = load_site(ODP849)
ODP849['data'].rename(columns={'Depth [m]':'old Depth','Depth cr [rmcd]':'Depth [m]
ODP849['data'].sort_values(by='Depth [m]',axis=0,inplace=True)
ODP849['meta'] = {'lat':0.1823,
                  'lon':-110.5197,
                  'depth':3839,
                  'ref':'Mix1995',
                  'offset':'none',
                  'basin':'Pac'}

ODP925 = {}
ODP925['url'] = 'https://doi.pangaea.de/10.1594/PANGAEA.871107?format=textfile'
ODP925['header'] = 36
ODP925['chron'] = 'Wil17'
ODP925['data'] = load_site(ODP925)
df = ODP925['data']
ODP925['data'] = df[(df['Foram bent']=='CWUE')]
ODP925['data'].rename(columns={'Depth [m]':'old Depth','Depth comp [mcd]':'Depth [m
ODP925['meta'] = {'lat':4.20415,
                  'lon':-43.4889,
                  'depth':3041,
                  'ref':'Wilkens2017',
                  'offset':'none',
                  'basin':'Atl'}

ODP1088 = {}
ODP1088['url'] = 'https://doi.pangaea.de/10.1594/PANGAEA.218111?format=textfile'
ODP1088['chron'] = 'Mix95'
ODP1088['header'] = 19
ODP1088['data'] = load_site(ODP1088)
ODP1088['data'].rename(columns={'Cibicidoides spp. δ18O [‰ PDB]':'d18O','Cibicidoic
ODP1088['meta'] = {'lat':-41.1361,
                  'lon':13.563,
                  'depth':2082,
                   'ref':'Hodell2003',
                   'offset':'none',
                   'basin':'Atl'}
```

```
ODP1090 = {}
ODP1090['url'] = 'https://doi.pangaea.de/10.1594/PANGAEA.218131?format=textfile'
ODP1090['header'] = 20
ODP1090['chron'] = 'Mix95'
ODP1090['data'] = load_site(ODP1090)
ODP1090['data'].rename(columns={'C. wuellerstorfi δ18O [‰ PDB]':'d18O','C. wuellers
ODP1090['meta'] = {'lat':-42.9137,
                   'lon':8.8997,
                   'depth':3700,
                    'ref':'Hodell2003',
                    'offset':'none',
                    'basin':'Atl'}

ODP1123 = {}
ODP1123['url'] = 'https://doi.pangaea.de/10.1594/PANGAEA.700860?format=textfile'
ODP1123['header'] = 39
ODP1123['data'] = load_site(ODP1123)
ODP1123['chron'] = 'nul'
ODP1123['data'] = ODP1123['data'].rename(columns={'Depth [m]':'old Depth','Depth cr
ODP1123['meta'] = {'lat':-41.786,
                   'lon':-171.499,
                   'depth':3290,
                     'ref':'Harris2002',
                    'offset':'d18O+0.64',
                    'basin':'Pac'}

ODP1143 = {}
ODP1143['url'] = 'https://doi.pangaea.de/10.1594/PANGAEA.784149?format=textfile'
ODP1143['header'] = 29
ODP1143['chron'] = 'TWC02'
ODP1143['data'] = load_site(ODP1143)
ODP1143['data'].rename(columns={'Depth [m]':'old depth','Depth comp [mcd]':'Depth [
ODP1143['data'].sort_values(by='Depth [m]',inplace=True)
ODP1143['meta'] = {'lat':9.35,
                   'lon':113.28,
                   'depth':2772,
                    'ref':'Cheng2004',
                    'offset':'none',
                    'basin':'Pac'}

GeoB3388 = {}
GeoB3388['url'] = 'https://doi.pangaea.de/10.1594/PANGAEA.686213?format=textfile'
GeoB3388['chron'] = 'SBP90'
GeoB3388['header'] = 16
GeoB3388['data'] = load_site(GeoB3388)
GeoB3388['data'].rename(columns={'C. wuellerstorfi δ13C [‰ PDB]':'d13C','C. wueller
GeoB3388['meta'] = {'lat':-25.22,
                   'lon':-75.525,
                   'depth':3558,
                     'ref':'Mohtadi2006',
                     'offset':'none',
                     'basin':'Pac'}

MD06_3018 = {}
MD06_3018['url'] = 'ftp://ftp.ncdc.noaa.gov/pub/data/paleo/contributions_by_author/
MD06_3018['header'] = 0
MD06_3018['chron'] = 'LR04'
MD06_3018['data'] = pd.read_csv('data/isotope_compilation_raw/russon2009.txt',delim
MD06_3018['data'].rename(columns={'Age(ka)':'Age [ka BP]'},inplace=True)
MD06_3018['meta'] = {'lat':-23,
                   'lon':166.15,
                   'depth':2470,
```

```
                    'ref':'Russon2009',
                    'offset':'d18O+0.64',
                     'basin':'Pac'}

ODP1063 = {}
ODP1063['url'] = 'https://www1.ncdc.noaa.gov/pub/data/paleo/contributions_by_author
ODP1063['header'] = 65
ODP1063['chron'] = 'LR04'
ODP1063['data'] = pd.read_csv('data/isotope_compilation_raw/poirier2014-1063comp.cs
ODP1063['data']['d18O'].values[ODP1063['data']['d18O']<-10] = np.nan
ODP1063['data']['d13C'].values[ODP1063['data']['d13C']<-10] = np.nan
ODP1063['meta'] = {'lat':33.6833,
                   'lon':-57.6167,
                   'depth':4583,
                      'ref':'Poirier2014',
                      'offset':'d18O+0.64',
                       'basin':'Atl'}


U1308 = {}
U1308['url'] = 'https://doi.pangaea.de/10.1594/PANGAEA.871936?format=textfile'
U1308['header'] = 26
U1308['chron'] = 'LR04'
U1308['data'] = load_site(U1308)
U1308['data'].rename(columns={'Cibicidoides sp. δ18O [‰ PDB]':'d18O','Cibicidoides
U1308['meta'] = {'lat':49.88,
                   'lon':-24.24,
                   'depth':3883,
                  'ref':'Hodell2016',
                  'offset':'none',
                   'basin':'Atl'}


U1476 = {}
U1476['chron'] = 'LR04'
U1476['data'] = pd.read_csv('data/isotope_compilation_raw/U1476_cib.csv')
U1476['meta'] = {'lat':-15.81,
                   'lon':41.76667,
                   'depth':2166,
                  'ref':'vanderLubbe2021; BArker2021',
                  'offset':'none',
                   'basin':'Ind'}


ODP1264 = {}
ODP1264['chron'] = 'LR04'
ODP1264['data'] = pd.read_csv('data/isotope_compilation_raw/bell2014-1264.txt',head
ODP1264['meta'] = {'lat':-28.53,
                   'lon':2.85,
                   'depth':2504,
                   'ref':'Bell2014',
                   'offset':'d18O+64',
                   'basin':'Atl'}
ODP1264['data'].rename(columns={'age_calkaBP':'Age [ka BP]','d13Cc.wuell':'d13C','d

ODP1267 = {}
ODP1267['chron'] = 'LR04'
ODP1267['data'] = pd.read_csv('data/isotope_compilation_raw/bell2014-1267.txt',head
ODP1267['meta'] = {'lat':-28.1,
                   'lon':1.71,
                   'depth':4355,
                   'ref':'Bell2014',
```

```
                  'offset':'d18O+64',
                  'basin':'Atl'}
ODP1267['data'].rename(columns={'age_calkaBP':'Age [ka BP]','d13Cc.wuell':'d13C','d

U1475 = {}
U1475['chron'] = 'LR04'
U1475['data'] = pd.read_csv('/home/aidan/Insync/StarrA1@cardiff.ac.uk/OneDrive Biz/
U1475['meta']  = {'lat':-41,
                  'lon':25,
                  'depth':3000,
                  'ref':'Starr2021',
                  'basin':'Ind'}
U1475['data'].rename(columns={'Cwu d13C (VPDB)':'d13C','Cwu d18O (VPDB)':'d18O','LR
```

Apply LR04 Age Models where nessecary

- many of the cores are already on the LR04 scale, however where they are not, they are mostly included in the LR04 stack
- use files from Lisiecki's website which contain a depth column and an LR04 age column

In [25]:

```
lr04s = 'data/isotope_compilation_raw/LR04cores_spec_corr/'
filz = os.listdir(lr04s)
sitz=[]
for site in sites:
    if eval(site)['chron'] != 'LR04':
        if os.path.isfile(lr04s+site+'.txt'):
            sitz.append(site)
            filee = pd.read_csv(lr04s+site+'.txt',delim_whitespace=True,header=None
            dataa = eval(site)['data']
            eval(site)['data']['Age [ka BP]'] = age_model(dataa['Depth [m]'], filee

dd = pd.DataFrame(columns=['site','lat','lon','depth'])
for site in sites:
    d = pd.DataFrame([eval(site)['meta']])
    d['site'] = site
    d['chron'] = eval(site)['chron']
    d['t_min'] = eval(site)['data']['Age [ka BP]'].min()
    d['t_max'] = eval(site)['data']['Age [ka BP]'].max()
    d['dt'] = eval(site)['data']['Age [ka BP]'].diff().mean()
    dd = pd.concat([d,dd])


#dd.to_latex(buf='fig/table1.tex',index=False,float_format="%.1f",columns=['site','
dd=dd.reset_index(drop=True)
dd.sort_values(by='depth')
```

Out[25]:

	lat	lon	depth	ref	offset	basin	site	chron
4	57.516667	-15.866667	1134	Venz1999; Venz2002	none	Atl	ODP982	S95
6	61.425117	-24.0825	1649	Raymo2004	none	Atl	ODP984	SBP90
5	60.403333	-23.640667	1983	Klieven2003; Raymo1998	none	Atl	ODP983	SBP90
14	-41.1361	13.563	2082	Hodell2003	none	Atl	ODP1088	Mix95
19	-15.81	41.76667	2166	vanderLubbe2021; BArker2021	none	Ind	U1476	LR04
3	55.485	-14.701667	2172	Oppo1998; Flower2000; McManus1999	none	Atl	ODP980	LR04
7	56.0427	-23.2313	2301	Shackleton1984	d18O+0.64	Atl	DSDP552	LR04
17	-23	166.15	2470	Russon2009	d18O+0.64	Pac	MD06_3018	LR04
1	-28.53	2.85	2504	Bell2014	d18O+64	Atl	ODP1264	LR04
16	9.35	113.28	2772	Cheng2004	none	Pac	ODP1143	TWC02
20	-41	25	3000	Starr2021	NaN	Ind	U1475	LR04
13	4.20415	-43.4889	3041	Wilkens2017	none	Atl	ODP925	Wil17
11	11.491	-79.3797	3051	deMenocal1992	d18O+0.64	Atl	DSDP502	TP607
9	-3.094933	-90.817967	3296	Mix1995	none	Pac	ODP846	SBP90
8	41	-32.2313	3427	Ruddiman1989; Raymo1989	d18O+0.64	Atl	DSDP607	LR04
15	-42.9137	8.8997	3700	Hodell2003	none	Atl	ODP1090	Mix95

	lat	lon	depth	ref	offset	basin	site	chron
10	0.1073	-23.2275	3806	Raymo1997	d18O+0.64	Atl	ODP664	LR04
12	0.1823	-110.5197	3839	Mix1995	none	Pac	ODP849	SPB90
18	49.88	-24.24	3883	Hodell2016	none	Atl	U1308	LR04
0	-28.1	1.71	4355	Bell2014	d18O+64	Atl	ODP1267	LR04
2	33.6833	-57.6167	4583	Poirier2014	d18O+0.64	Atl	ODP1063	LR04

Now interpolate and smooth

- interpolate onto a common timescale
- smooth using LOESS (same as for U1475)

In [ ]:

```
from src.clean_TS import bin_AS

def interpolate_records(site):

    x = eval(site)['data']['Age [ka BP]']
    y = eval(site)['data']['d18O']
    d18O_bin = bin_AS(x,y, bin_size=5,start=1,stop=3500,evenly_spaced=False,func='M
    result = pd.DataFrame()
    result['Age [ka BP]'] = d18O_bin['age']
    result[site+'_d18O'] = d18O_bin['values']
    result[site+'_d18O_error'] = d18O_bin['stat_error']

    y = eval(site)['data']['d13C']
    d13C_bin = bin_AS(x,y, bin_size=5,start=1,stop=3500,evenly_spaced=False,func='M
    result['Age [ka BP]'] = d13C_bin['age']
    result[site+'_d13C'] = d13C_bin['values']
    result[site+'_d13C_error'] = d13C_bin['stat_error']

    return result

binned = interpolate_records(sites[0])


for site in sites[1:]:
    result = interpolate_records(site)
    binned = binned.merge(result,on='Age [ka BP]')
```

In [34]:

```
##### Clean and export
binned_d18O = pd.DataFrame()
binned_d13C = pd.DataFrame()

for site in sites:
    binned_d18O[site] = binned[site+'_d18O']
    binned_d13C[site] = binned[site+'_d13C']
binned_d18O['Age [ka BP]'] = binned['Age [ka BP]']
binned_d18O.set_index('Age [ka BP]',inplace=True)
binned_d13C['Age [ka BP]'] = binned['Age [ka BP]']
binned_d13C.set_index('Age [ka BP]',inplace=True)

binned_d18O.to_csv('data/interim/d18O_benthic_compilation.csv')
binned_d13C.to_csv('data/interim/d13C_benthic_compilation.csv')
binned.to_csv('data/interim/full_compilation_benthic.csv')
```

In [21]:

```
dd.to_csv('data/interim/isotope_comp_meta.csv')
```